An Exploration of Iron(III) Complexes with Phenylpyrazole-Derived Ligands

Insights from Classical Redox Analyses and Advanced NMR-Spectroscopy

Tanja Hirschhausen

Zur Erlangung des Titels
Doktor der Naturwissenschaften

Universität Paderborn
Department Chemie
Februar 2024

General Information

The experimental investigations of this thesis were performed between April 2019 and June 2023 in the research group of Prof. Dr. Matthias Bauer.

Chairman:	Prof. Dr. Jan Paradies
First Reviewer:	Prof. Dr. Matthias Bauer
Second Reviewer:	PD Dr. Hans Egold
Third Reviewer:	Prof. Dr. Martin Brehm

Declaration

I hereby accept the regulations to achieve a doctoral degree of the faculty of natural sciences of the Paderborn University dated March 31, 2021. Issued by Paderborn University on the basis of Section §2 Section 4 and §67 Section 3 of the Higher Education Act of the State of North Rhine-Westphalia (Higher Education Act - HG) of September 16, 2014 (GV.NRW. p. 547), last amended by Article 1 of the Act of December 1, 2020 (GV. NRW. p. 1110).

Paderborn, ...
Tanja Hirschhausen

I hereby certify that I have written this thesis independently and that I have only used the the sources and aids listed here. The ideas directly or indirectly from external sources are identified as such. I have not applied for the opening of the doctoral procedure at any other place and this dissertation has not been rejected by any other department or faculty.

Paderborn, ...
Tanja Hirschhausen

Acknowledgements

An dieser Stelle ist es Zeit allen Personen zu danken, die durch ihre anhaltende Unterstützung maßgeblich zum Erfolg dieser Arbeit beigetragen haben und mich durchgehend bei diesem Vorhaben motivierten.

Prof Dr. Matthias Bauer gilt mein Dank in erster Linie für die Betreuung während der gesamten Arbeit und der Überlassung des Forschungsthemas. Dies gilt vor allen den konstruktiven Diskussionen und Freiheiten innerhalb des Themas, die die Tiefe der Auswertung erst möglich machte.

Ein besonderer Dank gilt Herrn PD Dr. Hans Egold, nicht nur für die Übernahme des Zweitgutachtens, sondern vor allem für die unermüdliche Arbeit bei der Erstellung und Auswertung zahlreicher NMR-Spektren.

Ein weiterer Dank gilt Herr Prof. Dr. Brehm für die Übernahme des Drittgutachtens und die Unterstützung bei den theoretischen Berechnungen, sowie Herr Prof. Dr. Paradies für die Übernahme des Prüfungsvorsitzes.

Ein sehr großer Dank gebührt allen Mitarbeitenden der zentralen Analytik. Dr. Roland Schoch für die Aufnahme der kristallographischen Daten, sowie zahlreichen Diskussionen und Messzeit-Nachtschichten. Dr. Adam Neuba gebührt Dank für die Erstellung der massenspektrometrischen und spektroeletrochemischen Messungen. Christiane Gloger möchte ich für die Massenspektren und zahlreiche Elementaranalysen danken und den Sonnenschein den sie immer mit ins Labor gebracht hat. Frau Stolte danke ich für Ihre Geduld mit meinen zahlreichen NMR-Spektren und dass ich nie für meine verrückten Ideen verurteilt wurden. Dr. Michał Nowakowski danke ich für die Unterstützung bei den NMR-bezogenen Berechnungen und anspruchsvollen Diskussionen in diesem Feld. Zusätzlicher Dank gebührt Msc. Lorena Fritsch für zahlreiche Berechnungen und Diskussionen, sowie die gute Zusammenarbeit bei unserer Veröffentlichung. Auch Jakob Steube sei an dieser Stelle besonders hervorzuheben, da sein drastisches Korrekturlesen den Texten den nötigen Feinschliff verliehen hat.

Diese Arbeit wurde auch durch die Zusammenarbeit mit externen Arbeitskreisen vorangebracht. Aus diesem Grund möchte ich an dieser Stelle bei Prof. Dr Meyer und im besonderen Dr. Serhiy Demeshko und Ajdin Velić für die Messung der SQUID und Mössbauer-Spektren danken.

Im Laufe dieser Promotion durfte ich auch zwei Studierende betreuen, vielen Dank an dieser Stelle an Nicole Dickmann und Franziska Lux, die beide durch ihre synthetischen und praktischen Arbeiten viele Ergebnisse zu dieser Arbeit beigetragen haben.

Diese Zeit wäre nur halb so schön gewesen, wenn die lieben Arbeitskolleg*innen gefehlt

hätten. Generell gebührt dem gesamten Arbeitskreis Dank, der den Alltag durch viele fachliche und nicht-fachliche Diskussionen verschönert hat. Vielen Dank an Dr. Yannik Vukadinovic und Dr. Steffen Schlicher für das Weitergeben ihrer Expertise an die nachfolgende Generation. Besondere Liebe geht an Anabel "Hells Bells" Miletic, Anke "Brahmke" Schoch und Pia "Herbert" Rehsies, die besten Laborladies, die man sich wünschen kann.

An die Volleyball-Abteilung des SV Benhausen, besonders Martin, Laura, Patricia und Steffen gilt mein Dank für das Rausholen aus dem Laboralltag. Dies gilt auch für die Truppe um Anabel, Laura, Lavinia, Nicole und Steffi, für die wöchentliche Sichtung niveauvoller Alltagsgeschichten von Laienschauspielern im dokumentatorischen Stil. Danke an Julia und Svenja, für ihre Treue die letzten Jahrzente(!) und das unerschütterliche Begleiten durch jedes Hoch und Tief.

Meiner Familie danke ich von ganzen Herzen, dass sie stets an meiner Seite waren und mir immer Raum gegeben haben in der stressigen Zeit. Ohne euch wäre diese Zeit nur halb so ertäglich gewesen. Dank auch an den Mann an meiner Seite, Arne, der mich jederzeit bedingungslos unterstützt hat.

> How lucky i am to have something that makes saying goodbye so hard.
>
> Winnie the Pooh

Abstract

The depletion of primary energy sources, like fossil fuels, forces scientists to reconsider energy consumption patterns and put procedures in place to ensure a future powered by renewable and sustainable energy sources. Utilizing solar radiation to produce hydrogen as alternative energy carrier through chemical processes offers a sustainable production method. A crucial component in this process is the photoactive component, which harnesses incoming solar light to enhance otherwise undesirable reactions.

In pursuit of a sustainable energy future, 3d-metals emerge as a promising alternative to noble metals. Therefore, this thesis focuses on developing a novel photoactive complexes using iron as a substitute for noble metals. Recent research has highlighted the effectiveness of iron(III) complexes, showcasing prolonged catalytically active states, particularly through activation from a singlet ground state to a doublet LMCT, providing an excited state with a longer lifespan compared to conventional iron(II) complexes.

A bis-tridentate ligand motif based on phenyl-1*H*-pyrazole was used to examine the photophysical characteristics of iron(III) complexes, building on the success of strong sigma-donating functions. Therefore, the tris(1-phenylpyrazolato-N,C^2)iron(III) complex scaffold is used to create eight complexes, enabling the examination of different functional groups on photophysical properties. Here, electron donating or withdrawing groups are introduced as well as π-extensions. Furthermore the position of these groups could be varied. Single crystal diffractometry, NMR-spectroscopy, UV-Vis-spectroscopy, and cyclic voltammetry were all used to properly study the samples. X-ray absorption and emission spectroscopy provide novel insights into the electronic structure, assisted by DFT computations.

The complex is synthesised in its iron(III)-form where it only generates *fac*-isomers. Both iron(II) and iron(IV) species were produced via chemical reduction and oxidation. Iron(II) transitions to the more stable *mer*-isomer, although iron(IV)-complexes remain in the *fac*-configuration. The ligand design leads to overlapping MLCT and LMCT absorption bands hindering emissive behaviour suppressed by low lying MC states. The complex demonstrates stability within specific wavelength ranges and various solvents, supporting its potential application in catalysis. Furthermore, the comprehensive resonance assignment made possible by the NMR methods used here aided in the investigation of the effects of functional groups and the paramagnetic iron(III) centre of the ligand scaffold. These complexes also exhibit reduced paramagnetism at higher temperatures and conformational stability over a wide temperature range.

Kurzzusammenfassung

Der Rückgang von Primärenergiequellen wie fossilen Brennstoffen zwingt die Wissenschaft dazu ihre Energiegewinnung zu überdenken und Maßnahmen zu ergreifen, um eine Zukunft mit nachhaltigen und erneuerbaren Energiequellen zu gewährleisten. Die Nutzung von Solarenergie zur Wasserstoffproduktion als alternativer Energieträger durch chemische Prozesse bietet eine nachhaltige Produktionsmethode. Ein entscheidender Bestandteil dieses Prozesses ist der Photosensitizer, der einfallendes Sonnenlicht nutzt, um ansonsten unfreiwillig ablaufenden Reaktion zu katalysieren.

Auf der Suche nach einer nachhaltigen Energiezukunft zeichnen sich 3d-Metalle als vielversprechende Alternative zu Edelmetallen ab. Daher konzentriert sich diese Arbeit darauf, einen neuen photoaktiven Komplex zu entwickeln, wobei Eisen als Ersatz für Edelmetalle verwendet wird. Eisen(III)-Komplexe zeigen eine Anregung von einem Singulett-Grundzustand in einen ^{2}LMCT, einen angeregten Zustand mit einer längeren Lebensdauer im Vergleich zu den konventionell verwendeten Eisen(II)-Komplexen.

Ein bis-tridentates Ligandenmotiv auf der Basis von Phenyl-1*H*-pyrazol wurde verwendet, um die photophysikalischen Eigenschaften von Eisen(III)-Komplexen zu untersuchen, aufbauend auf dem Erfolg starker σ-donierender Funktionen. Aufbauend auf den Komplex Tris(1-phenylpyrazolato-*N*,*C*^{2})iron(III) wurden acht Komplexe synthetisiert, die den Einfluss verschiedener funktioneller Gruppen auf die photophysikalischen Eigenschaften zeigen sollen. Hierbei konnten positionsvariable eletronenziehende und -schiebende Gruppen, sowie eine Erweiterung des π-Systems ermöglicht werden. Einkristalldiffraktometrie, Cyclovoltammetrie, NMR- und UV-Vis-Spektroskopie wurden eingesetzt, um die Probe photophysikalisch zu untersuchen. Röntgenabsorptions- und -emissionsspektroskopie bieten erweiterte Einblicke in die elektronische Struktur unterstützt durch DFT-Berechnungen.

Der Eisen(III)-Komplex bildet ausschließlich *fac*-Isomere. Sowohl die Eisen(II)- als auch Eisen(IV)-Spezies können durch chemische Reduktion und Oxidation hergestellt werden. Eisen(II) geht in das stabilere *mer*-Isomer über, während Eisen(IV)-Komplexe in der *fac*-Konfiguration bleiben. Das Ligandendesign führt zu überlappenden MLCT- und LMCT-Absorptionsbanden, wodurch das Emissionsverhalten durch tief liegende MC-Zustände inhibitiert wird. Es ist möglich, die Stabilität des Komplexes innerhalb eines bestimmten Wellenlängenbereichs und in einer Vielzahl von Lösungsmitteln nachzuweisen. Die umfassende Zuordnung der NMR-Resonanzen zeigte die Auswirkungen der funktionellen Gruppen und des paramagnetischen Eisen(III/IV)-Zentrums auf das Ligandengerüst. Diese Komplexe profitieren von einem reduzierten Paramagnetismus bei höheren Temperaturen und Konformationsstabilität über einen weiten Temperaturbereich.

Contents

Declaration of Independence III

Acknowledgements VI

Abstract IX

Contents XIII

List of Abbreviations XV

1 Introduction 3
- 1.1 Motivation . . . 3
- 1.2 Hydrogen as Alternative Energy Carrier . . . 6
- 1.3 Systems for Photocatalytic Water Splitting . . . 8
- 1.4 Photosensitizer . . . 10
  - 1.4.1 General Functions . . . 11
  - 1.4.2 Photosensitizers with Ruthenium . . . 13
  - 1.4.3 Iron Based Photosensitizers . . . 14
    - 1.4.3.1 Iron(III) Complexes . . . 19

2 Objective 25

3 Ligand Design and Complex Syntheses 27
- 3.1 Ligand Syntheses . . . 27
- 3.2 Complex Synthesis . . . 33
  - 3.2.1 Complex Oxidation and Reduction . . . 40

4 Characterisation 43
- 4.1 Single-Crystal X-Ray Diffraction . . . 43
- 4.2 NMR . . . 49
  - 4.2.1 General Observations . . . 49
  - 4.2.2 Resonance Assignment . . . 54
  - 4.2.3 ^{13}C-NMR Spectroscopy . . . 60
- 4.3 Mössbauer Spectroscopy and Magnetic Measurements . . . 63
- 4.4 Ground State Characterization . . . 64

4.4.1 CV . . . 64
4.4.2 UV-Vis . . . 70
4.4.3 Spectroelectrochemistry . . . 73
4.4.4 Behaviour under Illumination . . . 74
4.5 Hard X-Ray Spectroscopy . . . 80
4.6 Advanced NMR Characterization . . . 84
4.6.1 Total Shift Determination . . . 84
4.6.2 Orbach Process . . . 88

5 Summary and Outlook **93**
5.1 Summary and Conclusions . . . 93
5.2 Outlook . . . 97

6 Experimental Details **99**
6.1 General Information . . . 99
6.2 Analytical and Spectroscopic Techniques . . . 99
6.3 Theoretical Calculations . . . 102
6.4 Syntheses . . . 102
6.4.1 Ligand Syntheses . . . 102
6.4.2 Complex Syntheses . . . 107

Bibliography **117**

List of Figures **127**

List of Tables **131**

Publications and Beamtimes **133**

Appendix **135**
DFT calculations . . . 135
Ligand Spectra . . . 139
Complex Spectra . . . 156

List of Abbreviations

Å	Angstrom
ATP	Adenosine triphosphate
CB	Conduction band
CCS	Carbon capture and storage
CT	Temperature Dependent-Coefficient
CtC	Core to Core
CV	Cyclic Voltammetry
DSSC	Dye Sensitized Solar Cells
e	Eulersche Zahl
EA	Elemental analysis
ED	Electron donor
EDG	Electron donating group
EJ	Exajoule
eq.	Equation
equiv.	Equivalents
et al.	et alia
ESRF	European Synchrotron Radiation Facility
eV	Electron volt
EWG	Electron withdrawing group
fac	Facial
FWHM	Full Width at half Maximum
D	Diffusion Coefficient
DCM	Dichloromethane
g	Grams
g/L	Grams per liter
GHG	Greenhouse gas
GMST	Global mean surface temperature change
GS	Ground State
h	Planck constant
h	Hour
HEC	Hydrogen evolving complex
HER	Hydrogen evolving reaction
HERFD	High Energy Resolution Fluorescence Detection
HOMO	Highest Occupied Molecular Orbital
HS	High-Spin
IC	Internal Conversion
IPCC	Intergovernmental Panel on Climate Change
IR	Infrared spectroscopy
irrev.	Irreversible
ISC	Intersystem crossing
IUPAC	International Union of Pure and Applied Chemistry
L	Liter

LIESST	Light-Inducesd Spin-State Trapping
LMCT	Ligand to Metal Charge Transfer
LUMO	Lowest Unoccupied Molecular Orbital
LS	Low Spin
M	Molar
MC	Metal Centered
mer	Meridional
MHz	Megahertz
MJ/kg	Megajoule per kilo
mL	Milliliter
MLCT	Metal to Ligand Charge Transfer
MS	Mass spectrometry
NADPH	Nicotinamide adenine dinucleotide phosphate, reduced form
NHC	*N*-heterocyclic carbenes
NHE	Normal hydrogen electrode
m\z	Mass to charge proportion
nm	Nanometer
NMR	Nuclear magnetic resonance spectroscopy
NOE	Nuclear Overhauser-Effect
ns	Nanoseconds
PGM	Platin Metal Group
PS	Photosensitizer
rev.	Reversible
TDDFT	Time-dependent density-functional theory
TMC	Transition metal complex
TLC	Thin layer chromatography
THF	Tetrahydrofuran
TWh	Terrawatt per hour
ν	Wavenumber
VB	Valence band
VTC	Valence to Core
WRC	Water reduction catalyst
WOR	Water oxidation reaction
XAS	X-Ray Absorption Spectroscopy
XANES	X-Ray Absorption Near Edge Structure
XES	X-Ray Emission Spectroscopy

It isn´t what we say or think that defines us, but what we do.

Jane Austen
Sense and Sensibility

1 Introduction

1.1 Motivation

Within the last century we encountered more and more scenes of extreme weather events and climate related catastrophes. Devastating destruction by wildfires, heatwaves and droughts amidst unprecedented storms and floods became an alarming recurrence.[1, 2] Humanity is live-witness of the increased impact of climate change, earths long-term atmospheric average. Unfortunately, the broad-scale impact of this change is mostly recognized in extreme weather events, like the flooding in Pakistan[3] August of 2022 or the severe droughts in west Africa[4] since 2020, where ten thousands of people were killed or left in precarious health and economic conditions.[5–7]

Scientists have observed the drastic atmospheric change within the last few decades in ecological surveys and especially encountered an increase of the average sea- and land-surface temperature, and additionally the decrease of permafrost extent, snow cover and glaciers.[8] Climate has always changed naturally over the past 2 million years, though the rate of global warming in the last 50 years has exceeded every other 50-year period.[2]

These alterations in climate are connected with the rise of industrialisation and therefore emission of greenhouse gases (GHG) by generation of electricity, and likewise from transport, industry and agricultural sectors.[9] As a non-governmental organization the Intergovernmental Panel on Climate Change (IPCC) assesses published literature and produces reports to contextualise different scenarios and provides scientific and technical background to these informations. They state that the unequivocal human contribution to global warming is estimated to 1.07 °C in 2021.[8] The global mean surface temperature change (GMST), relative to the baseline of 1850-1900 in the sixth Assessment Report (AR6), displays the values from four different datasets (fig. 1.1). The calculated rise of the GMST would have remained around the 1850-1900 level, even with increased natural change from solar or volcanic activities.[10]

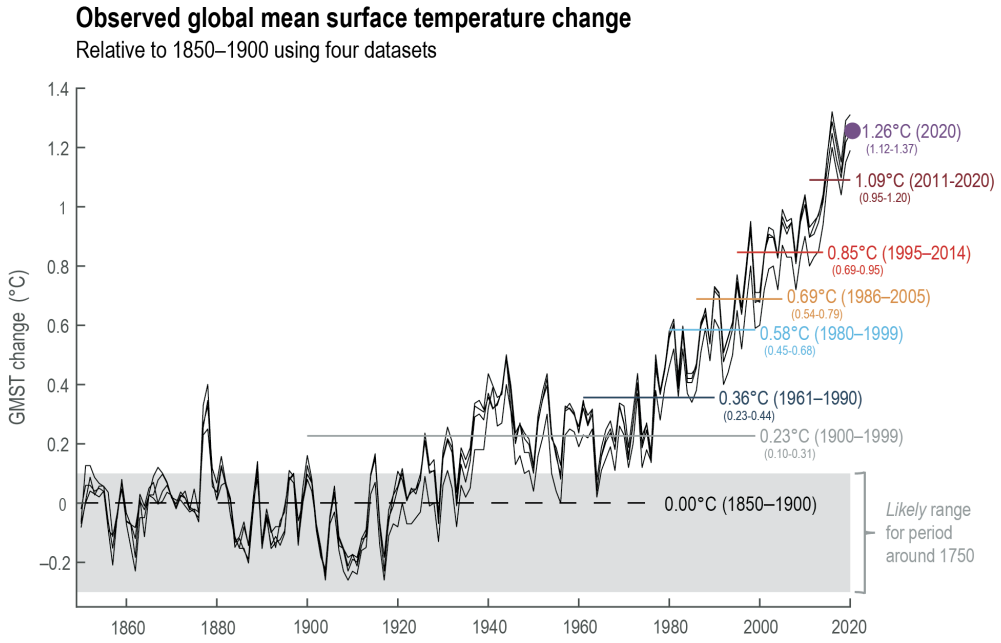

Figure 1.1: Observed global mean surface temperature change, relative to 1850-1900 using four datasets. Grey shaded band indicates the most likely range around 1750. Colored horizontal lines show different reference periods.[8]

The acceleration of global warming since the industrial period is non-negliable, as the atmospheric concentration of GHGs, specifically carbon dioxide (CO_2), methane (CH_4) and nitrous oxide (N_2O), increases.[11] In moderate concentration these gases secure a habitable temperature within a planetary equilibrium, however the increasing GHG concentration traps more and more heat in the atmosphere. Additionally they alter lifetimes and reactivity in atmospheric processes, further escalating the GMST-acceleration.[8] Stopping this process includes the reduction of anthropogene GHG, thence redefining our utilisation of fossil fuels and bio-materials, considering their combustion as one of the central issues.[11]

Within these discussions, the global energy system and therefore its supply are intrinsic parts concomitant with the challenge of a safe, affordable and stable energy source, without endangering the health or ecological well-being of the planet and its inhabitants.[12] Approximately 40% of CO_2 emissions originate from electricity generation and heating. The electricity generation mix, as shown in fig. 1.2, relies to more than 60% on fossil fuel based technologies. The renewable energy mix contributes around 30%, representing a heterogeneous mix of bio-, geothermal, wind and solar energy.[13] Concisely a growth of 10% within the last decade, especially through solar and wind technologies, contributed to a slight change in renewable energy supply. Nevertheless, the increase in energy demand is continuing, therefore phasing out fossil fuels, mainly coal and oil, and focusing on the development of environmentally sustainable energy technologies is obliged to be the focal point.[8, 9]

An energy supply by 100% renewables is not yet feasible under the premise of a high reliability, high safety and most beneficial outcome with the current technologies.[14] The severity of climate change demands exceptional innovations, e.g. deforestation reducement, resource recovery, etc., which requires more energy to be designed operational as a first step of a long-term strategy, followed by mandatory rapid implementation into existing energy cycles.[14]

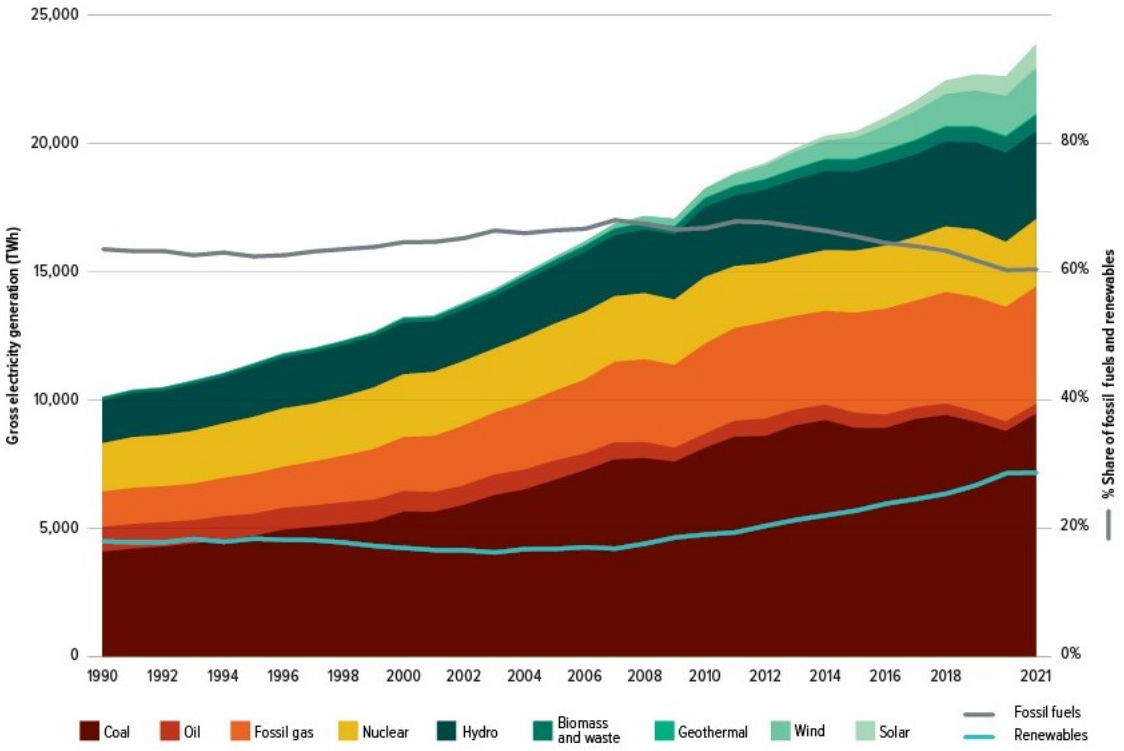

Figure 1.2: Primary energy supply in terawatt per hour (TWh) as provided by primary source. Cumulative share of the renewables is represented by the blue line, fossil fuels by the grey line in percentage.[13]

A sustainable energy supply includes the identification of abundant primary energy sources, inventions for a safe use and conversion, and their integration into the existing systems. Two of the most abundant resources of this planet are water and oncoming solar radiation.[15] With 3.4 million EJ the annual solar energy in earth´s surface exceeds the demand of humankind indefinitely.[16] Many recent studies have focused on water as the primary energy source for hydrogen, which implementation as energy carrier provides a medium to be stored on-demand, as well as a building block for chemical and industrial sectors.[17]

Interest in hydrogen as fuel alternative has come and go in the last years, yet the tipping point has not been reached. With the declining cost of renewable energy, production of environmentally friendly hydrogen becomes feasible and at same time necessary to contribute to the ever-growing technological developments and their subsequent energy

demand.[14] By introducing hydrogen for multiple fields of applications, the decrease of GHG emissions and independence from fossil-based energy would secure energy safety and promote further socio-economic development. Main problem of this change is the feasibility of producing hydrogen sustainable, which is the main goal of the research done within this thesis.

1.2 Hydrogen as Alternative Energy Carrier

Hydrogen is first in the periodic table and represents an estimated mass fraction of 90% in the universe.[18] Gaseous under room temperature, with a density of 0.089 g/L, a negative Joule-Thompson coefficient (temperature drops while compressing the gas) and a lower heating value (net calorific value) of 119.9 MJ/kg hydrogen procures an optimal fuel alternative.[19] The interest in hydrogen is high, considering the combustion results in water exclusively, shown in eq. 1.2.1.[18]

$$H_2 + \frac{1}{2} O_2 \longrightarrow H_2O \tag{1.2.1}$$

The priceless advantage of this reaction is a consistent high air quality within its operating distance and a decreased overall GHG emission, if the source and production of hydrogen are sustainable. Unfortunately, hydrogen in its pure form is scarce in the earths atmosphere since it is mainly bound to either oxygen, e.g. water, or carbon in form of hydrocarbons, such as fossil fuels or biomaterials.[20] Hence, the degree of sustainability of hydrogen is classified by its primary energy source and the conversion method. The categorisation includes grey hydrogen, based on fossil hydrocarbons, blue hydrogen, produced by fossil fuel as well but with a carbon capture and storage system, turquoise hydrogen, from thermal methane splitting and green hydrogen, e.g. via the electrolysis, of water or other renewable primary energy sources (fig. 1.3).[17]

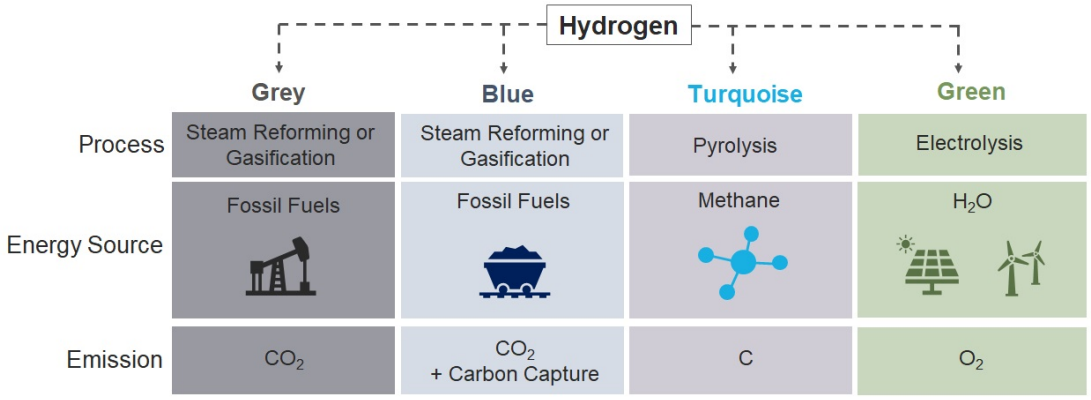

Figure 1.3: Hydrogen production pathways, sub-classified by their source of hydrogen. Classes consist of grey, blue, turquoise and green hydrogen.[19]

Of the four classes, grey hydrogen emits the most GHG, due to the use of fossil fuels as hydrogen source. In the last years around 88% of the overall generated hydrogen was produced by steam reforming either by natural gas, naptha or coal.[19] Steam reforming combines a hydrocarbon material with water steam at high temperatures of 850-900 °C, with a nickel-based catalyst, to generate hydrogen and carbon oxides (eq. 1.2.2).[19]

$$C_nH_m + n \cdot H_2O \longrightarrow n \cdot CO + (n + \frac{1}{2}m)H_2 \tag{1.2.2}$$

Reduction of these emissions is achieved with a CO/CO_2 capture and storage (CCS) technique, e.g. in geological reservoirs, whereupon it is classified as blue hydrogen. Nevertheless, CO_2-emissions are never zero for blue hydrogen, since the generation of high reaction temperatures, extraction and preparation of the raw materials is energy-intensive and success of the CCS strategy is yet a rough-estimated assumption.[21]

Methane as source of hydrogen dissociates at high temperatures of around 980°C, even with catalysators, which in addition deactivate over time and are in need of regular replacement. Besides steam reforming, methane pyrolysis allows a more different approach for hydrogen production, where carbon as by-product, in form of e.g. graphite, provides a secondary commercially usable appliance.[19, 22]

$$CH_4 \longrightarrow C + 2 \cdot H_2 \tag{1.2.3}$$

Nevertheless natural gas as hydrogen source is constantly accompanied by environmental risk during its extraction, transport, and when required, reprocessing.[23] Therefore, the replacement of fossil fuel based hydrogen sources must be promoted.

Besides the potential of the priorly mentioned hydrogen production pathways, green hydrogen is the most promising one, as it combines the implementation of sustainable hydrogen feedstock with abundant renewable energy sources as propulsive power of the reaction. To promote the energetically unfavorable reactions, driving force stems from thermal, photonic, electrical or biochemical sources or a combination of these.[24] Hydrogen sources reach from water to biomass.[19, 25] Several methods of production fall in this category, including biological processes, thermolysis, electrolysis or photoelectrolysis.[19, 24]

Biochemical processes use steam reforming methods with water or biomass, such as wood sawdust or sugar cane bagasse, to yield natural gas and hydrogen in high temperature processes. These biomass-based hydrogen feedstocks may also be used in fermentation or enzymatic reactions to extract hydrogen.[24] In an equal manner thermolysis methods split either water molecules or convert biomass to bio-fuels, where geothermal or other sources of energy as well as catalytic processes favor these reactions, compared to conventional steam reforming.[24] Both techniques rely on an emission neutral carbon cycle, where former grown biomass is converted to bio-fuels or the primary energy source is implemented with net-zero carbon emissions.[26]

Water as hydrogen source is supposedly the most unsophisticated approach for a sustainable hydrogen source taking into account that the decomposition into H_2 and O_2 requires only 1.23 eV, nevertheless the separation and transport of electrons are crucial steps, and not easily implemented. With an electric current applied to water, electrolysis is possible. Electricity produced by solar (photovoltaic) and wind power can drive electrolysers and produce hydrogen. Common electrolysers are the proton exchange membrane (PEM), where a solid polymer as electrolyte and distilled water as staring material splits water at a noble metal cathodic/anodic materials.[27] Nevertheless, the conversion of electricity trough sustainable resources is currently insufficient for large-scale use and requires development. A growing research field in the last decades is the implementation of energy derived from solar radiation with catalytic active materials to split water in a photo-chemical reaction (eq. 1.2.4).[28]

$$H_2O \xrightarrow{h\nu} H_2 + \frac{1}{2}O_2 \tag{1.2.4}$$

The reaction is divided in water-oxidation (eq. 1.2.5) and the water-reduction (eq. 1.2.6), where the necessary electron transport becomes more apparent. Additionally this offers the separate examination and customisation of the materials and conditions, before applying them mutually. Therefore, eq. 1.2.5 and eq. 1.2.6 are separate fields in research with different strategies for application.

$$H_2O \longrightarrow 2e^- + 2H^+ + \tfrac{1}{2}O_2 \tag{1.2.5}$$

$$2e^- + 2H^+ \longrightarrow H_2 \tag{1.2.6}$$

Photocatalysts interact with photons, defined by the Planck constant (h) and the wavenumber (ν), and absorb this energy to reach a catalytically active state. The excitation of the catalyst introduces a charge separation with the ability to interact in a photo-chemical reaction. As a result, hydrogen may be formed and reduced with electrons resulting from charge separation. This approach to green hydrogen is yet in its early stages, where diverse systems are investigated.

1.3 Systems for Photocatalytic Water Splitting

The natural world serves as an inspiration for photocatalytic water splitting. Autotrophic organisms have the ability to create their own energy source by converting solar energy into chemical energy, which is then stored and used on demand. Therefore, plants synthesise glucose from CO_2 and H_2O, with O_2 as by-product (fig. 1.4).

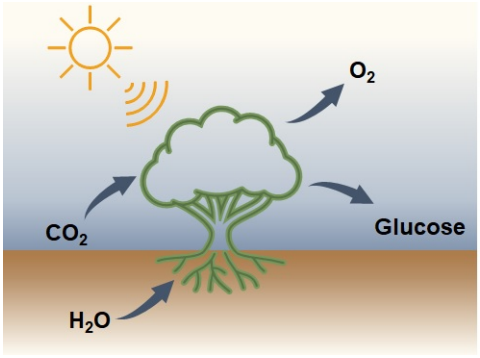

Figure 1.4: Photosynthesis in plants, powered by solar radiation with H_2O and CO_2 as starting materials, producing O_2 and glucose.[29]

The overall reaction pathway is shown in eq. 1.3.1.

$$6\,CO_2 + 6\,H_2O \longrightarrow C_6H_{12}O_6 + 6\,O_2 \tag{1.3.1}$$

Though the overall reaction may appear as a tolerably simple, it is an extremely complex reaction series and is not yet fully understood in its details. In plants, two light-induced reactions proceed within chloroplasts. Photosystem I, comprised of an iron-sulphur cluster as integral part, acts as light-collecting complex and promotes electron transfer to neighbouring molecules while reducing protons to hydrogen, thus named hydrogen evolving complex (HEC).[29, 30] In addition, photosystem II, a manganese comprised metallo-oxo cluster, is the active site for water oxidation, therefore formation of O_2, and consequently labelled oxygen-evolving complex (OEC).[29, 31, 32]

To mimic this ante-type, the water splitting reaction is divided in its half-reactions, in the water oxidation reaction (WOR, eq. 1.2.5), where an oxidizing agent is required, and the hydrogen evolving reaction (HER, eq. 1.2.6), with a reducing catalyst. In both cases the reactor and light-source need to be adjusted towards the inserted constituents and their long-term employment. Additionally, the catalytically active medium requires electron donors (ED) and electrolytes for charge transport and balance. Most significant part is the photocatalyst, or the photocatalytic system, where the transition from light to chemical energy is promoted, requiring a catalyst with excelling abundancy and efficiency as well as sustaining stable and long-lived properties during its employment (fig. 1.5).[33]

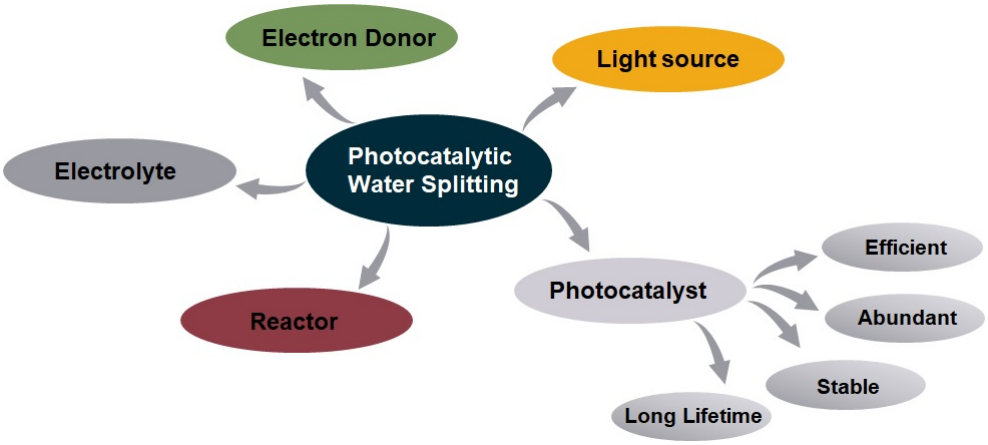

Figure 1.5: Schematic representation of the requirements for photocatalytic water splitting.

This photocatalyst, a photosensitizer (PS), provides electrons upon photoexcitation towards the water reduction or oxidation catalyst (WRC/WOC), where either hydrogen or oxygen are produced on site. Additionally an ED substitutes the electrons, otherwise originating from the OER, to conclude the catalytic cycle in a laboratory scale, which makes separate research of these reactions more practicable.

For a successful transition towards efficient hydrogen supply, tremendous breakthroughs in catalyst design are necessary, since the recently published PS were not able to fulfil the catalyses successfully.[19, 34] The structurally demanding step of water reduction, thus sufficient excitation and transport of electrons, is part of intense research and focuses on the design and improvement of the PS. In upcoming chapters, the principal function will be explained with emphasis on the structural aspects to enhance charge accumulation after excitation and the electron transfer steps.

1.4 Photosensitizer

The combination of photoexcitation and electron transport is undoubtedly the main obstacle in catalytic water splitting and as mentioned in ch. 1.3, various requirements have to be fulfilled. Therefore, it is inevitable to understand the underlying physicochemical properties completely, like light absorption, charge separation and electron transfer.[35]

In order to increase the likelihood of excitation during this reaction cycle, the complex has to absorb the oncoming photons efficiently, preferably by broad-range absorption, with a high absorption coefficient. Additionally, excited states with an appropriate lifetime for a successful charge transfer are necessary, which could enable interaction with other substrates. Therefore, the ground and excited state properties must be appropriate for the process under investigation. Long-term use requires the system to be stable on a

chemical and physical level and to go through the catalytic cycle several times.[36, 37]

1.4.1 General Functions

First PS, already reported in 1972 by FUJISHIMA and HONDA, were applied as semiconducting materials. For example TiO_2, WO_3 or CdS were employed in single-component, heterogeneous catalysis.[38, 39] In semiconductors, electrons are excited by solar radiation from a valence band (VB) into the conducting band (CB).[35, 40] Electrons in the VB are transported to the surface, where reduction of protons produces hydrogen. Remaining holes in the VB are refilled at the material surface by the second half reaction to O_2 (fig. 1.6, A). For efficient catalysis, recombination of holes and electrons must be prohibited, while simultaneously requiring band gaps smaller than 3 eV to match radiation energy. Secondly, the potential of the band gaps requires more negative values than the H^+/H_2 energy level (around 0 V vs. the normal hydrogen electrode (NHE)) and more positive values to match the O_2/H_2O redox potential (1.23 eV).[40] To enhance the catalytic performance of oxides, doping with co-catalysts like platinum or ruthenium became more common recently.[41, 42]

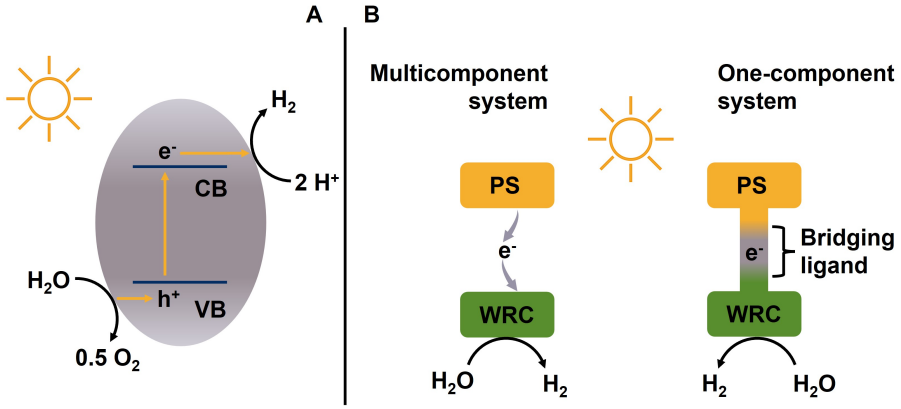

Figure 1.6: A) Semiconducting materials are separated in hole at the valence band (VB) and electron in the conducting band (CB), catalytic active site is the semiconductor surface. B) One- or multi-component system for homogeneous water splitting; PS: photosensitizer, WRC: water reduction catalyst.

Single-component semiconductors might increase their flexibility by driving each of the water splitting half-reactions on different catalysts with adjusted band gaps in a Z-scheme (electron transfer between two semiconductors with adjusted band-gaps).[35] In analogy to the heterogeneous approach, molecular photocatalytical systems in homogeneous solutions (fig. 1.6, B) use a light absorbing catalyst and a catalytic centre for WRC/WOC.[35] Here the electron transport from the photocatalyst is either intra- or intermolecular. The multicomponent system enables electron transfer upon contact, whereas the one-component system implements a bridging unit to support electron transfer and charge accumulation for electron relay.[35, 43] Construction of these catalyst

involve a metal centre as active site and an organic ligand environment, in which activity and selectivity are adjustable. Characteristics are easily traced by spectroscopic and electrochemical methods, to further enhance performance.

Light induced charge transfer and transport at the PS might be the most challenging step. After excitation two reaction pathways are applicable, either reductive or oxidative quenching (fig. 1.7).

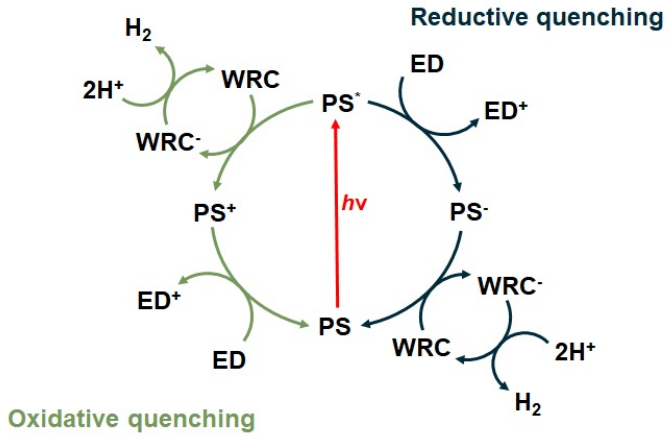

Figure 1.7: Reaction pathways for the PS. After excitation it might undergo reductive (blue) or oxidative (green) quenching. PS: photosensitizer, ED: electron donor, WRC: water reduction catalyst, WOC: water oxidation catalyst.

In the oxidative quenching pathway the PS delivers one electron to the WRC before getting reduced by the ED (fig. 1.7, green), whereas in the reductive quenching pathway (fig. 1.7, blue) the excited PS is first reduced by the ED before transferring that electron towards the WRC. Electron transport from PS to WRC might be enhanced by an intermediate molecules. One option here are organic molecules, like methyviologen. Within this section, the focus is on homogeneous PS based on transition metals, which are of interest because of their photostability and their tunable redox behavior of their excited state potentials.

The duration of the excited state is significant since electron transfer is only feasible during this time. Within this lifetime the PS and WRC or WOC should collide, to facilitate the electron transfer. The excited state lifetime describes the common decay to a decrease of the population of 1/e.[44] Collisions with other reactants occur during this time period based on the distance the molecules may travel and the existence of all other necessary molecules within this distance. Besides the lifetime, the key parameters are temperature, viscosity of the solution and radius of the complex, following the diffusion coefficient D.

$$D = \frac{k_B T}{6\pi\eta R_M} \tag{1.4.1}$$

With: D = Diffusion coefficient; k_B = Boltzmann constant; T = Temperature; η = solvent viscosity; R_M = Molecular radius of the complex.

This equation overall demonstrates the dependency of lifetime of the excited states and the circumjacent characteristics during the catalytic application. Next to the fine-tuning of the catalysis, an prolonged excited state is beneficial for efficient water splitting, especially considering big-scale application of this technique.

1.4.2 Photosensitizers with Ruthenium

Classic PS are based on noble metals, and often contain ruthenium (Ru(II)) or iridium (Ir(II)) centres.[45–47] They consist of a organic ligand environment with a positive metal-center. These complexes fulfill all key requirements for an PS and were thoroughly examined. The prime example of possible applications is $[Ru(bpy)_3]^{2+}$, with an octahedral ligand field, which splits into three t_{2g}- and two e_g-orbitals (fig. 1.8).[48, 49] If the field is strong enough, six valence electrons occupy the t_{2g}-orbital, which is therefore the highest occupied molecular orbital (HOMO). The lowest unoccupied molecular orbital (LUMO), consisting of ligand based π^*-orbital, is slightly lower in energy than the e_g^*-orbital, due to the distinct splitting of the t_{2g}- and e_g-orbital. This is typical for 4d- and 5d-metal complexes, hence the low-spin configuration is commonly known here.[50]

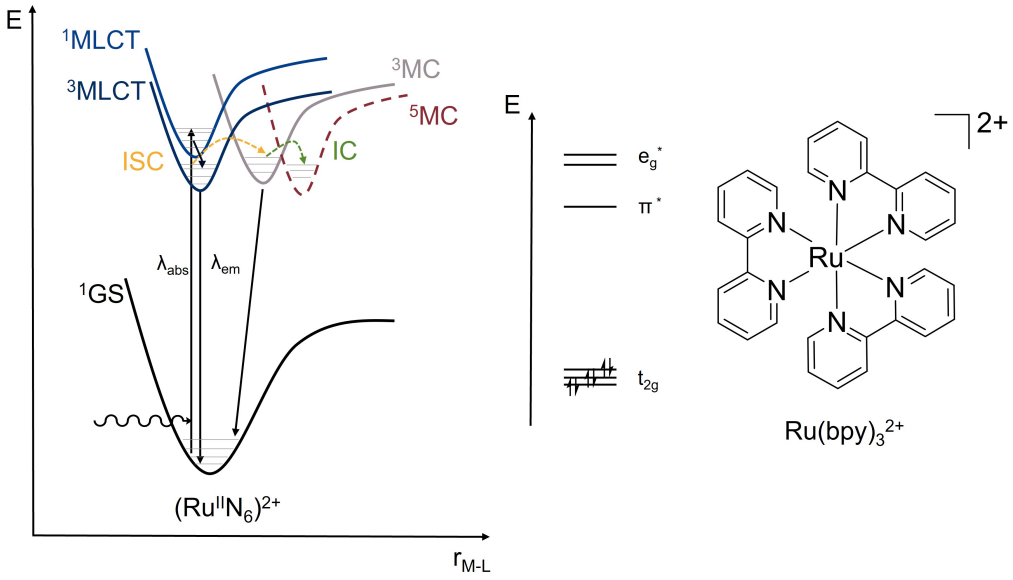

Figure 1.8: Left: Excited state energy landscape, corresponding energy relative to the distance metal to ligand; Middle: Simplified MO-scheme; Right: Chemical structure of $[Ru(bpy)_3]^{2+}$.[51]

Therefore excitation with the minimum transition energy from HOMO, in this case the ground state (^{1}GS), to LUMO results in a metal to ligand charge transfer (MLCT). Within this process, the spin multiplicity is constant. The triplet ^{3}MLCT, which exhibits more stability, is populated from the originally populated ^{1}MLCT during an intersystem crossing (ISC) via a spin flip.[36] According to Kasha's rule, relaxation to the ground state is only possible from the lowest excited state, which will be reached by all molecules as a result, indicating that the ^{3}MLCT is the most important catalytically active state. Hence, higher ^{3}MLCT lifetimes increase the change for a successful electron transfer. The spin forbidden relaxation into the singlet ground state is also beneficial for longer lifetimes.

Additionally, metal centred states (MC) states exist whose energetic position can interfere with the relaxation process. If these states are as high as for $[Ru(bpy)_3]^{2+}$, an additional activation barrier has to be overcome to populate these states, additionally contributing to the longevity of the ^{3}MLCT. Unfortunately, by further adjustments to the ligand structure, weaker ligand field splitting could result in an energetically decrease of the $^{3/5}$MC state. Their lower energy would result in a population from which catalytic activity is impossible, therefore non-radiative internal conversion (IC) leads to relaxation back to the ground state, decreasing the lifetime (^{3}MLCT) to hundreds of ns.[36]

Relaxation into the ground state could therefore occur by electron transition to other molecules, but also by energy transfer. However, tunability of the ligands provides numerous possibilities to fine-tune the photophysical redox-properties. Many examples are presented in literature, with huge success in their application to catalysis. However, due to their scarcity and high price, the usage of ruthenium, iridium, or other transition metals from the platinum group (PGM), may prevent their widespread application. Furthermore, their toxicity as complexes must be taken into account.[52] The prospect of enabling widespread implementation of this technique may move the focus toward environmentally benign fuel alternatives by switching the metal centre to more accessible, ecologically friendly substitutes. One option is iron, which was considered due to its similarity to ruthenium. Additionally its abundance and therefore cheap manufacturing costs favour this metal for big scale applications. Moreover, its appearance in many biochemical process offer a less toxic metal, compared to the PGMs.[51] This will be covered in more detail in the section that follows.[53, 54]

1.4.3 Iron Based Photosensitizers

Despite iron's similar complexation behaviour to other elements, such as ruthenium, the precognition of interplay between metal and ligand scaffold, which was effective with other PGM, is more difficult with iron. The photophysics of Ru(II) to the isoelectronic iron(II) complexes reveal that the ligand filed splitting (fig. 1.9, middle) is significantly weaker since the orbital overlap is not as good for 3d metals than for the 4d/5d analogues.[50]

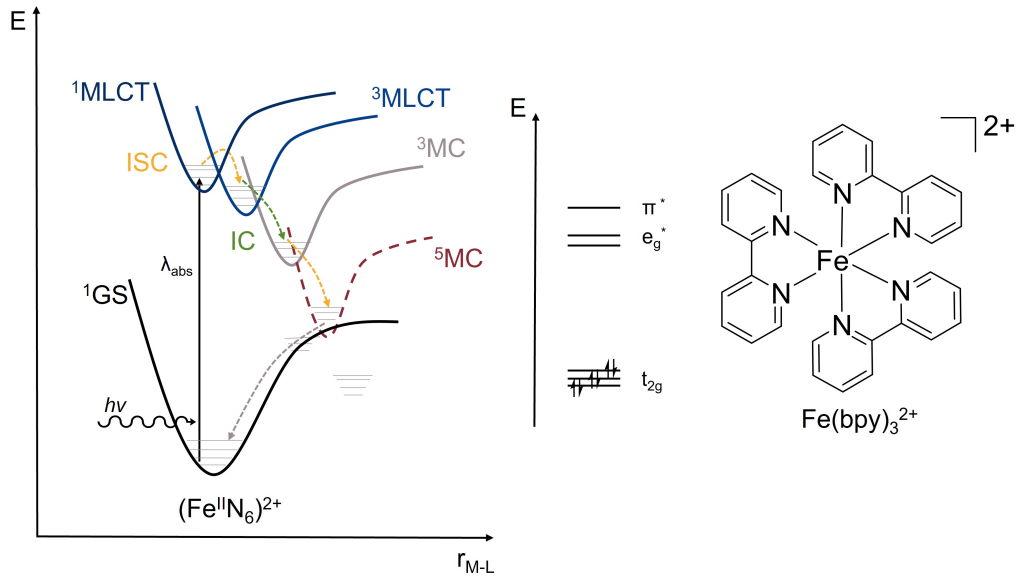

Figure 1.9: Left: Excited state energy landscape, corresponding energy relative to the metal to ligand distance; Middle: Simplified MO-scheme; Right: Chemical structure of $[Fe(bpy)_3]^{2+}$.

Despite the lower lying e_g*, an MLCT from t_{2g} to e_g* (or the ^{1}MLCT) occurs due to the laporte-rule, which forbids the conservancy of parity in a transition of centrosymmetric molecules. Thus, rapid ISC towards the ^{3}MLCT occurs. Since there is no barrier to the adjacent, lower-lying MC states a radiationless deactivation cascade occurs. Relaxation from the ^{5}MC state is again laporte-forbidden, direct relaxation into the ground state is hindered. Thus, the lifetime of the catalytic active states remains low, mostly around the picosecond timescale.[55] In this context, also changing the ligand motif to a tridentate like 2,2´:6´,2´´-terpyridine (tpy) towards $[Fe(tpy)_2]^{2+}$ shows this deactivation cascade. The ^{3}MLCT has a lifetime of 150 ps before relaxing into the ^{3}MC state, from which the ^{5}MC state is directly populated, with itself has an average lifetime of 5.35 ns.[56, 57] The catalytic active state has an insufficiently short lifetime to be useful, while the long-lived, non-emissive MC states prevent reactivation on a short timeframe. Light-induced excited spin-state trapping (LIESST), which populates from the ^{1}GS to the ^{5}MC state, can be accounted for the greater lifespan of the undesirable MC states.

In order to create an active iron-complex, the energies of the states must be changed appropriately, which must result in a decrease of the MLCT and while simultaneously decrease the MC energies. This targets both, the instability of MC states and the stabilisation of the MLCT. Attention must be paid to the energetically lowering of the ^{3}MLCT, since the energy still has to be efficient enough to perform the catalysis. These contemporary techniques have amassed a plethora of assessments about their adaptation to the iron centre.[36, 37, 51, 58, 59] The most prominent examples will be shortly outlined.

Improved Octahedral Geometry

The octahedral angles can be modified to be more optimal by focusing on the ligand design, which would result in a 180° N-Fe-N trans-trans angle. Therefore, better overlap between metal and ligand orbitals occurs, which stabilises the MLCT states. An example of this tactic are the complexes shown in fig. 1.10. Here the elongation between the connecting variables increases the trans-angle of the compounds.

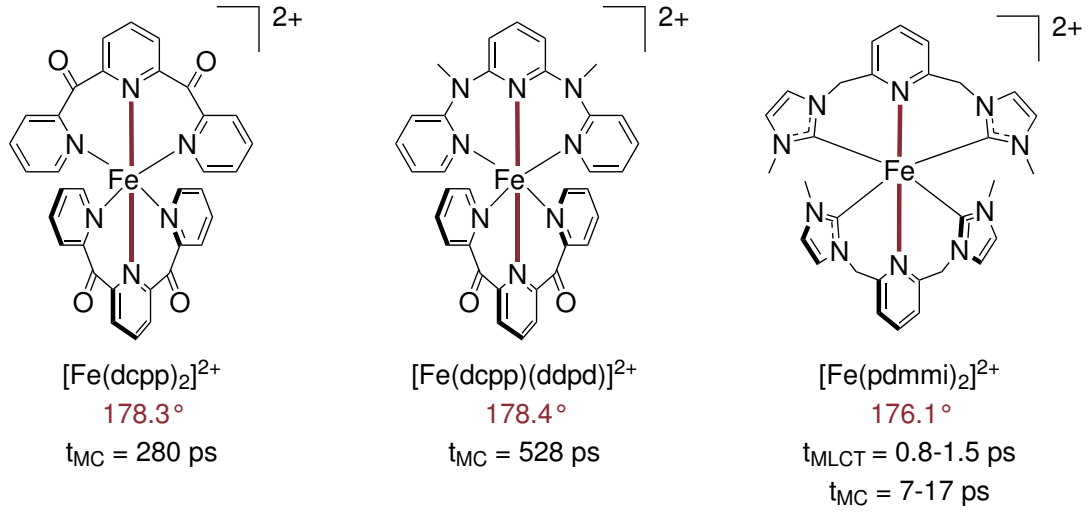

Figure 1.10: Chemical structure of: Left: $[Fe(dcpp)_2]^{2+}$ (dcpp = 2,6-bis(2-carboxypyridyl)pyridine)[56] with 280 ps MC-based lifetime; Middle: $[Fe(dcpp)(ddpd)]^{2+}$ (ddpd = *N,N´*-dimethyl-*N,N´*-dipyridine-2-yl-pyridine-2,6-diamine)[60] with 528 ps MC-based excited state lifetime; Right: $[Fe(pdmmi)_2]^{2+}$ (pdmmi = 3,3´-pyridine-2,6-diyl(methylene)bis(1-methylimidazole)), presenting both MLCT (0.8-15 ps) and MC (7-17 ps) excited state lifetimes.

$[Fe(dcpp)_2]^{2+}$ (fig. 1.10 left) by McCusker *et al.* shows a close to optimal trans angle of 178.3°.[56] Here, the EWG nature of the oxygen of the carbonyls additionally stabilises the π^* orbital. Thus, an excited state lifetime of 280 ps could be observed.[56, 59] With the ligand dcpp heteroleptic complexes were synthesized ($[Fe(dcpp)(ddpd)]^{2+}$ (fig. 1.10, middle) by the group of Heinze, thus employing a push-pull system with two detrimetal ligands, resulting in an trans-angle of 178.4°.[60–62] Although the metal-based MC lifetime of 528 ps is impressive, the MC states are significantly lower-lying, which results in fast deactivation of the ^{3}MLCT. MLCT could not be observed in two of the complexes reported here.

Improvement of the octrahedral angle reported by Gros could also be applied to an C^N^C-tridentate ligand, based on strongly σ-donating carbens, as in $[Fe(pdmmi)_2]^{2+}$ (fig. 1.10 right).[63] With a trans angle of 176.1°, a ^{3}MLCT lifetime of 0.8-1.5 ps and a ^{3}MC-lifetime of 7-17 ps were found. The two possible deactivation pathways include parallel or mixed relaxation from the ^{3}MLCT and the ^{3}MC into ^{1}GS. ^{5}MC state is

energetically lower and therefore excluded from these pathways, nonetheless the exact relaxation pathway is still part of intense research.

σ-donating NHC Ligands

Destabilisation of e_g^*-orbitals, hence lowering the MLCT could be achieved by strong σ-donors, which introduce a stronger ligand filed splitting. Therefore *N*-heterocyclic carbenes (NHC) were introduced by WÄRNMARK et *al.* opening a complete new research field within iron PS. A benchmark ^{3}MLCT lifetime of 9 ps for $[Fe(pbmi)_2]^{2+}$ (fig. 1.11, left) was reported.[57] The assignment, assisted by DFT calculations, confirmed the destabilised MC states, which makes the ^{5}MC state inaccessible. Their population would require drastic, rearrangement of the chemical structure, like bond lengths adjustments, unlikely to happen overall. The standard complex structure $[Fe(pbmi)_2]^{2+}$ has been further modified to study the impact of different functionalities, like the exchange of the methyl-functionality for a longer alkyl chain, such as *tert*-butyl or *n*-hexyl. The increased steric demand of the side chains elongates the iron-carbene bond, which ultimately reduces the orbital overlap in addition to a shielding of the metal centre. Thus, an equal deactivation behaviour of the excited state can be observed, since the MC-states are more accessible, effectively reducing the excited state lifetime to 0.3 ps for the *tert*-butyl chain.[57]

Despite an increase of the σ-donating capacity of NHCs, their π-accepting ability remains troublesome. To accommodate an MLCT excitation π-accepting moieties are indispensable, which could be enhanced by an increase of the π-conjugation of the ligand scaffold. $[Fe(pbmbi)_2]^{2+}$ (fig. 1.11 right) is one example with increased π-system on the carbene functionality, which dominates the behavior of the ligand.[64] An increased HOMO-LUMO gap (fig. 1.11) is the result by stabilisation of the LUMO and HOMO (t_{2g}-orbitals). The influence of both contributing orbitals results in a band-gap, that is less likely to be populated. The MLCT lifetime of 16 ps in nonetheless remarkably increased and a hypsochromic shift can be observed.[64]

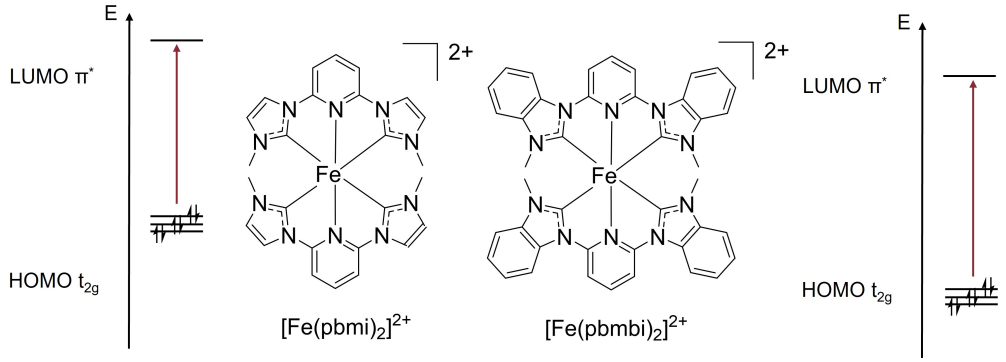

Figure 1.11: Chemical structure of: Left: $[Fe(pbmi)_2]^{2+}$ (pbmi = (pyridine-2,6-diyl)bis(1-methyl-imidazol-2-ylidene)), showing a excited state lifetime of 9 ps (in CH_3CN at rt)[57]; Right: $[Fe(pbmbi)_2]^{2+}$ (pbmbi = (pyridine-2,6-diyl)bis(1-methyl-benzimidazol-2-ylidene), changing the imidazole to benzimidazole provides better π-accepting abilities of the ligand.[64]

A study by BAUER et *al.* adds to these findings by making a relation between the number of σ-donating groups an the excited state lifetime. They demonstrated that increasing the number of σ-donors in a complex raises the HOMO level. Unfortunately, the LUMO energy level is also enhanced since more donors equals fewer pyridine π-acceptor functions.[65] Nevertheless, the π-system enhancement was also reported here to positively influence the absorptive behavior, resulting in a slight blue shift of the absorption. Hence π-acception of the ligand should be targeted with one example being the benzimidazole functionalized $[Fe(pbmbi)_2]^{2+}$.[64, 66]

To enhance the π-accepting character missing in these type of ligands, the pyridine, EWGs were implemented in the backbone of the structure by GROS and SUNDSTRÖM.[67, 68] An additional carboxyl-group to form $[Fe(cpbmi)_2]^{2+}$ (cpbmi = (carboxypyridine-2,6-diyl)bis(1-methyl-imidazol-2-ylidene)) shows an MLCT lifetime of 16 ps. In addition, this functionality opens the possibility to be implemented in dye sensitized solar cells (DSSC) by grafting the complex onto a TiO_2 surface. Although the photon currency of 2.3% was the first to be observed, the implementation of homoleptic complexes with two EWG may not be the ideal solution. The use of heteroleptic complexes with a push-pull mechanism, EWG on one site and EDG on the other, did not provide the expected results. The cause is believed to be insufficient electron coupling between PS and semi-conducting material.[64, 66, 69]

Cyclometalating Ligands

The σ-donating ability of the imidazole-based complexes is not sufficient to sustain a significant switch in the MLCT/MC energy state position. First attempts were theoretical DFT-calculations based on tridentate polypyridine terpyridine compounds where two cyclometalating phenyl-units were built in, which could achieve an ^{3}MLCT/^{3}MC inversion, as demonstrated by DIXON and JAKUBIKOVA et *al.*.[70–72] According to the calculations only a terminal cyclometalated position would be effective, resulting in a N^N^C ligand, in which case destabilisation of the ^{3}MC states could occur.[70, 73] First successful synthesis of a cyclometalated complex was reported by BAUER et *al.* with $[Fe(pbpy)(tpy)]^+$ (Hpbpy = 6-phenyl-2,2´-bipyridine) which exhibits a strong absorptive behaviour with a ^{3}MLCT lifetime of 0.8 ps.[74]

The strategies of improving the octahedral geometry, implementing carbenes or cyclometalating were introduced in this section, to enhance the excited state lifetime and accessibility of iron PS. Additional strategies include push-pull systems, an electron transport along an complex axis or mesoionic carbene ligands, which offer additional charges within the ligand structure.[75] Overall the combination of these strategies could lead to emissive iron-complexes. Nevertheless, the combination of these techniques should be considered further for new complex synthesis.

1.4.3.1 Iron(III) Complexes

Besides the strategies discussed in the previous section, the change from employing iron(III) instead of iron(II)-complexes has sparked wide-spread interest and recently became part of strategies towards successful PS.[36, 59] With a complete new excitation behaviour, iron(III) complexes convince by their different ground- and excited state landscape. Contrary to iron(II) in $3d^6$-configuration, the $3d^5$-iron(III) complexes, transitions are not based on an MLCT, but rather a ligand-to-metal charge-transfer (LMCT). The scheme shown in 1.12.

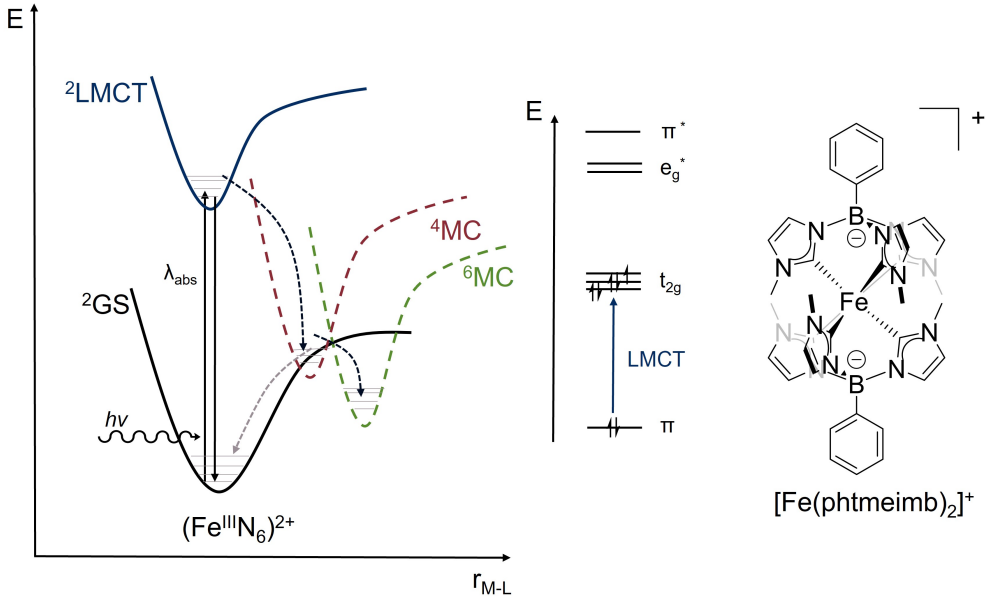

Figure 1.12: Excited state landscape for iron(III)-complexes, $[Fe(phtmeimb)_2]^+$ (phtmeimb = phenyl-tris(3-methylimidazole-1-ylidene)borate).

After direct excitation from the ^{2}GS into the ^{2}LMCT direct fluorescent relaxation to the ground state can occur. Other relaxation mechanism include non-radiative decay from the ^{2}LMCT or the MC states. Though these states can only be reached, by stretching the bond-length between metal centre and ligand. MC states are therefore not easily accessible.

One of the prime examples of a successful iron(III) complex in its low-spin (LS) configuration is $[Fe(phtmeimb)_2]^+$ (phtmeimb = phenyl-tris(3-methylimidazole-1-ylidene)borate), where the energy landscape of the ground and excited state could be determined completely. This complex with the electron-rich ligand-scaffold with strong σ-donating imidazoles represents one of the first luminescent iron complexes (fig. 1.12).[59, 76, 77] Emissive behaviour could already be observed at room temperature in CH_3CN at λ_{Em} = 600 and 655 nm, with an ^{2}LMCT lifetime of 0.1 and 1.96 ns. One explanation for the fluorescence can be found by a closer look on the microstates of $[Fe(phtmeimb)_2]^+$, depicted in 1.13.[78]

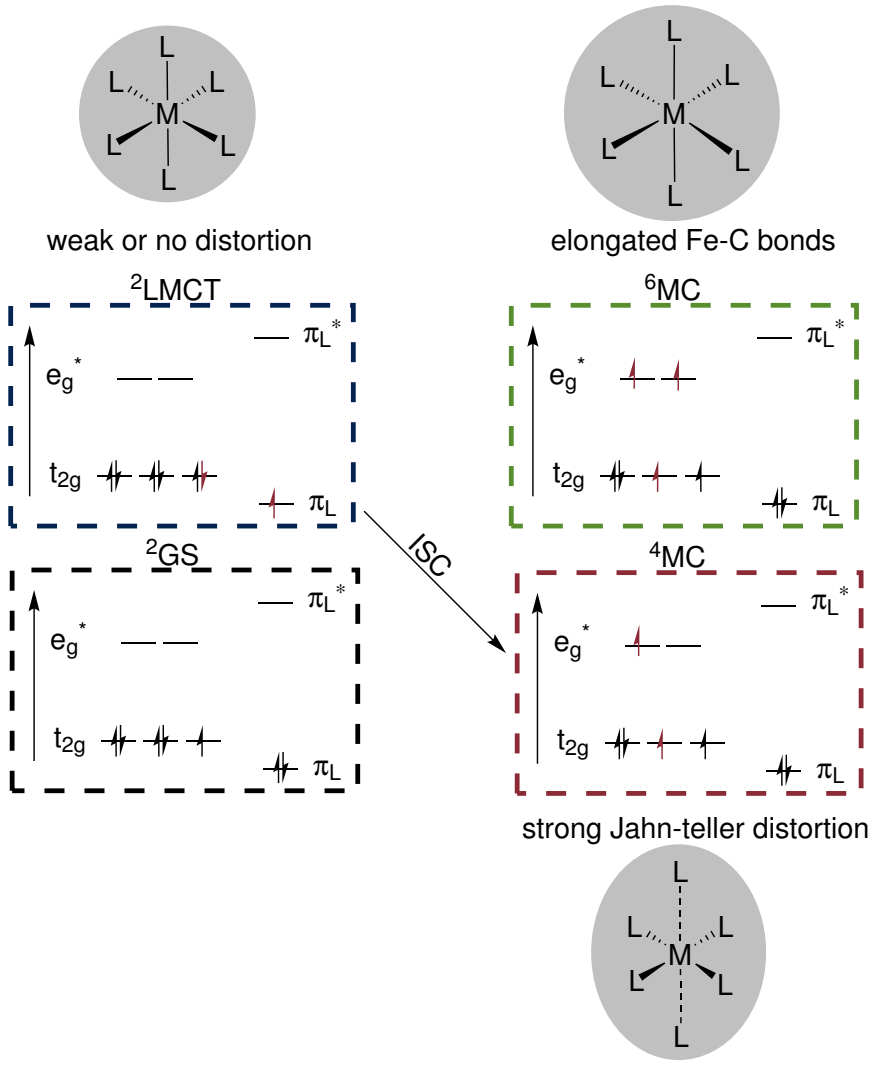

Figure 1.13: Microstates for the complex $[Fe(phtmeimb)_2]^+$, with all contributing molecular orbitals.[58, 59, 76, 77]

As the scheme shows, excitation of the complex excites one electron from the ground into the excited state via an LMCT. The complex conformation stays stable during this process, with the ^{2}LMCT nested with large Franck-Condon factors for emissive behavior. Due to the rigidity of the ligand and the stark ligand field splitting, the $^{4/6}$MC states are significantly destabilised. Therefore an activation barrier has to be overcome for the MC states to be populated, leading to a high quantum yield and a high LMCT lifetime. Another advantage is the nature of the doublet excited state, which can not be quenched by triplet oxygen, therefore only minor influence of atmosphere can be expected.[58] Nevertheless, non-radiative decay over the ^{4}MC state is only possible with a large Jahn-Teller distortion, or for ^{6}MC in elongated iron-carbon bond-lengths.

$[Fe(btz)_3]^{2+}$ (btz = 4,4'-bis(1,2,3-triazol-5-ylidene) was already reported as an example for the application of mesoionic carbenes as iron(II) species, but could also be reported

as iron(III) in form of $[Fe(btz)_3]^{3+}$. This compound also occurs in a LS form in which the π-orbital is entirely filled while the t_{2g}-orbital has five electrons, leaving one unpaired electron. ^{2}LMCT emission at $\lambda = 528$ and 558 nm with a charge-transfer lifetime of 100 ps occurs.[76]

Recently, a tridentate emissive iron(III)complex has been reported, that adapted the ligand structure of WÄRNMARK.[57] The complex $[Fe(ImP)_2][PF_6]$ (HImP = 1,1´-(1,3-phenylene)-bis(3-methyl-1-imidazol-2-ylidene)) with a CˆCˆC-connection, shows an impressive excited state behavior. The emission from the LMCT and MC states, with lifetimes of 240 and 4.6 ps respectively, is unparalleled in the contemporary literature. Although no studies have been undertaken concerning the catalytic activity, the strongly reducing and oxidizing nature of the LMCT-dominated states may be extremely favourable for application in catalysis.

Based on a cyclometalating function, phenypyrazoles have been reported to complexate iron in a transmetalation towards a tris-bidentate iron(III) complex. Besides its first successful synthesis has been published in 1978 by DREVS.[79, 80] DREVS also demonstrated the complex to undergo chemical reduction and oxidation, which are both good characteristics for a photocatalytically active complex. This ligand has also been applied to build complexes with iridium and cobalt as shown exemplarily in fig. 1.14.[81, 82]

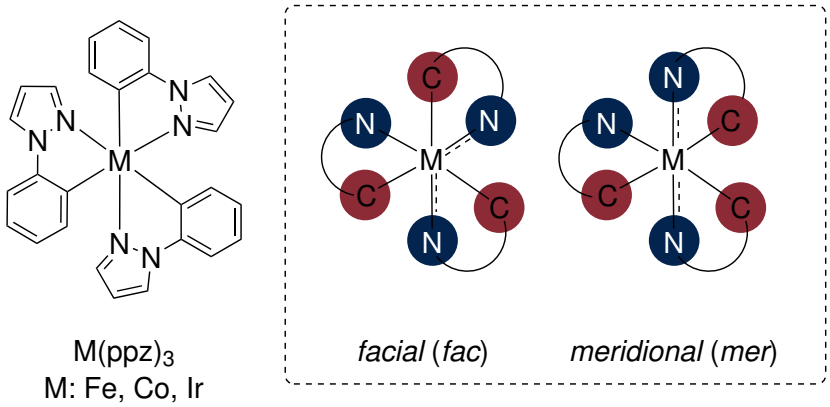

Figure 1.14: Scheme for $M(ppz)_3$ with M = Fe, Co or Ir metal centres.[81, 82] All tris-bidentate complexes display the ability to form *facial* or *meridional* isomers.

The bidentate ligand design enables *meridional* (*mer*) and *facial* (*fac*) arrangements (fig. 1.14, right). However, for $Co(ppz)_3$ only the *fac*-formation could be synthesised. $Ir(ppz)_3$ allowed for the independent synthesis of both isomeric forms in good yields (up to 80%). Both isomers are expected to exhibit different photophysical behaviour, as it has been demonstrated with iridium or ruthenium analogues.[82–84]

The approximation to a perfect octahedral form might additionally enhance the resultant ligand overlap. BY switching from tridentate to bidentate complexes an optimised orbital overlap could be reached. Complexes like $[Fe(pbmi)_2]^{2+}$ have an excellent trans

angle for nitrogen atoms (178.6°), however the carbon-carbon angle has to be improved significantly (158°).[57] By switching to the above-mentioned bidentate ligand motif, more flexible structure may rearrange to a more optimal octahedral structure.

2 Objective

To follow the strategy of implementing noble-metal free photosensitizer for water-splitting applications, main goal of this thesis is to synthesize novel iron-complexes. Therefore this study embarks the multifaceted exploration centred on the synthesis, characterisation and analysis of iron(III)-complexes derived from bidentate phenylpyrazole based ligands, with the work-flow proposed in fig. 2.1.

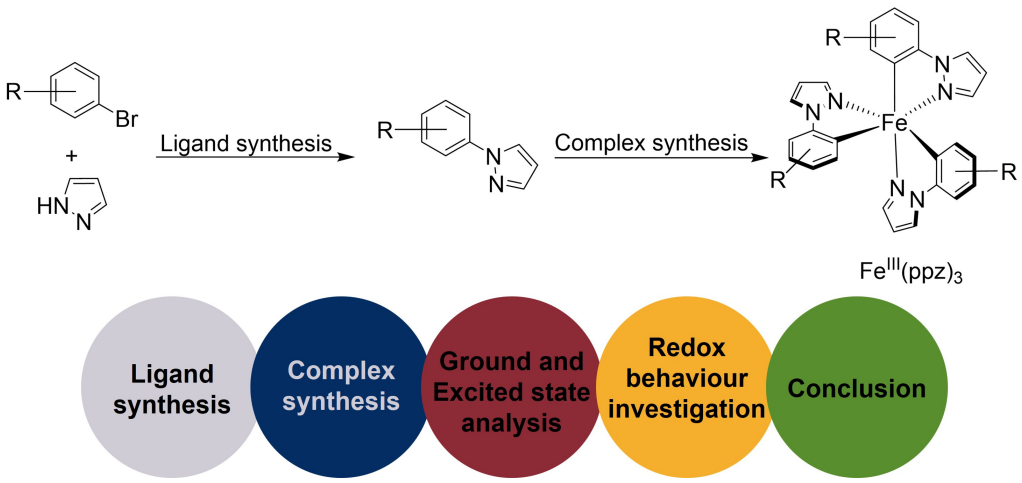

Figure 2.1: Proposed workflow of this thesis, with the anticipated synthesis and the following analysis of the synthesised compounds.

The first objective involves the synthesis of the complexes utilising previously mentioned ligands. Since the *N*-arylation of phenylbromides is well understood, various variations will be build in order to encompass electron-donating or withdrawing substituents as well as π-extensions, aim to unravel their impact in the subsequent complex formation. With the use of this ligand, the ratio of *mer*/*fac*-isomers is also of high interest, since both species are expected to show different photochemical behaviour.

The second aim of this thesis is the synthesis of iron-based photosensitizer. For this process the ligand activation through deprotonation and subsequent orthometalation is necessary. Noteworthy is the challenge to implement a appropriate iron precursor to form iron-carbene and iron-nitrogen bonds. The complex $Fe^{III}(ppz)_3$ has been reported in literature, but its photochemical behaviour has been completely neglected. Further investigation might provide more insights into the ground and excited state behaviour

of iron(III) complexes due to their exceptional excited state lifetimes. Within this thesis, multiple strategies will be applied in ligand and complex synthesis. It is possible to apply cyclometalating functions to produce a powerful ligand field. Non-ideal ligand and metal orbital overlap causes a weak ligand field splitting, which can also be reduced by using bidentate ligands. Additionally, it is simple to utilize the ligand's adaptability towards evaluating functional groups with varied effects.

Third and final objective will be a comprehensive analysis of the synthesised complexes, delving into their ground and excited state behaviour, as well as their redox properties. With a variety of analytical tools the complex ability and stability will be elucidated. With these the interplay between ligand properties and substitution effects is examined, which might pave the way for a profound understanding of iron(III)-complexes. The findings not only contribute to fundamental knowledge but also lay the groundwork for potential catalytic applications.

3 Ligand Design and Complex Syntheses

This section addresses the synthesis of ligands and the complexes that they form. Although several ligands have been discussed in the literature, the choice of ligand replacement is the important component of this work. To fine-tune intricate characteristics under the influence of numerous functional groups, a large selection is required, therefore ligand attributes must be considered.

3.1 Ligand Syntheses

As ligand motive, *N*-arylated heterocyclics will be employed. Strong σ-donating carbenes in bidentate ligands with a heterocyclic component as an electron acceptor will be studied in complex synthesis. Therefore phenyl-1*H*-pyrazole as motif was elected, since simple structural adjustments provide insights into their influence on photo-chemical complex behaviour. These motifs are applied in a variety of sectors, including biology, pharmaceutics, and synthesis building blocks.[85, 86]

In the past, poisonous substances or harsh reaction conditions were used to create phenylpyrazole-based compounds using a Pd-catalysed C-N-coupling. Now, cross coupling processes are used instead.[86, 87] Alternatively Cristau et *al.*, reported an Ullmann-type condensation using stoichiometric amounts of copper in a catalysed C-N-coupling in mild temperatures to link a pyrazole, imdiazole, or pyrrole with variously functionalised arylbromides.[86, 87]

In this context, the ligand syntheses adapted from Cristau et *al.* included the reaction of variously functionalised phenylbromide and pyrazoles. Therefore pyrazole (1.5 equiv.) was reacted with phenylbromides (1 equiv.). 10 mol% Copper(I)oxide (Cu_2O) as catalyst, (4 equiv.) caesium carbonate (Cs_2CO_3) and (0.4 equiv.) salicylaldoxime (salicylaldehyde oxime) as co-catalyst gave excellent yields within 24-48 h, with acetonitrile (MeCN) as solvent at 85 °C, under dry argon atmosphere. Cs_2CO_3 was employed as base, but special attention must be made to the porosity, which might therefore require in additional grounding before application in synthesis is recommended. Work up includes dilution with dichloromethane (DCM) and filtering through celite. After removing the solvent and dissolving the residue in DCM, the organic phase was washed with water and brine twice. After drying with magnesium sulfate ($MgSO_4$) and solvent

removal, flash column chromatography, with silica as stationary phase and mixture of *n*-hexane and ethyl acetate as mobile phase, was applied. Ratio different between the various functionalities. Overall reaction scheme is displayed in fig. 3.1.[87, 88]

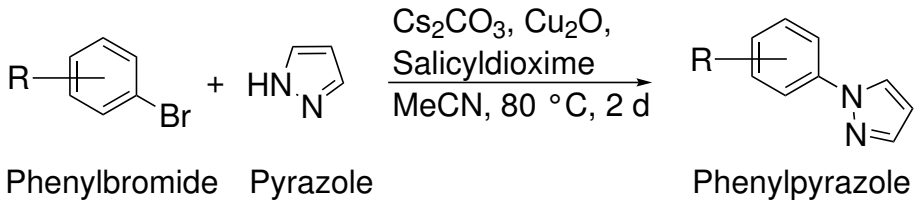

Figure 3.1: Reaction scheme of ligand syntheses, Ullmann-type coupling of functionalised phenyls with pyrazole. The product is differently substituted ligand based on the phenylpyrazole scaffold.[87] R displays a variety of functionalities, as EDG, EWG or π-systems.

It has been shown in the literature that functional groups in this synthesis can tolerate both electron withdrawing (EWG) and donating groups (EDG).[86–88] Yields range from adequate to quantitative. Differences of the yield reported in the literature and synthesis presented here might be due to difficulty in the up-scaling of the process, as well as the porosity issues with the catalyst Cs_2CO_3.

The non-substituted standard version of this ligand class is 1-phenyl-1*H*-pyrazole (**ppz**, fig. 3.2), which is commercially available. Substitution was implemented in various positions on the phenyl or on the pyrazole part, therefore changing the electron density distribution within the aromatic rings. This directly impacts the acidity of the protons, which is important for subsequent activation and therefore complexation, as explained in ch. 3.2. EWG, EDG, and aromaticity extension were among the ligands considered. An overview of the ligand scope with EDG and π-system extension is given in fig. 3.2.

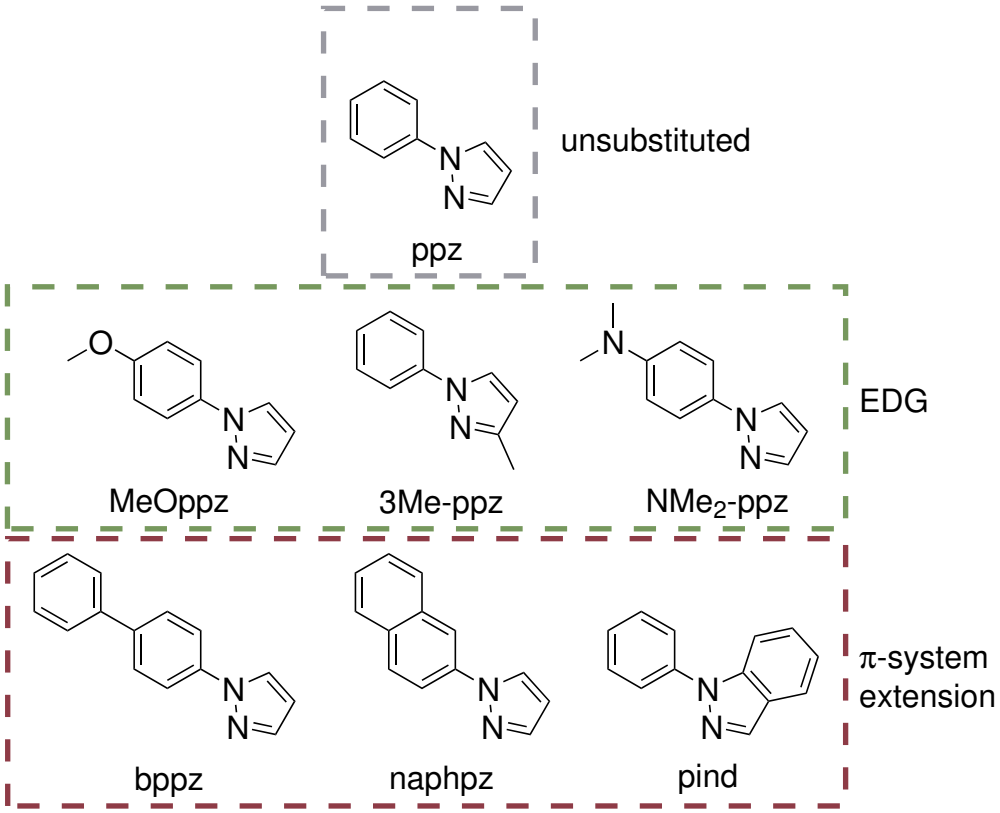

Figure 3.2: Overview of the ligand scope implemented in complex synthesis; top (grey): non-substituted ligand; middle (green): ligands functionalised with electron donating groups (EDG: methoxy-, methyl- and dimethyl-amine-functional group); bottom (red): ligands with π-system extension (biphenyl, naphtyl, and indazole functional group).

EDG includes a methoxy-functionality on the phenyl, to gain 1-(4-methoxyphenyl)-1*H*-pyrazole (**MeOppz**, fig. 3.2 green box). Methoxy functionalities have a negative inductive impact from the highly electronegative oxygen, which is compensated by the larger positive mesomeric effect of free electron pairs into the aromatic ring.[89] Second, *N,N*-dimethyl-4-(1*H*-pyrazole-1-yl)aniline (**NMe_2-ppz**, fig. 3.2 green box) was synthesized. Equal influence can be analysed with the 3-methyl-1-phenyl-1*H*-pyrazole (**3Me-ppz**, fig. 3.2 green box) which is also part of the ligand scope. This also shows a positive inductive effect, which directly affects the adjacent nitrogen atom. Unfortunately, methyl-groups on other pyrazole positions undergo photo-transposition to the 1-phenylimidazole or photo-cleavage to 3-(*N*-phenylamino)propenenitril.[90] Photo-transposition could result in 2-methyl-1-phenyl-1*H*-imidazole if **3Me-ppz** does not undergo photo-cleavage. These properties favour **3Me-ppz**, despite the fact that the methyl-group has a lesser electron donating function than other EDG.[90]

To extend the π-system, an additional phenyl was added, either as unconjugated 1-([1,1'-biphenyl]-4-yl)-1*H*-pyrazole (**bppz**, fig. 3.2 red box) or conjugated 1-(naphthalen-2-yl)-1*H*-pyrazole (**naphpz**, fig. 3.2 red box). To analyse the influence of aromatic-extension on the pyrazole, **1-phenyl-1H-indazole (pind)** (fig. 3.2, red box) was synthesised.

Aromatic compounds with an extended aromaticity frequently show advanced stability and may be able to capture incoming irradiation more efficiently. Furthermore, conjugated aromatic molecules are more easily oxidised and may give or take electrons more readily.[91]

With the implementation of the EDG-functionalities and π-extension, the electron density on the ligand scaffold will be significantly increased. The direct opposite could be enabled by withdrawing the electron-density. EWG-ligand scope is summarised in fig. 3.3.

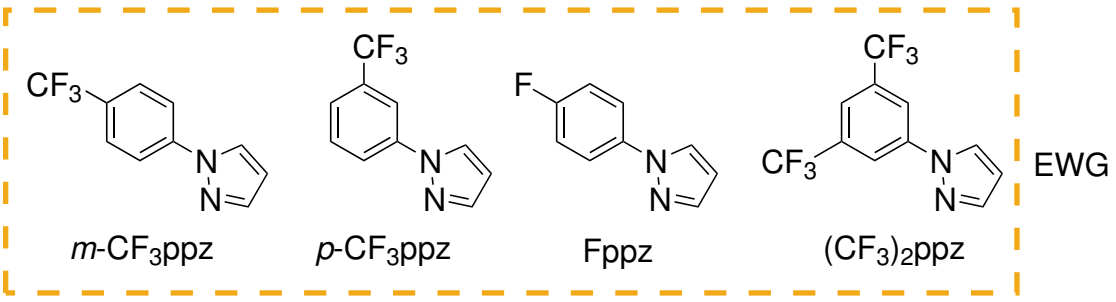

Figure 3.3: Overview of the ligand scope implemented in complex synthesis with electron withdrawing groups. Trifluormethyl-functionality in two different positions and one double-substituted ligand, one fluor directly attached to the phenyl.

Within this work, the influence of EWG groups, especially fluor-containing ones, was part of detailed analyses. Implementation of fluorinated groups and multi-fluorinated groups, included 1-(4-trifluormethylphenyl)-1*H*-pyrazole (***p*-CF$_3$ppz**, fig. 3.3 yellow box) and 1-(3-trifluormethylphenyl)-1*H*-pyrazole (***m*-CF$_3$ppz**, fig. 3.3 yellow box). These dissimilar positioned functional groups enable for additional investigation into the effect of group location on the ligand. As direct comparison on the influence of trimethylfluoride and directly attached fluoride 1-(4-fluormethylphenyl)-1*H*-pyrazole (**Fppz**, fig. 3.3 yellow box) was part of the ligand scope. 1-(3,5-bis(trifluoromethyl)phenyl)-1*H*-pyrazole (**(CF$_3$)$_2$ppz**, fig. 3.3 yellow box), was successfully synthesised, to test the possibility to implement multiple EWG. Two meta-positions in particular are intriguing since they may impede complexation owing to the steric requirement of three fluor-atoms.

Additionally, the influence of more functional groups was tested, especially with more EWG, since they are expected to influence the metal-centre the most. When more than one fluor is added to the phenyl ring, it produces not only the intended or 1-(3,4,5-trifluorophenyl)-1*H*-pyrazole, but also the multi pyrazole-substituted side product. Unfortunately, not only bromide substitution was seen when the starting material was fluor-containing phenylbromide. Fluor-functionality substitution was also prevalent. Therefore, multiple species could be found in the GC-MS (fig. 3.4).

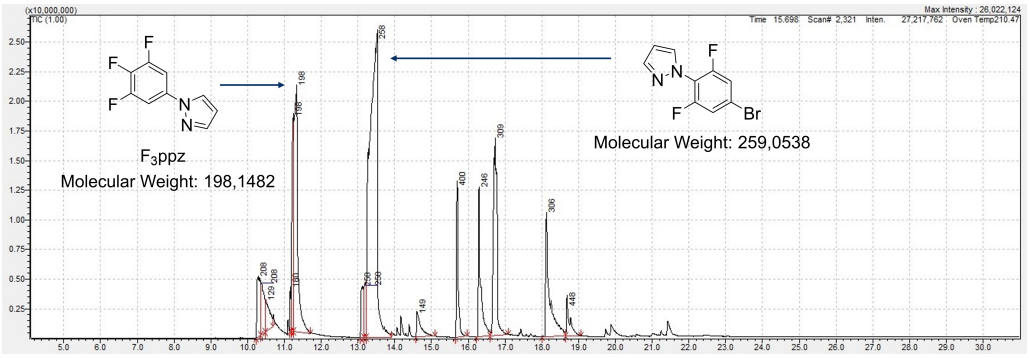

Figure 3.4: GC-MS overview of multi fluor-substituted phenylpyrazoles. 5-bromo-1,2,3-trifluorobenzene as staring material is substituted at multiple positions. Two of the products are shown in the picture. Other side-products are not shown explicitly for other substitution patterns, for better clarity.

Changing the co-catalyst from salicylaldioxime to cyclohexane-1,2-diamine, which has been suggested in the literature to avoid numerous substitutions, did not produce the desired ligand in its pure form.[92] Unfortunately, no work-up technique was capable of distinguishing between the numerous multi-substituted compounds and undefined by-products. GC-MS revealed that the by-products were pyrazole-substituted in the required position as well as in all other locations. The same was tested for 1-(3,5-difluorophenyl)-1*H*-pyrazole, but equal randomly conducted substitution was observed to the tris-fluoro-scaffold.

The utilised abbreviation for the product, as well as the starting material and yield following the reaction, are all summarized in Table 3.1.

Table 3.1: Overview of ligand scope, their respective abbreviations and their synthetic yield.

Ligand[a]	**Abbrevation**	**Starting Material**	**Yield /%**
1-phenyl-1*H*-pyrazole[b]	ppz	-	-
1-(4-methoxyphenyl)-1*H*-pyrazole	MeOppz	4-bromanisole	74.9
3-methyl-1-phenyl-1*H*-pyrazole[b]	3Me-ppz	-	-
1-(4-trifluormethylphenyl)-1*H*-pyrazole	*p*-CF_3ppz	4-bromobenzotrifluoride	84.1
1-(3-trifluormethylphenyl)-1*H*-pyrazole	*m*-CF_3ppz	1-bromo-3-(trifluoromethyl)benzene	60.5
1-(4-fluormethylphenyl)-1*H*-pyrazole	Fppz	1-bromo-4-fluorobenzene	52.7
1-(3,5-bis(trifluoromethyl)phenyl)-1H-pyrazole	$(CF_3)_2$ppz	1-bromo-3,5-bis(trifluoromethyl)benzene	24.6
1-([1,1'-biphenyl]-4-yl)-1*H*-pyrazole	bppz	4-bromobiphenyl	76.7
1-(naphthalen-2-yl)-1*H*-pyrazole	naphppz	2-bromonaphthalene	84.0

[a] Reactions conditions: 4 equiv. Cs_2CO_3, 10 mol% Cu_2O, 0.4 equiv. salycyaldioxime, acetonitrile, 85 °C, 2 d under dry argon atmosphere. Aqueous work up and flash column chromatography.

[b] Product commercially available.

Ligands **ppz** and **3Me-ppz** were commercially available and applied in complex synthesis without further purification. All other ligands were synthesized according to the procedure mentioned above, their purity confirmed by NMR-spectroscopy, MS and elemental analysis.

The ligands produced in this section could be synthesised by applying the reported synthetic procedure. Therefore a variety of functional groups could be attached, some of them have not yet been reported in published literature. They will be applied in complex synthesis, as described in detail in ch. 3.2.

3.2 Complex Synthesis

Complex synthesis required two critical steps in order to be successful. The first step is ligand activation by orthometalation, followed by transmetalation via an appropriate iron precursor. The ability to implement various functionalities was thoroughly investigated and the reaction pathway examined. The results are presented in the following section.

The effective activation of an iron-carbene and iron-nitrogen bond is the main technique for successful complex synthesis. The iron-carbene link requires ligand activation, whereas the iron-nitrogen bond forms more readily. A proton is more easily activated the more acidic it is. This should be considered while adding functional groups to the scaffold. DFT investigations of **ppz** with various functions found that the ortho-position is most acidic for all para-substituted compounds, regardless of the functional groups nature.[93] The most acidic site was moved by shifting the functional group to a meta-positioned relative to the pyrazole; the unfavourable proton was then surrounded by the pyrazole and the additional function. When sterically demanding deprotonating chemicals are used, the non-encased proton may be activated to assist balance the acidity differential. Otherwise, the steric requirement of the functional group inside complexation surrounding the metal core may impede complex formation.[93]

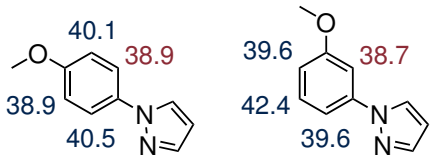

Figure 3.5: Calculated pk_a values in THF for differently substituted phenylpyrazole with a methoxy-functional group.[93] Free rotation of the pyrazole renders both adjacent protons equal, the pK_a will presumably be between the two calculated values.

As can be seen in fig. 3.5, activation with a grignard may be challenging. However, the DFT calculations do not consider the free rotation of the pyrazole, which may render protons equivalent, when the functional group is in *para*-position to the pyrazole. This is due to the free rotation of the two aromatic rings relative to each other, which could not be considered in the DFT calculations of Mongin et *al.*[93]

In this context, the reaction of 1-phenylpyrazoles and their derivates with various grignards or analogous metalorganic compounds has already been documented in the literature. *N*-Butyllithium (*n*-BuLi) deprotonates 1-phenylpyrazoles on the pyrazole part.[94, 95] However, functional groups in different positions on the pyrazole may operate as redirectors, preventing activation in undesirable regions. Ethyl magnesium bromide (EtMgBr), on the other hand, exclusively deprotonates the ortho-position, as shown in fig. 3.6. Nevertheless, literature suggest the formation of other adducts as well, though in small percentages. Substitution of the pyrazole with other five-membered heterocycles, like pyrrole or imidazole, did not yield the desired intermediate.[94]

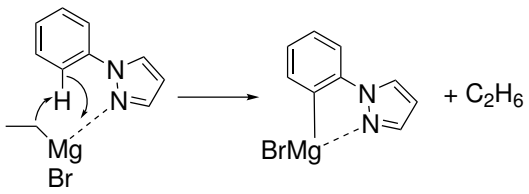

Figure 3.6: Reaction scheme towards the activated ligand with grignard, phenylpyrazole is deprotonated on the ortho-position on the phenyl. The resulting intermediate might be stabilised by an additional coordinative nitrogen-magnesium bond.[94]

For the transmetalation, a ligand-grignard solution was typically activated by refluxing it overnight at 80 °C using schlenk-technique in dry THF under argon atmosphere. Depending on the ligand utilised, the reaction mixture colour results in a change from a clear uncoloured to a red-orange solution during the reaction time. The solution was cooled to room temperature before being further chilled to -85 °C, at which point the pre-cooled metal precursor solution was added in-situ. Overview of this reaction is depicted in fig. 3.7.

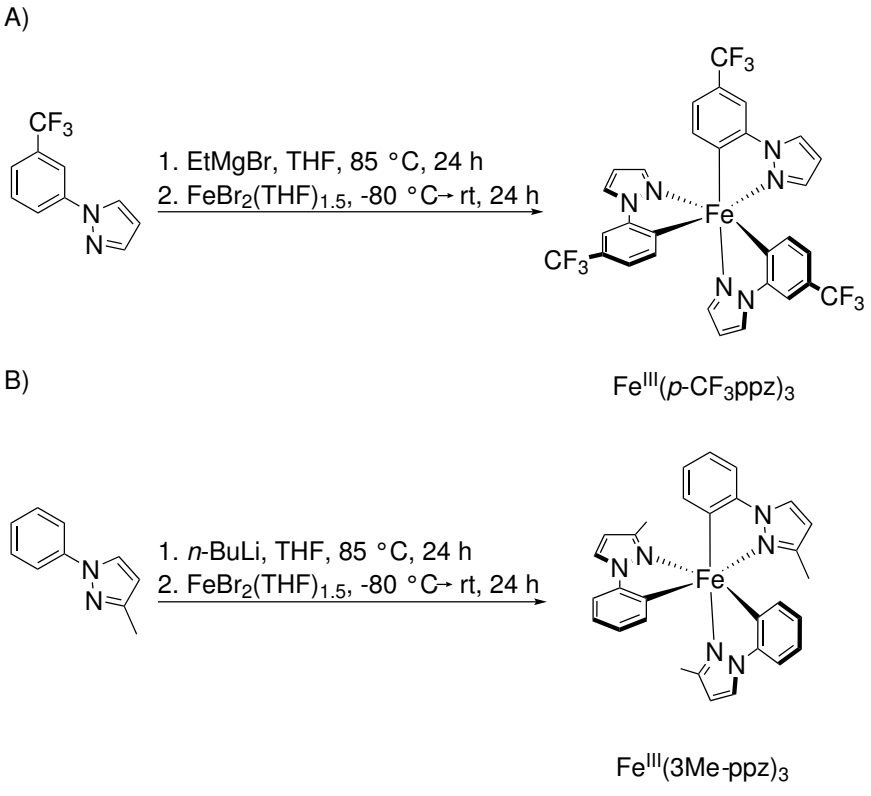

Figure 3.7: Reaction scheme of the complexation reaction. A: Exemplary reaction scheme with ethylmagnesium bromide (EtMgBr) towards $\mathbf{Fe^{III}(p\text{-}CF_3ppz)_3}$ and all other substituted complexes, B: reaction scheme with *n*-butyllithium (*n*-BuLi) towards $\mathbf{Fe^{III}(3Me\text{-}ppz)_3}$.

Within the practical work of this thesis, the reactivity of various iron-precursors was tested, which included $FeBr_2$, $FeCl_3$ and $FeCl_2 \cdot 4\ H_2O$ in THF solutions and as solid.

Neither created any detectable complexation; only the precursor $(FeBr_2)THF_{1.5}$ produced the expected complex. Understanding the composition of $(FeBr_2)THF_{1.5}$ is still part of research, its exact structure is not yet reported. Different combinations of $FeCl_2$, $FeCl_3$ and $FeBr_2$ seemingly give variable results, depending on the iron source and its purity. Analyses indicated various levels of THF ranging from 1.5 to 2, therefore both interpretations are used when referring to it, albeit 1.5 is more common.[96, 97] Following a successful synthesis, the precursor was produced as colourless crystals. Nevertheless, it is more feasible and retains a greater precursor yield to be generated *in-situ*, since ligand deprotonation requires the precursor to be in solution. Because the complicated synthesis most likely involves a disproportion reaction, 1.5 equivalents iron were used.[79, 98]

Consequently, the iron-precursor $(FeBr_2)THF_{1.5}$ was freshly prepared prior to application in synthesis. Therefore, $FeBr_2$ was dissolved in dry THF under argon atmosphere, with iron powder acting as co-catalyst. Overnight refluxing transformed the solution from dark brown to clear and colourless. After refluxing, the iron-precursor solution was cooled to room temperature before being added dropwise to the ligand solution at -85 °C. If insufficient volumes of solvent were used, colourless crystals formed during cooling to room temperature, limiting the transfer of the iron-precursor $(FeBr_2)THF_{1.5}$ into the activated ligand solution when transferred *in-situ*.

While combining the solutions, the colour rapidly changes to deep black. Further work up included removal of grignard-based residues by addition of an aqueous solution of NH_4Cl and DCM. Washing the organic phase twice with NH_4Cl solution and water, drying with $MgSO_4$ and solvent-removal gave raw-complex. To remove those impurities, like excess ligand, column chromatography was applied, where the product front was clearly visible as bright yellow to red spot, running in front of a broad ligand spot. Despite the fact that a wide range of solvents and stationary phases were tested, the product spot on thin layer chromatography plates (TLC) changed colour after drying, from yellow to deep blue (fig. 3.8).

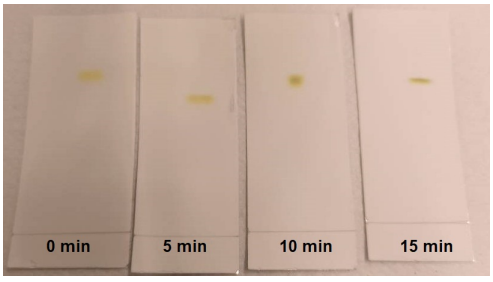

Figure 3.8: Oxidation of the complex **Fe(ppz)$_3$** on silica, time delayed (0, 5, 10, 15 min) shots of the complex on TLC, displaying a shift of colour from bright yellow to dark blue.

The cobalt complex $Co(ppz)_3$ produced similar blue-coloured bands in column chromatography, which were ascribed to the *mer*-isomer of the complex, whilst the exiting yellow product was proven to be entirely *fac*-isomer. Further research on the iron

complexes investigated here reveals that the generation of blue product during column chromatography may be unrelated to structure. When the contact duration between the complex and stationary phase is long enough, a rather gradual oxidation of the complex seems to emerge. Therefore, it is necessary to prevent time-consuming column chromatography, thus selecting DCM as the eluent for all complexes. Unfortunately, the poor solubility and its sticking to the stationary phase, prohibits the iron(IV)-species to further workup like column chromatography or crystallization.

After collecting the complex fractions, removal of the solvent, single crystals were grown by slow vapour diffusion technique, or slow evaporation of solvent. Filtered solid crystals were dried several days under high-vacuum at 50 °C. Yields of most complexes is poor (<20%). Exception is the complexation with *n*-BuLi, which was only possible for **3Me-ppz**, and resulted in yields up to 48%. The complexes were found in the iron(III)-configuration without any counterion, which was confirmed by NMR- and mass-spectroscopy. Additional elemental analysis proofed the purity of the compounds.

Not all ligands listed in ch. 3.1 gave the appropriate complexes. Aside from the non-substituted parental complex $\mathbf{Fe^{III}(ppz)_3}$, complexes with EDG-characteristics, both $\mathbf{Fe^{III}(MeOppz)_3}$ and $\mathbf{Fe^{III}(3Me\text{-}ppz)_3}$, were successfully prepared. Before immediate workup, mass spectrometry detected residues various by-products, including unreacted ligand, which could not be assigned further. Other functional groups on the pyrazole, other than a methyl in 3-position, did not result in successful complexation. It may be effective to activate with several metal-organic compounds in this situation, such as lithium-organyles. $\mathbf{Fe^{III}(3Me\text{-}ppz)_3}$ could not be synthesised via EtMgBr, but rather *n*-BuLi, which might be related the different activation points on the pyrazole, here blocked by the methyl functionality.

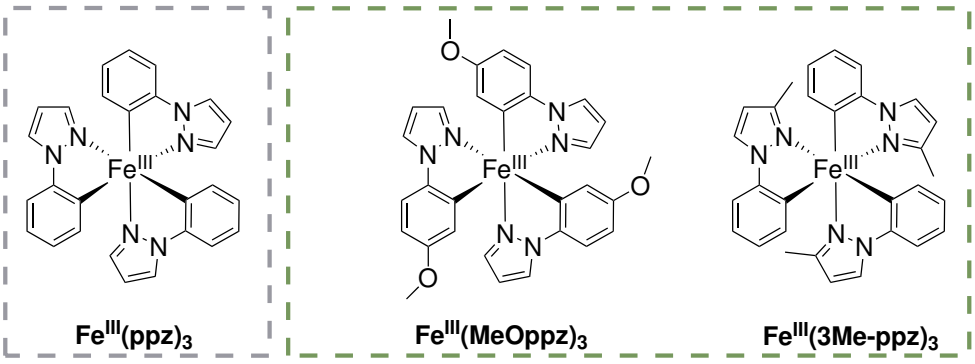

Figure 3.9: Complex overview for the unsubstituted standard complex $\mathbf{Fe^{III}(ppz)_3}$ and electron donating groups $\mathbf{Fe^{III}(MeOppz)_3}$ and $\mathbf{Fe^{III}(3Me\text{-}ppz)_3}$.

The extension of aromatic π-systems resulted in the unconjugated $\mathbf{Fe^{III}(bppz)_3}$ and conjugated $\mathbf{Fe^{III}(naphpz)_3}$, which were both isolated as red solid, see fig. 3.10. Unfortunately, complexation with **pind** did not give the desired complex. As mentioned before, substitution on the pyrazole is difficult. Different metall-organyles were employed with-

out success.

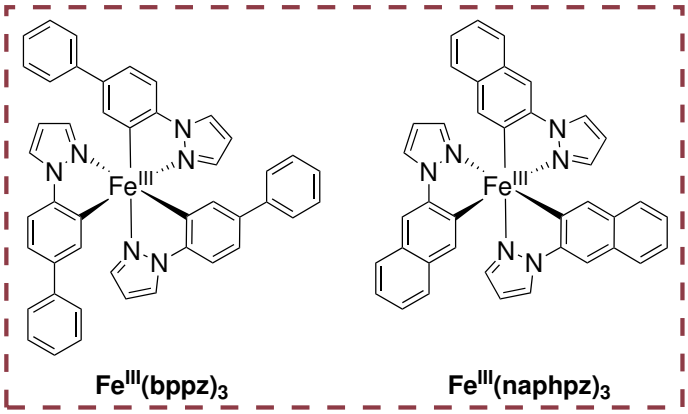

Figure 3.10: Complex overview for π-system extension, resulting in **Fe^{III}(bppz)$_3$** and **Fe^{III}(naphpz)$_3$**.

As it could be seen for the complexes with *N*-heterocyclic carbenes, EWGs could further enhance the MLCT-lifetime, which were therefore implemented. During the work-up procedure, these functionalities seemed to be more stable and produced single crystals easily.

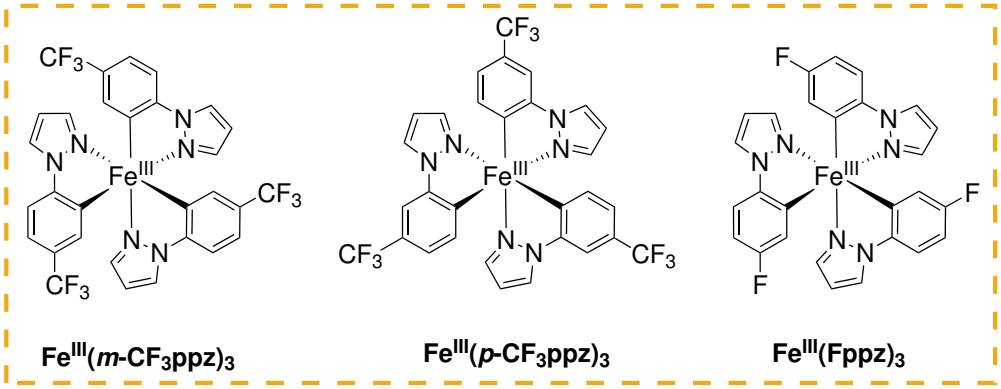

Figure 3.11: Complex overview for EWG substitutions, **Fe^{III}(*m*-CF$_3$ppz)$_3$**, **Fe^{III}(*p*-CF$_3$ppz)$_3$** and **Fe^{III}(Fppz)$_3$**.

With this increased stability, the complexation with multiple substitution of the phenylpyrazole scaffold complexes was also investigated. The ligand **(CF$_3$)$_2$ppz** was employed, since EWG groups were usually more stable during the work-up procedure. The astonishing result of this complexation, was the evidence of successful syntheses in NMR- and mass-spectrometry, **Fe((CF$_3$)$_2$ppz)$_3$** with theoretical mass of 893.0420 g/mol in fig. 3.12. Unfortunately, the bis-bidentate complex (**Fe((CF$_3$)$_2$ppz)$_2$**, theoretical: 614.0063 g/mol, found: 614.0062 [M$^+$]) is equally build. The signal for the bis-bidentate species was not seen in the other complexes, additionally the diamagnetic signals could be seen in the ^{1}H-NMR-spectra. This prevents removal of this species, since these two complex behave equal during column chromatography and crystallisation. Despite an

considerable effort, the separation of these two species and the free-unreacted ligand, like the addition of an halogen-attachment, was impossible. Other iron-precursors or metal-organyls for synthesis must be taken into consideration. Therefore, these complexes are not summarised in fig. 3.11, since they could not be isolated.

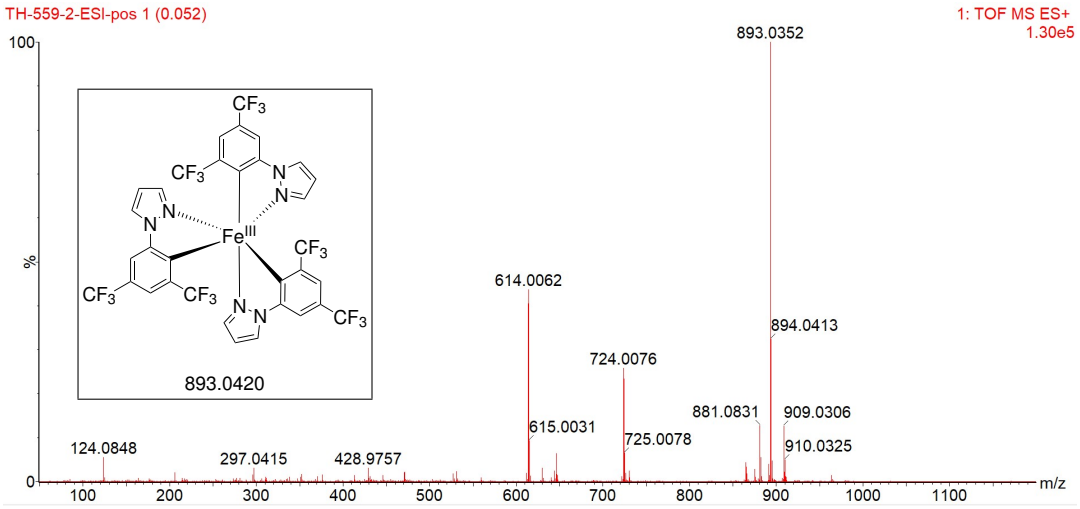

Figure 3.12: Mass spectrum for double substituted ligands, signal at m/z 893.0352 is presumably the desired complex, whereas, the signal at m/z 614.0062 represents the species with two attached ligands, the second signal was not seen for other complexes.

To recapitulate the complex synthesis tab. 3.2 gives the complexes with their IUPAC name and their respective abbreviation and a summary of their yields. Additional analytics are summarised for each complex in ch. 3.2.

Table 3.2: Overview of ligand scope,their respective abbreviations and their synthetic yield.

Complex	Abbreviation	Yield /%
Tris(1-phenylpyrazolato-N,C^2)iron(III)[a]	$Fe^{III}(ppz)_3$	7.5%
Tris(1-(4-methoxyphenyl)pyrazolato-N,C^2)iron(III)	$Fe^{III}(MeOppz)_3$	2.6%
Tris(3-methyl-1-phenylpyrazolato-N,C^2)iron(III)[a]	$Fe^{III}(3Me\text{-}ppz)_3$	48.1%
Tris(1-(([1,1'-biphenyl])-4-yl)phenyl)pyrazolato-N,C^2)iron(III)	$Fe^{III}(bppz)_3$	3.9%
Tris(1-(naphthalen-2-yl)pyrazolato-N,C^2)iron(III)	$Fe^{III}(naphpz)_3$	5.3%
Tris(1-(4-(trifluoromethyl)phenyl)pyrazolato-N,C^2)iron(III)	$Fe^{III}(m\text{-}CF_3ppz)_3$	17.2%
Tris(1-(3-(trifluoromethyl)phenyl)pyrazolato-N,C^2)iron(III)	$Fe^{III}(p\text{-}CF_3ppz)_3$	10.6%
Tris(1-(4-(fluoromethyl)phenyl)pyrazolato-N,C^2)iron(III)	$Fe^{III}(Fppz)_3$	2.73%

[a] Product commercially available.

The complex yields are generally low. The increased stability of the EWGs in complexes synthesis can be seen here, since $Fe^{III}(m\text{-}CF_3ppz)_3$ and $Fe^{III}(p\text{-}CF_3ppz)_3$ display yields above 10%. Every other complex is below 10% yield, except for the complex $Fe^{III}(3Me\text{-}ppz)_3$. The redirecting ability of the methyl-group enables the use of *n*-BuLi. This seems to be more efficient in ligand-activation or transmetalation resulting in nearly 50% yield.

Most complexes that could be linked to the ligand structure itself have relatively low yields of complexation. The complex's coordination must be taken into account first. Using bidentate ligands gives tris-coordinated complexes of *facial*- and *mer*-isomers. A *meridional* structure based on phenylpyrazoles would entail the crossing of two potent sigma-donor carbenes. As a result, the *mer*-isomers may be more fragile and, if not transformed into the *fac*-complex, may disintegrate. Second, the construction of both the tris- and bis-bidentate complexes is possible. These might as well be unstable and disintegrate when exposed to air or while undergoing work-up procedure. Additionally, the workup procedure does not stop the complex from being oxidised, which could also result in a yield shortage.

The five complexes $Fe^{III}(ppz)_3$, $Fe^{III}(MeOppz)_3$, $Fe^{III}(bppz)_3$, $Fe^{III}(naphpz)_3$ and $Fe^{III}(m\text{-}CF_3ppz)_3$ were classified as the five standard complexes which were thor-

oughly analysed in this thesis. They represent the broad variety of functional groups and were published in open access literature[99]. All other complexes were synthesised following this publication to bridge the gap to further understanding the influence of functional groups.

The syntheses of the product as iron(III) complex was verified by elemental analysis (EA), mass spectrometry (MS), single crystal X-ray spectroscopy, and nuclear magnetic resonance spectroscopy (NMR).

3.2.1 Complex Oxidation and Reduction

The capacity of the complexes to vary their oxidation number is a critical property for their use in photosensitizing processes. The complexes can be tested first by chemically oxidising or reducing them (fig. 3.13).

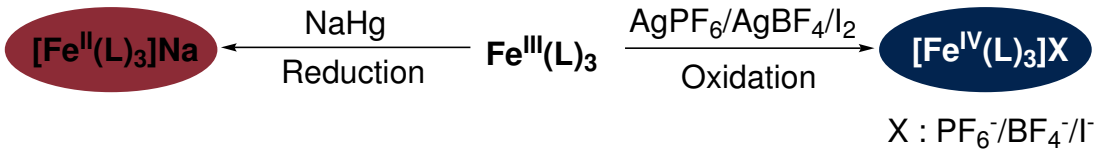

Figure 3.13: Left: Reaction towards the reduced iron(II) species with NaHg. Right: Oxidation pathway towards iron(IV) with a silver salt ($AgPF_6/AgBF_4$) or pure iodine (I_2).

The iron(IV) species for the investigations were obtained *in-situ* by oxidation of the respective compound with either a silver salt ($AgPF_6/AgBF_4$) or iodide (I^-), as shown in fig. 3.13. This produced predominantly dark blue to green solids with drastically altered solubility, so most solvents no longer produced a clear solution. $[Fe^{IV}(ppz)_3]PF_6$ resulted in a dark blue solid. Workup techniques could not be used due to solubility difficulties and the dramatic change in characteristics, especially the oxidation behaviour. The dark blue spot produced by column chromatography of $\mathbf{Fe^{III}(ppz)_3}$ might represent the iron(IV)-species, which could not be recovered from the column, even after testing with several eluents. However, NMR-, MS-, and Mößbauer-spectroscopy might still be used to complete the characterisation.

The iron(II) congeners for the investigation were also obtained *in-situ*. Unfortunately, due to instability the reduced species could not be isolated and purity of the complexes in this oxidation state could not be guaranteed. Therefore, only NMR-spectra were obtained for these to proof their successful reduction. Sodium amalgam or lithium naphthalenide were used for the reduction. A significant colour shift from predominantly yellow or orange solutions to dark blue, green, or purple was observed during the reaction. The chemical identity was only confirmed by full NMR assignment (ch. 4.2) of the diamagnetic signals, due to high reactivity towards atmospheric conditions.

Table 3.3: Success of the reduction and oxidation of the synthesized complexes.

Complex	Reduction	Oxidation
$Fe^{III}(ppz)_3$	+	+
$Fe^{III}(MeOppz)_3$	+	+
$Fe^{III}(3Me\text{-}ppz)_3$	+	+
$Fe^{III}(bppz)_3$	-	+
$Fe^{III}(naphpz)_3$	-	+
$Fe^{III}(m\text{-}CF_3ppz)_3$	+	+
$Fe^{III}(p\text{-}CF_3ppz)_3$	-	+
$Fe^{III}(Fppz)_3$	[a]	[a]

[a] Not found during syntheses

Unfortunately the reduction and oxidation was not possible for all complexes. The reduction most likely leads to unstable reduced complexes, which were unstable and could not be confirmed. The oxidation was successful for all complexes, but the solubility of these became increasingly worse the larger the ligand scaffold was. Nevertheless full characterization was at least possible for all complexes by NMR-spectroscopy.

4 Characterisation

The ground- and excited state characterisation of the successfully synthesised compounds is covered in the following chapter. This comprises information from cyclic voltammetry (CV), single crystal diffraction, UV-Vis-, spectro-electrochemistry, and extended NMR-spectroscopy. Calculations based on quantum chemical calculations support these findings.

4.1 Single-Crystal X-Ray Diffraction

Single crystals of the complexes could be grown by slow diffusion of an anti-solvent into a high concentrated complex solution. Single crystals of selected complexes could be grown for the iron(III)-species only, by slow evaporation of cyclopentane or ether as antisolvent into a complex solution in MeCN or DCM. The different shapes and colours of the single crystals might potentially be explained by different degrees of integrated solvent molecules (fig. 4.1). Suitable single crystals for the complexes with the oxidation number for iron(II/IV)-species could not be achieved.

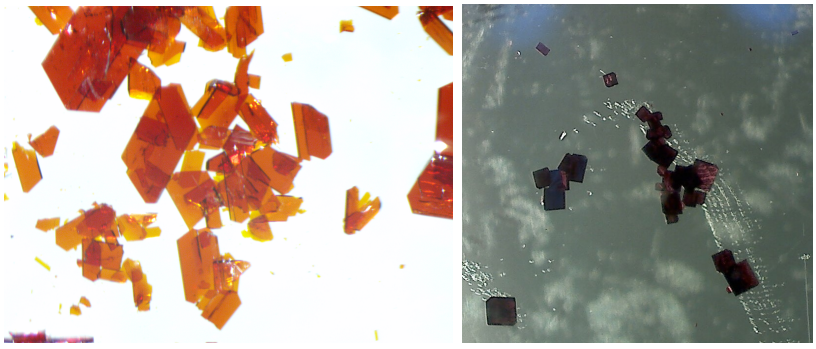

Figure 4.1: Microscopic view of complex crystals of $\mathbf{Fe^{III}(3Me\text{-}ppz)_3}$ (left) and $\mathbf{Fe^{III}(bppz)_3}$ (right).

Every complex exhibits a C_3-symmetric, distorted octahedral geometry. While both the facial (*fac*)- and meridional (*mer*)-isomers can form in complexes with tris-bidentate ligands generally, only the *fac*-species was found for all compounds.

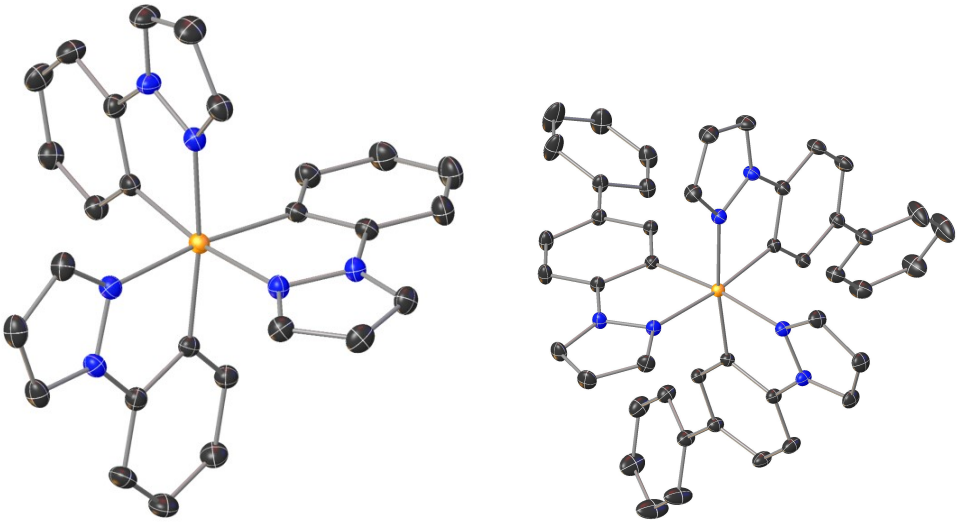

Figure 4.2: The anisotropic displacement ellipsoids in the single crystal structures are shown with 50% probability; the hydrogen atoms have been removed for clarity. Left: $\mathbf{Fe^{III}(ppz)_3}$; Right: $\mathbf{Fe^{III}(bppz)_3}$.

Shown in fig. 4.2, the exemplary crystal structure of $\mathbf{Fe^{III}(ppz)_3}$ and $\mathbf{Fe^{III}(bppz)_3}$ display the C_3-structure of the complexes. The appendix summarises the crystallographic data for all measured complexes. The Δ- and Λ-enantiomers can be formed within the *fac*-isomer and both were found in every obtained single crystal structure. This was found in every complex, exemplary displayed in fig. 4.3. This observation was independent from the functional group.

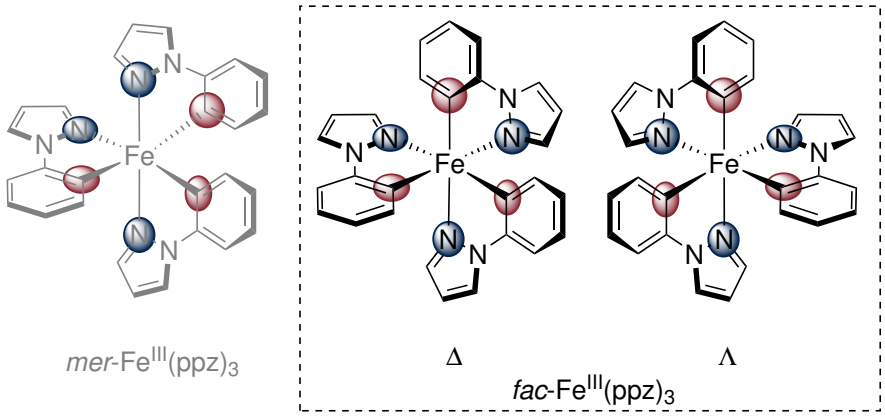

Figure 4.3: *mer*-$\mathbf{Fe^{III}(ppz)_3}$ (left) and *fac*-$\mathbf{Fe^{III}(ppz)_3}$ (right), with Δ- and Λ- enantiomers.

Despite the application of several synthetic routes, separation techniques, like fractioned crystallisation or column chromatography, the enantiomers (Δ/ Λ) could both be obtained in their pure form. The crystal structure indicates that there is an equal likelihood for each enantiomer. The phenylpyrazole-based ligands are crystallographically inequivalent due to the racemic (Δ/Λ) combination. As a result, the total of the bond lengths and angles must be averaged over both enantiomers. As a consequence, six values were

obtained and averaged, which was only possible since the variation was low or non-existent. Since the *fac*-isomers were formed as a single product.

The key structural parameters are summarised in tab. 4.1.

Table 4.1: Crystallographic data for the investigated iron(III)-complexes; averaged over all binding distances.[99]

Complex	Fe-N /Å	Fe-C /Å	chelate bite angle /°	C-Fe-N /°
$Fe^{III}(ppz)_3$	2.0030(15)	1.9508(13)	87.07(7)	171.54(7)
$Fe^{III}(MeOppz)_3$	2.0129(15)	1.9512(13)	94.52(5)	170.89(5)
$Fe^{III}(3Me\text{-}ppz)_3$	2.0453(14)	1.9543(6)	85.14(5)	177.67(5)
$Fe^{III}(bppz)_3$	2.0122(7)	1.9536(7)	91.68(1)	172.90(1)
$Fe^{III}(naphpz)_3$	2.0134(12)	1.9530(17)	93.59(17)	169.99(7)
$Fe^{III}(m\text{-}CF_3ppz)_3$	2.0075(15)	1.9520(16)	85.88(6)	170.46(6)
$Fe^{III}(p\text{-}CF_3ppz)_3$*	-	-	-	-
$Fe^{III}(Fppz)_3$*	-	-	-	-

* Complex could not produce measurable single crystals.

The Fe-C bonds in the reported complexes are about 0.05-0.09 Å shorter than the Fe-N bonds, most likely due to the carbon's greater donor and π-accepting characteristics. The Fe-C bond lengths in the analysed set of compounds are essentially similar, suggesting that the impact of the meta-substituents is negligible. Nonetheless, the Fe-N bond length and chelate bite angles vary depending on the functional groups. The shortest Fe-N bonds and smallest bite angles are observed for $Fe^{III}(ppz)_3$ (2.0030(15) Å, 87.07(7)°) and $Fe^{III}(m\text{-}CF_3ppz)_3$ (2.0075(15) Å, 85.88°), while $Fe^{III}(MeOppz)_3$ and $Fe^{III}(naphpz)_3$ exhibit the longest Fe-N bonds (2.0129(15) and 2.0134(12) Å, respectively) and the largest bite angles (94.52(5)°, 93.59(7)°). The longest bond-lengths are found in $Fe^{III}(3Me\text{-}ppz)_3$ (2.0453(14) Å), but also the shortest chelate bite angle (85.12(5)°). There is a little distortion in the ligand's planarity. Because of the C_3-symmetry, a repulsion between the functional methyl-group might not be ruled out. The *fac*-geometry dictates that the methyl-groups are contained inside a single plane. More space demanding groups may result in a rearrangement, favouring the *mer*- instead of the *fac*-enantiomer. Since complexation with functional groups in the meta- and ortho-position show *fac*-isomer only, the position of the functional group does not influence this further.

The trans-angle of the complexes is generally closer to the optimal ideal octahedral

structure than in bis-tridentate complexes. $[Ru(tpy)_2]^{2+}$ shows an N-Fe-N trans angle of 158.6°, whereas the synthesized complexes are between 169.9° and 177.7°. This could be compared to the $[Fe(dcpp)_2]^{2+}$ with an angle of 178.3°, which is considered as an example for the strategy to optimize the octahedral structure and produce a better orbital overlap. This could increase ^3MLCT-lifetimes, resulting in a longer excited state lifetime of the catalytic active state. Similar complexes, such as *fac*-$Co(ppz)_3$ (1.943 Å) and *fac*-$Ir(ppz)_3$ (2.021 Å) show equal distances with respect to the metal centre size.[82, 98] This demonstrates the stability and rigidity of the ligand structure, which could therefore result in stable complexes with a good metal-ligand overlap. Same could be seen for the bond lengths in tris-(1,10-phenanthroline)iron(III) complex, with a bond length of 1.977(3) Å.[100] This octahedral low-spin iron(III)-analogue displays equal values, and shows good redox- and absorptive behaviour.

The resonance impact of the functional groups appears to affect both, the Fe-N bond length and the chelate bite angle, by changing the electron density on the coordinating nitrogen. This would explain why the bond lengths in $\mathbf{Fe^{III}(ppz)_3}$ and $\mathbf{Fe^{III}(\textit{m}\text{-}CF_3ppz)_3}$ are comparable, because the trifluoro-methyl group exhibits very small resonance effects, the methoxy and naphthyl moieties exhibit large resonance effects. Another factor to explain the bond-lengths and angles could be the orientation of the ligands, which results in two imaginary levels. Here, the nitrogen atoms are within one imaginary level, whereas the bonded-carbon atoms are diametral in another level, as depicted in fig. 4.4.

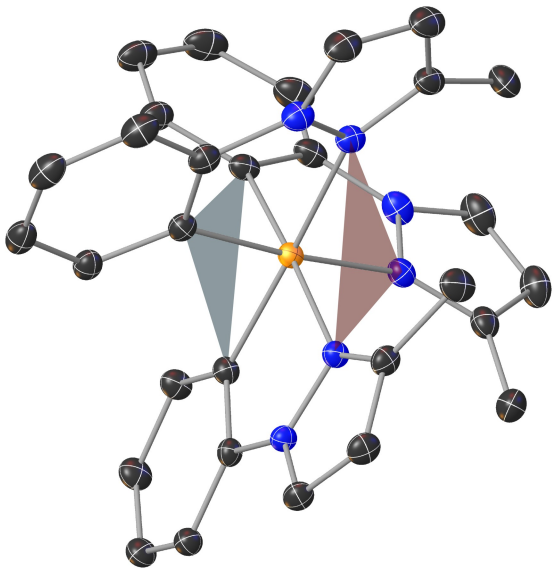

Figure 4.4: Single crystal structure of $\mathbf{Fe^{III}(3Me\text{-}ppz)_3}$ with the indicated planes for the ligand orientation. The nitrogen atoms (red triangle) are orientated in one plane, whereas the bonding carbon (blue triangle) are orientated diametral.

Therefore the functional groups are on one side of these imaginary planes, which could lead to a slight repulsion between these, especially if they are room-demanding, like the phenyl or naphthyl-functionalities.

DFT calculations are performed to determine the bond lengths and angles, as well as Gibb´s energy difference between the *fac*- and the *mer*-enantiomers. The optimised *fac*-isomers' computed bond lengths and angles correspond with the crystal structure, showing a strong agreement between the calculation and experimental results. These calculations were made for the five standard complexes, but the tendency will most likely be the same for the remaining complexes. For $\mathbf{Fe^{III}(3Me\text{-}ppz)_3}$, $\mathbf{Fe^{III}(\textit{p}\text{-}CF_3ppz)_3}$ and $\mathbf{Fe^{III}(Fppz)_3}$, only the *fac*-enantiomer could be observed as well. The only angles that differ between the theoretical calculation and the experiment are those of the C-Fe-N atoms that are arranged in opposition to each other. This indicates that the gas phase optimised structure approximates a perfect octahedral structure better than the solid crystal, as was expected (tab. 4.2).

Table 4.2: Data for the PBEh-3c geometry optimised *fac*-complexes.

Complex	Ø Fe-N / Å	Ø Fe-C / Å	∠ C-Fe-$N_{(ax)}$ / °
$\mathbf{Fe^{III}(ppz)_3}$	2.020	1.954	173.7
$\mathbf{Fe^{III}(MeOppz)_3}$	2.020	1.956	174.3
$\mathbf{Fe^{III}(bppz)_3}$	2.018	1.952	174.8
$\mathbf{Fe^{III}(naphpz)_3}$	2.019	1.952	174.5
$\mathbf{Fe^{III}(\textit{m}\text{-}CF_3ppz)_3}$	2.015	1.956	174.5

The PBEh-3c optimised lowest quartet state of *fac*-$\mathbf{Fe^{III}(ppz)_3}$ could also be visualised (fig. 4.5).

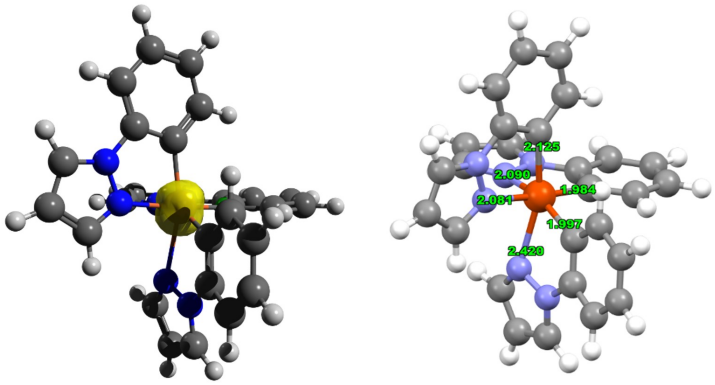

Figure 4.5: PBEh-3c optimised lowest quartet state of *fac*-$\mathbf{Fe^{III}(ppz)_3}$. Left: Spin density plot. Right: Depicted Fe-ligand bond lengths.

This shows the spin density plot for *fac*-$\mathbf{Fe^{III}(ppz)_3}$ (left) and the iron-carbene and iron-nitrogen (right) bond-lengths. Additionally, with the crystal structures data, the preferred enantiomer could be calculated, as summarised in fig. 4.6.

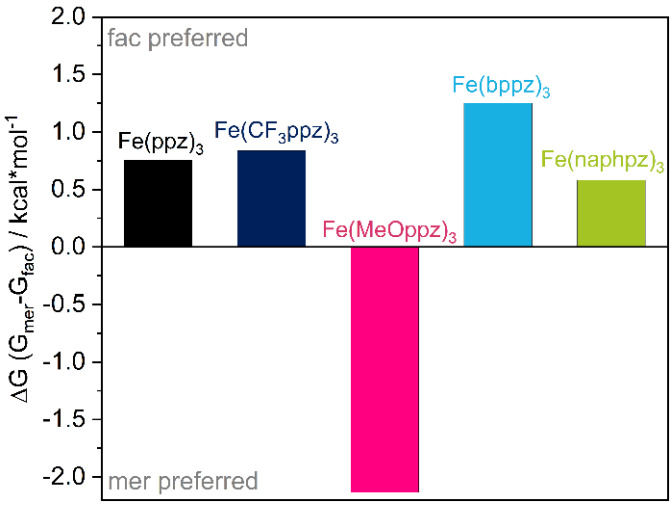

Figure 4.6: Gibbs energy difference (ΔG) between the *fac*- and *mer*-isomers of optimised geometries computed at the DFT/PBEh-3c level of theory.[99]

Using the PbEh-3c composite method, the Gibbs free energy (G) for the optimised structures was computed for this purpose.[101] In the case of the complexes $\mathbf{Fe^{III}(ppz)_3}$, $\mathbf{Fe^{III}(\textit{m}\text{-}CF_3ppz)_3}$, $\mathbf{Fe^{III}(bppz)_3}$, and $\mathbf{Fe^{III}(naphpz)_3}$, the *fac*-conformer is energetically favoured by 0.5-1.5 kcal·mol^{-1}. Similar complexes such as Co(ppz)$_3$ and Ir(ppy)$_3$ have also been found to exhibit better stability in the *fac*-conformer, which can be explained by the position of the phenyl groups in relation to the pyrazolyl groups, as previously discussed.[82, 98] Remarkably, *mer*-$\mathbf{Fe^{III}(MeOppz)_3}$ appears to have a greater thermodynamic stability in calculations even though it crystallises in the *fac*-isomer. One issue is that the basis of the computations only takes into account stability in the gas phase, not the required stability in a solid state or solution.

4.2 NMR

The following chapter is yet part of ongoing research and its manuscript is under preparation.[102]
The complexes were thoroughly examined using nuclear magnetic resonance spectroscopy (NMR). The unpaired electron causes the compounds, which were initially received as iron(III)-complexes, to be paramagnetic. Two unpaired electrons, like in iron(IV), can also produce paramagnetic centres by removing one electron from the iron centre. Exception in this series represent the iron(II)-species, received after reduction with NaHg. Because of the diamagnetic core, typical NMR-pulse programs and common assignment may be used. However, this is not possible for iron(III)- and iron(IV)- complexes. Paramagnetic transition metal complexes (pTMC) and other open shell systems are difficult to characterise and evaluate due to their wide chemical shift range and resonance-broadening caused by the unpaired electron of the metal centre.

Nonetheless, analyses of paramagnetic molecules such as iron(III) complexes and the development of paramagnetic NMR (pNMR) techniques has sparked considerable interest, for example for insights into photoreactions and catalytic cycles. Originating in the 1950, paramagnetic compounds studied in solid-state led the path towards application of these techniques in chemistry and biochemistry. Since then, basic concepts and interpretation of NMR data is a well established method, especially in biochemistry fields.[103] Nonetheless, NMR has not yet been the favoured approach for further investigating electron distribution and conformational dynamics in solution of photosensitizers.[104, 105] NMR is an exceptional and convenient tool for the determination and analysis of paramagnetic centres, which is often neglected in the investigation of comparable paramagnetic compounds. Nevertheless, this technique has been used to fully characterise the complex in their different oxidation states and gain more information about the behaviour in solution. The applied techniques allowed for the analysis of the resonance shifts and their respective relaxation time in relation to the temperature, functional group, and oxidation state.[106]

4.2.1 General Observations

Mononuclear, bidentate complexes like the ones presented in this work, can form *meridional* (*mer*-) and facial (*fac*-)-coordination isomers. Single crystal diffractometry confirmed that the originally produced iron(III)-complexes only exhibit the *fac*-isomer, shown in ch. 4.1.[99]

^{1}H-NMR spectra of the iron(III)-complexes show relatively sharp singlet signals. Obtained spectra include the respective amount of proton signals for each of the paramagnetic complexes, seven signals for $\mathbf{Fe^{III}(ppz)_3}$ and six for every other monosubstituted complex, plus signals for eventually attached methyl-groups, eleven signals

for $\mathbf{Fe^{III}(bppz)_3}$, and nine signals for $\mathbf{Fe^{III}(naphpz)_3}$. Therefore, the quantity of resonances represents the formation of *fac*-isomer exclusively, since the C_3-symmetry of this formation is rendering the three ligands magnetically equivalent. *Mer*-isomers would have three magnetically inequivalent ligands, causing three times as many ^{1}H-resonances, and both sets of signals if they were mixed. The spectra of the three species are shown in fig. 4.7.

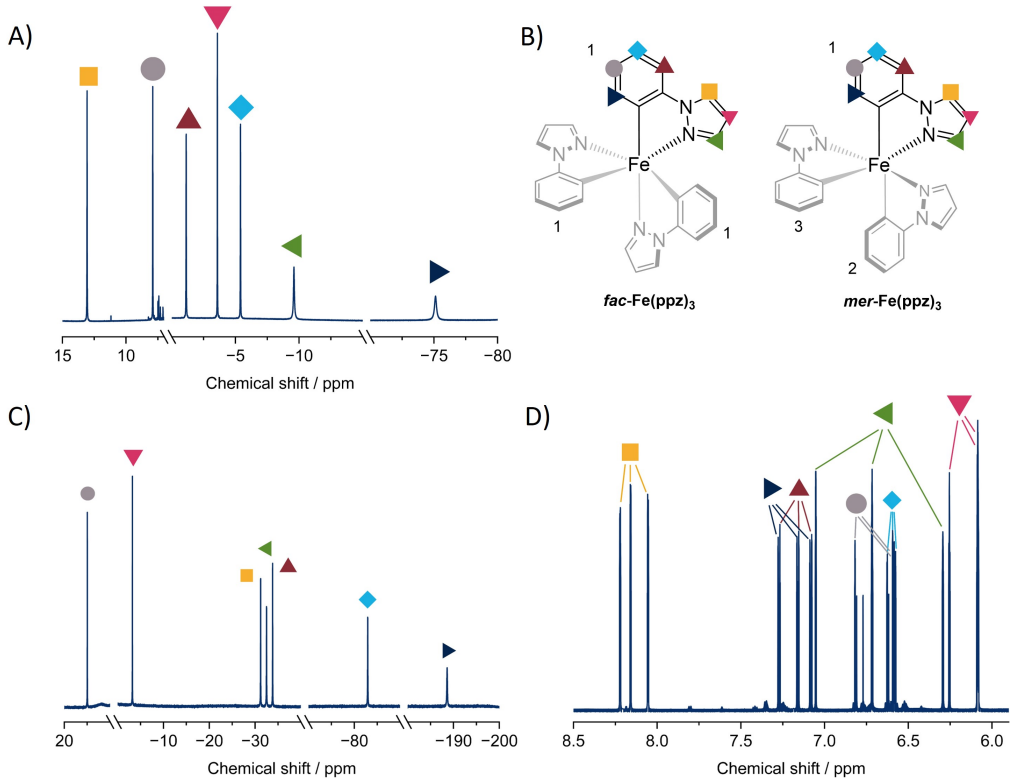

Figure 4.7: B) Structure of the two isomers, left structure: *fac*-isomer with three equivalent ligands, right structure: *mer*-isomer with three inequivalent ligands. ^{1}H-NMR of: A) $\mathbf{Fe^{III}(ppz)_3}$ showing the *fac*-species only, measured in MeCN at 298 K; C) $\mathbf{[Fe^{IV}(ppz)_3]^+}$ showing the *fac*-species only, measured in MeCN at 298 K; D) $\mathbf{[Fe^{II}(ppz)_3]^-}$ reduced in THF, marked positions are resonances for the *fac*-species. Every other visible signal is ligand or undefined by-product.

Stability of complexes under oxidation and reduction is critical, since they might occur in catalytic pathways via oxidative or reductive quenching of the excited state.[107] The ^{1}H-NMR of the iron(IV) (fig. 4.7, B) compounds show the same quantity of signals as the iron(III)-species, confirming that the stability of the *fac*-isomer transfers to two unpaired electrons as well. However, three times the number of signals are recorded in the case of iron(II) complexes. Traditional NMR pulse procedures revealed that the signals belonged to a single species with three magnetically inequivalent ligands (fig. 4.7, B). Therefore, upon reduction, a symmetry breaking transition occurs to form the predominantly stable *mer*-isomer of the complex (fig. 4.7). Carbon donors are on one plane in the *mer*-species, while nitrogen donors are in the other. As a result, two of the strong carbon donors are

opposite each other, resulting in a linear C-Fe-C-bond. This positioning of the phenyl-functionalities is thermodynamically non-favoured in the iron(III)- and iron(IV)-species, nevertheless DFT studies on the isomer-stability for different oxidation states support the experimental observations.

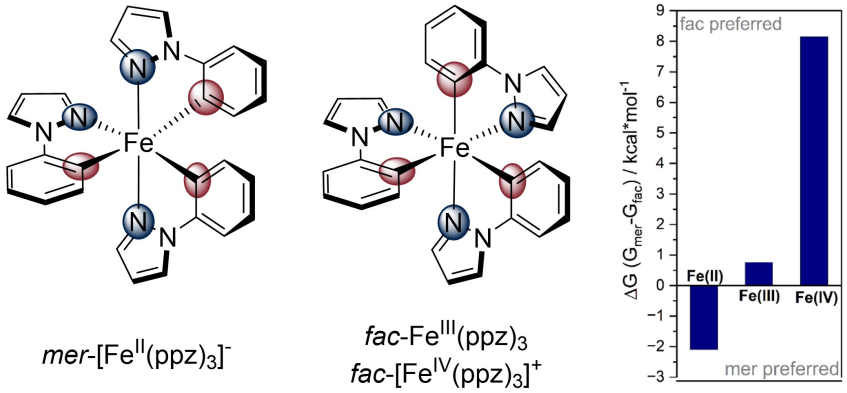

Figure 4.8: Left: Chemical structure for the $[\textit{mer}\text{-}Fe^{II}ppz_3]^+$ and the $\textit{fac}\text{-}Fe^{III}(ppz)_3$ and $[\textit{fac}\text{-}Fe^{II}ppz_3]^-$ exemplarily for the ppz substituted complex. Right: DFT calculations () on the preferred species for all oxidation states. The DFT calculations were performed by MSc. Lorena Fritsch.

During the reduction to $\textit{mer}\text{-}Fe^{II}ppz_3$, the *mer*-isomer undergoes conformational change, which can be either thermodynamic or kinetic. In addition, free ligand can be seen in the solution as a result of a reprotonation. The origin of the proton for re-protonation towards the free ligand could not be confirmed completely.

Therefore extend stability tests on the reduced species were performed. While reduced complexes result in well-defined spectra immediately after reduction, uncertain dynamics occur afterwards. When the spectra of instantly after reduction are compared to spectra within a short time frame (2 h), the ligand signal increases, but a new, unidentified species appears. As a result, the observed changes may be the result of a conversion to the *fac*-isomer. Unfortunately, the attribution of these signals was not possible. During the measurement, the signals expand even further, making direct assignment impossible (fig. 4.9).

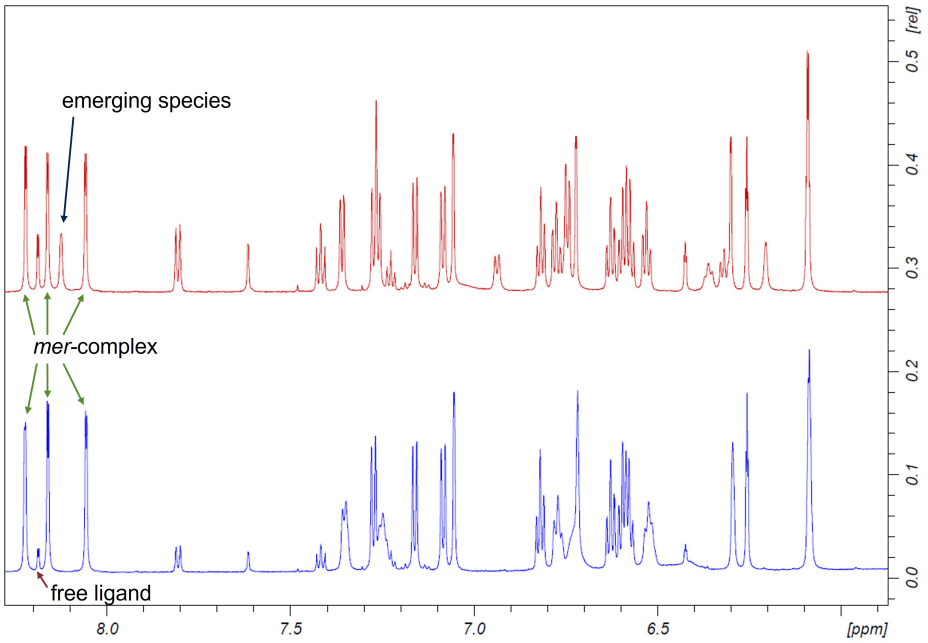

Figure 4.9: Blue: ^{1}H-NMR spectrum in THF-d_8 for $[Fe^{II}ppz_3]^+$ directly after reduction shift exemplarily assigned above 8 ppm, which also shows traces of free ligand in the solution; Red: $[Fe^{II}ppz_3]^+$-complex solution after 5 h. Emerging species may be a mixture of two isomers *mer*- and *fac*-isomer of the complex or free ligand and paramagnetic impurities. Complete assignment was not possible due to instability.

However, stability test at room temperature for 7 days, illuminating the solution for 18 h with a 300 W Xenon lamp, or mild temperatures for 18 h resulted in a steady increase of a secondary species.

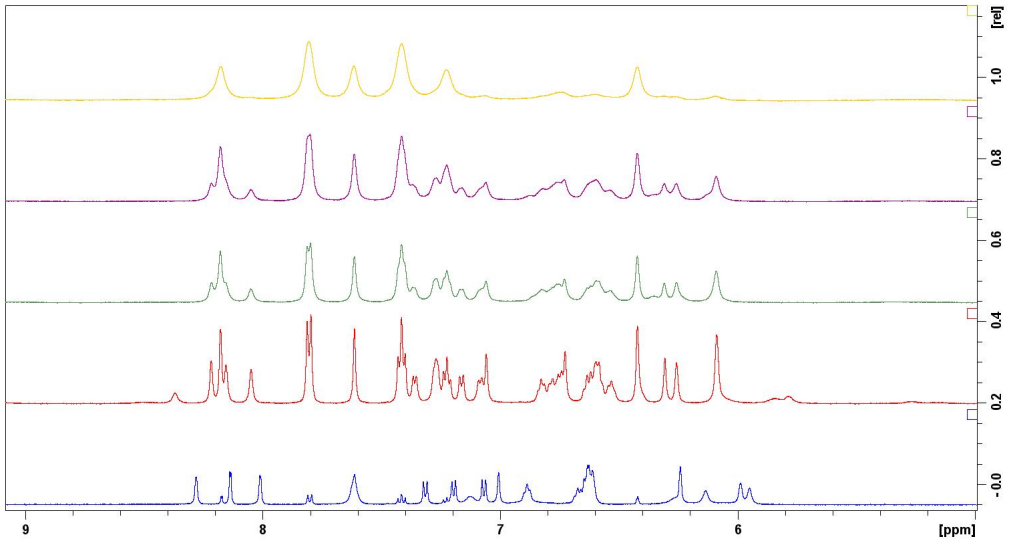

Figure 4.10: ^{1}H-NMR spectrum in THF-d_8 for $[Fe^{II}ppz_3]^+$ directly after reduction (blue), time-dependent measurements while submitting the solution to 60 °C; after 1 h (red), 2 h (green), 3 h (purple), 18 h (yellow).

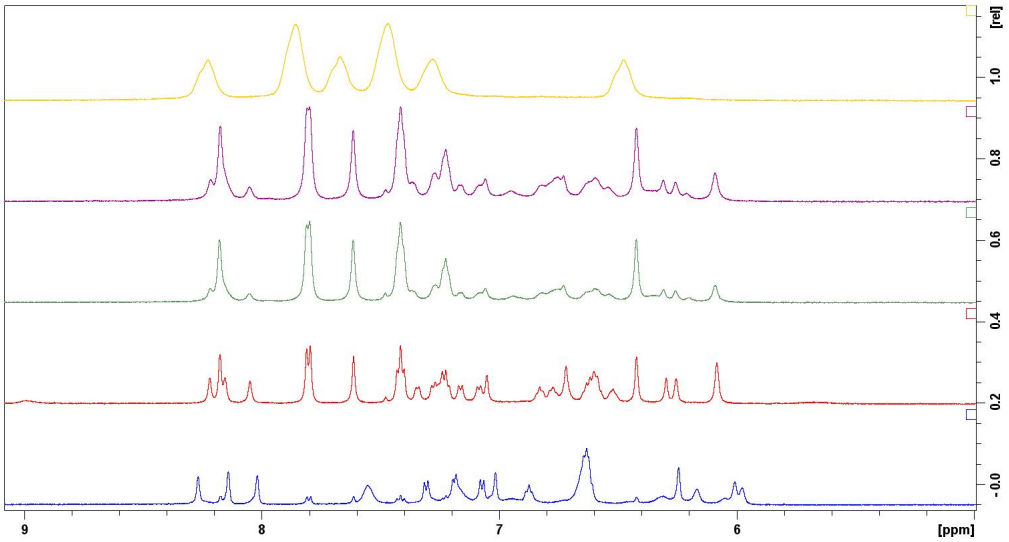

Figure 4.11: ^{1}H-NMR spectra of $[\mathbf{Fe}^{II}\mathbf{ppz}_3]^+$ in THF-d_8 directly after reduction (blue), time-dependent measurements while submitting the solution to broad band illumination with a 300 W Xenon lamp; after 1 h (red), 2 h (green), 3 h (purple), 18 h (yellow).

Furthermore, the peaks in all three tests are broadening over time. One possible explanation for this might be the generation of a highly paramagnetic degradation product in low quantities. Another reason might be the presence of more free ligand over time or due to the complex´s low rigidity and instability. Fluxional molecules, especially octahedral complexes, occasionally transfer via the Ray-Dutt- or the Bailar-twist.[107, 108] Therefore, competing isomers are able to interchange above a certain temperature, despite the *mer*-isomer being the more thermodynamically stable complex in the iron(II)-configuration, as shown in fig. 4.8. In this scenario, due to signal coalescence, the breakdown or delayed isomerisation may compete and cannot be assigned fully. Other dynamic processes, however, may underlay this observation, as different unknown aspects must be considered. Besides THF, which showed less by-products and free ligand, the reduction of $\mathbf{Fe}^{III}\mathbf{(ppz)}_3$ was also possible in MeCN, DMSO and DMF, but not benzene. Due to safety concerns, reduction was not tested in DCM and chloroform.[109]

After exposition of the reduced complex solution to normal atmospheric environment, a sudden colour change back to yellow/orange was noticeable, as were the NMR spectra, which remigrated to the broad-range resonances of the iron(III)-species. The complex was confirmed to go back to the pure *fac*-iron(III). This validates this series of complexes to be completely reducible and oxidisable. Nevertheless, the instability of the reduced species must be taken into consideration during a reaction. Catalytic applications might be even enhanced through the structural adjustments during a redox reaction, which could probably stabilise the complexes within a certain time-frame of a cycle.

4.2.2 Resonance Assignment

Because of their sharp signals and relatively long relaxation times, the low-spin character of the paramagnetic complexes aided in allocating the resonance shifts to their position. This is usually difficult and has only been done a few times in the literature. Several toolboxes used in this context were reported in literature and helped by solving the NMRs of these complexes.[108, 110] The toolbox enabled the assignment of all NMR active atoms. Traditional 1D-NMR spectra showed the observed resonances to be in line with the expected quantity. Further determination with COSY, NOESY and HMQC spectra allowed the complete signal classification with high confidence. Nonetheless the ligator atoms (fig. 4.12) could not be visualised. In case of the nitrogen atoms of the ligands ^{15}N-HMBC spectra could visualise the atoms not directly attached to the metal centre. This was only achievable for iron(III) complexes; no nitrogen resonance was found for iron(IV)-species, due to their presumed extreme chemical shift and line-widths.

Same observation could be made for the carbon ligator atoms, which presumably show extreme chemical shifts with increased line-width. The unpaired electrons exert a significant impact on the neighbouring atoms, resulting in significantly shifted resonances outside the typical measuring range and signals with extremely low signal-to-noise ratios that tend to disappear in the baseline.[111] Additional theoretical calculations could assist in locating predetermined ranges to scan for these resonances. Similar procedures have been reported for analogous sensitive atomic nuclei such as ^{1}H and ^{31}P.

As mentioned before, allocation of the proton resonances to their designated position was carried out by well-established methods of 1D- and 2D-NMR-spectra assisted by TOCSY-NMR and utilisation of the nuclear-overhauser-effect (NOE). With the chosen pulse-programs, acquisition time was generally below the diamagnetic congeners.[110] The tab. 4.3 displays a thorough overview of the resonances for all oxidation states, together with their allocated position, as illustrated in fig. 4.12.

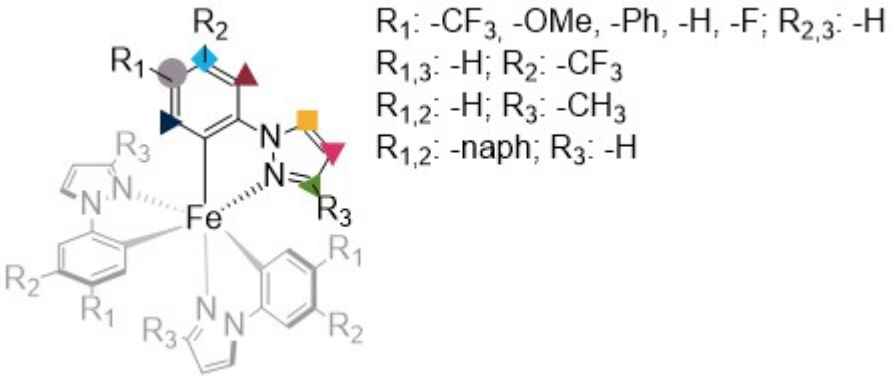

Figure 4.12: Schematic representation of the complexes and their proton assignment.

Table 4.3: Assigned chemical proton shifts of the iron complexes in all three oxidation states, if not noted otherwise solvent is acetonitrile-d_3, 25 °C.

Complex	Ox.	^{1}H-NMR chemical shift in marked position / ppm Longitudinal relaxation time / (ms)						
		▶	●	◆	▲	■	▼	◀
$Fe(ppz)_3$	II[a]	7.35 7.25 6.77	6.81 6.58 6.58	6.62 6.62 6.52	7.27 7.16 7.05	8.22 8.16 8.05	6.25 6.08 6.08	7.05 6.71 6.29
	III	-75.20 (4.57)	7.90 (63.72)	-5.25 (89.87)	-1.15 (48.47)	13.04 (47.79)	-3.35 (64.31)	-9.27 (7.10)
	IV	-187.60	14.91	-82.46	-33.62	-32.27	-3.15	-30.98
$Fe(m\text{-}CF_3ppz)_3$	II[a]	7.62 7.10 6.57	-	6.84 6.73 6.45	7.27 7.13 6.90	8.35 8.14 8.00	6.30 6.04 6.01	7.01 6.38 6.18
	III[a]	-75.17 (4.4)	-	-3.17 (98.86)	0.27 (52.70)	11.23 (50.68)	-3.39 (67.18)	-10.47 (7.26)
	IV[a]	-200.79	-	-71.21	-47.68	-41.64	4.28	-31.46
$Fe(p\text{-}CF_3ppz)_3$	II[a]	-	-	-	-	-	-	-
	III[a]	-72.54 (4.38)	9.35 (63.35)	-	1.30 (55.02)	11.75 (46.93)	-3.60 (61.18)	-10.51 (6.53)
	IV	-182.17	18.48	-	-25.41	-39.37	-4.23	-39.37
$Fe(Fppz)_3$	II[a]	-	-	-	-	-	-	-
	III[a]	-75.89 (5.52)	-	-4.15	-4.82	10.99 (8.63)	-3.11	-10.61
	IV	-	-	-	-	-	-	-
$Fe(MeOppz)_3$	II[a]	7.00 6.83 6.31	-	6.32 6.17 6.08	7.22 7.08 7.07	8.12 8.05 7.95	6.21 6.04 6.03	7.07 6.73 6.24
	III[d]	-79.93 (4.96)	[1.44 MeO (276.90)]	-5.12 (98.78)	-5.36 (53.53)	12.06 (51.80)	-3.19 (70.78)	-10.34 (7.48)
	IV	-192.10	[1.99 MeO]	-82.29	-48.29	-33.34	-4.45	-30.47

$Fe(bppz)_3$	II[a]	-	-	-	-	-	-	-
	III	-77.61 (4.84)	-	-4.64 (97.49)	-1.74 (51.74)	11.84 (50.74)	-3.21 (68.95)	-10.18 (7.42)
	IV	-198.19	-	-81.01	-39.16	-36.52	-3.05	-34.23
$Fe(naphpz)_3$	II[a]	-	-	-	-	-	-	-
	III[c]	-77.61 (4.14)	-	-	1.10 (46.30)	11.16 (48.14)	-1.31 (62.65)	-12.52 (7.42)
	IV[c]	-250.70	-	-	-33.61	-24.50	-1.07	-28.05
$Fe(3Me\text{-}ppz)_3$	II[a]	-	-	-	-	8.23 8.13 7.92	5.98 5.82 5.79	[1.74 1.34 1.25]
	III	-72.28 (2.17)	3.41 (31.53)	-6.39 (41.49)	-0.58 (21.92)	13.50 (21.89)	-2.31 (28.92)	[-12.42 CH_3(7.11)]
	IV	-137.77	39.63	-72.16	-34.07	-29.03	-0.65	[-6.64 CH_3]

* If data not reported, functional group at this position gives no resonance, value in rectangular [] breaks is the ^{1}H-signal of the functional group, if it is not otherwise substituted, with the respective relaxation time T_1(); [a] THF-d_8; [b] CD_3CN; [c] DMF-d_7, [d] DMSO-d_6.

The position, amount and shape of the resonances point to the creation of a *fac*-iron(III) complex in its d^5 LS configuration with S = 1/2. In addition to its very sharp resonance, iron(III)-LS complexes have a signal range of less than 100 ppm and a severe high-field shift of certain paramagnetic signals in close proximity to the paramagnetic centre.[99] Due to shorter relaxation times, iron(III) high-spin (HS) complexes would have larger resonances, which could result in non-observable signals for resonances too close to the paramagnetic centre (within 5 Å range around the metal centre).[108] Most resonances had equal integrated intensities, and values around the irradiation point had acceptable integration ratios. More negatively shifted signals have slightly lower integration values due to the large offset of these resonances. The lack of proton coupling in the singlet-only spectra is consistent with the quick relaxation rates.

Longitudinal T_1-relaxation times for the individual protons were measured by inversion recovery experiments at 25 °C. If the protons could not be assigned using the techniques mentioned above, they may have been assigned by comparing the M-H distances with the T_1-times calculated using the Solomon equations. Here a longer T_1 generally corresponds to the proton located farthest from the paramagnetic centre.[110, 112–114] To verify these relaxation times, the through-space distances of protons to the iron(III) centre were calculated using single crystal structures.[99]

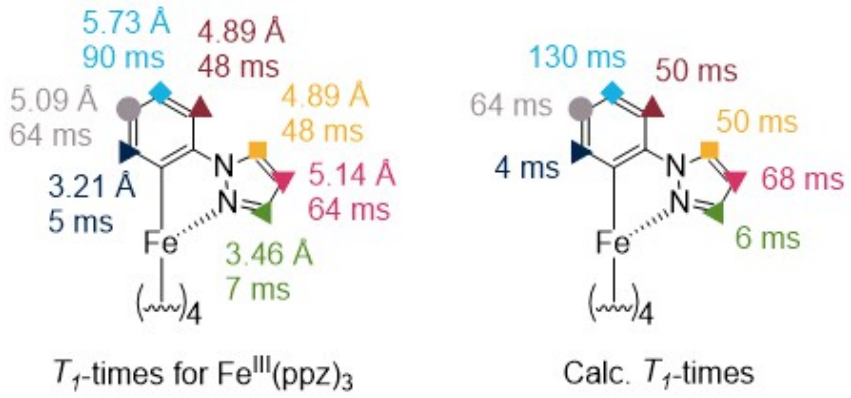

Figure 4.13: Left: Through-space distance between proton and iron(III)-centre in angstrom (Å). Values were taken from the crystal structures reported before for $\mathbf{Fe^{III}(ppz)_3}$.[99]; Right: Calculated relative T_1-times normalized to the value of X.[113]

As a example of $\mathbf{Fe^{III}(ppz)_3}$, the proton with 3.205 Å positioned on the phenyl in ortho-position has the smallest relaxation time with 4.57 ms, while the proton with 90 ms and a distance of 5.733 Å to the iron(III) centre has the longest T_1 (fig. 4.13, left). The comparison of the estimated relative T_1 times, normalised to the T_1 time of one of the protons in meta-position to the iron centre, works well. In the literature, normalisation is frequently performed on the proton with the shortest T_1 duration, which does not yield satisfactory results in this circumstance. This can be attributed to the relatively large error in determining the T_1 times with comparatively short T_1-times. Especially the para-position shows a deviation from the measured T_1-time (factor 1.4). However, this is within the range of occurrences recognised from the literature and would not put the assignment into question.

The same may be said for pyrazolyl, where greater distances from the paramagnetic centre result in longer T_1-times. Notably, paramagnetism does propagate into functional groups; for example, relaxation times for neighbouring aromatic phenyl protons in $\mathbf{Fe^{III}(bppz)_3}$ range between 166 and 1640 ms. Nevertheless, relaxation times here are generally longer. Replacement of the terminal phenyl substituent $\mathbf{Fe^{III}(bppz)_3}$ by a fused phenyl-ring $\mathbf{Fe^{III}(naphpz)_3}$ results in comparatively short T_1 lifetimes, which was even observed for the more remote protons of the naphtyl ligand. The pervasive structure of the conjugated ligand led to a T_1 lifetime of the 518 ms for the most distant proton from the metal centre of $\mathbf{Fe^{III}(naphpz)_3}$. One explanation for this discovery could be the propagation of the paramagnetic effect via conjugation, which results in shorter relaxation times. In contrast, the hetero oxygen atom, the methyl-group in $\mathbf{Fe^{III}(MeOppz)_3}$ is less affected, with a 276.9 ms shift. Here the oxygen atom probably stops the propagation of the paramagnetism. The $\mathbf{Fe^{III}(3Me\text{-}ppz)_3}$ relaxation time is 7.11 ms due to the methyl functionalities closer proximity to the iron(III) centre (3.593 Å).

There is no clear pattern of the chemical shifts of the protons, only tendencies can

be observed. The proximity of the metal centre to the ortho-positioned protons lead to a particular intense effect of the pseudo-contact shift, resulting in a strong highfield shift. Additionally, the para-positioned proton is always shielded as well, independent from eventual substitutions. This was supported by the electron density distribution determined by DFT calculations, which may have resulted from resonance stabilization.

The complex $\mathbf{Fe^{III}(MeOppz)_3}$ exhibits the broadest range of proton signals, from -79.93 to 11.18 ppm. The phenyl ring's electron density rises as a result of the strong electron-donor group, increasing the shielding of the ortho-proton and number of high-field shifted resonances. This is further emphasized by the obvious relevance of functional group location on the phenyl ring, by showing the exact opposite downfield shift for electron withdrawing groups. By directly comparing the shifts, particularly the ortho-positioned proton shift, of $\mathbf{Fe^{III}(\textit{m}\text{-}CF_3ppz)_3}$ and $\mathbf{Fe^{III}(\textit{p}\text{-}CF_3ppz)_3}$, the enhanced influence of electron withdrawing groups in para-position becomes evident. $\mathbf{Fe^{III}(\textit{p}\text{-}CF_3ppz)_3}$ displays the most pronounced downfield shift-effect for all phenyl-based resonances with -72.54, 9.35 and 1.30 ppm, compared to -75.20, 7.90 and -1.15 ppm in $\mathbf{Fe^{III}(ppz)_3}$.

In contrast, the meta-position of the trifluoromethyl-group has a lower influence on the electron density. Therefore, $\mathbf{Fe^{III}(\textit{m}\text{-}CF_3ppz)_3}$ exhibits resonances at the most influenced ortho position of -75.17 ppm. In both trifluoromethyl-based complexes, the influence on the pyrazolyl can be considered equal. The resonance shifts in the other meta-substituted compounds are remotely impacted. It is noteworthy that the conjugation in $\mathbf{Fe^{III}(naphpz)_3}$ exhibits this effect over the entire naphthalene part (-1.68 to 12.38 ppm), whereas the additional phenyl-ring in $\mathbf{Fe^{III}(bppz)_3}$ is unaffected by the paramagnetic centre and exhibits resonances within the aromatic region, from 5.36 to 7.08 ppm. Additionally, the naphthalene functionality exhibits a distant electron withdrawing effect, which is likely driven by both the mesomeric effect and the significant electron delocalisation, in addition to the positive inductive effect. However, it must be emphasised that not all chemical shifts can be explained by simple considerations with regard to inductive or mesomeric effects. Due to their significantly altered positions, the carbon and nitrogen atoms coordinated to the paramagnetic iron(III) core could not be observed in the spectra, as was explained before. They are strongly influenced by the unpaired electrons because of their link to the metal centre, which dramatically skews their shifts and causes them to be hidden by the baseline of the spectrum.[111] Therefore, further DFT calculations could help to narrow the zone and permit certain observations inside a computed region.

Afterward, the stable iron(IV) complexes were analysed. Heme-enzymes, such as compound I (Cytochrome P450[104, 115, 116]), are more frequently found in stable iron(IV) complexes, which are rather uncommon, even though there have been recent reports of homoleptic iron(IV) complexes.[117] Nonetheless, full signal assignment is seldom, if ever, provided, particularly for other NMR active nuclei (e.g. ^{13}C). The iron(IV) complexes presented herein show a greatly altered solubility behaviour. The iron(III)-species

were mostly soluble in MeCN, but some iron(IV)-complexes required different solvents. When comparing complexes with differing oxidation numbers, this must be taken into consideration. As a result, detailed comparison of the shifts for the parental $\mathbf{Fe^{III}(ppz)_3}$ in various solvents was done. The proton shift values difference for widely used solvents such as THF, DMSO, MeCN, and DMF was evaluated, where the difference was observed to be within 1 ppm. When taking into account the diverse spectrum of signals, the variation may be calculated to be around 1%. This leads to the conclusion that the solvents utilised have a negligible influence on the chemical shift.

The same methods that were described above were used to measure, classify, and interpret the spectra of the iron(IV)-species. While the proton resonance shifts (tab. 4.3) are similarly sharp like to the iron(III) complexes ($FWHM_{max}$ = 36.73 Hz; 84.77 Hz for the ortho-positioned proton), they exceed the aforementioned 100 ppm range by far. However, this shows that the *fac*-geometries for the iron(III) and -(IV) in solution are equivalent. Two unpaired electrons in the triplet ground state are present on the metal centre as a result of oxidation, which directly impacts resonance shifts and has a stronger impact on ortho-positioned protons. This would imply that no conformational changes occur during the oxidation to iron(IV) and subsequent reduction to iron(III) within a catalytic cycle. Conformational complex stability during photosensitization redox processes may result in a greater TOF and a longer life span of the catalyst. A change in the electron density distribution causes the signals to be greatly downshifted, compared to the iron(III)-congener, to around -187 ppm (tab. 4.3) for the phenyl-ring and ∼32 ppm within the pyrazole ring, for the protons in the closest adjacency to the metal centre. Nonetheless the functional groups effect pattern, as described in the previous section stays unchanged. Protons farther from the metal centre can likewise exhibit this effect.

The proton resonances of the diamagnetic iron(II)-species lie within the range of 8.31 to 6.01 ppm. Within these resonances, the *mer*-species is easily discernible due to the threefold increase in resonances. The signals overlap sometimes but may be distinguished using standard 2D-NMR methods. Unfortunately, detectable complexes of $\mathbf{[Fe^{II}(\textit{p}\text{-}CF_3ppz)_3]^+}$, $\mathbf{[Fe^{II}(bppz)_3]^+}$, $\mathbf{[Fe^{II}(Fppz)_3]^+}$ and $\mathbf{[Fe^{II}(naphpz)_3]^+}$ could not be produced. Due of the instability noted before, free ligand was also seen in every reduced complex within the spectra of the complexes. $\mathbf{[Fe^{II}(3Me\text{-}ppz)_3]^+}$ was reduced, but the phenyl-signals could not be assigned to their respective position. Nonetheless, the quantity of signals confirmed a successful reduction to the *mer*-complex, even if not for all complexes. The true cause of the varying reducibility could not be determined, but a number of factors need to be taken into account, such as the solvent, the functional group's nature, or other factors like the reducing agent, which could adversely affect the stability towards a successful reduction and destroy the complex in the process.

In conclusion, the complexes based on the iron(III)-configuration could be reduced, to iron(II) and oxidised to iron(IV). Throughout analysis of the complexes via NMR-spectroscopy showed the influence of the functional groups on the shift of the chemical resonances. Especially a close vicinity of protons to the paramagnetic centre lead to dras-

tic offset of the proton resonances. Despite challenging stability of the reduced species and solubility of the oxidised species, signal assignment could be done in most cases. Additionally, the symmetry-breaking reduction of the complexes could be observed, while also displaying the stability of the *fac*-isomers for the iron(III/IV)-species. Those insights could aid in develop a long-lived catalytic process, when the redox-behaviour is taken into consideration.

4.2.3 ^{13}C-NMR Spectroscopy

The ^{13}C-resonances may be ascribed in addition to the proton resonances being correctly assigned to their positions. Using the previously described toolkit, all of the data could be recorded and their assignment successfully deducted. Only the non-substituted complex $\mathbf{Fe^{III}(ppz)_3}$ is shown in fig. 4.14 and data for the other complexes are included in the appendix.

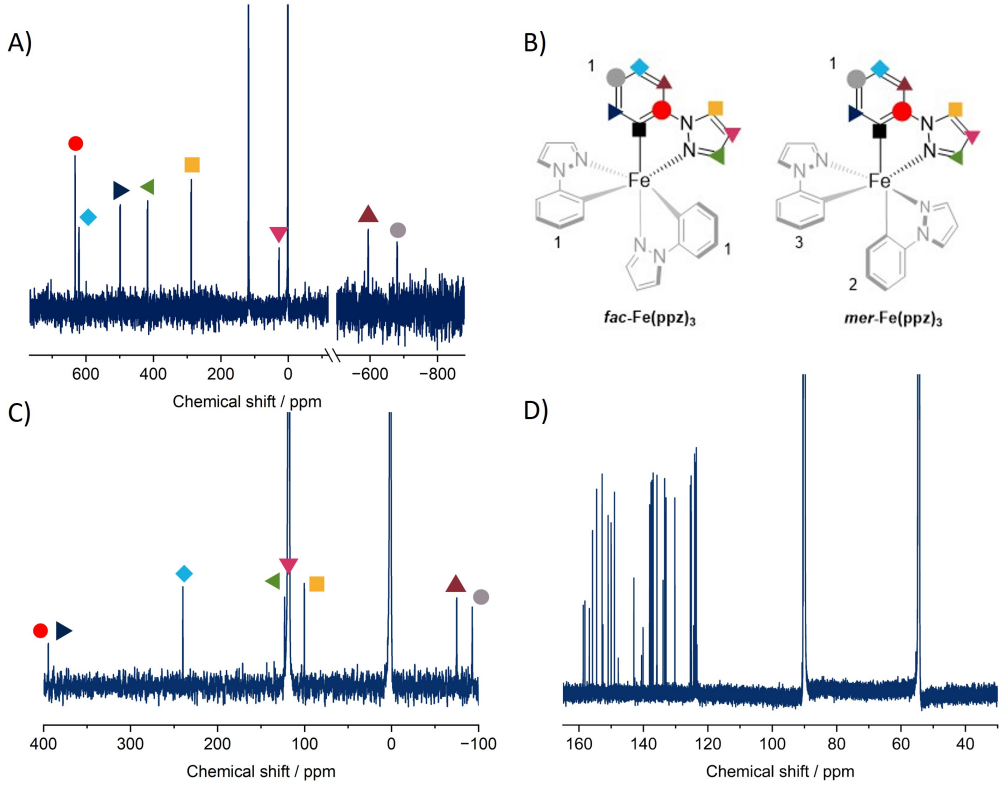

Figure 4.14: A) $\mathbf{[Fe^{IV}(ppz)_3]^+}$ showing the *fac*-species only. Measured in MeCN at 298 K; B) Structure of the two isomers, left: *fac*-isomer with three equivalent ligands, right: *mer*-isomer with three inequivalent ligands; C) $\mathbf{Fe^{III}(ppz)_3}$ showing the *fac*-species only, measured in MeCN at 298 K; D) $\mathbf{[Fe^{II}(ppz)_3]^-}$ reduced in THF, signal assignment not visualised (see appendix).

Table 4.4: ^{13}C-NMR data of ***mer***-$[Fe^{II}(ppz)_3]Na$, $Fe^{III}(ppz)_3$ and $[Fe^{IV}(ppz)_3]PF_6$ (position as marked in fig. 4.14) in comparison, data for other complexes is summarised in the supporting information. Spectra were recorded in THF_8 (iron(II)) or MeCN (iron(III) and iron(IV)).

Complex	Position								
	■	▶	●	◆	▲	●	■	▼	◀
$[Fe^{II}(ppz)_3]^-$	197.4	137.5	117.3	117.9	108.2	140.5	122.9	106.3	140.9
	198.8	122.4	123.4	118.5	108.1	134.9	122.1	106.6	142.9
	201.9	122.5	118.5	117.9	107.2	136.3	120.7	106.9	144.4
$Fe^{III}(ppz)_3$	-	389.1	-92.7	239.9	-74.8	396.6	100.2	117.0	122.9
$[Fe^{IV}(ppz)_3]^+$	-	498.9	-680.2	621.1	-594.3	632.4	288.4	27.9	417.7

Because the ligands are magnetically inequivalent, the meridional configuration upon reduction to the iron(II) complexes results in a tripled number of resonances, as can be observed in the proton resonance shifts. Spectra were obtained using standard pulse algorithms for ^{13}C-NMR, as the diamagnetic composition of the complexes leads to resonances within the predicted range for this kind of metalorganic iron-complexes.

There are very few examples of the assignment of ^{13}C-NMR resonances for paramagnetic compounds in common literature, much alone the full recording of the signals. Resonances are often broad and cover a large range. As a result, signals become non-measurable, making full signal assignment impossible. Using the previously indicated methods, the resonances for the iron(III) and iron(IV) complexes reported here were successfully assigned.[110] With the exception of the ligator atoms, whose wide resonance is probably substantially shifted and too broad to discern from the base line, all carbon resonances could be seen in this context. The spectra were divided into many sections due to the complexes' decreased solubility, which resulted in smaller spectral widths being recorded. When the resonances were assigned with a HMQC pulse program, the ^{1}H- and ^{13}C-signals produced distinct cross-peaks.

As a result, it was possible to assign resonances to every iron(III) and iron(IV) complex. This is one of the earliest paramagnetic complexes that we are aware of, possessing almost all ^{13}C-NMR resonances in two distinct oxidation states.

A distinct resonance pattern was found, with values that were very highfield shifted next to values that were significantly downfield shifted; this produced an alternating resonance pattern that is exemplary described in tab. 4.4 for $Fe^{III}(ppz)_3$. For iron(III), the resonances range from strong upfield shifts of -92.7 ppm to noticeably downfield changes of 396.6 ppm. As was previously noted for other iron(III) complexes, the influence of the functional groups changes the ^{13}C-resonance slightly downfield in the case of electron-donating groups and highfield in the case of electron-withdrawing groups.[118, 119] Additionally, in DFT calculations of the spin density distribution, shown in fig. 4.15, this distinct resonance pattern of the iron(III/IV) complexes may be observed. Consequently,

it can be said that the resonance shift of a particular nucleus directly represents its spin density, and that the unpaired electron has an impact on this shift.

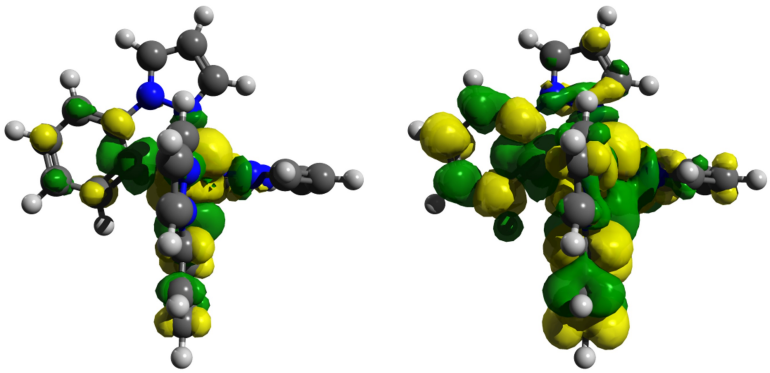

Figure 4.15: Spin density plot of the PBEh-3c optimized ***fac*-Fe^{III}(ppz)$_3$** structure. Left: isovalue of 0.0005; Right: 0.0001.

In this case, the aromatic ring may be significantly influenced by the unpaired electron, leading to a mesomeric resonance structure. Furthermore, the functional groups' effect is evident, causing the ^{13}C-resonances to change appropriately. It is noteworthy that the iron(IV) species exhibits a far stronger effect from the complex's paramagnetic core. Resonances between 498.9 and -680.2 ppm are produced by the purportedly two unpaired electrons. Here, too, the alternating pattern observed in the iron(III)-species is evident. It is evident from an iron(III) and iron(IV) complex mesomeric resonance structure that structural stabilisation is possible. According to this, a stable photocatalyst may be produced by a reactional pathway that converts iron(III) to iron(IV) and back.

4.3 Mössbauer Spectroscopy and Magnetic Measurements

The following data has been recorded and analysed by Serhiy Demeshko and Ajdin Velic. Mössbauer spectroscopy is mostly used to differentiate between iron(III) and iron(IV).[120]

To substantiate that the redox processes occur only on the metal centre, all complexes were investigated by Mössbauer spectroscopy, which are shown in fig. 4.16. The obtained isomer shifts were determined to be 0.03 mms^{-1} and -0.07 mms^{-1} for the iron(III) and iron(IV) compounds, respectively. In addition, the quadrupole splitting for the iron(III) species was found to be 1.85 mms^{-1}, while the iron(IV) compound showed a quadrupole splitting value of 0.91 mms^{-1}. Consequently, all complexes can be confirmed as low-spin complexes in the respective oxidation state of +III and +IV.[120] In addition, magnetic measurements were performed for the paramagnetic iron(III) and (IV) complexes.

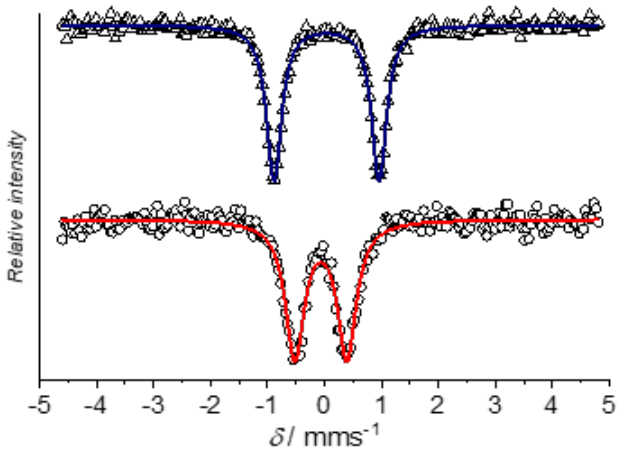

Figure 4.16: ^{57}Fe Mössbauer spectra of species iron(III) (blue) and iron(IV) (red) recorded at 80 K. Iron(IV) recorded in a BN matrix.

Magnetic susceptibility measurements show the $X_M T$ values of 0.66 and 0.93 $cm^3 mol^{-1} K$ at 295 K for iron(III) and iron(IV), respectively (fig. 4.17).

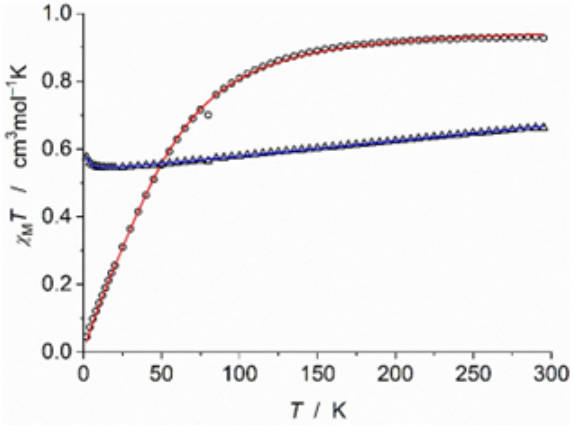

Figure 4.17: Experimental X_HMMT vs. T values for iron(III) (triangles) and iron(IV) (circles). The coloured lines represent the best fits with parameters: g = 2.38, TIP (temperature independent paramagnetism) = 460·10^{-6} cm^{3}mol^{-1}, Weiss temperature Θ = 0.18 K for iron(III) and g = 1.95, d = 119 cm^{-1} for iron(IV).

These values a closed to the expected spin-only values of 0.375 cm^{3}mol^{-1} (for S = $\frac{1}{2}$) and 1.0 cm^{3}mol^{-1}K (for S = 1). The substantial decrease in the magnetic moment below 100 K for iron(IV) can be explained by the large zero-field splitting D = 119 cm^{-1}. Therefore, magnetic measurements reveal the S = $\frac{1}{2}$ and S = 1 spin states and additionally confirm the low-spin d^5 and d^4 configurations for iron(III) and iron(IV), respectively.

4.4 Ground State Characterization

An essential component of optimising a possible photosensitizer is examining its photophysical characteristics. The functional groups' inclination may reveal the subsequent stages of ligand- and therefore, complex-synthesis. Comparing the absorptive and emissive behaviour and the redox-parameters reveals the complexes capability to split water successfully.

4.4.1 CV

Cyclic voltammetry in MeCN, under light exclusion, was used to determine the redox characteristics of the studied compounds. As electrolyte, the tested solutions (10^{-3} M) of the different compounds included 0.1 M tetrabutylammonium hexafluorophosphate ([Bu$_4$N]PF$_6$). The numbers presented below are in comparison to Fc/Fc$^+$ and are shifted 5 μA against each other for better comparison.

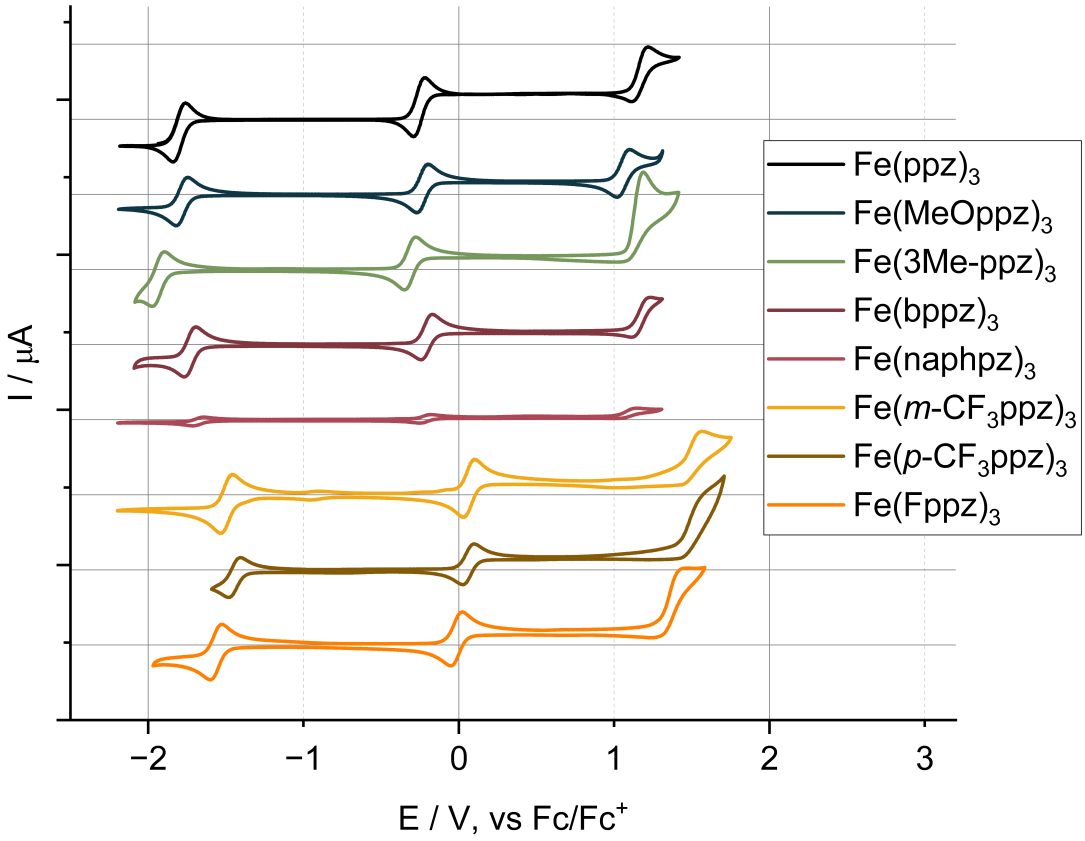

Figure 4.18: Cyclic voltammograms of all investigated complexes (10^{-3} M) in MeCN with 0.1 M $[Bu_4N]PF_6$ as electrolyte at a scan rate of 100 mV/s under light exclusion. Plots are shifted 5 μA, starting from $\mathbf{Fe^{III}(Fppz)_3}$.

The electrochemical properties are summarised in tab. 4.5.

Table 4.5: Electrochemical properties of the complexes, with 10^{-3} M in MeCN with 0.1 M $[Bu_4N]PF_6$ as electrolyte.

Complex	$Fe_{(II/III)}$ /V	$Fe_{(III/IV)}$ /V	Fe_{Ligand} /V	ΔE /V ([b])
Fe(ppz)$_3$	-1.80 (rev)	-0.26 (rev)	1.17 (irrev)	2.97 (418 nm)
Fe(MeOppz)$_3$	-1.78 (rev)	-0.23 (rev)	1.11 (irrev)	2.89 (429 nm)
Fe(3Me-ppz)$_3$	-1.93 (rev)	-0.31 (rev)	1.14 (irrev)	3.07 (407 nm)
Fe(bppz)$_3$	-1.73 (rev)	-0.21 (rev)	1.17 (irrev)	2.89 (429 nm)
Fe(naphpz)$_3$	-1.68 (rev)	-0.22 (rev)	1.08 (irrev)	2.76 (449 nm)
Fe(*m*-CF$_3$ppz)$_3$	-1.50 (rev)	0.07 (rev)	1.54[a] (irrev)	3.04 (408 nm)
Fe(*p*-CF$_3$ppz)$_3$	-1.56 (rev)	-0.02 (rev)	1.49 (irrev)	2.72 (452 nm)
Fe(Fppz)$_3$	-1.44 (rev)	0.06 (rev)	1.36 (irrev)	2.80 (435 nm)

[a] Anodic peak potential

[b] Calculated from the difference of $E_{1/2}$(ligand) and $E_{1/2}(Fe^{II/III})$.

The difference in intensity of the signals in fig. 4.18, is most likely due to the differences in solubility of the complexes. Especially **Fe(naphpz)$_3$** displays a better solubility in THF or DMF, but was characterized in MeCN for better comparison to the other complexes.

In the potential window for all complexes, three redox-processes were discovered. Transitions attributable to an iron(III/IV) redox-mechanism are seen in the -0.26 to 0.07 V range.[75, 117, 121] These values are comparable to those in the compound $[Fe(ImP)_2]^{2+}$ (0.08 V) discussed earlier, which contains two cyclometalating moieties. Except for **Fe(*m*-CF$_3$ppz)$_3$**, functionalisation of the meta-position in the phenyl unit did not significantly alter the iron(III/IV) redox-potentials relative to **Fe(ppz)$_3$**. An anodic change in the oxidation potential is found here, consistent with the stabilisation of metal-based levels by the electron-drawing CF_3-group. The similar pattern is observed for the iron(II/III) redox reactions, which occur between -1.50 and -1.80 V. The effect of the position of the CF_3-group is rather marginal, showing no increased or decreased effect. For both metal-based processes, the para-position of the functional group results in a decrease of the redox-potential, however the value remains higher than the non-functionalised species. Within the complexes with EWG-groups, **Fe^{III}(Fppz)$_3$** shows one of the smallest electronic band gap. This demonstrates, that the impact of direct functionalities could even increase the effect of these.

Irreversible ligand-based oxidation occurs above potentials of 1 V. Despite the fact that these processes are irreversible, the results may be used to evaluate the effect of different substituents on the electron density in the ppz-ligand scaffold. While **Fe(bppz)$_3$**

has the same oxidation potential as $\mathbf{Fe^{III}(ppz)_3}$, the cathodically altered oxidation potentials of $\mathbf{Fe(MeOppz)_3}$ and $\mathbf{Fe(naphpz)_3}$ imply an enhanced electron density on the coordinating phenylene. This is in line with the findings in crystal structures, which show that longer Fe-N bonds are produced by higher electron densities from EDG. $\mathbf{Fe(\textit{m}\text{-}CF_3ppz)_3}$ exhibits the most anodically shifted ligand oxidation as a result. Electro-chemical bandwidths for an LMCT transition may be found by comparing the iron(II/III) transition and the difference between the ligand oxidation potential. Since all complexes greatly exceed the band gap of $[Fe(ImP)_2]^{2+}$ (2.47 V), their band gaps represent the same trends. $\mathbf{Fe(ppz)_3}$ (2.97 V) and $\mathbf{Fe(\textit{m}\text{-}CF_3ppz)_3}$ (3.04 V) have the highest E values.

Since only facial complexes were synthesised, comparison to the behaviour of meridional complexes is impossible. Since the meridional form consists of two trans phenyl ligands, assumptions of lengthening of the Fe-C bond might be reasonable, therefore leading to a destabilised HOMO and LUMO. As a result, meridional isomers tend to be slightly easier to oxidize and reduce.[82]

The weak π-accepting ability of pyrazole-based ligands has been described before.[82, 122] Through π-backbonding, the pyrazolyl ligands do affect the energies of metal orbitals, whereas the effect on the HOMO is rather weak. The π-accepting ability of pyrazolyl is therefore comparably low, in comparison the pyridyl or terpyridyl based ligand systems.[82] Further research could therefore combine the positive affects of more than one ligand scaffold.

The iron(III)/iron(IV) redox potentials may be connected to the HOMO energy levels, which mostly have a metal character. MSc. Lorena Fritsch performed the calculations, which were published in the literature, for the five standard complexes.[99]

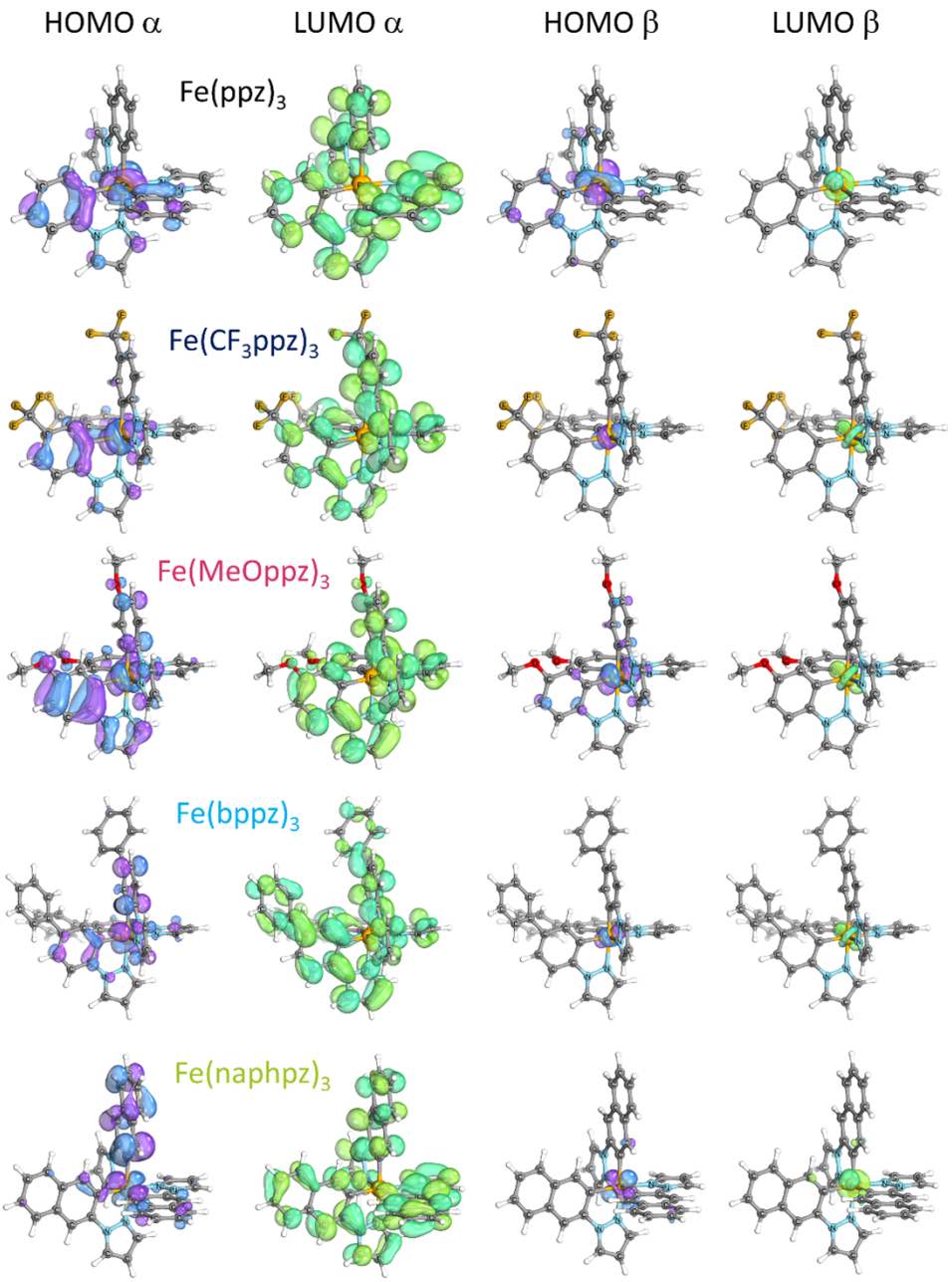

Figure 4.19: The geographical distribution of the frontier orbitals of the five primary complexes was determined via TPSSh/def2-TZVP.[99]

The computed HOMOs' energy order trend follows the observed CV data.

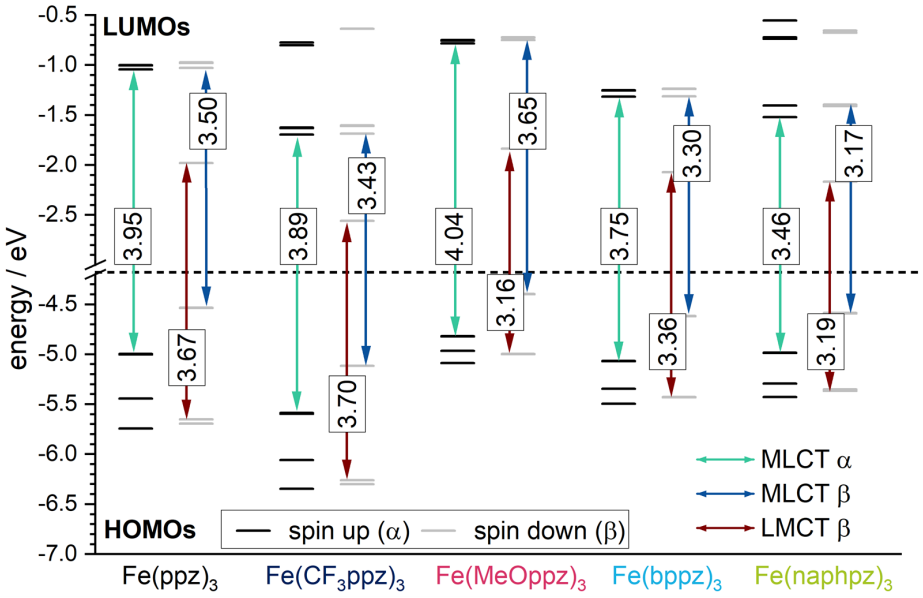

Figure 4.20: The HOMOs and LUMOs of the DFT predicted spin up and spin down orbitals are displayed in the molecular orbital schemes that TPSSh calculated for each of the five main complexes. The calculations were done by MSc. Lorena Fritsch.[99]

With an oxidation potential of 0.07 eV and the most stabilized HOMO at -5.12 eV, in particular, $\mathbf{Fe^{III}(\textit{m}\text{-}CF_3ppz)_3}$ exhibits the highest level of oxidation. $\mathbf{Fe^{III}(MeOppz)_3}$, $\mathbf{Fe^{III}(ppz)_3}$, $\mathbf{Fe^{III}(naphpz)_3}$, and $\mathbf{Fe^{III}(bppz)_3}$ have HOMO energy values with only small deviations of -4.40 eV, -4.54 eV, -4.59 eV, and -4.62 eV, respectively. These values are in agreement with the small deviations for the experimental potentials of 0.23 eV, -0.26 eV, -0,22 eV and 0.21 eV, respectively. The iron(II)/(III) redox potential can be connected with the metal-based β LUMO. $\mathbf{Fe^{III}(\textit{m}\text{-}CF_3ppz)_3}$ exhibits the lowest negative potential for the reduction, at -1.50 eV, and, as predicted, has the lowest LUMO energy in the calculations, at -2.56 eV. This is because a lower negative potential for the reduction corresponds with a lower orbital energy. Following this, the predicted LUMO energies of $\mathbf{Fe^{III}(naphpz)_3}$ (-2.17 eV), $\mathbf{Fe^{III}(bppz)_3}$ (-2.07 eV), $\mathbf{Fe^{III}(MeOppz)_3}$ (-1.84 eV), and $\mathbf{Fe^{III}(ppz)_3}$ (-1.98 eV) all marginally increase, reflecting the rising negative potentials of -1.68 eV, -1.73 eV, -1.78 eV, and -1.80 eV, respectively. Additionally, it is possible to compare the lowest ground state LMCT energies (excluding excited states) computed from CV potentials to those obtained from the energy differences between the HOMO-2β and LUMO β (fig. 4.20, red arrow). Although the observed potential differences are usually somewhat larger by 0.3–0.7 eV when the difference between the frontier orbitals is taken into account, the order for $\mathbf{Fe^{III}(\textit{m}\text{-}CF_3ppz)_3}$, which has the greatest anticipated LMCT energy of 3.70 eV (calculated) and 3.04 eV (experimental), $\mathbf{Fe^{III}(ppz)_3}$ (3.67 eV/2.97 eV), $\mathbf{Fe^{III}(bppz)_3}$ (3.36 eV/2.90 eV) and $\mathbf{Fe^{III}(naphpz)_3}$ (3.19 eV/ 2.76 eV) remains the same. The calculations only indicate the lowest energy difference for $\mathbf{Fe^{III}(MeOppz)_3}$ (3.16 eV/2.89 eV), whereas the experimental δE_{LMCT} reveals the second smallest.

4.4.2 UV-Vis

Due to the greater stability of the complexes in butyronitrile (BuCN, ch. 4.4.4), with a concentration of 10^{-5} M, UV-Vis spectra were acquired in order gain reliable results. The final pictures are shown in fig. 4.21.

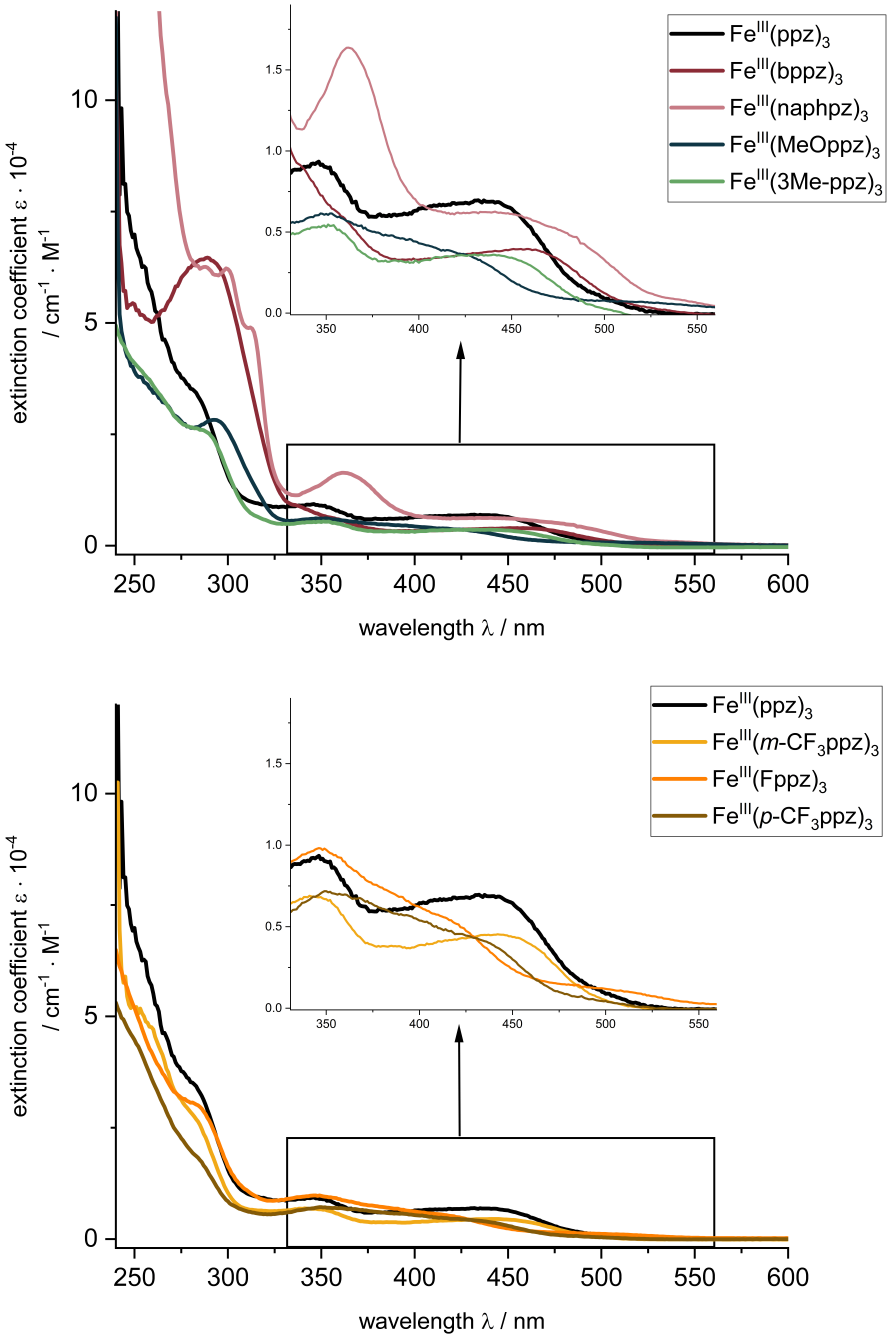

Figure 4.21: Absorption spectra in BuCN for the investigated compounds (10^{-5} M). Inset: 330 to 550 nm absorption region. Top: Parental non-substituted complex, complexes with EDG and π-system extension. Bottom: Complexes with EWG, inset focuses on absorption behaviour from 330 to 550 nm.

For a better overview the graph was divided between the parental complex, EDG-functionalities and π-system extension (top) and complexes with EWG-functions (bottom). The absorption behaviour can be summarised in tab. 4.6 slightly easier to oxidise and reduce.[82]

Table 4.6: Electronic properties of the reported complexes, in BuCN (10^{-5} M).

Complex	λ_{absmax} / nm (ϵ / $cm^{-1}M^{-1}$)	λ_{maxend} / nm
$Fe^{III}(ppz)_3$	109 (6.18) 346 (1.63) 450 (0.64)	522
$Fe^{III}(MeOppz)_3$	290 (6.45) 356 (0.62) 453 (0.39)	580
$Fe^{III}(3Me\text{-}ppz)_3$	287 (2.59) 353 (0.54) 430 (0.36)	506
$Fe^{III}(bppz)_3$	277 (2.99) 343 (0.68) 440 (0.45)	540
$Fe^{III}(naphpz)_3$	284 (3.35) 362 (0.93) 442 (0.68)	590
$Fe^{III}(m\text{-}CF_3ppz)_3$	293 (2.82) 350 (0.61) 417 (0.38)	530
$Fe^{III}(p\text{-}CF_3ppz)_3$	284 (1.83) 356 (0.70) 444 (0.36)	523
$Fe^{III}(Fppz)_3$	282 (3.06) 346 (0.98) 415 (0.14)	581

Three zones may be identified in the spectra. Intensive absorption bands are visible in the high energy range below 325 nm. These are ascribed to transitions between π and π*. As a result of the extended π-systems, $Fe^{III}(bppz)_3$ and $Fe^{III}(naphpz)_3$ exhibit the greatest intensities within this region.

Between 350 and 400 nm, the complexes exhibit a pronounced feature, which is the most intense for $Fe^{III}(naphpz)_3$ at 362 nm. The remaining complexes show less in-

tense, blue shifted signals at 346 nm for $\mathbf{Fe^{III}(ppz)_3}$, 350 nm for $\mathbf{Fe^{III}(\textit{m}\text{-}CF_3ppz)_3}$, 356 nm for $\mathbf{Fe^{III}(MeOppz)_3}$, and 343 nm for $\mathbf{Fe^{III}(bppz)_3}$. Origin of this absorption is presumably a MLCT.[98] Above 375 nm and 400 nm (for $\mathbf{Fe^{III}(naphpz)_3}$), all complexes exhibit a broad absorption band. This is especially prolonged $\mathbf{Fe^{III}(MeOppz)_3}$, $\mathbf{Fe^{III}(naphpz)_3}$ and $\mathbf{Fe^{III}(Fppz)_3}$.

No fluorescence of the complexes could be detected. To determine the origin of the absorption bands, theoretical calculations or further analyses like transient absorption are possible. Additional DFT calculations (vide infra, fig. 4.22) were made by MSc. Lorena Fritsch. TPSSh calculated vertical transitions (shown in the appendix, tab. A4) for $\mathbf{Fe^{III}(ppz)_3}$ were compared to the measured UV-Vis-spectrum.

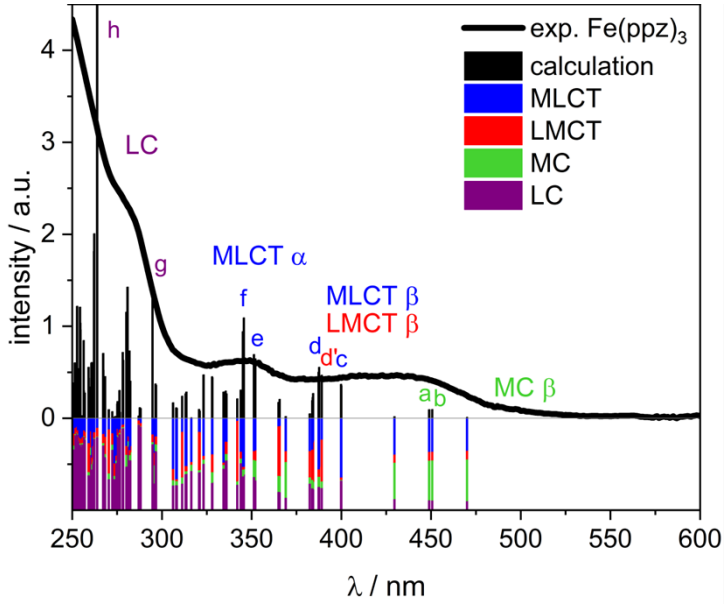

Figure 4.22: TPSSh calculated vertical transitions for the *fac*-optimised structure of $\mathbf{Fe^{III}(ppz)_3}$ in comparison with the experimental UV-Vis spectrum. Analysis of excited states is shown from 0 to -1. Further analysis of designated transitions a-h can be found in the appendix tab. A4. Adapted from literature.[99]

Calculations show that the bands' composition inhibit both MLCT and LMCT transitions. The MLCT transitions, however, have a dominant character, which are significantly higher for phenylpyrazolyl-based ligands, than their phenylpyridyl congeners, as shown in iridium and ruthenium metal centres.[82] This is counter-intuitive to the previously reported iron(III) complexes, since they exhibit mainly energetically low LMCT-absorptions and, in general, MLCT-absorption only as an exception.[76, 77, 121] The unique ligand design employed here is the source of this atypical behaviour. The interaction of pyrazole and phenylene as donors generates π and π*-orbitals, which are at the correct energy distance from the metal orbitals to allow for energetically lowest mixed MLCT/LMCT bands with a dominant MLCT character. Due to this exceptionally strong donor environment, created by the ligand, no fluorescence could be detected by any of the complexes. This is also unexpected, as other iron(III) complexes showed impressive excited

state lifetimes. According to the literature, through an ISC the excited state exchanges from an ^{2}MLCT into a ^{4}MLCT, from which possible fast relaxation into energetically lower ^{4}MC states occurs.[123] One possible reason is that in these bidentate complexes, breathing and deformation modes lead to this deactivation pathway, which is not conceivable in the more rigid tridentate $[Fe(ImP)_2]^+$, which emits from both ^{2}MLCT and ^{2}LMCT.[121, 124, 125] *Fac*-Ir(ppz)$_3$ exhibits higher emission energies and longer lifetimes than penylpyridyl-based analogues, especially in glassy matrices.[82]

Apart from the possibility of chemically oxidising and reducing the complexes, no sequential measurements of the *in-situ* species were achievable. The complex's limited solubility in its iron(IV) species complicates measurement in a suitable solvent. The instability and rapid production of byproducts during complex reduction makes reliable measurement of pure complexes difficult. Spectroelectrochemistry experiments, as an estimation, bridge the gap between the iron(III) and iron(II)/iron(IV)-species.

4.4.3 Spectroelectrochemistry

To trace the optical absorption in relation to their oxidation states, the spectra were recorded while applying a change in adequate voltage.

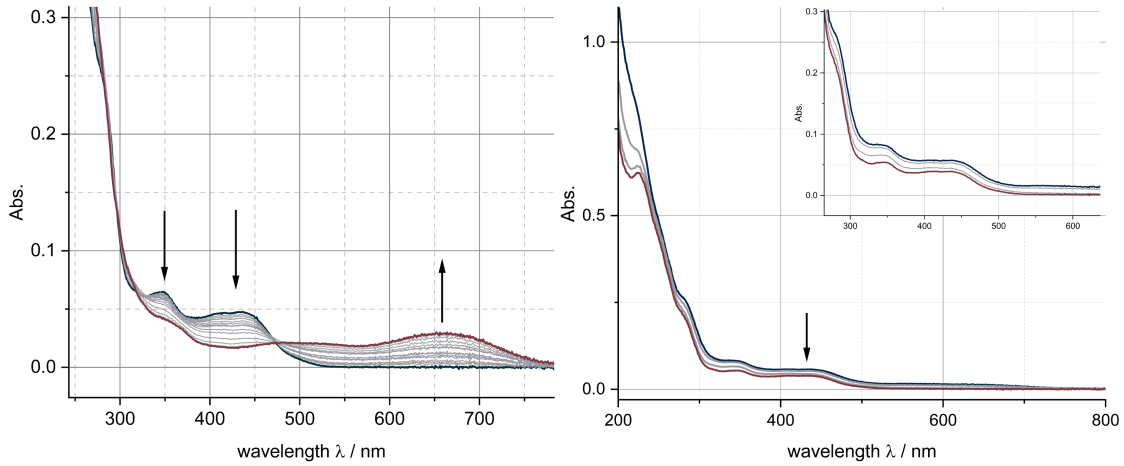

Figure 4.23: Change in the absorptive behaviour of $\mathbf{Fe^{III}(ppz)_3}$ with an applied potential of: left: 0.5-2 V, right: -2 to -2.5 V.

The Oxidation of the complex $\mathbf{Fe^{III}(ppz)_3}$ (exemplarily in fig. 4.23, for the rest see appendix) at around 1.3 V decreased the formerly high absorption bands at 346 and 442 nm, simultaneously a band at 660 nm arises, while the solution changed colour from yellow via green to blue. Chemical oxidation of the complex with oxidants like $AgPF_6$ gave a deep blue solution of $\mathbf{[Fe^{III}(ppz)_3]^+}$, which was also confirmed by NMR and mass spectroscopy. Further analyses of these species was done by NMR in ch. 4.2.

The oxidative species, predominantly soluble, showed reversibility in bulk, without the formation of insoluble by-product, as well as a red-shifted, broadened absorption band. Electrolysis with voltages at -2 V generated an unstable species, which origin is presumably the reduced iron(II) species. Longer time periods at this voltage gave by-products in the spectra. For both redox-processes an over-voltage was required.

While oxidation of the complex produces a rather stable iron(IV)-species, reduction leads to an unstable iron(II)-complex and additional precipitation of a colourless solid. This behaviour could also be seen for the other five standard complexes. These spectra are summarised in the appendix, concluded in the complexes spectra. Behaviour of the complexes with functional group is similar to the parental complex.

4.4.4 Behaviour under Illumination

The behaviour of examined complexes under continuous irradiation was investigated to evaluate possible implementation as photoactive chemicals. The experiment was carried out using a 300 W Xenon lamp and wavelengths ranging from 390-800 nm to observe changes in the complex geometry or stability. Therefore ^{1}H-NMR spectra were compared, before and after illumination (fig. 4.25).

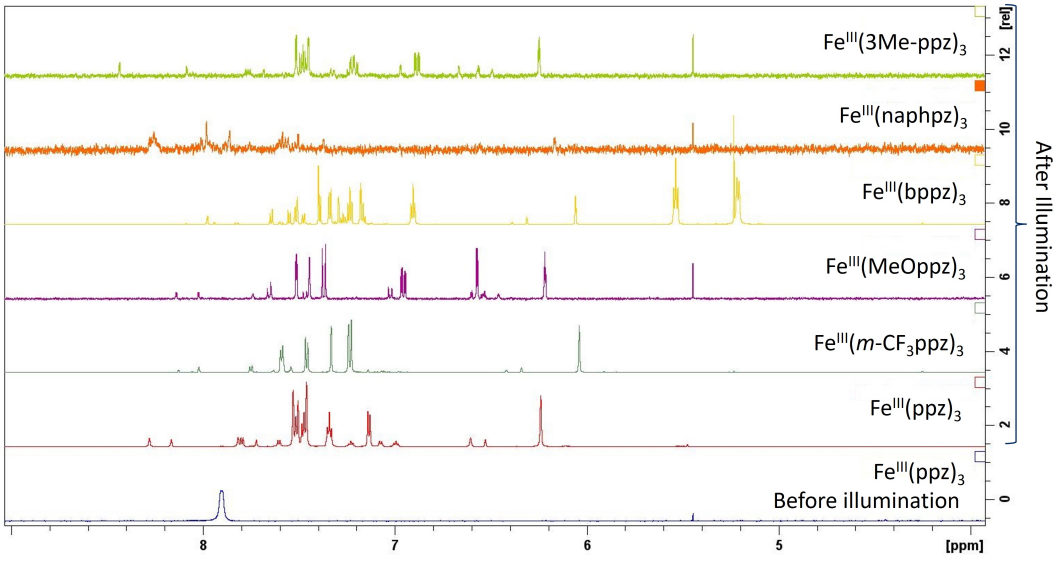

Figure 4.24: Experiments on complex stability for all functionalities ^{1}H-NMR. Comparison of **Fe^{III}(ppz)$_3$** before irradiation (blue); after irradiation: **Fe^{III}(ppz)$_3$** (red), **Fe^{III}(*m*-CF$_3$ppz)$_3$** (green), **Fe^{III}(MeOppz)$_3$** (purple), **Fe^{III}(bppz)$_3$** (yellow) and **Fe^{III}(naphpz)$_3$** (orange, decreased solubility weakens signal intensity), **Fe^{III}(3Me-ppz)$_3$** (bright green) in deuterated MeCN via.[99]

As seen in the plotted ^{1}H-NMR spectra, 24 h of illuminating the complex solution results in the increase of resonances in the aromatic region, while simultaneously, the complex-signal decrease or vanish completely. This behaviour is observable for all the complexes mentioned here. A ne species seem to form only during the illumination of the solutions,

leading to the conclusion, that the complex solution is not stable under these conditions. In terms of stability, nine deuterated solvents were tested and could be visually assessed (fig. 4.25), to further examine the solvent influence itself. The experiment was conducted for $\mathbf{Fe^{III}(ppz)_3}$ exemplarily.

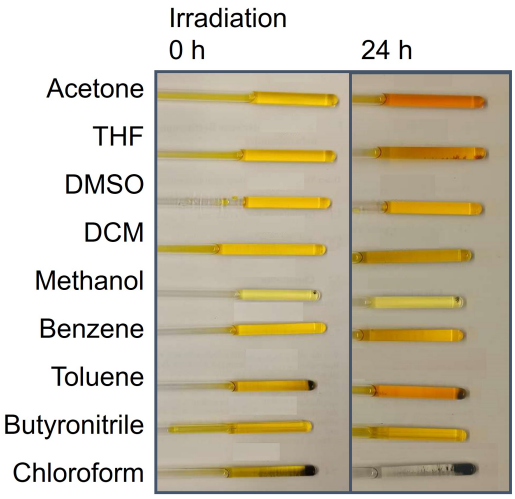

Figure 4.25: Irradiation of $\mathbf{Fe^{III}(ppz)_3}$ in deuterated MeCN, left: before irradiation; right: after 24 h irradiation with a 300 W Xenon lamp.

Changes were noticeable, with the previously yellow liquids displaying precipitated solid or darkish solutions after irradiation. Especially noteworthy are the darkening solution in acetone and THF, and the complete precipitation of the complex in chloroform. Precipitation in toluene and chloroform resulted in a dark blue solid, which might as well be the oxidised iron-complex. To further access the behaviour in different solutions, ^{1}H-NMR spectra were recorded before and after the illumination (fig. 4.26). Therefore potential solvents for catalytic applications can be assessed.

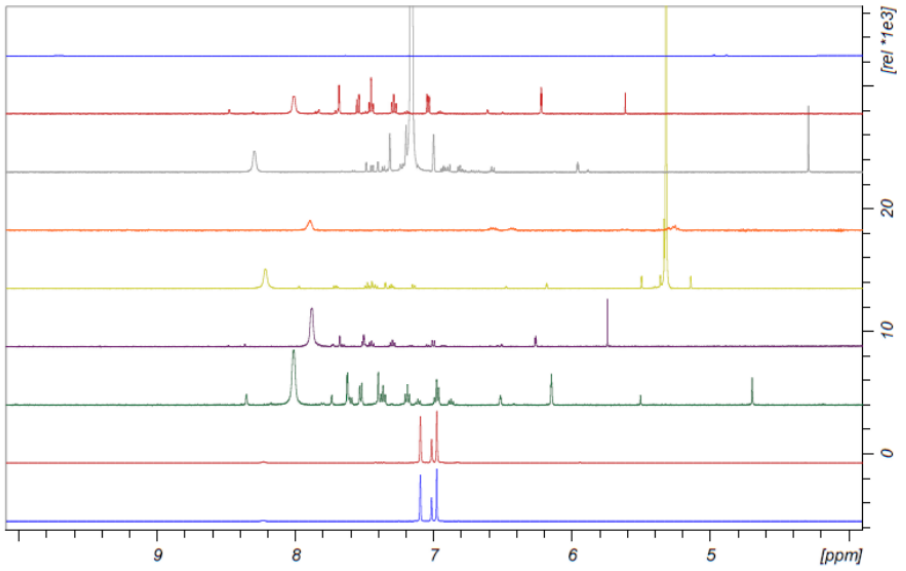

Figure 4.26: Irradiation of $\mathbf{Fe^{III}(ppz)_3}$ in deuterated solvent, from bottom to top: blue: before illumination in toluene; from there upwards after illumination: toluene (red), THF (green), DMSO (purple), DCM (yellow), BuCN (orange), benzene (grey), acetone (red), 2Me-THF (blue).[99]

Measurements in acetone, DMSO, THF, dichloromethane, methanol, benzene, toluene, chloroform, butyronitrile (BuCN) and 2-methyltetrahydrofuran (2-MeTHF) showed that the complex was only broad band stable in the last two solvents. In those two solvents, no by-product formation could be detected. With assistance from mass spectroscopy (found: $m/z_{exp} = 287.1268$) and additional 2D-NMR spectra, the C-C-homocoupled ligand-dimer 2,2'-di(1*H*-pyrazol-1-yl)-1,1'-biphenyl ($m/z_{theo} = 286.1218$) was identified as the main decomposition product after illumination of $\mathbf{Fe(ppz)_3}$.

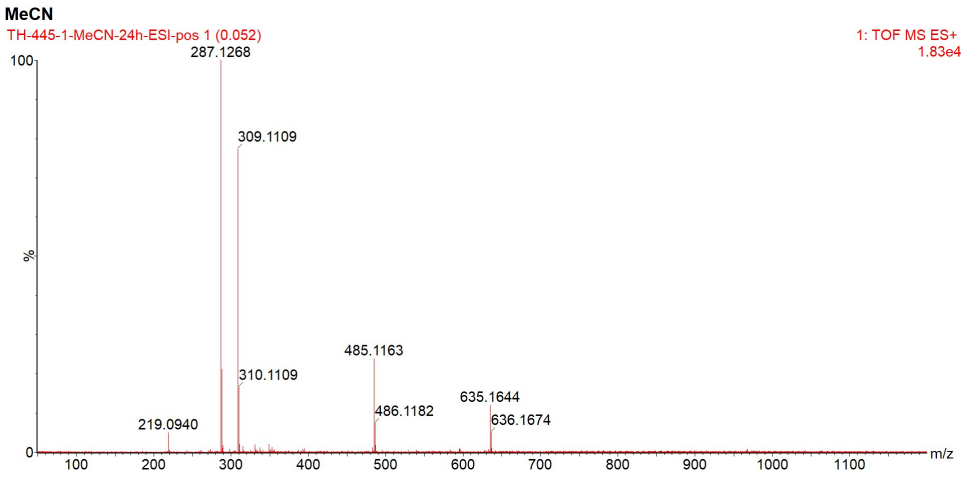

Figure 4.27: Mass spectrum of $\mathbf{Fe^{III}(ppz)_3}$ after irradiation in MeCN, highest signal belongs to the resulting C-C-homocoupled product 2,2'-di(1*H*-pyrazol-1-yl)-1,1'-biphenyl ($m/z_{theo} = 286.1218$).[99]

Accordingly, irradiated $\mathbf{Fe^{III}(ppz)_3}$, and the functionalised complexes as well, undergo reductive ligand elimination. The C-C-coupling mechanism (fig. 4.28) is presumably close to the related $Co(ppz)_3$ complex, which was already investigated by THOMPSON *et al.*.[98]

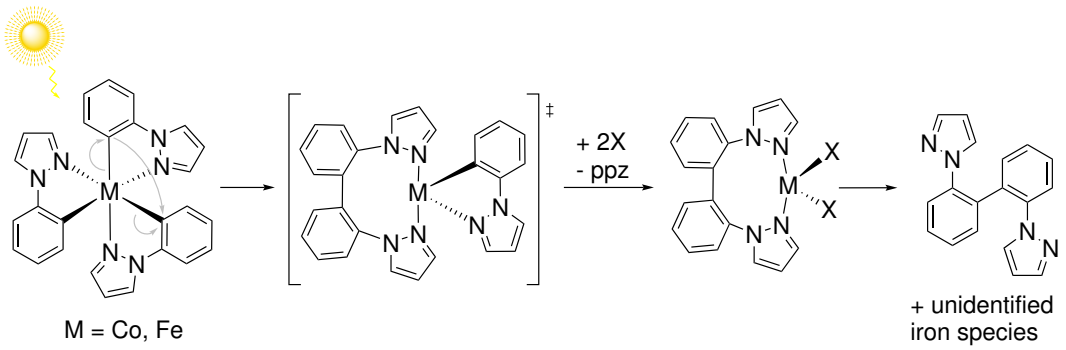

Figure 4.28: Proposed degradation mechanism after illumination of the initial $\mathbf{Fe^{III}(ppz)_3}$ complex towards 2,2´-di(1*H*-pyrazol-1-yl)1,1´biphenyl. Adapted from literature.[98, 99]

The reason for this solvent-dependent behaviour needs to be explored in the future. The UV-Vis-spectra had to be accordingly recorded in BuCN and the CV was conducted under light exclusion. In this context, the use of 2-MeTHF might be a promising alternative. Its good miscibility with water, beneficial stability and its possible origin from renewable sources makes it a promising candidate for applications in organometallic catalysis.[126]

Additionally interesting is the time frame in which the degradation occurs. Therefore, time-dependent measurements with a specified concentration of a $\mathbf{Fe^{III}(ppz)_3}$-complex solution were measured and the integrated signals were compared.

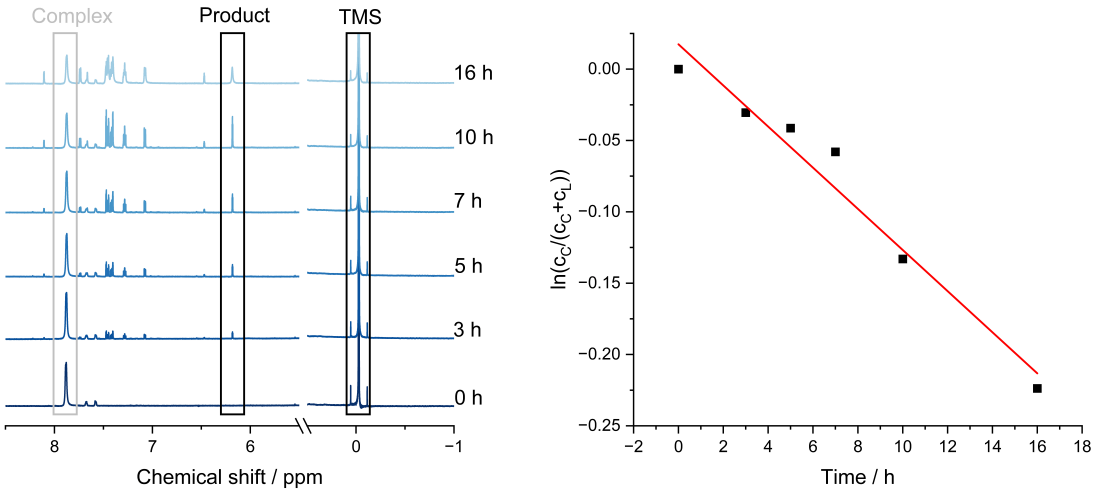

Figure 4.29: Left: NMR-spectra after irradiation for (from bottom to top): 0, 3, 5, 10, 16 h, referenced against TMS; Right: Decomposition of **Fe(ppz)**$_3$, time against relative concentration of the signal at 6.21 ppm for two protons at the coupled ligand and 7.90 ppm, for three protons at the complex. Calculation included the relative intensity, multiplied by their fracture of the protons. The linear regression shows a slope of -0.0144 h^{-1}.[99]

About 4% of the complex disintegrated during the first five hours of radiation, and 15% did so after 16 hours. This indicates that even after 24 hours of light, at least 85% of the complex remains intact, indicating a first order reaction (fig. 4.29) with a breakdown constant of k = -0.0144 h^{-1}. With the linear plot of the time against the natural logarithm of the complex and ligand concentration, the slope was determined as 0.0014 and the intercept as -0.014, with a R-square of 0.96.

Lastly, a variety of wavelengths were used to monitor the breakdown of $\mathbf{Fe^{III}(ppz)_3}$. In order to facilitate wavelength-dependent measurements, bandwidth filters at 320, 360, and 390 nm as well as long-pass filters at 400 and 495 nm were installed.

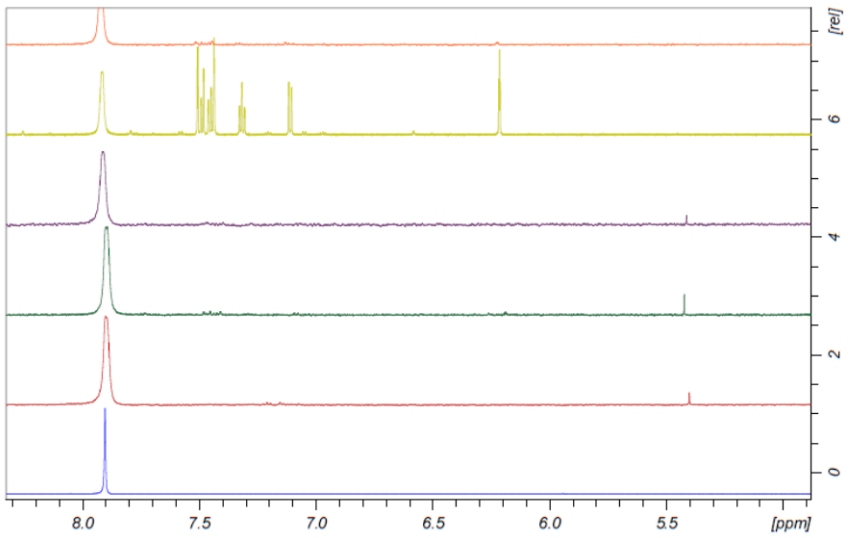

Figure 4.30: Decomposition of $\mathbf{Fe^{III}(ppz)_3}$, with different filters. Blue: before irradiation; red: 320 nm bandwidth filter, green: 360 nm bandwidth filter, purple: 390 nm bandwidth filter; yellow: 400 nm longpass filter, orange: 495 longpass filter. At 7.90 ppm complex signal, additional diamagnetic species in yellow spectra is the product of the reductive elimination.[99]

Decomposition only occurred for wavelengths higher than 400 nm and smaller than 495 nm. Therefore, excitation into the broad band composed of ^{2}LMCT and ^{2}MLCT transitions leads inevitably to decomposition of the compound, whereas the ^{2}MC-transitions do not lead to decomposition.

A tentative explanation reiterates the absence of luminescence: Excitation of the ^{2}MLCT state leads to ISC into the ^{4}MLCT state, which relaxes into a ^{4}MC state. Due to population of the anti-bonding metal based -orbitals, the bonds of the pyrazole to the iron are elongated further or completely dissociated, as seen in photochemically induced ligand release, allowing the coordination of solvent molecules and possibly leading to reductive elimination.[127]

4.5 Hard X-Ray Spectroscopy

The electronic structure of selected complexes was further accessed by synchrotron X-ray spectroscopy. The samples of the complexes $\mathbf{Fe^{III}(ppz)_3}$, $\mathbf{Fe^{III}(\textit{m}\text{-}CF_3ppz)_3}$ and $\mathbf{Fe^{III}(bppz)_3}$ could be measured at the European Synchrotron Radiation Facility (ESRF) in Grenoble, France, at the beamline ID26. Advanced calculations were made by MSc. Ms. Fritsch and have been reported previously.[99]

The techniques of X-ray absorption (XAS) and X-ray emission (XES) spectroscopy are helpful in obtaining electronic and structural details about metal complexes.[128] In the pre-edge of the XANES (X-ray absorption near edge structure) region, transitions from the 1s to the lowest unoccupied molecular orbital (LUMO) occur in K-edge spectra. For d^5 transition metals, the LUMO usually contains high fractions of the metal d-orbitals. Since 1s $\rightarrow$ nd transitions are dipole forbidden, intensity increases by ligand mediated hybridisation with metal p-orbitals. Information on the complex's geometry and symmetry is gained, since the overlap depends on these parameters.[129] By measuring its energy, the prepeak also offers details about the oxidation state. Since the signal line-width is inversely proportional to the lifespan of the observed final states (HERFD-XANES), it is possible to identify a defined emissive final state and improve the experimental resolution.[130, 131]

XES examines the relaxation processes after the photoionization described above.[132, 133] Core-to-core (CtC)-XES spectra result from 3p $\rightarrow$ 1s transitions, where information about the spin state, the oxidation state of the metal and the covalency of the bond between ligand and metal is obtained due to the 3p-3d exchange interaction. 3d $\rightarrow$ 1s transitions are the origin of valence-to-core (VtC)-XES spectra.[134]

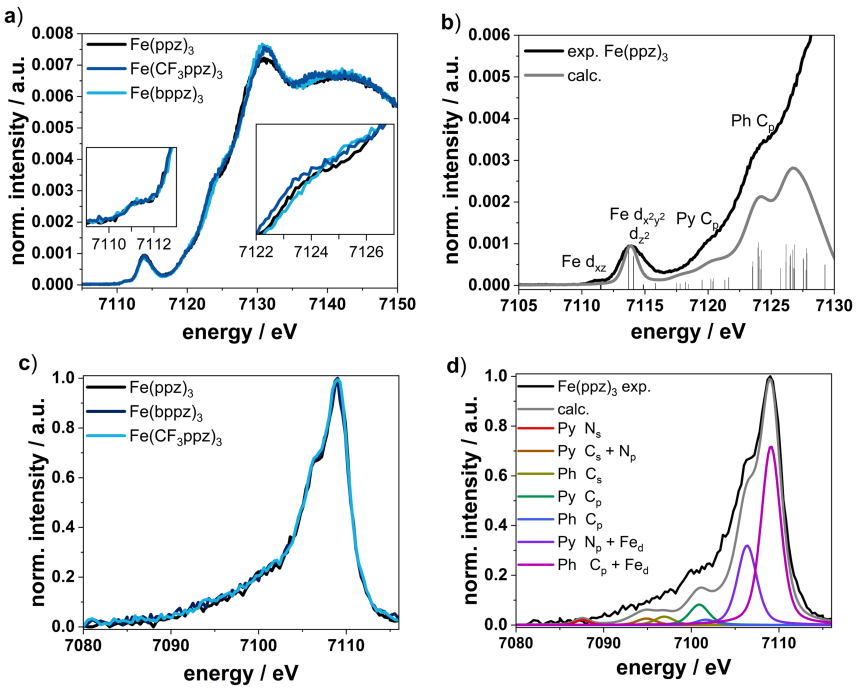

Figure 4.31: Experimental XANES (a) and VtC (c) spectra of $\mathbf{Fe^{III}(ppz)_3}$, $\mathbf{Fe^{III}(bppz)_3}$, $\mathbf{Fe^{III}(CF_3ppz)_3}$ and comparison of experimental and calculated XANES (b) and VtC (d) spectra exemplary for $\mathbf{Fe^{III}(ppz)_3}$ with main character of acceptor (b) and donor (d) orbitals accountable for the peak.[99]

The experimental XANES (fig. 4.31) was compared to theoretically calculated XANES (fig. 4.32), which has also been done for the VtC spectra of the three complexes, $\mathbf{Fe^{III}(ppz)_3}$, $\mathbf{Fe^{III}(bppz)_3}$, $\mathbf{Fe^{III}(CF_3ppz)_3}$.

The XANES spectra of $\mathbf{Fe^{III}(ppz)_3}$, $\mathbf{Fe^{III}(bppz)_3}$ and $\mathbf{Fe^{III}(CF_3ppz)_3}$ shown in fig. 4.31 look nearly identical, indicating the very similar chemical and electronic structure in all three compounds. Due to the non-inversion symmetric character of the C_3-point group, hybridization leads to two prepeak signals at 7111 eV and 7114 eV. These two prepeaks imply accessible empty states in the non-degenerate ligand field states. TDDFT calculations based on the TPSSh functional along with the def2-TZVPP basis set and the def2/J auxiliary basis set furthermore show, that the first signal at 7111 eV can be ascribed to iron d_{xz}-orbitals as acceptor orbitals. The second signal at 7114 eV shows the transitions to the $d_{x^2-y^2/z^2}$ orbital set. Because of the greater number of accessible holes in this d-orbital set, the intensity is substantially higher here, indicating a low-spin state. This is also confirmed by CtC spectra (fig. 4.33), showing just a small splitting between the K$\beta_{1,3}$ main line at around 7058 eV and the Kβ' signal at 7045 eV for the three complexes.

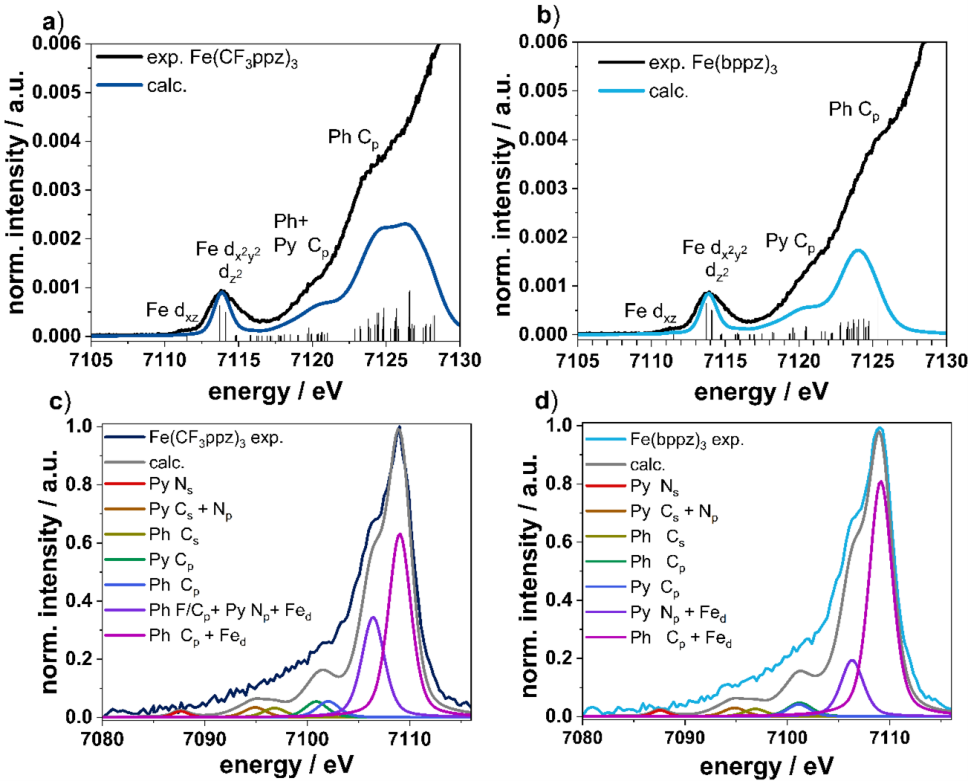

Figure 4.32: Comparison of experimental and calculated XANES (a, b) and VtC (c,d) spectra with main character of acceptor (a,b) and donor (c,d) orbital components for pyrazol (Py) and phenyl (Ph) accountable for the peak.[99]

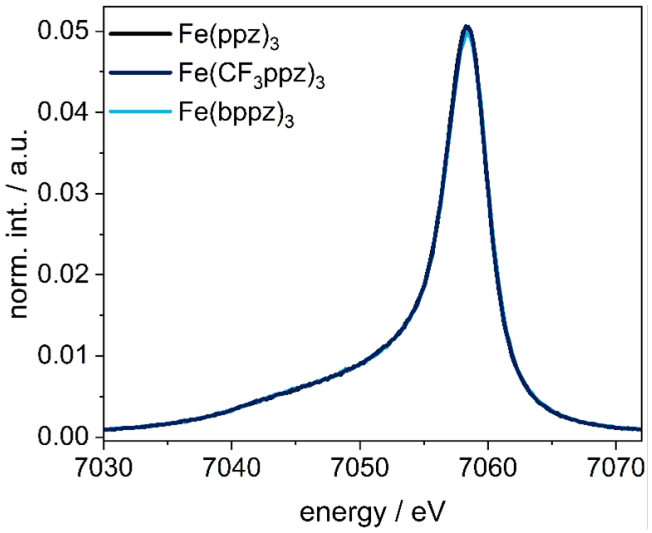

Figure 4.33: Experimental CtC spectra of $Fe^{III}(ppz)_3$, $Fe^{III}(bppz)_3$ and $Fe^{III}(CF_3ppz)_3$.[99]

Moreover, none of the complexes show a shift in the XANES spectra signal, indicating that all oxidation states are the same. Therefore, it may be inferred that all of the complexes that are being studied here share this characteristic.

In the further course, two features appear at 7120 and 7124 eV. The first signal at 7120 eV emerges mainly from transitions into the pyrazole C_p orbitals and the signal at 7124 eV can be related to transitions into the phenyl C_p orbitals. While the spectra at 7120 eV overlap exactly, small differences become apparent in the further course at 7124 eV. This can be attributed to the different substituents on the phenyl, shifting the C_p orbitals in energy. The slight shift to higher energy follows the order $\mathbf{Fe^{III}(CF_3ppz)_3} < \mathbf{Fe^{III}(ppz)_3} < \mathbf{Fe^{III}(bppz)_3}$ and shows the electron withdrawing and donating effects of CF_3- and phenyl-substituents, respectively.

The VtC spectra, in fig. 4.31, show a similar behaviour. For analysis DFT calculations using the TPSS functional along with the def2-TZVPP basis set and def2/J auxiliary basis set for the RI-J approximation are used. The computed spectra and the experimental data show good agreement. This allows the main peak at 7109 eV to be attributed to transitions from the phenyl C_p-orbital with an admixture of iron-d-orbitals (20%) in all cases. The shoulder at 7106.5 eV can be attributed to transitions from the N_p-orbitals of the pyrazole with an admixture of iron-d-orbitals. At lower energies the cross-over transitions are located. From 7101 to 7105 eV transitions from the phenyl- and pyrazole p-orbitals and around 7085 to 7100 eV from ligand s-orbitals.

4.6 Advanced NMR Characterisation

The effectiveness of pNMR approaches is demonstrated by the accurate resonance assignments in sec. 4.2. These methods also provide new insights into how these complexes behave in solutions, which may provide new information on catalytic applications. As a result, it is possible to measure the resonance's temperature dependency, the total shift, and the relaxation process. Regardless of the data collecting challenges, adapted pulse sequences and measurement parameters for paramagnetic complexes allows for the collection of structural information that would otherwise be hidden by their diamagnetic counterparts.[110]

4.6.1 Total Shift Determination

In paramagnetic complexes, the observed chemical shift (δ^{Total}) is made up of contributions from the diamagnetic (δ^{diam}) and paramagnetic (δ_T^{para}, hyperfine or paramagnetic) shifts. The temperature-dependent shift δ_T^{para} is composed of the (fermi-) contact (δ_T^{con}) and the pseudo-contact (δ_T^{pcon}) shift with varying pronounced ratios.[111, 135]

$$\delta^{Total} = \delta^{diam} + \delta_T^{para} \tag{4.6.1}$$

$$\delta_T^{para} = \delta_T^{con} + \delta_T^{pcon} \tag{4.6.2}$$

The predominant NMR shift in this context is referred to as δ_T^{pcon} and is the consequence of dipolar-coupling, which are frequently temperature-dependent and result from spin-spin interactions.[105] Unpaired electron trough-bond transfer generates δ_T^{pcon}, which is directly related to the adjacent nucleus´ electron density. Since the experimental assessment is difficult, one way of determination is via DFT computations.[105, 135] Further comprehension of the behaviour in solution and following excitation can be aided by the longitudinal relaxation time T_1 and their temperature dependency relative to the appropriate resonance. Influence of the unpaired electron, and therefore the electron density distribution, on the ligand scaffold is temperature dependent as well, which may be directly related to catalytic electron transfer reactions of these iron complexes. Considering the predominantly LMCT-based photoexcitation of iron(III) complexes, the electron density distribution and its ability for electron-transfer to the metal centre crucially characterises the catalytic activity.[99] With the temperature dependent measurements and assignment of the composition of the proton shift (eq. 4.6.1 and eq. 4.6.2), predetermination of reaction conditions could be established by this methods.

Typically, δ_T^{para} is more dominant than δ^{diam}, therefore the effect of chemical properties and functional groups may be marginal.[111] For direct comparison to iron(III)-complexes, the diamagnetic congener is usually a gallium(III)-complex or the free ligand. Since *fac*-$\mathbf{Fe^{III}(ppz)_3}$ was successfully reduced to the diamagnetic complex ***mer***-$\mathbf{[Fe^{II}(ppz)_3]^-}$, so that the calculations of δ^{total} can be carried out without detours. δ_T^{para} is either dominated by the contact δ_T^{con} or pseudo-contact δ_T^{pcon} term. δ_T^{con} has

a linear dependence of the inverse temperature (T^{-1}). Spin-orbit coupling in δ_T^{pcon} has an influence and leads to a dependency of T^{-2}.[111, 136] This component may be identified by analysing the resonance shift as a function of temperature. Calculating the overall major chemical contribution can be calculated by eq. 4.6.1. Since the other complexes' behaviours could be roughly defined as being similar, transferability could be assumed for all of them as well. These computations were demonstrated for the unfunctionalised parental complex. Consequently, $\mathbf{Fe^{III}(ppz)_3}$ the ^{1}H-NMR resonance shifts were recorded from 253 to 333 K (fig. 4.34).

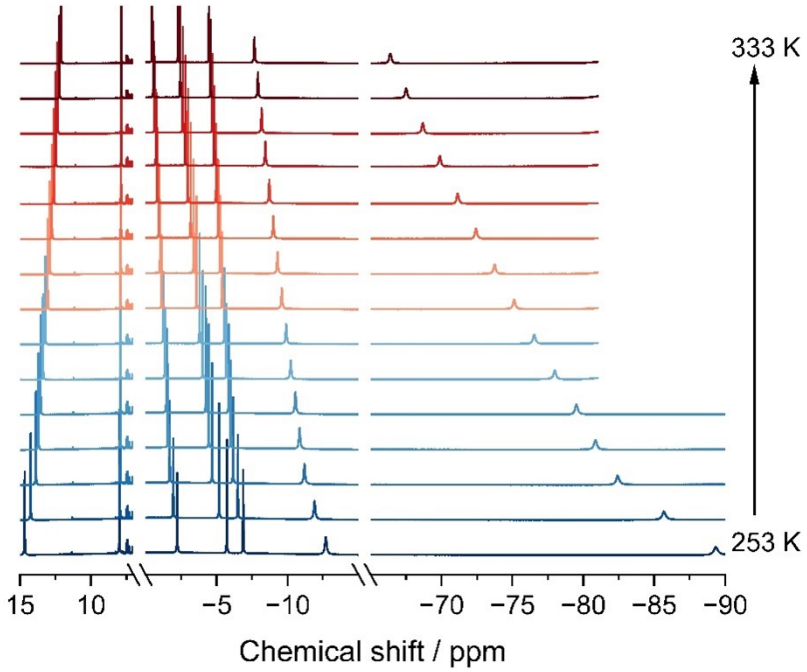

Figure 4.34: ^{1}H-NMR-resonance shift for $\mathbf{Fe^{III}(ppz)_3}$ from 253 to 333 K (from 253 to 273 K in 10 K steps, from 273 to 333 K in 5 K steps).

The resonance signals do not sharpen or expand considerably when temperature increases or decreases. Therefore, the FWHM at different temperatures was determined for comparison. This steady behaviour is demonstrated by the highest (FWHM (333 K) = 15.80 Hz) and lowest (FWHM (253 K) = 15.60 Hz) temperatures for the trans-positioned proton. This is not the case for the iron(IV) species, which may indicate exchange mechanisms, yet unidentified, within the complex (FWHM (333 K)= 15.60 Hz, FWHM (243 K)= 10.40 Hz). The proton resonance shift of paramagnetic complexes drifts low field with increasing temperature, as previously established in other iron(III) complexes such as $[(TSMP)_2Fe^{II}]K_2$ (TSMP = tris-skatylmethylphosphonium) and $[(TSMP)_2Fe^{IV}]$.[108, 137] The degree of the shift is proportional to the distance between the proton and the iron(III) centre; closer protons exhibit a bigger shift.

When the resonance shift is plotted against the temperature, the linearity of the iron(III) and iron(IV) species can even be seen more clearly (fig. 4.35).

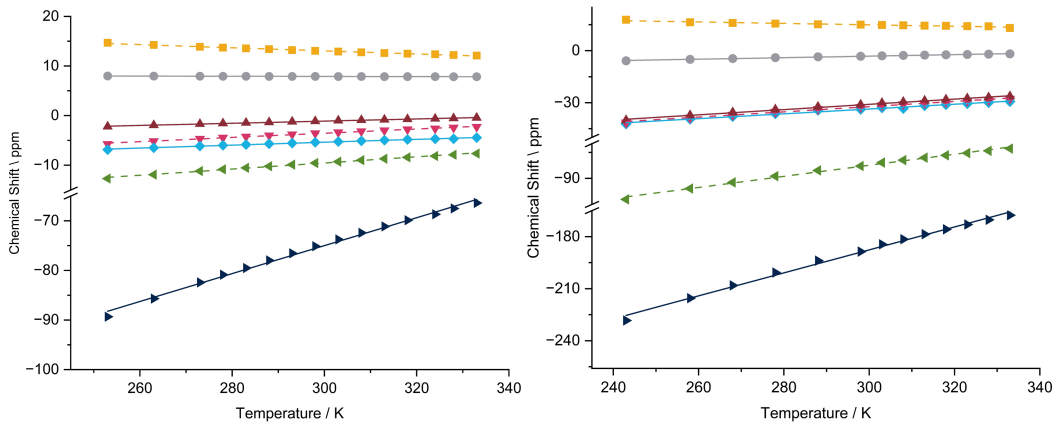

Figure 4.35: Temperature dependent shift of $\mathbf{Fe^{III}(ppz)_3}$ against the chemical shift in ppm for the respective position. Left: $\mathbf{Fe^{III}(ppz)_3}$; Right: $\mathbf{[Fe^{IV}(ppz)_3]^+}$. Dashed line: signal on the pyrazole, straight line: signal on the phenyl part.

With these, the fit parameters were summarised in tab. 4.7.
The chemical shifts are temperature sensitive, with a maximum temperature dependent-

Table 4.7: Fit-parameters (intercept and slope) for $Fe^{III}(ppz)_3$ and $\mathbf{Fe^{IV}(ppz)_3}$ for fig. 4.35.

Complex		Position						
		▶	●	◆	▲	■	▼	◀
$Fe^{III}(ppz)_3$	Slope	0.28	-0.001	0.03	0.02	-0.03	0.04	0.06
	Intercept	-159.50	8.30	-14.17	-7.62	22.49	-16.29	-28.12
$Fe^{IV}(ppz)_3$	Slope	4.32	0.29	1.43	0.90	0.86	0.95	2.12
	Intercept	-386.38	16.32	-75.19	-76.21	27.35	-77.32	-178.28

coefficient (CT) at the ortho-proton of the phenyl-ring with $(\delta_{exp}/\delta T) = 0.28\ \frac{ppm}{K}$ for iron(III) and 4.32 $\frac{ppm}{K}$ for iron(IV). Other positions produce a slope in a range of -0.03 to 0.06 $\frac{ppm}{K}$ for iron(III) and 0.29 - 2.12 $\frac{ppm}{K}$ for iron(IV), respectively. The slight negative slope may imply non-Curie behaviour, but since the values are relatively low and only occur in two positions (only on the iron(III) complex), in the remaining positions Curie-behaviour and hyper-Curie behaviour can still be expected.[138, 139]

Unfortunately, the temperature shift per kelvin is insufficient for the application of the iron(III) ($\mathbf{Fe^{III}(ppz)_3}$) in temperature-dependent paraSHIFT applications.[106] The steady line widths with temperature change may be beneficial, but the CT values are too low, in comparison to similar complexes.[140] Additionally, paraSHIFT agents should exhibit a T^1 relaxation time of 0.37 - 2.4 ms, to allow fast acquisition times.[106] This application would at least be possible for the iron(IV) species with CT = 4.32 ppm/K and relaxation times of 14 - 147 ms. Therefore, measurements in albumin serum solution could be considered to compare these to other MRI paraSHIFT agents.

The inverse temperature is plotted against the chemical shift for each proton to establish the major contribution to the paramagnetic shift δ_T^{para}. In the event of a dominant contact shift δ_T^{con}, a linear behaviour based on Curie's rule that depends on T^{-1} is seen. In the event of a pseudocontact shift dominated contribution, an extra T^{-2} dependency develops, which includes the contribution from the Boltzmann-distribution of inhabited states.[104, 108, 141]

$$Curie\ Law: \delta_T^{para} = \frac{C}{T} \tag{4.6.3}$$

$$Boltzmann - D.: \delta_{S=1} = \left(\frac{A}{\hbar}\right)\frac{2\bar{g}\mu_B}{3\gamma_I kT}\left[1 - \frac{g_{\parallel} - g_{\perp})D}{9\bar{g}kT}\right] \tag{4.6.4}$$

$$= BT^{-1} + CT^{-2} \tag{4.6.5}$$

Note: A = Contact coupling constant /J, $\hbar$ = Plank constant /J·Hz^{-1}, $\bar{g}$ = Average g-tensor, μ_B = Bohr magneton gyromagnetic ratio /JK^{-1}, k = Boltzmann constant /JK^{-1}, T = Temperature /K, $g_{\parallel}/g_{\perp}$ = Anisotropic g-tensor, D = ZFS parameter.

Both examples were plotted to identify the best fit, and the R^2-values for both plots were compared.

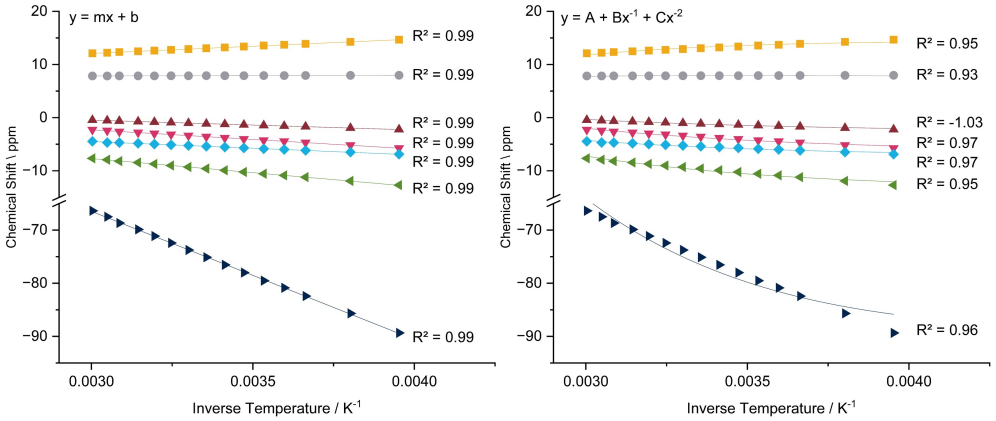

Figure 4.36: Plot of the temperature dependence in case of: Left: Curie´s law applies; Right: dominant Boltzmann-distribution, fit with A=0. Plot was exemplarily plotted for **Fe^{III}(ppz)$_3$** at temperatures from 253 to 333 K.

The temperature dependent signals for **Fe^{III}(ppz)$_3$** display a linear function of the inverse temperature, thus indicating a behaviour according to the Curie-law (eq. 4.6.1). Additionally, the intercept of at 1/T = 0, does not represent δ_{diam}, as has been reported in the literature. Temperature induced spin-crossovers can occur, as in (X[Fe_2L_3])$^{3+}$ (L = 1,3-bis(3-(pyridin-2-yl)-1*H*-pyrazol-5-yl)benzene), where a low-spin turns into a high-spin configuration or vice versa.[141, 142] The signals do not merge nor do the Curie-plots show any curvature, implying that relatively modest dynamic processes of the complex, i.e. no conformational rearrangement, occur in the solution and that no spin crossover is seen, therefore the Curie-law behaviour is constant across the temperature

range studied. The spectra reveal just the *fac*-isomer and no traceable decomposition, demonstrating thermodynamic and kinetic stability in addition. The only concern that developed was the low temperature solubility of certain compounds. Observations at lower temperatures, on the other hand, may be necessary to complete the picture.

The overall orbital shift might be determined using the diamagnetic shift from $\mathbf{Fe^{III}(ppz)_3}$, as detailed below (tab. 4.8). For this, the iron(III) and iron(IV) species three magnetically inequivalent states of the reduced iron(II) complex and the free ligand were calculated individually (tab. 4.8).

Table 4.8: Determination of the total chemical shift by eq. 4.6.1 and the use of the paramagnetic and the diamagnetic shift $\mathbf{Fe^{III}(ppz)_3}$.

Complex	Red. Species	Position						
		▶	●	◆	▲	■	▼	◀
$\mathbf{Fe^{III}(ppz)_3}$	Ligand	-67.94	15.32	2.01	6.55	20.93	3.09	-1.59
$\mathbf{Fe^{III}(ppz)_3}$	1[b]	-67.85	14.71	1.37	6.12	21.26	2.90	-2.22
$\mathbf{Fe^{III}(ppz)_3}$	2[b]	-67.95	14.48	1.37	6.01	21.20	2.73	-2.56
$\mathbf{Fe^{III}(ppz)_3}$	3[b]	-68.43	14.48	1.27	5.90	21.09	2.73	-2.98
$\mathbf{Fe^{IV}(ppz)_3}$	Ligand	-180.35	22.33	-75.20	-25.92	-23.10	3.29	-24.59

a) The complex $\mathbf{Fe^{III}(ppz)_3}$ and $\mathbf{Fe^{IV}(ppz)_3}$, as well as the free ligand have been measured in CD_3CN, the $\mathbf{Fe^{II}(ppz)_3}$ was measured in THF-d_8

b) Numbered ligand of *mer*-$Fe^{II}(ppz)_3$

To summarise the findings, the contribution of paramagnetic or hyperfine shift δ_T^{para} is most likely dominated by the pseudocontact shift. This may be induced by the non-centrosymmetric nature of the complexes. This allows for both isotropic and anisotropic contributions to the chemical shift. Furthermore, the computation of the chemical shift with the free ligand or the *mer*-complex species is in good agreement despite the solvent-problem, with the variation on respective shifts being within 1 ppm. The comparison of the changes to computed temperature dependence values was unsuccessful. Considering the broad shift range, no comparable situation has been reported for these cases, further analyses are necessary.

5 Summary and Outlook

This chapter provides a conclusion based in the research data provided in ch. 3 and ch. 4. A short review of the data will show the purpose of this research, contextualizes the data to the literature and summarizes the findings. By adding recommendations and an outlook for further research, a continuation of this topic might be provided.

5.1 Summary and Conclusions

An essential step towards renewable energy sources could be by water splitting as an inspiration to develop a novel energy landscape. By using solar radiation for photocatalysis, energy production might be revolutionised and carbon-based emissions could be reduced.

One aim of this thesis was the synthesis of complexes with the previous synthesised ligands. The ligands use *N*-arylated heterocycles, specifically phenyl-1*H*-pyrazole, as a motif. Utilising copper as a catalyst, the synthesis makes use of cross-coupling procedures and Ullmann-type condensation. Variously functionalised phenylbromides and pyrazoles are reacted with copper(I) oxide as a catalyst, caesium carbonate as a base, and salicylaldoxime as a co-catalyst in the ligand synthesis process, in excellent yields during 24-48 hours. The ligand scope includes various substitutions, with the intention of examining their effects on the metal centre in the complex formation that follows, electron donating or withdrawing, as well as π-system expansion on the phenyl or pyrazole part, impacting the electron density distribution within the aromatic rings. Challenges occurred when applying multiple substitutions, where the pattern of substitutions did not always result in the anticipated outcome.

The synthesis of an iron-based bidentate complex with the previously described ligands was the second goal of this thesis. The complex synthesis involves two critical steps: ligand activation by orthometalation and transmetalation via an appropriate iron precursor, building an iron-carbene and iron-nitrogen bond. One important element influencing the activation process is the proton's acidity in the ortho-position of the phenylpyrazole ligand, which could be deprotonated by reagents as *n*-BuLi and EtMgBr. For transmetalation, a ligand-grignard solution is reacted with an iron precursor solution. The iron-precursor $(FeBr_2)THF_{1.5}$ is freshly prepared and added to the deprotonated ligand. The resulting complex is obtained through further workup, including removal

of grignard-based residues, washing, and drying. The complexes synthesized include $\mathbf{Fe^{III}(ppz)_3}$, $\mathbf{Fe^{III}(3Me\text{-}ppz)_3}$, $\mathbf{Fe^{III}(MeOppz)_3}$, $\mathbf{Fe^{III}(bppz)_3}$, $\mathbf{Fe^{III}(naphpz)_3}$, $\mathbf{Fe^{III}(p\text{-}CF_3ppz)_3}$, $\mathbf{Fe^{III}(\textit{m}\text{-}CF_3ppz)_3}$ and $\mathbf{Fe^{III}(Fppz)_3}$. Yields vary, with *n*-BuLi activation resulting in higher yields, up to 48% for $\mathbf{Fe^{III}(3Me\text{-}ppz)_3}$. Complexes with additional ligands or substitutions on the pyrazole were challenging to isolate, and separation issues were encountered.

Third aim was a throughout analysis of theses complexes, especially concerning their ground and excited state behaviour and redox properties. First, analysis of the single crystals, generated by the slow diffusion technique, displayed a *fac*-only, C_3-symmetric, distorted octahedral geometry, forming both Δ- and Λ-enantiomers, which could not be separated. The functional groups of the ligand influenced structural factors such as Fe-N and Fe-C bond lengths, chelate bite angles, and trans angles. DFT calculations agreed with crystallographic data and indicated thermodynamic stability of *fac*-conformers for most complexes. Especially successful is the analysis through NMR spectroscopy. The existence of unpaired electrons in iron(III) and iron(IV) complexes makes them paramagnetic, causing issues in NMR characterisation. Because of the large chemical shift ranges and resonance widening generated by unpaired electrons, paramagnetic transition metal complexes are challenging to study and the corresponding pulse programs were carefully chosen. The complexes revealed sharp signals in the ^{1}H-NMR spectra, in line with a *fac*-complex. Attempts were made to chemically reduce and oxidise the complexes to iron(II) species, resulting in significant colour shifts for both directions. For the iron-complexes a switch from *fac*- to the *mer*-isomer occurred, resulting in an instability and prevented isolation. *In situ* oxidation to iron(IV) species gave blue to green solids, though solubility decreased with increased ligand scaffold size.

The investigated compounds exhibit three redox processes within their potential window. The iron(III/IV) and iron(II/III) redox potentials are influenced by different substituents, but the impact is marginal. The ligand-based redox process shows irreversibility in all cases. The electrochemical bandwidths indicate trends in electronic properties, in line with a small influence of the functional groups. The computed HOMO energies correlate with experimental CV data, providing insights into oxidation potentials and metal-based orbitals.

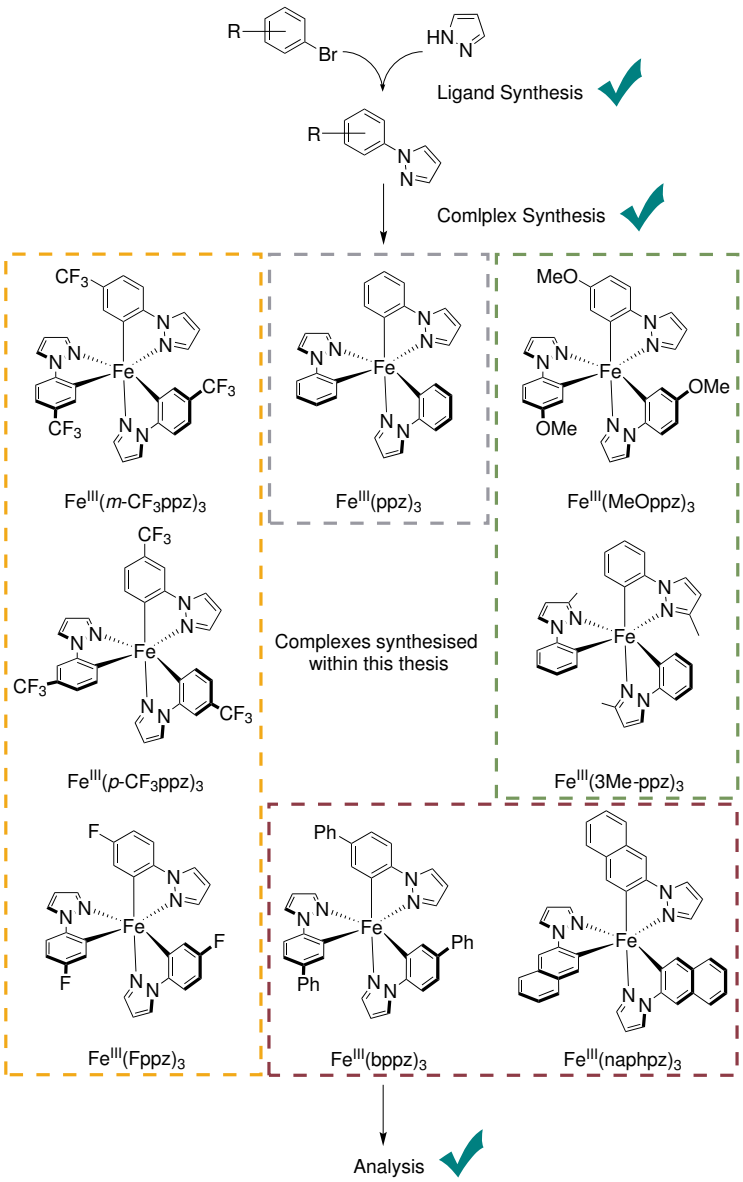

Figure 5.1: Achieved Complexes within this work, after previously synthesizing ligands and successful complexation, throughout analyses gave in-depth insights into their characteristics.

After stability test of the complexes in various solvents, butyronitrile did not lead to complex segregation during irradiation. The spectra reveal three distinct zones, including intense absorption bands below 325 nm attributed to transitions between π- and π*-orbitals. A pronounced feature within 350 and 400 nm suggests a metal-to-ligand charge transfer (MLCT) process. Above 375 nm, a broad absorption band is observed. Theoretical calculations support MLCT and ligand-to-metal charge transfer (LMCT) transitions, with the MLCT dominating and being more pronounced. The unexpected absence of fluorescence in all complexes can be attributed to the strong donor environment created by the ligands, which suppresses the emissive behaviour by low-lying MC states. No catalytic active reaction, especially not water-splitting, could be discovered

since there were no catalytic active states.

Selected complexes, including $\mathbf{Fe^{III}(ppz)_3}$, $\mathbf{Fe^{III}(\textit{m}\text{-}CF_3ppz)_3}$, and $\mathbf{Fe^{III}(bppz)_3}$, underwent synchrotron X-ray spectroscopy at ESRF, Grenoble, utilizing X-ray absorption (XAS) and X-ray emission (XES) techniques. XAS probed transitions from 1s to the LUMO, revealing insights into geometry, symmetry, and oxidation state. Pre-edge features in XANES spectra indicated low-spin states with accessible empty states. CtC spectra supported a low-spin state as well, showing minimal splitting. VtC spectra analysis showed agreement between experimental and calculated data. The main peak (7109 eV) represented transitions from the phenyl Cp-orbital with iron-d-orbitals. Shifts in spectra indicated electron-withdrawing and donating effects of substituents on the phenyl ring. Albeit with marginal impact on the metal centre. Overall, the study provided valuable electronic structure details for the examined iron complexes.

The effectiveness of advanced pNMR techniques could already be demonstrated by successful resonance assignment, for most complex even in all three oxidation states. Techniques allow measuring temperature-dependent resonance, total shift determination, and insights in relaxation processes. Despite challenges, adapted pulse sequences enable collecting structural information for paramagnetic complexes, revealing hidden details compared to diamagnetic counterparts. In paramagnetic complexes, the observed chemical shift (δ^{total}) combines diamagnetic (δ^{diam}) and paramagnetic (δ_T^{para}) shifts. The temperature-dependent shift δ_T^{para} includes fermi-contact (δ_T^{con}) and pseudo-contact (δ_T^{pcon}) shifts. Notably, δ_T^{pcon}, arising from dipolar coupling, depends on adjacent nucleus-electron density, affecting the ligand scaffold temperature behaviour. Preliminary demonstrated on $\mathbf{Fe^{III}(ppz)_3}$, showing linear behaviour in chemical shift versus inverse temperature which indicates a Curie-Weiss-like behaviour. While potential applications like paraSHIFT-agents are considered, the low temperature shift per Kelvin for $\mathbf{Fe^{III}(ppz)_3}$ challenges its use in temperature-dependent applications, although it could be considered for the iron(IV)-species.

In summary, the study provides in-depth insights into the electronic and structural aspects of iron(III)-complexes with phenylpyrazole based ligands through advanced spectroscopic techniques, paving the way for understanding their behaviour in solution and potential catalytic applications for photoactive compouns.

5.2 Outlook

The results presented here are just a minor step towards catalytic active iron-complexes. Additionally the understanding of the complexes presented here are still part of ongoing research. Despite the impressing NMR-spectroscopic investigations, numerous questions remain unsolved. DFT-calculations could assists in some of these problems, like the

extensive search for the remaining signals in the ^{1}H- and ^{13}C-spectra. Likewise, the chemical shift could not be explained to its full extent, like the different impact on the shift in paramagnetic compounds on proton and carbon signals. The Orbach-relaxation was shortly introduced here, but its full impact n iron(III) and iron(IV) complexes must be compared to related complexes, to get a full picture on relaxation pathways.

Thus, further steps towards photoactive iron-complexes is still ongoing. The synthesis presented here can be used as inspiration to improve the ligand structure positively. The next logical step towards new complexes would be to combine ligands with different functional groups. Therefore, push-pull systems with both EDG and EWG could be implemented, or the better absorptive behaviour of the π-conjugated **bbpz** or **naphpz** could compliment the characteristic behaviours. As demonstrated by VUKADINOVIC et *al.*, two ligands with contrary effect on the electron distribution on iron-NHC complexes.[147]

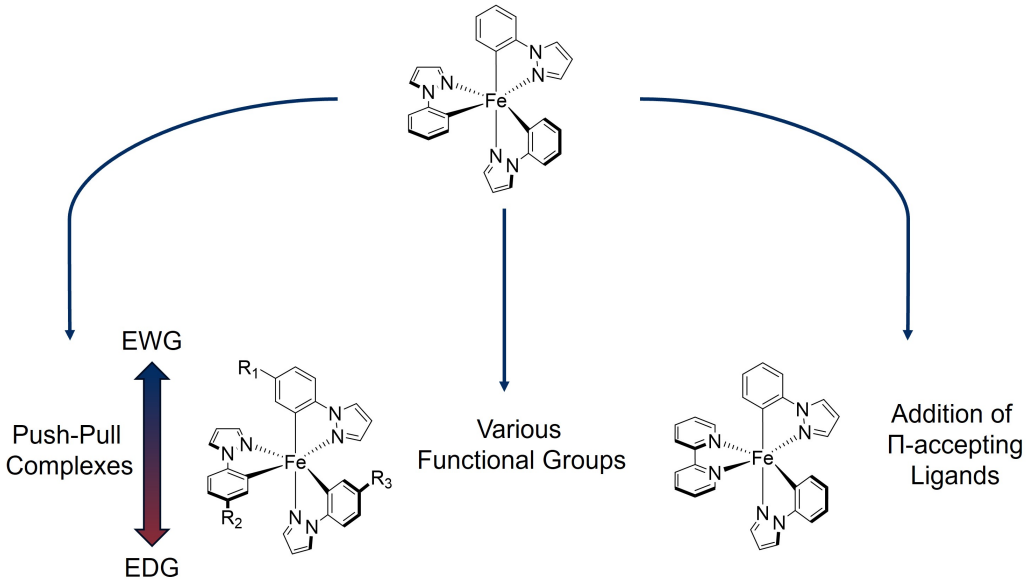

Figure 5.2: Possible new reaction pathways towards novel PS. Left: Push-Pull Systems with countering functional groups, middle: varying functional groups on different ligands, right: addition of better π-accepting ligands.

Furthermore, the bidentate structure not only offers the freedom of tuning the ligand itself, but also the potential of building heteroleptic bis-tridentate complexes. By carefully selecting σ-donating and π-accepting components, the adaptability grows dramatically and numerous functions may be implemented. First steps in this direction were made, by change of the starting material from $Fe(THF)_{1.5}Br_2$ to $Fe(bpy)Br_2$. These showed the desired heteroleptic complex, when the reaction conditions were the same as for the homoleptic complexes, introduced in ch. 3.2.

Third alternative direction of complex synthesis here, the redirecting effect of the pyrazole amine is missing, which complicates the ligand activation. The formerly used grig-

nards might be able to activate the phenyl-carbene, hence tests towards ligand activation is inevitable. Secondly, the activation of the pyrrole on the desired position demands further research. Here preconditioned syntheses with imidazole as carbene-functionality might give insight for possible bases for deprotonation. The interplay between the two separate deprotonations needs delicate adjustments of the reactions conditions. Correct choice of the iron-precursor could also help in complexation.

6 Experimental Details

The following chapter summarizes the used general working techniques, spectroscopic methods and synthetic pathways. Detailed insights are given in the corresponding literature.

6.1 General Information

Unless otherwise described, the syntheses were carried out under inert conditions, working with standard schlenk-techniques under dry argon atmosphere (Argon 5.0). Glassware was evacuated by oil pump vacuum ($1{\cdot}10^{-3}$ mbar), heated and refilled with argon at least three times. Dry solvents were taken from a solvent purification system from MBraun of the type SPS-800. Other solvents were dried according to the literature.[148] All solvents were flushed with argon for 15-30 min prior use. As an alternative the pump-freeze method was used. The degassed solvents were used directly by using syringes, which were flushed several times with argon, and septum technique. The products were purified by column chromatography with silica 60 or aluminum oxide and the corresponding solvents noted. Used chemicals were purchased from the company Merck/Sigma-Aldrich, TCI, Thermo Fischer Scientific and Abcr. Chemicals were used without further purification, with their assigned purity. Exception were solvents for UV-Vis-spectra and Cyclic Voltammetry, which were HPLC grade for spectroscopy.

6.2 Analytical and Spectroscopic Techniques

Nuclear Magnetic Resonance Spectroscopy

The nuclear magnetic resonance measurements (NMR) were recorded at a Bruker Avance 500 (500 MHz) and a Bruker Ascent 700 (700 MHz) spectrometer. This includes the ^{1}H-, the ^{13}C-and the DEPT135-spectroscopy. Additional two-dimensional and diffusion-ordered NMR spectroscopy was performed. The measurements were carried out at 30°C if not noted otherwise. The chemical shifts were given at the ppm-scale and calibrated by the non-deuterated part of the solvent.[149] Exact classification of the signals was ensured by the use of two-dimensional NMR through COSY, HMBC and HSQC experiments.[150] Analysis of the spectra is executed with the Bruker Topspin NMR Software. The failure of the relaxation time can be estimated be 1 ms since this

represents the deviation of the used device. Calculations of the total chemical shift were within a failure of 1 ppm since different solvents must be used in some circumstances.

Mass Spectrometry

Mass spectrometry was measured with a quadrupol time-of-flight mass spectrometer (MS) Synapt 2G by the company WATERS. The solvent used is given with every analysis and the result is noted in the mass-to-charge proportions m\z and compared with the theoretical mass of the compounds.[151]

Elemental Analysis

Elemental analysis measurements were performed with a Micro Cube by ELEMENTAR and were compared with the theoretical calculated mass.

IR

A BRUKER Vertex FT-IR spectrometer in ATR mode enabled the measurements without the use of an extra medium.

Single Crystal X-Ray Analysis

The presented X-ray single crystal data were collected on a BRUKER Venture D8 three-cycle diffractometer equipped with a Mo Kα μ-source (λ=0.71073 Å). Monochromatization of the radiation was obtained using INCOATEC multilayer Montel optics and a Photon III area detector was used for data acquisition. All crystals were kept at 120 K during measurement. Data processing was carried out using the BRUKER **APEX 4** software package: This includes SAINT for data integration and SADABS for a multi-scan absorption correction. Structure solution was obtained by direct methods and the refinement of the structures using full-matrix least squares method based on F2 were achieved in SHELX. All non-hydrogen-atoms were refined anisotropically and the hydrogen atom positions were refined at idealized positions riding on the carbon atoms with isotropic displacement parameters U_{iso}(H)=1.2 U_{eq}(C) resp. 1.5 U_{eq}(-CH_3) and C-H bond lengths of 0.93-0.96 Å. All CH_3 hydrogen atoms were allowed to rotate but not to tip.

Crystallographic data have been deposited at the Cambridge Crystallographic Data Centre with their corresponding deposition numbers. Copies are available free of charge via www.ccdc.cam.ac.uk.

Electro Chemistry: Cyclic Voltammetry

A METRONOHM-AUTOLAB POTENTIOSTAT PGSTAT 101 with a three electrode mode was used to record the cyclic- and square-wave-voltammograms. A based working elec-

trode (d = 1 mm) and counter electrode were used with an $Ag/AgNO_3$ (0.01 M) reference electrode. At room temperature under the exclusion of light with a inert argon atmosphere measurements were conducted in water-free, degassed acetonitrile. Concentration of the complex was $1{\cdot}10^{-3}$ M with NBu_4PF_6 (0.1 M) as supporting electrolyte while Ferrocene as an internal standard was used to reference (Fc/Fc^+) the measurements, which was added after the original data was recorded.

X-Ray Absorption and Emission Spectroscopy

X-ray absorption and emission experiments were performed at beamline ID26 at the European Synchrotron Radiation Facility (ESRF) in Grenoble.[152] The electron energy was 6.0 GeV, and the ring current varied between 180 and 200 mA. Incident energy calibration was performed using a Fe foil. For K-edge measurements, the solid samples were prepared as wafers using degassed cellulose as a binder to avoid self-absorption effects. The XANES spectra were monitored using a photodiode installed at about a 90° scattering angle and at 45° to the sample surface. To exclude radiation damage, fast measurements over the pre-peak were carried out under the measurement conditions (attenuated beam, cryostat to cool the sample to 80 K). No signs of radiation damage could be detected. VtC-XES spectra were recorded at an excitation energy of 7300 eV measured with a Johann type spectrometer.[153]

Mößbauer Spectroscopy

Mössbauer spectra were recorded with a ^{57}Co source in a Rh matrix using an alternating constant acceleration Wissel Mössbauer spectrometer operated in the transmission mode and equipped with a Janis closed-cycle helium cryostat. Isomer shifts are given relative to iron metal at ambient temperature.

Simulation of the experimental data was performed with the mf2.SL program using Lorentzian line doublets (E. Bill, Max-Planck Institute for Chemical Energy Conversion, Mülheim/Ruhr, Germany).

Magnetic Suceptibility Measurements

Temperature-dependent magnetic susceptibility measurements were carried out with a Quantum Design MPMS3 SQUID magnetometer equipped with a 7 Tesla magnet in the range from 295 to 2.0 K at a magnetic field of 0.5 T. The powdered samples were contained in a in a polycarbonate capsule and fixed in a non-magnetic straw. Each raw data file for the measured magnetic moment was corrected for the diamagnetic contribution of the sample holder. The molar susceptibility data were corrected for the diamagnetic contribution.

Experimental data for were modelled by using a fitting procedure to the appropriate

Heisenberg-Dirac-van-Vleck (HDvV) spin Hamiltonian for Zeeman splitting and zero-field splitting: $\widehat{H} = g\mu_B\vec{B}\vec{S} + D[\widehat{S}_z^2\text{-}\frac{1}{3}S(S+1)]$. Temperature-independent paramagnetism (TIP) and a Curie-behaved paramagnetic impurity (PI) with spin S = 1 (6.9 % for iron(IV)) were included according to c_{calc} = (1-PI)· + PI·c_{PI} + TIP. Simulation of the experimental magnetic data was performed with the *julX* or *julX_2s* program (E. Bill: Max-Planck Institute for Chemical Energy Conversion, Mülheim/Ruhr, Germany).

6.3 Theoretical Calculations

All calculations presented here were conducted with the ORCA quantum chemistry package (version 5.0.3).[154] Unconstrained geometry optimization was performed using the PBEh-3c[101] composite method, whereas a frequency calculation was performed and checked for the absence of negatives values to confirm a minimum structure. Optimized structures are used as input for further calculations. Time depended (TD)-DFT calculations for the extraction of orbital energies and the prediction of vertical transitions were conducted using the TPSSh functional[155] together with the def2-TZVP basis set, as well as def2/J auxiliary basis set[156] and the RIJCOSX approximation[157] for the Hartree-Fock component. The tight convergence criterion was imposed on all calculations and the D4 dispersion correction[157] was always employed when not using the PBEh-3c method. The conductor-like polarizable continuum model (CPCM)[158] for MeCN accounting for solvent effects was applied. For the simulation of XANES and VtC XES spectra, the same settings except the CPCM model were used. Whereas for XANES the TD-DFT approach with the TPSSh basis set and the expanded CP(PPP) basis set[159] only for iron was applied. VtC-XES spectra, were calculated based on the DFT approach using the TPSS and CP(PPP) functional.[155] XANES transitions were plotted with linearly increasing broadening to higher energies, starting from 0.6 (fwhm) at the prepeak and were shifted by 155.3 eV to match the experimental spectrum. VtC-XES transitions were broadened by 2.5 eV (fwhm) and all spectra were shifted by 170.6 eV. Ligand or atom projected VtC-XES spectra were created by taking only a set of donor orbitals with significant populations of a given atom or fragment into account. The analysis of fractions of the molecular orbitals is based on the Löwdin population analysis, which was extracted from the ORCA output file using MOAnalyzer (version 1.3).[160] Spatial distributions of orbitals were visualized using IboView (version 20150427).[161]

6.4 Syntheses

6.4.1 Ligand Syntheses

General procedure of ligand syntheses
Under dry argon atmosphere, was charged with solid C_2CO_3 (5 equiv.), Cu_2O (0.1 equiv), functionalised brom-phenyl (2 equiv), pyrazole (3 equiv) and salycilaldioxime (0.4 equiv) and suspended with acetonitrile and refluxed at 85°C for 72 h under vigorous stirring.

After cooling to room temperature, suspension with DCM, the suspension was filtered through a plug of celite and washed with additional DCM. The organic layer was washed with water (2x150 mL) and a saturated NaCl-solution (2x150 mL). After drying with water and removal of the solvent, the residue was absorbed on silica. Flash column chromatography further purified the product and was directly applied in complex synthesis.

The ligands **ppz** and **3Me-ppz** were bought from the vendors mentioned before and were used in complex synthesis without further purification.

1-(4-Methoxyphenyl)-1*H*-pyrazole

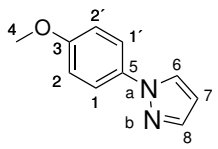

MeOppz

The typical protocol for ligand syntheses was followed in the synthetic process. 1-Brom-4-(trifluoromethyl)benzol (12.9 g, 68.8 mmol) and pyrazole (7.0 g, 103 mmol) resulted in a yield of 13.4 g (77.1 mmol, 74.9%).
^{1}H-NMR (700.38 MHz, $CDCl_3$): δ = 7.82 (d, $^3J_{HH}$ = 2.28 Hz, 1H, 6-H), 7.69 (d, $^3J_{HH}$ = 1.50 Hz, 1H, 8-H), 7.58 (d, $^3J_{HH}$ = 9.07 Hz, 2H, 1,1´-H), 6.97 (d, $^3J_{HH}$ = 9.06 Hz, 2H, 2,2´-H), 6.43 (t, $^3J_{HH}$ = 1.40 Hz, 1H 7-H), 3.84 (s, 3H, 4-H) ppm.
^{13}C-NMR (176 MHz, $CDCl_3$): δ = 158.47 (1C, 3-C), 140.76 (1C, 8-C), 134.17 (1C, 5-C), 127.08 (1C, 6-C), 121.15 (2C, 2,2´-C), 114.72 (2C, 1,1´-C), 107.37 (1C, 7-C), 55.77 (1C, 4-C) ppm.
^{15}N-NMR (70.97 MHz, $CDCl_3$): δ = 300.0 (1N, N-b), 219.5 (1N, N-a) ppm.
MS (ESI in MeCN): m\z 175.0905 (for $C_{10}H_{10}N_2O$ calc. 174.0793).
Elemental Analysis: calc. for $C_{10}H_{10}N_2O$: C: 68.95%, H: 5.79%, N: 16.08%, found: C: 68.71%, H: 5.57%, N: 15.83%.

1-(4-Trifluormethylphenyl)-1*H*-pyrazole

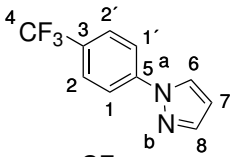

p-CF_3ppz

The typical protocol for ligand syntheses was followed in the synthetic process. 1-Brom-4-(trifluoromethyl)benzol (7.05 mL, 50.1 mmol) and pyrazole (5.1 g, 55 mmol) resulted in a yield of 8.92 g, (42.1 mmol, 84.1%).
^{1}H-NMR (700.38 MHz, $CDCl_3$): δ = 7.99 (d, $^3J_{HH}$ = 2.50 Hz, 1H, 8-H), 7.83 (d, $^3J_{HH}$ = 8.40 Hz, 2H, 2,2´-H), 7.77 (d, $^3J_{HH}$ = 1.54 Hz, 1H, 6-H), 7.72, (d. $^3J_{HH}$ = 8.43 Hz, 2H, 1,1´-H), 6.51 (t, $^3J_{HH}$ = 2.34 Hz, 1H 7-H) ppm.
^{13}C-NMR (176 MHz, $CDCl_3$): δ = 108.73 (1C, 7-C), 119.02 (2C, 2,2´-C), 123.37 (1C, 8-C), 124.91 (1C, 3C), 126.97 (m, 2C, 1,1´-C), 128.49 (m, 1C, 4-C) 142.15 (1C, 6-C), 142.73 (1C, 5-C) ppm.
^{15}N-NMR (70.97 MHz, $CDCl_3$): δ = 301.47 (1N, N-b), 217.38 (1N, N-a) ppm.
^{19}F-NMR (658.7 MHz, $CDCl_3$): δ = -62,30 (s, 3F) ppm.
MS (ESI in MeCN): m\z 213.0622 (for $C_{10}H_8F_3N_2$ calc. 212.1752).

Elemental Analysis: calc. for $C_{10}H_8F_3N_2$: C: 56.61%, H: 3.33%, N: 13.20%, found: C: 58.16%, H: 3.26%, N: 13.32%.

1-(3-Trifluormethylphenyl)-1*H*-pyrazole

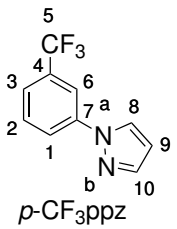

p-CF_3ppz

The typical protocol for ligand syntheses was followed in the synthetic process. 1-Brom-3-(trifluoromethyl)benzol (7.05 mL, 50.1 mmol) and pyrazole (5.1 g, 55 mmol) resulted in a yield of 6.42 g, (30.3 mmol, 60.5%).
^{1}H-NMR (700.38 MHz, $CDCl_3$): δ = 7.97 (d, 1H, 10-H), 8.0 (s, 1H, 6-H), 7.89 (d, $^3J_{HH}$ = 8.79 Hz, 1H, H-1), 7.76 (s, 1H, H-10), 7.58 (t, $^3J_{HH}$ = 7.95 Hz, 1H, 2-H), 7.54 (d, $^3J_{HH}$ = 7.74 Hz, 1H, 3-H), 6.51 (t, $^3J_{HH}$ = 1.96 Hz, 1H, 9-H) ppm.
^{13}C-NMR (176 MHz, $CDCl_3$): δ = 142.0 (1C, C-9), 140.7 (1C, C-5), 132.3 (m, C-5), 130.3 (1C, C-4), 127.0 (1C, C-2), 124.7 (1C, C-10), 123.2(1C, m, C-3), 122.2 (1C, C-1), 116.2 (1C, m, C-6), 108.6 (1C, C-9) ppm.
^{15}N-NMR (70.97 MHz, $CDCl_3$): δ = 217,1 (1N, N-a) , 301,2 (1N, N-b) ppm.
^{19}F-NMR (658.7 MHz, $CDCl_3$): δ = -62.81 (s, 3F) ppm.
MS (ESI in MeCN): m\z 213.0632 (for $C_{10}H_8F_3N_2$ calc. 213.0561).
Elemental Analysis: calc. for $C_{10}H_8F_3N_2$: C: 56.61%, H: 3.33%, N: 13.2%, found: C: 56.25%, H: 3.36%, N: 13.44%.

1-(4-Fluormethylphenyl)-1*H*-pyrazole

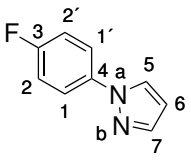

Fppz

The typical protocol for ligand syntheses was followed in the synthetic process. 1-Bromo-4-fluorobenzene (7.05 mL, 50.1 mmol) and pyrazole (5.1 g, 55 mmol) resulted in a yield of 3.42 g (21.1 mmol, 52.7%).
^{1}H-NMR (700.38 MHz, $CDCl_3$): δ = 7.86 (d, $^3J_{HH}$ = 2.63 Hz, 1H, H-7), 7.71 (d, $^3J_{HH}$ = 1.60 Hz, 1H, H-5), 7.65 (m, 2H, H-3), 7.14 (m, 2H, H-2), 6.46 (dd, $^3J_{HH}$ = 2.06 Hz, $^3J_{HH}$ = 2.06 Hz, 1H, H-6) ppm.
^{13}C-NMR (176 MHz, $CDCl_3$): δ = 162.0 (1C, C-4), 160.6 (1C, C-1), 141.3 (1C, C-5), 127.0 (1C, C-7), 121.2 (2C, C-3), 116.4 (1C, C-2), 107.9 (1C, C-6) ppm.
^{15}N-NMR (70.97 MHz, $CDCl_3$): δ = 301.19 (1N, N-a), 217.68 (1N, N-b) ppm.
^{19}F-NMR (658.7 MHz, $CDCl_3$): δ = -116.00 (m, 1F) ppm.
MS (ESI in MeCN): m\z 163.0688 (for $C_9H_8FN_2^+$, calculated: 163.0593).
Elemental Analysis: calc. for $C_9H_7FN_2$: C: 66.66%, H: 4.35%, N:17.27%, found: C:66.47%, H: 4.68%, N: 17.55%.

1-(3,5-Bis(trifluoromethyl)phenyl)-1*H*-pyrazole

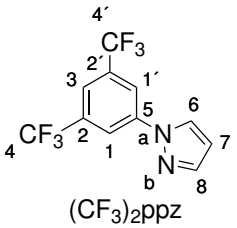

(CF3)2ppz

The typical protocol for ligand syntheses was followed in the synthetic process. 1-Bromo-3,5-bis(trifluoromethyl)benzene (6.92 ml, 40.1 mmol) and pyrazole (4.1 g, 60.2 mmol) resulted in a yield of 2.76 g (9.68 mmol, 24.6%).
^{1}H-NMR (700.38 MHz, $CDCl_3$): δ = 8.18 (s, 2H, 1,1´-H), 8.03 (d, $^3J_{HH}$ = 2.59 Hz ,1H, 6-H), 7.79 (d, $^3J_{HH}$= 1.71 Hz, 1H, 8-H), 7.77 (s, 1H, 3-H), 6.56 (t, $^3J_{HH}$ = 2.22 Hz, 1H, 7-H) ppm.
^{13}C-NMR (176 MHz, $CDCl_3$): δ = 142.71 (1C, 8-C), 141.32 (1C, 5-C), 133.29 (m, 2C, 2,2´-C), 127.03 (1C, 6-C), 125.45-120.85 (m, 2C, 4,4´-C), 119.76 (m, 1C, 3-C), 118.96 (m, 2C, 1,1´-C), 109.44 (1C, 7-C) ppm.
^{15}N-NMR (70.97 MHz, $CDCl_3$): δ = 301.7 (1N, N-a), 214.7 (1N, N-b) ppm.
^{19}F-NMR (658.7 MHz, $CDCl_3$): δ = -63.1 (s, 6F) ppm.
MS (ESI in MeCN): m\z 281.0501 (for $C_{11}H_6F_6N_2^+$, calculated: 280.0435).
Elemental Analysis: calc. for $C_{11}H_6F_6N_2$: C: 47.16%, H: 2.16%, N:10.0%, found: C: 47.42%, H: 2.63%, N: 9.84%.

1-([1,1´-Biphenyl]-4-yl)-1*H*-pyrazole

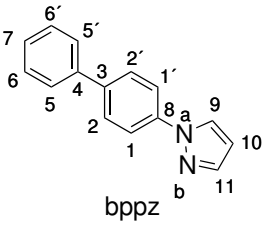

bppz

The typical protocol for ligand syntheses was followed in the synthetic process. 4-Bromo-1,1'-biphenyl (23.41 g, 100.0 mmol) and pyrazole (10.20 g, 151.0 mmol) resulted in a yield of 16.70 g, (75.7 mmol, 76.7%).
^{1}H-NMR (700.38 MHz, $CDCl_3$): δ = 7.96 (d, $^3J_{HH}$ = 2.42 Hz, 1H, 7-H), 7.77 (m, 3H, 6,6´,9-H), 7.61 (m, 2H, 5,5´-H), 7.47 (m, 2H, 2,2´-H), 7.46 (m, 2H, 1,1´-H), 7.37 (m, 1H, 11-H), 6.51 (t, $^3J_{HH}$ = 2.12 Hz, 1H, 10-H) ppm.
^{13}C-NMR (176 MHz, $CDCl_3$): δ = 141.40 (1C, 11-C), 140.31 (1C, 4-C), 139.58 (1C, 8-C), 139.56 (1C, 3-C), 129.10 (2C, 6,6´-C), 128.28 (2C, 2,2´-C), 127.72 (1C, 7-C), 127.18 (2C, 5,5´-C), 126.95 (1C, 9-C), 119.68 (2C, 1,1´-C), 107.93 (1C, 10-C) ppm.
^{15}N-NMR (70.97 MHz, $CDCl_3$): δ = 217.1 (1N, N-a) , 301.2 (1N, N-b) ppm.
MS (ESI in MeCN): m\z 220.1000 (for $C_{15}H_{12}F_3N_2$ calc. 213.0561).
Elemental Analysis: calc. for $C_{15}H_{12}F_3N_2$: C: 81.79%, H: 5.49%, N: 12.72%, found: C: 80.77%, H: 5.50%, N: 12.44%.

1-(Naphthalen-2-yl)-1*H*-pyrazole

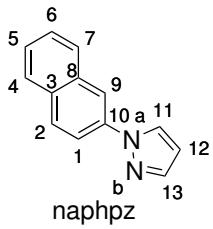

naphpz

The typical protocol for ligand syntheses was followed in the synthetic process. 2-Bromonaphthalene (7.46 g, 35.0 mmol) and pyrazole (4.23 g, 65.0 mmol) resulted in a yield of 6.53 g, (33.6 mmol, 84.0%).
^{1}H-NMR (700.38 MHz, $CDCl_3$): 8.12 (d, $^3J_{HH}$ = 2.03 Hz, 1H, 4-H), 8.07 (d, $^3J_{HH}$ = 2.38 Hz, 1H, 7-H), 7.95 (d, $^3J_{HH}$ = 8.84

Hz, 1H, 2-H), 7.88 (m, 3H, 5,6,11-H), 7.79 (d, $^3J_{HH}$ = 1.57 Hz,
1H, 9-H), 7.53 (m, 1H, 13-H), 7.49 (m, 1H, 1-H), 6.53 (t, $^3J_{HH}$ = 2.21 Hz, 1H, 12-H) ppm.
^{13}**C-NMR** (176 MHz, $CDCl_3$): δ = 141.47 (1C, 13-C), 137.83 (1C, 10-C), 133.81 (1C, 8-C), 132.09 (1C, 3-C), 129.76 (1C, 5-C), 128.18 (1C, 6-C), 128.02 (1C, 2-C), 127.25 (1C, 4-C), 127.22 (1C, 7-C), 126.13 (2C, 11-C), 118.81 (1C, 9-C), 116.63 (1C, 1-C), 108.00 (1C, 12-C) ppm.
^{15}**N-NMR** (70.97 MHz, $CDCl_3$): δ = 219.7 (1N, N-a) , 300.6 (1N, N-b) ppm.
MS (ESI in MeCN): m\z 195.0908 (for $C_{13}H_{10}N_2$ calc. 194.0844).
Elemental Analysis: calc. for $C_{13}H_{10}N_2$: C: 80.39%, H: 5.19%, N: 14.42%, found: C: 79.94%, H: 5.17%, N: 14.25%.

6.4.2 Complex Syntheses

Method A
Under Argon atmosphere respective ligand (3 equiv) was suspended in tetrahydrofuran (THF) (10 mL). Ethylmagnesium bromide (4 equiv, 0.9 M in THF) was added dropwise and refluxed overnight. In a second round bottom flask, iron powder (12 equiv) was added to THF solution of iron(II) bromide (1.5 equiv) (40 mL) and refluxed overnight. After refluxing, the flask was cooled to room-temperature and the ligand-solution was cooled in an ethanol-nitrogen bath to -80°C. The iron(II) bromide solution was added dropwise and slowly warmed to room temperature under an argon atmosphere. To the reaction mixture a solution of NH_4Cl (100 mL, 15 g/L) was added, and extracted with dichloromethane (DCM) (3x100 mL). The combined organic portions were dried with $MgSO_4$ and concentrated under reduced pressure. Column chromatography with silica as solid phase and DCM as eluent was applied. The combined fractions were concentrated under reduced pressure and crystallized with slow diffusion of cyclopentane into the DCM-analyte solution. After removing the crystalline product and drying at 50°C at high vacuum, the compound was received as elemental analysis pure product.

Method B
The synthesis of the complex was conducted with methods previously described.[99] In 10 mL of tetrahydrofuran (THF), the ligand (3-Methyl-1-phenyl-1*H*-pyrazole) (3 equiv) was suspended under an argon environment. Dropwise addition of n-buthyllithium (4 equiv, 2.5 M in hexanes) followed by overnight refluxing. Iron powder (12 equiv) was added to a THF solution of iron(II) bromide (1.5 equiv) (40 mL) and refluxed overnight in a second round button flask. Refluxing was followed by cooling the flask to ambient temperature and cooling the ligand solution to -80°C in an ethanol-nitrogen bath. Under an argon environment, the iron(II) bromide solution was added dropwise and gradually warmed to room temperature. To the reaction mixture, a solution of NH_4Cl (100 mL, 15 g/L) was added, and extracted with dichloromethane (DCM) (3x100 mL). The combined organic components were concentrated under low pressure after being dried with $MgSO_4$. Column chromatography with silica as solid phase and DCM as eluent was applied. The combined fractions were concentrated under reduced pressure and crystallized with slow diffusion of cyclopentane into the DCM-analyte solution. Afterwards, removing the crystalline product and drying at 50°C at high vacuum gave the compound was received as elemental analysis pure product.

Tris(1-phenylpyrazolato-N,C^2)iron(III)

Complex synthesis followed method A and was obtained as yellow powder (7.45%).

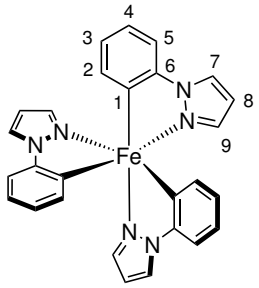

Fe(ppz)$_3$

Fe^{III}(ppz)$_3$
^{1}H-NMR (700.38 MHz, CD_3CN): δ = -75.20 (s, 3H, 2-H), -9.27 (s, 3H, 9-H), -5.25 (s, 3H, 4-H), -3.35 (s, 3H, 8-H), -1.15 (s, 3H, 5-H), 7.90 (s, 3H, 3-H), 13.04 (s, 3H, 7-H) ppm.
^{13}C{^{1}H}-NMR (176.1 MHz, CD_3CN): δ = 93.3 (3C, 3-C), -75.2 (3C, 5-C) 100.4 (3C, 7-C), 118.4 (3C, 8-C), 123.1 (3C, 9-C), 240.2 (3C, 4-C), 388.1 (3C, 2-C), 394.0 (3C, 6-C) ppm.
MS (ESI in MeCN): m\z 485.1160 (for $C_{27}H_{21}FeN_6$ calc. 485.1177).
Elemental Analysis: calc. for $C_{27}H_{21}FeN_6$: C: 66.82%, H: 4.36%, N: 17.32%, found: C: 66.77%, H: 4.56%, N: 17.25%.
IR (ATR, [cm^{-1}]): 3139w, 3041w, 1573w, 1506w, 1461m, 1434m, 1417m, 1398m, 1328w, 1270m, 1236w, 1193w, 1153w, 1099w, 1064m, 1043m, 1012m, 960m, 918w, 871w, 825w, 742s, 715m, 698m, 661w, 644w, 609m.

[Fe^{IV}(ppz)$_3$]PF$_6$
^{1}H-NMR (700.38 MHz, CD_3CN): δ = -187.60 (s, 3H, 2-H), -82.46 (s, 3H, 4-H), -33.62 (s, 3H, 5-H), -32.27 (s, 3H, 9-H), -30.98 (s, 3H, 7-H), -3.15 (s, 3H, 8-H), 14.91 (s, 3H, 3-H) ppm.
^{13}C{^{1}H}-NMR (176.1 MHz, CD_3CN): δ = -680.2 (d, 168.49 Hz, 3C, 3-C), -594.3 (d, 153.37 Hz, 3C, 5-C), 27.9 (d, 186.39 Hz, 3C, 8-C), 288.4 (d, 195.76 Hz, 3C, 7-C), 417.7 (d, 197.37 Hz, 3C, 9-C), 498.9 (d, 168.08 Hz, 3C, 2-C), 621.1 (d, 160.51 Hz, 3C, 4-C), 632.4 (s, 3C, 6-C) ppm.
^{15}N-NMR(70.96 MHz, CD_3CN): δ = 136.20 ppm.
MS (ESI in MeCN): m\z 485.1161 (for $[C_{27}H_{21}FeN_6]^+$ calc. 485.1177).

***mer*-[Fe^{II}(ppz)$_3$]Na**
^{1}H-NMR (700.38 MHz, THF-d_8): δ = 6.08 (m, 2H, $8^{2,3}$-H), 6.25 (t, $^3J_{HH}$ = 2.18 Hz, 1H, 8^1-H), 6.29 (s, 1H, 9^2-H), 6.52 (t, $^3J_{HH}$ = 7.20 Hz, 1H, 4^2-H), 6.62 (m. 2H, $4^{1,3}$-H), 6.58 (m, 2H, $3^{2,3}$-H), 6.77 (m, 1H, 2^2-H), 6.71(1H, 9^3-H), 6.81 (t, $^3J_{HH}$ = 7.00 Hz, 1H, 3^1-H), 7.05 (d, $^3J_{HH}$ =1.09, 1H, 9^1-H), 7.08 (d, $^3J_{HH}$ = 7.51 Hz, 1H, 5^2-H), 7.16 (d, $^3J_{HH}$ = 7.51 Hz, 1H, 5^3-H), 7.25 (d, $^3J_{HH}$ = 6.44 Hz, 1H, 2^1-H), 7.27 (d, $^3J_{HH}$ = 7.36 Hz, 1H, 5^1-H), 7.35 (d, $^3J_{HH}$ = 6.79 Hz, 1H, 2^3-H), 8.05 (d, $^3J_{HH}$ = 2.52 Hz, 1H, 7^3-H), 8.16 (d, $^3J_{HH}$ = 2.59 Hz, 1H, 7^2-H),), 8.22 (d, $^3J_{HH}$ = 2.03 Hz, 1H, 7^1-H) ppm.
^{13}C-NMR (176.1 MHz, THF-d_8): δ = 17.2 (1C, 1^1-C), 18.0 (2C, $1^{2,3}$-C), 106.3 (1C, 8^1-C), 106.6-106.9 (2C, $8^{2,3}$-C), 107.2 (1C, 5^2-C), 108.1 (1C, 5^3-C), 108.2 (1C, 5^1-C), 114.1 (1C, 4^2-C), 117.3 (1C, 3^1-C), 117.9 (1C, $4^{1,3}$-C), 118.5 (1C, 4^3-C), 120.70 (1C,

7^3-C), 122.1 (1C, 7^2-C), 122.4-122.5 (2C $2^{2,3}$-C), 122.9 (1C, 7^1-C), 123.4 (1C, 3^2-C), 134.9 (1C, 9^2-C), 136.3 (1C, 6^3-C), 137.5 (1C, 2^1-C), 140.5 (1C, 6^1-C), 140.9 (1C, 9^1-C), 142.9 (1C, 6^2-C), 144.4(1C, 9^3-C), 145.6(1C, 3^3-C) ppm.
^{15}N-NMR (70.96 MHz, THF-d_8): δ = 243.5 ($N2^1$), 247.3 ($N2^2$), 249.0 ($N1^3$), 281.0 ($N1^1$), 283.7 ($N2^1$), 284.5 ($N1^3$) ppm.

Tris(1-(4-(trifluoromethyl)phenyl)pyrazolato-*N*,*C*^{2})iron(III)

Complex synthesis followed method A and was obtained as yellow powder (17.2%).

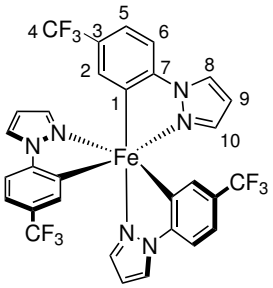

Fe(*m*-CF$_3$ppz)$_3$

Fe^{III}(*m*-CF$_3$ppz)$_3$

^{1}H-NMR (700.38 MHz, THF-d_8): δ = -75.17 (s, 3H, 2-H), -10.47 (s, 1H, 10-H), -3.39 (s, 3H, 9-H), -3.17 (s, 3H, 5-H), 0.27 (s, 3H, 6-H), 11.23 (s, 3H, 8-H) ppm.
^{13}C{^{1}H}-NMR (176.1 MHz, THF-d_8): δ = -93.4 (3C, 3-C), -68.6 (3C, 6-C), 108.9 (3C, 8-C), 112.6 (3C, 9-C), 126.5 (dd, $^1J_{CF}$ = 272.85 Hz 275.09 Hz, 4-C), 3C, 132.8 (3C, 10-C), 229.9 (3C, 5-C), 361.9 (3C, 2-C), 382.0 (3C, 7-C) ppm.
^{15}N-NMR (70.96 MHz, THF-d_8): δ = 84.0 ppm.
^{19}F-NMR (659.0 MHz, THF-d_8): δ = -71.5 (s, 9F) ppm.
MS (ESI in MeCN): m\z 689.0800 (for $C_{30}H_{18}F_9FeN_6$ calc. 689.0799).
Elemental Analysis: calc. for $C_{30}H_{18}F_9FeN_6$: C: 52.27%, H: 2.63%, N: 12.19%, found: C: 51.90%, H: 2.81%, N: 12.12%.
IR (ATR, [cm^{-1}]): 3155w, 3033w, 2360w, 2335w, 1585w, 1508w, 1477w, 1396m, 1315s, 1272s, 1249m, 1159m, 1110s, 1066s, 1045s, 960m, 900m, 838w, 821w, 804m, 746s, 702m, 661m, 607w.

[Fe^{IV}(*m*-CF$_3$ppz)$_3$]PF$_6$

^{1}H-NMR (700.38 MHz, THF-d_8): δ = -200.79 (s, 3H, 2-H), -71.12 (s, 3H, 4-H), -47.68 (s, 3H, 5-H), -41.64 (s, 3H, 7-H), -31.46 (s, 3H, 8-H), 4.28 (s, 3H, 9-H) ppm.
^{13}C{^{1}H}-NMR (176.1 MHz, THF-d_8): δ = -679.0 (3C, 3-C), -555.9 (3C, 6-C), -9.3 (d, 188.7 Hz, 3C, 9-C), 134.07 (dd, 834.5 Hz, 270.8 Hz, 3C, 4-C), 354.4 (d, 197.87 Hz, 3C, 8-C), 435.8 (d, 159.9, 3C, 10-C), 447.2 (d, 189.4, 3C, 5-C), 573.2 (1C, 2-C), 576.9 (d, 169.7 Hz, 3C, 7-C) ppm.
^{19}F-NMR (659.0 MHz, THF-d_8): δ = -155.66 (s, 9F) ppm.
Nitrogen atoms could not be detected.

mer-[Fe^{II}(*m*-CF$_3$ppz)$_3$]Na

^{1}H-NMR (700.38 MHz, THF-d_8): = 6.01 (s, 1H, 9^3-H), 6.04 (s, 1H, 9^2-H), 6.18 (s, 1H, 10^3-H), 6.30 (s, 1H, 9^1-H), 6.38 (s, 1H, 10^2-H), 6.45 (d, $^3J_{HH}$ = 7.35 Hz, 1H, 5^3-H), 6.57 (s, 1H, 2^3-H), 6.73 (d, $^3J_{HH}$ = 7.41 Hz, 1H, 5^2-H), 6.84 (d, $^3J_{HH}$ = 7.67 Hz, 1H,

5^1-H), 6.90 (d, $^3J_{HH}$ = 7.81 Hz, 1H, 6^3-H), 7.01 (s, 1H, 10^1-H), 7.10 (s, 1H, 2^2-H), 7.13 (d, $^3J_{HH}$ = 7.85 Hz, 1H, 6^2-H), 7.27 (d, $^3J_{HH}$ = 7.89 Hz, 1H, 6^1-H), 7.62 (s, 1H, 2^2-H), 8.00 (s, 1H, 8^3-H), 8.14 (d, $^3J_{HH}$ = 1.47 Hz, 1H, 8^2-H), 8.35 (s, 1H, 8^1-H) ppm.
^{13}C-NMR (176.1 MHz, THF-d_8): δ = 105.7 (1C, 6^3-C), 106.4 (1C, 6^2-C), 107.2 (1C, 9^3-C), 107.5 (1C, 6^1-C), 107.7 (1C, 9^2-C), 107.9 (1C, 9^1-C), 112.8 (1C, 5^3-C), 115.1 (1C, 5^2-C), 115.7 (1C, 5^1-C), 121.9 (1C, 8^3-C), 123.2 (1C, 8^2-C), 123.6 (m, 3C, 1-C), (124.1 (1C, 8^1-C), 125.6 (m, 3C, 7-C), 127.2 (m, 4^3-C), 128.7 (m, 1C, 4^2-C), 130.2 (m, 1C, 4^1-C), 135.9 (1C, 10^3-C), 136.5 (1C, 10^1-1), 136.8 (1C, 10^2-C) ppm.
^{15}N-NMR (70.96 MHz, THF-d_8): δ = 247.5 ($N2^1$), 247.0 ($N2^2$), 242.5 ($N2^3$), 271.1 ($N1^1$), 272.9 ($N1^2$), 281.33 ($N1^3$) ppm.

Tris(1-(3-(trifluoromethyl)phenyl)pyrazolato-*N*,C^2)iron(III)

The compound was received as elemental analysis pure, yellowish-red product (10.6%).

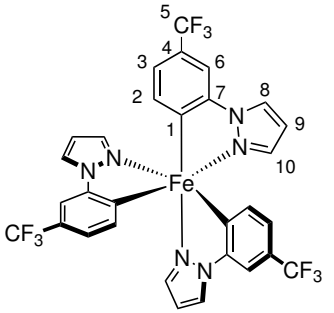

Fe(*p*-CF_3ppz)$_3$

Fe^{III}(*m*-CF_3ppz)$_3$
^{1}H-NMR (700.38 MHz, CD_3CN): δ = -72.54 (s, 3H, 2-H), -9.98 (s, 3H, 10-H), -3.60 (s, 3H, 9-H), 1.31 (s, 3H, 6-H), 9.36 (s, 3H, 3-H), 11.75 (s, 3H, 8-H) ppm.
^{13}C{^{1}H}-NMR (176.1 MHz, CD_3CN): δ = -102.6 (d, 165.81 Hz, 3C, 3-C), -72.6 (d, 156.01 Hz, 3C, 6-C), 91.1 (q, 265.2 Hz, 810.23 Hz, 3C, 5-C), 105.7 (d, 198.87 Hz, 3C, 8-C), 113.9 (d, 191.51 Hz, 3C, 9-C), 129.1 (d, 198.80 Hz, 3C, 10-C), 243.5 (d, 33.1 Hz, 3C, 4-C), 375.4 (d, 136.4 Hz, 3C, 2-C), 390.1 (3C, 7-C) ppm.
^{15}N-NMR (70.96 MHz, CD_3CN): δ 84.8 ppm.
^{19}F-NMR (659.0 MHz, THF-d_8): δ = -45.95 (s, 3F) ppm.
MS (ESI in MeCN): m\z 689.0798 (for $C_{30}H_{18}F_9FeN_6$ calc. 689.0799).
Elemental analysis: calc. for $C_{30}H_{18}F_9FeN_6 \cdot C_4H_{10}O$: C: 53.49%, H: 3.70%, N: 11.01%, found: C: 54.16%, H: 4.07%, N: 10.26%.
IR (ATR, [cm^{-1}]): 3143w, 3130w, 3010w, 2921m, 2852m, 1909w, 1747w, 1716w, 1664w, 1598m, 1513m, 1477m, 1444m, 1409m, 1340m, 1317s, 1269s, 1240m, 1161s, 1108s, 1070s, 1047s, 1010s, 966s, 931m, 967m, 831s, 806m, 748s, 721m, 707s, 667m, 642m, 603m, 522m.

[Fe^{IV}(*m*-CF_3ppz)$_3$]PF_6
^{1}H-NMR (700.38 MHz, THF-d_8): δ = -182.17 (s, 3H, 2-H), -39.37 (a, 6H, 8-H, 10-H), -25.41 (s, 3H, 6-H), -4.23 (s, 3H, 9-H), 18.48 (s, 3H, 3-H) ppm.
^{13}C{^{1}H}-NMR (176.1 MHz, THF-d_8): δ = -681.8 (3C, 3-C), -564.1 (3C, 6-C), 8.9 (3C, 9-C), 328.0 (3C, 8-C), 436.6(3C, 10-C), 463.8 (d, 160.03 Hz, 3C, 2-C), 576.8 (s, 3C, 7-C), 607.7 (3C, 4-C) ppm.

***mer*-[Fe^{II}(*p*-CF$_3$ppz)$_3$]Na** could not be achieved.

Tris(1-(4-(fluoromethyl)phenyl)pyrazolato-*N*,*C*^{2})iron(III)

Complex synthesis followed method A and was obtained as red powder (2.73%).

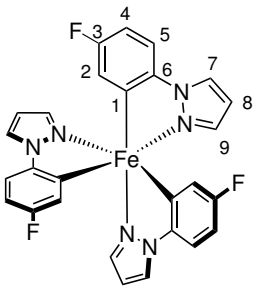

Fe(Fppz)$_3$

Fe^{III}(Fppz)$_3$
^{1}H-NMR (700.38 MHz, CD_3CN): δ = -75.89 (1s, 3H, 2-H), -10.61 (s, 3H, 9-H) -4.82(s, 3H, 5-H), -4.15(s, 3H, 4-H), -3.11 (s, 3H, 8-H), 10.99 (s, 3H, 7-H) ppm.
^{13}C{^{1}H}-NMR (176.1 MHz, CD_3CN): δ = -119.23 (d, 247.2 Hz, 3C, 3-C), -110.10 (d, 162.2 Hz, 3C, 5-C), 107.6 (d, 186.9 Hz, 3C, 7-C), 112.3 (d, 177.6 Hz, 3C, 8-C), 134.3 (d, 205.7 Hz, 3C, 8-C), 234.2 (d, 158.9 Hz, 3C, 3C, 4-C), 359.1 (3C, 2-C), 398.1 (3C, 6-C) ppm
^{19}F-NMR (659.0 MHz, CD_3CN): δ = 158.4 (3F) ppm.
MS (ESI in MeCN): m\z 539.0904 (for $C_{27}H_{18}F_3FeN_6$ calc. 539.0894).
IR (ATR, [cm^{-1}]): 3151w, 3153w, 3083w, 3037w, 2663w, 2320w, 1830w, 1756w, 1710w, 1591m, 1562m, 1508m, 1469s, 1421s, 1404s, 1332m, 1265m, 1240m, 1176s, 1110m, 1066m, 1041m, 1016m, 960m, 873m, 850m, 838m, 792s, 746s, 713m, 659m, 619m, 607m, 574m, 526m, 445m.

[Fe^{IV}(Fppz)$_3$]PF$_6$ and [Fe^{II}(Fppz)$_3$]Na were not synthesized during the course of this thesis.

Tris(1-(4-methoxyphenyl)pyrazolato-*N*,*C*^{2})iron(III)

Complex synthesis followed method A and was obtained as red powder (2.65%).

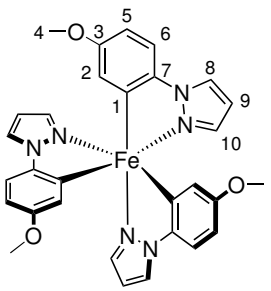

Fe(MeOppz)$_3$

Fe^{III}(MeOppz)$_3$
^{1}H-NMR (700.38 MHz, CD_3CN): δ = -79.93 (s, 3H, 2-H), -10.34 (s, 3H, 10-H), -5.36 (s, 3H, 6-H), -5.12 (s, 3H, 5-H), -3.19 (s, 3H, 9-H), 1.44 (s, 9H, 4-H), 12.06 (s, 3H, 8-H) ppm.
^{13}C{^{1}H}-NMR (176.1 MHz, CD_3CN): δ = -106.1 (3C, 156.6 Hz, 6-C), -93.0 (3C, 3-C), 49.1 (3C, 139.07 Hz, 4-C), 103.9 (3C, 182.9 Hz, 8-C), 114.1 (3C, 191.7 Hz, 9-C) 130.1 (3C, 182.9 Hz, 10-C), 232.4 (3C, 159.9 Hz, 5-C), 360.8 (3C, 129.6 Hz, 2-C), 403.2 (3C, 7-C) ppm.

^{15}N-NMR (70.96 MHz, CD_3CN): δ = 80.2 (N2) ppm.
MS (ESI in MeCN): m\z 575.1530 (for $C_{30}H_{27}FeN_6O_3$ calc. 575.1494).
Elemental analysis: calc. for $C_{30}H_{27}FeN_6O_3$: C: 62.62%, H: 4.73%, N: 14.61%, found: C:62.49%, H: 5.19%, N: 14.35%.

[Fe^{IV}(MeOppz)$_3$]PF$_6$
^{1}H-NMR (700.38 MHz, CD_3CN): δ = -192.10 (s, 3H, 2-H), -82.29 (s, 3H, 5-H), -48.29 (s, 3H, 6-H), -33.34 (s, 3H, 8-H), -30.47 (s, 3H, 10-H), -4.45 (s, 3H, 9-H), 1.99 (d, 9H, 4-H) ppm.
^{13}C{^{1}H}-NMR (176.1 MHz, CD_3CN): δ = -756.2 (3C, 3-C), -702.5 (d, 162.8 Hz, 3C, 6-C), 29.5 (d, 182.9, 3C, 9-C), 40.0 (3C, 4-C), 286.9 (d, 189.59 Hz, 3C, 8-C), 416.5 (d, 188.6 Hz, 3C, 10-C), 428.6, (d, 160.27 Hz, 3C, 2-C), 635.7 (d, 162.57 Hz, 3C, 5-C), 681.2 (3C, 7-C) ppm.
The nitrogen atoms could not be detected.

***mer*-[Fe^{II}(MeOppz)$_3$]Na**
^{1}H-NMR (700.38 MHz, THF-d_8): δ = 6.03 (s, 3H, 9^3-H). 6.04 (s, 3H, 9^2-H) 6.08 (d, $^3J_{HH}$ = 7.12 Hz, 3H, 5^3-H), 6.17 (dd, $^3J_{HH}$ = 10.90 Hz, $^2J_{HH}$ = 2.81 Hz, 3H, 5^2-H), 6.21 (t, $^3J_{HH}$ = 1.71 Hz, 3H, 9^1-H), 6.24 (s, 3H, 10^3-H), 6.31 (d, $^3J_{HH}$ = 2.25 Hz, 3H, 2^3-H), 6.32 (d, $^3J_{HH}$ = 2.24 Hz, 3H, 5^1-H), 6.83 (s, 3H, 2^2-H), 6.73 (s, 3H, 10^2-H), 7,00 (s, 3H, 2^1-H), 7.02 (d, $^3J_{HH}$ = 8.20 Hz, 3H, 6^3-H), 7.07 (s, 3H, 10^1-H), 7.08 (d, 3H, 6^2-H), 7.22 (d, $^3J_{HH}$ = 8.21 Hz, 3H, 6^1-H), 7.95 (d, $^3J_{HH}$ = 2.32 Hz, 3H, 8^3-H), 8.05 (d, $^3J_{HH}$ = 2.26 Hz, 3H, 8^2-H), 8.12 (d, $^3J_{HH}$ = 2.06 Hz, 3H, 8^1-H) ppm.
^{13}C-NMR (176.1 MHz, THF-d_8): δ = 54.7 (3C, 4^3-C), 55.04 (3C, 4^2-C), 55.2 (3C, 4^1-C), 101.7 (3C, 5^3-C), 103.6 (3C, 5^1-C), 104.6 (3C, 5^2-C), 106.7 (3C, 9^1-C), 107.1 (3C, 9^3-C), 107.7 (3C, 9^2-C), 108.9 (3C, 6^2-C), 108.8 (3C, 6^3-C), 109.3 (3C, 6^2-C), 121.3 (3C, 8^3-C), 122.6 (3C, 8^2-C), 122.8 (3C, 2^3-C), 123.3 (3C, 8^1-C), 124.3 (3C, 2^2-C), 124.4 (3C, 1^3-C), 127.1 (3C, 1^2-C), 129.2 (3C, 1^1-C), 129.3 (3C, 2^1-C), 137.0 (3C, 7^3-C), 140.9 (3C, 10^3-C), 141.3 (3C, 10^1-C), 141.4 (3C, 7^1-C), 143.22 (3C, 10^2-C), 143.4 (3C, 7^2-C), 156.9 (3C, 3^2-C), 157.1 (3C, 3^3-C), 157.9 (3C, 3^1-C) ppm.
^{15}N-NMR (70.96 MHz, THF-d_8): δ = 242.5 (N1^3), 242.6 (N1^2), 246.7 (N1^3), 246.7 (N2^2), 248.2 (N2^1), 248.4 (N2^3) ppm.

Tris(3-methyl-1-phenylpyrazolato-N,C^2)iron(III)

Complex synthesis followed method B and was obtained yellowish-red product (48.1%)

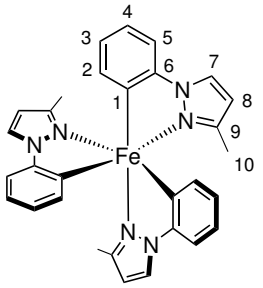

Fe(3Me-ppz)$_3$

Fe^{III}(3Me-ppz)$_3$

^{1}H-NMR (700.38 MHz, CD^{3}CN): δ =-72.28 (s, 3H, 2-H), -12.42 (s, 9H, 10-H), -6.39 (s, 3H, 4-H), -2.31 (s, 3H, 8-H), -0.58 (s, 3H, 5-H), 3.41 (s, 3H, 3-H), 13.50 (s, 3H,7-H) ppm.
^{13}C{^{1}H}-NMR (176.1 MHz, CD_3CN): δ = -121.7 (d, 189.1 Hz, 3C, 3-C), -77.5 (d, 139.4 Hz, 3C, 5-C), 7.6 (d, 129.4 Hz, 3C, 10-H), 89.3 (d, 179.2 Hz, 3C, 7-C), 213.8 (d, 179.2 Hz, 3C, 8-C), 163.2 (3C, 9-C), 238.6 (d, 159.3 Hz, 3C, 4-C), 278.7 (3C, 2-C), 377.2 (3C, 6-C) ppm.
MS (ESI in MeCN): m\z 527.1625 (for $C_{30}H_{27}FeN_6$ calc. 527.1647).
Elemental analysis: calc. for $C_{30}H_{27}FeN_6$: C: 52.27%, H: 2.63%, N: 12.19%, found: C: 51.90%, H: 2.81%, N: 12.12%.
IR (ATR, [cm^{-1}]): 3141w, 3120w, 3045w, 1573w, 1556w, 1513m, 1458w, 1438m, 1375m, 1357m, 1272m, 1232m, 1155w, 1114w, 1083w, 1051m, 1010m, 950m, 927m, 846w, 744s, 713s, 659m, 644m, 619m, 514m.

[Fe^{IV}(3Me-ppz)$_3$]PF_6

^{1}H-NMR (700.38 MHz, CD_3CN): δ = -137.77 (s, 3H, 2-H), -72.16 (s, 3H, 4-H), -34.07 (s, 3H, 5-H), -29.03 (s, 3H, 7-H), -6.64 (s, 9H, 4-H), -0.65 (d, $^3J_{HH}$ = 5.6 Hz, 3H, 8-H), 39.63 (s, 3H, 3-H) ppm.
^{13}C{^{1}H}-NMR (176.1 MHz, CD_3CN): δ = -660.8 (d, 151.5 Hz, 1C, 3-C), -553.8 (d, 170.9 Hz, 3C, 5-C), -41.3 (d, 137.3 Hz, 3C, 10-C), 64.8 (d, 190,8 Hz, 3C, 8-C), 197.1 (d, 201.4 Hz, 3C, 7-C), 336.7 (d, 169.6, 3C, 2-C), 483.6 (3C, 9-C), 555.5 (d, 169.6, 3C, 4-C), 621.2 (3C, 6-C) ppm.

mer-[Fe^{II}(3Me-ppz)$_3$]Na

^{1}H-NMR (700.38 MHz, THF-d8): δ = 1.25 (s, 3H, 10^1-H), 1.34 (s, 3H, 10^2-H), 1.74 (s, 3H, 10^3-H), 5.79 (d, $^3J_{HH}$ = 2.3 Hz, 1H, 8^3-H), 5.82 (d, $^3J_{HH}$ = 2.3 Hz, 1H, 8^2-H), 5.98 (d, $^3J_{HH}$ = 2.2 Hz, 1H, 8^1-H), 6.28 (d, $^3J_{HH}$ = 6.7 Hz, 1H, phenyl), 6.46 (m, 3H, phenyl), 6.57 (t, $^3J_{HH}$ = 6.8 Hz, 1H, phenyl), 6.67 (m, 2H, phenyl), 6.96 (m, 2H, phenyl), 7.17 (m, 4H, phenyl), 7.92 (d, $^3J_{HH}$ = 2.4 Hz, 1H, 7^3-H), 8.13 (d, $^3J_{HH}$ = 2.3 Hz, 1H, 7^2-H), 8.23 (d, $^3J_{HH}$ = 2.2 Hz, 1H, 7^1-H) ppm.
^{13}C-NMR (176.1 MHz, THF-d$_8$): δ = 12.01, (1C, 10^3-C), 13.9 (1C, 10^2-C), 15.1 (1C, 10^1-C), 107.9 (1C, 8^3-C), 108.1 (1C, 9^2-C), 108.5 (1C, phenyl), 108.8 (1C, 9^1-C), 108.9 (1C, phenyl), 109.0 (1C, phenyl), 109.2 (1C, phenyl), 114.2 (1C, phenyl), 116.1 (1C, phenyl), 118.5 (1C, phenyl), 121.5 (7^3-C), 122.9 (1C, 7^2-C), 122.9 (1C, 7^1-C), 123.1 (1C, phenyl), 123.5 (1C, phenyl), 123.8 (1C, phenyl), 138.2 (1C, phenyl), 140.0 (1C, phenyl), 141.6 (1C, phenyl), 146.1 (1C, phenyl), 150.3 (1C, phenyl), 150.3 (1C, phenyl), 150.3 (1C, phenyl), 150.4 (1C, phenyl), 150.7 (1C, phenyl), 152.7 (1C, phenyl), 153.6

(1C, phenyl) ppm.
^{15}N-NMR (70.96 MHz, THF-d_8): δ = 239.7 ($N1^3$), 239.8 ($N2^3$), 244.0 ($N1^2$), 244.3 ($N2^2$), 245.9($N1^1$), 246.1 ($N2^1$) ppm.

Tris(1-(([1,1'-biphenyl])-4-yl)phenyl)pyrazolato-*N*,C^2)iron(III)

Complex synthesis followed method A and was obtained as red powder (3.97%).

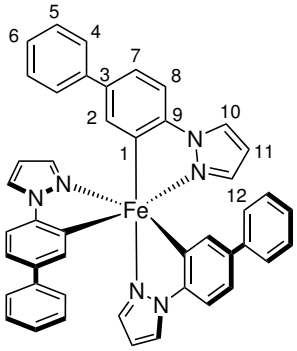

Fe(bppz)$_3$

Fe^{III}(bppz)$_3$
^{1}H-NMR (700.38 MHz, CD_3CN): δ = -77.61 (1s, 3H, 2-H), -10.18 (s, 1H, 13-H), -4.64 (s, 3H, 8-H), -3.21 (s, 3H, 12-H), -1.74 (s, 3H, 9-H), 5.39 (d, $^3J_{HH}$ = 8.19 Hz, 6H, 5,5´-H), 5.75 (t, $^3J_{HH}$ = 7.60 Hz, 6H, 6,6´-H), 7.10 (t, $^3J_{HH}$ = 7.14 Hz, 3H, 6-H), 11.84 (s, 3H, 11-H) ppm).
^{13}C{^{1}H}-NMR (176.1 MHz, CD_3CN): δ = -77.9 (3C, 9-C), -75.8 (3C, 3-C), 106.5 (3C, 11-C), 114.7 (3C, 12-C), 114.8 (6C, 5,5´-C), 123.1 (3C, 7-C), 130.9 (6C, 6,6´-C), 133.8 (3C, 13-C), 154.1 (3C, 4-C), 240.6 (3C, 8-C), 365.7 (3C, 2-C), 392.5 (3C, 10-C) ppm.
MS (ESI in MeCN): m\z 713.2150 (for $C_{45}H_{33}FeN_6$ calc. 713.6460).
Elemental Analysis: calc. for $C_{45}H_{33}FeN_6$: C: 75.74%, H: 4.66%, N: 11.78%, found: C: 71.15%, H: 4.84%, N: 10.78%.
IR (ATR, [cm^{-1}]): 3108w, 3056w, 3020w, 1598w, 1564w, 1502w, 1465m, 1400m, 1373w, 1330w, 1261m, 1112w, 1064m, 1047m, 1016w, 958w, 916w, 894w, 808s, 757s, 734s, 694s, 663w, 649w, 607w.

[Fe^{IV}(bppz)$_3$]PF$_6$
^{1}H-NMR (700.38 MHz, CD_3CN): δ = -198.19 (1s, 3H, 2-H), -81.01 (s, 3H, 8-H), -3.05 (s, 3H, 12-H), -39.16 (s, 3H, 9-H), -36.52 (s, 3H, 11-H), -34.22 (s, 3H, 13-H), 9.21/8.56 (d, 6H, 5,5´-H), 9.75 (d, $^3J_{HH}$ = 7.14 Hz, 3H, 6-H), 9.99 (t, $^3J_{HH}$ = 6.67 Hz, 6H, 7,7´-H), ppm.
^{13}C- and ^{15}N-signals could not be assigned, due to poor solubility in several solvents.

***mer*-[Fe^{II}(bppz)$_3$]Na** could not be achieved.

Tris(1-(naphthalen-2-yl)pyrazolato-N,C^2)iron(III)

Complex synthesis followed method A and was obtained as red powder (5.31%).

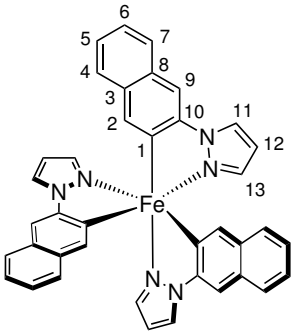

Fe(naphpz)$_3$

Fe^{III}(naphpz)$_3$
^{1}H-NMR (700.38 MHz, DMSO-d$_6$): δ = -85.19 (s, 3H, 2-H), -12.51 (s, 3H, 13-H), -1.68 (d, $^3J_{HH}$ = 6.3 Hz, 3H, 4-H), -1.31 (s, 3H, 12-H), 1.10 (s, 3H, 9-H), 1.25 (t, $^3J_{HH}$ = 7.10 Hz, 3H, 6-H), 8.12 (t, $^3J_{HH}$ = 6.30 Hz, 3H, 5-H), 11.15 (s, 3H, 11-H), 12.83 (d, $^3J_{HH}$ = 8.50 Hz, 3H, 7-H) ppm.
^{13}C{^{1}H}-NMR (176.1 MHz, DMSO-d$_6$): δ = -97.6 (3C, 3-C), -56.79 (d, 150.66 Hz, 3C, 9-C), 80.3 (d, 150.66 Hz, 3C, 7-C), 81.6 (d, 160.34 Hz, 3C, 5-C), 99.4 (d, 180.91 Hz, 3C, 12-C), 124.3 (d, 188.74 Hz, 6C, 11-C), 126.6 (d, 88.74 Hz, 3C, 13-C), 3C, 172.1 (d, 157.98 Hz, 6C, 6-C), 180.5 (d, 157.98 Hz, 3C, 4-C), 216.3 (3C, 8-C), 365.3 (3C, 2-C), 413.9 (3C, 10-C) ppm.
MS (ESI in MeCN): m\z 635.1640 (for $C_{39}H_{27}FeN_6$ calc. 635.1647).
Elemental Analysis: calc. for $C_{39}H_{27}FeN_6$: C: 73.71%, H: 4.28%, N: 13.22%, found: C: 74.29%, H: 5.10%, N: 12.42%.
IR (ATR, [cm^{-1}]): 3126w, 6047w, 2917w, 2854w, 1585w, 1593w, 1560w, 1510w, 1486w, 1459m, 1405m, 1332w, 1313w, 1251w, 1197w, 1134w, 1107w, 1062m, 1037w, 977w, 935w, 889w, 856m, 831w, 736s, 682w, 651w.

[Fe^{IV}(naphpz)$_3$]PF$_6$
^{1}H-NMR (700.38 MHz, DMSO-d$_6$): δ = -250.70 (s, 3H, 2-H), -38.75 (s, 3H, 6-H), -33.81 (s, 3H, 9-H), -28.05 (s, 3H, 13-H), -27.43 (s, 3H, 4-H), -24.50 (s, 3H, 11-H), -1.07 (s, 3H, 12-H), 18.41 (s, 3H, 5-H), 26.12 (s, 3H, 7-H) ppm.
^{13}C{^{1}H}-NMR (176.1 MHz, DMSO-d$_6$): δ = -776.0 (3C, 3-C), -455.9 (3C, 9-C), -116.9 (d, 158.1 Hz, 3C, 7-C), -103.2 (d, 157.3 Hz, 3C, 5-C), 46.5 (d, 184.5 Hz, 3C, 12-C), 271.7 (d, 204.69 Hz, 3C, 11-C), 356.3 (d, 211.3 Hz, 3C, 13-C), 367.9 (d, 156.2 Hz, 3C, 4-C), 379.5 (d, 156.2 Hz, 3C, 6-C), 464.4 (3C, 8-C), 482.3 (3C, 10-C), 679.8 (3C, 2-C) ppm.

***mer*-[Fe^{II}(naphpz)$_3$]Na** could not be achieved.

Bibliography

[1] K. E. Trenberth, J. T. Dasullo, Shepherd, Theodore G., *Nat. Clim. Change* **2015**, *5*, 725–730.

[2] D. I. Armstrong McKay, A. Staal, J. F. Abrams, R. Winkelmann, B. Sakschewski, S. Loriani, I. Fetzer, S. E. Cornell, J. Rockström, T. M. Lenton, *Science* **2022**, *377*.

[3] M. A. Waqas, *Science* **2022**, *378*, 482.

[4] B. Ayugi, E. O. Eresanya, A. O. Onyango, F. K. Ogou, E. C. Okoro, C. O. Okoye, C. M. Anoruo, V. N. Dike, O. R. Ashiru, M. T. Daramola, R. Mumo, V. Ongoma, *Pure and applied geophysics* **2022**, *179*, 1365–1386.

[5] N. Watts, W. N. Adger, P. Agnolucci, J. Blackstock, P. Byass, W. Cai, S. Chaytor, T. Colbourn, M. Collins, A. Cooper, P. M. Cox, J. Depledge, P. Drummond, P. Ekins, V. Galaz, D. Grace, H. Graham, M. Grubb, A. Haines, I. Hamilton, A. Hunter, X. Jiang, M. Li, I. Kelman, L. Liang, M. Lott, R. Lowe, Y. Luo, G. Mace, M. Maslin, M. Nilsson, T. Oreszczyn, S. Pye, T. Quinn, M. Svensdotter, S. Venevsky, K. Warner, B. Xu, J. Yang, Y. Yin, C. Yu, Q. Zhang, P. Gong, H. Montgomery, A. Costello, *Lancet* **2015**, *386*, 1861–1914.

[6] A. Haines, J. A. Patz, *JAMA* **2004**, *291*, 99–103.

[7] R. S. J. Tol, *Review of Environmental Economics and Policy* **2018**, *12*, 4–25.

[8] Masson-Delmotte, V., P. Zhai, A. Pirani, S.L. Connors, C. Péan, S. Berger, N. Caud, Y. Chen, L. Goldfarb, M.I. Gomis, M. Huang, K. Leitzell, E. Lonnoy, J.B.R. Matthews, T.K. Maycock, T. Waterfield, O. Yelekçi, R. Yu, and B. Zhou **2023**, 2391 pp.

[9] UNEP, UNEP Copenhagen Climate Centre, *The heat is on: A world of climate promises not yet delivered*, Vol. 2021 of *The emissions gap report*, United Nations Environment Programme, Nairobi, **2021**.

[10] S. Jenkins, C. Smith, M. Allen, R. Grainger, *Nat. Clim. Change* **2023**, *13*, 127–129.

[11] EPA-2023, *Inventory of U.S. Greenhouse Gas Emissions and Sinks: 1990-2021. U.S. Environmental Protection 9 Agency*, **2023**.

[12] BP, *Statistical Review of World Energy 2022*, London, United Kingdom, **2021**.

[13] S. Wegner, F. Mersmann, M. Gutieerrez Grados, *Climate Transparency transport - G20 Response to the Energy Crisis*, **2022**.

[14] B. P. Heard, B. W. Brook, T. Wigley, C. Bradshaw, *Renew. Sust. Energ. Rev.* **2017**, *76*, 1122–1133.

[15] N. L. Panwar, S. C. Kaushik, S. Kothari, *Renew. Sust. Energ. Rev.* **2011**, *15*, 1513–1524.

[16] M. Thirugnanasambandam, S. Iniyan, R. Goic, *Renew. Sust. Energ. Rev.* **2010**, *14*, 312–322.

[17] Federal Ministry for Economic Affairs and Energy Public Relations Division, *The National Hydrogen Strategy*, Berlin, **2020**.

[18] W. Grochala, *Nat. Chem.* **2015**, *7*, 264.

[19] P. Nikolaidis, A. Poullikkas, *Renew. Sust. Energ. Rev.* **2017**, *67*, 597–611.

[20] A. F. Holleman, N. Wiberg, E. Wiberg, *Lehrbuch der Anorganischen Chemie*, Walter de Gruyter, **2007**.

[21] R. W. Howarth, M. Z. Jacobson, *Energy Sci. Eng.* **2021**, *9*, 1676–1687.

[22] T. I. Korányi, M. Németh, A. Beck, A. Horváth, *Energies* **2022**, *15*, 6342.

[23] P. Spath, M. Mann, *Life cycle assessment of hydrogen production via natural gas steam reforming- technical report NREL/TP-570-27637*, Colorado, United States, **2000**.

[24] I. Dincer, *International Journal of Hydrogen Energy* **2012**, *37*, 1954–1971.

[25] R. Kothari, D. Buddhi, R. L. Sawhney, *IJGEI* **2004**, *21*, 154.

[26] S. Fankhauser, S. M. Smith, M. Allen, K. Axelsson, T. Hale, C. Hepburn, J. M. Kendall, R. Khosla, J. Lezaun, E. Mitchell-Larson, M. Obersteiner, L. Rajamani, R. Rickaby, N. Seddon, T. Wetzer, *Nat. Clim. Change* **2022**, *12*, 15–21.

[27] M. Nasser, T. F. Megahed, S. Ookawara, H. Hassan, *Environ. Sci. Pollut. Res.* **2022**, *29*, 86994–87018.

[28] R. Raman, V. K. Nair, V. Prakash, A. Patwardhan, P. Nedungadi, *Energy Rep.* **2022**, *8*, 9242–9260.

[29] K. Villa, J. R. Galán-Mascarós, N. López, E. Palomares, *Sustain. Energy Fuels* **2021**, *5*, 4560–4569.

[30] J. H. Golbeck, *BBA* **1987**, *895*, 167–204.

[31] D. J. Vinyard, G. W. Brudvig, *Annu. Rev. Phys. Chem.* **2017**, *68*, 101–116.

[32] J. M. Berg, J. L. Tymoczko, G. J. Gatto jr., L. Stryer (Eds.), *Stryer Biochemie 8th ed.*, Springer Berlin Heidelberg, Berlin, Heidelberg, **2018**.

[33] C. Acar, I. Dincer, G. F. Naterer, *Int. J. Energy Res.* **2016**, *40*, 1449–1473.

[34] S. Sharma, S. K. Ghoshal, *Renew. Sust. Energ. Rev.* **2015**, *43*, 1151–1158.

[35] C. Kranz, M. Wächtler, *Chem. Soc. Rev.* **2021**, *50*, 1407–1437.

[36] S. Kaufhold, K. Wärnmark, *Catalysts* **2020**, *10*, 132.

[37] M. Dorn, N. R. East, C. Förster, W. R. Kitzmann, J. Moll, F. Reichenauer, T. Reuter, L. Stein, K. Heinze, *Inorg. Chem. Commun.* **2023**, 707–788.

[38] A. Fujishima, K. Honda, *Nature* **1972**, *238*, 37–38.

[39] D. C. Fabry, J. Zoller, M. Rueping, *Org. Chem. Front.* **2019**, *6*, 2635–2639.

[40] P. Chowdhury, G. Malekshoar, A. Ray, *Inorganics* **2017**, *5*, 34.

[41] S. Fukuzumi, D. Hong, Y. Yamada, *J. Phys. Chem. Lett.* **2013**, *4*, 3458–3467.

[42] S. Chen, T. Takata, K. Domen, *Nat. Rev. Mater.* **2017**, *2*.

[43] B. Zhang, L. Sun, *Chem. Soc. Rev.* **2019**, *48*, 2216–2264.

[44] P. W. Atkins, J. de Paula (Eds.), *Physikalische Chemie 4th ed.*, Wiley-VCH, Weinheim, **2006**.

[45] C. K. Prier, D. A. Rankic, D. W. C. MacMillan, *Chem. Rev.* **2013**, *113*, 5322–5363.

[46] J. I. Goldsmith, W. R. Hudson, M. S. Lowry, T. H. Anderson, S. Bernhard, *J. Am. Chem. Soc.* **2005**, *127*, 7502–7510.

[47] J. I. Day, K. Teegardin, J. Weaver, J. Chan, *OPR&D* **2016**, *20*, 1156–1163.

[48] J.-P. Sauvage, J.-P. Collin, J.-C. Chambron, S. Gullirez, C. Coudret, V. Balzani, F. Barigelletti, L. de Cola, L. Flamigni, *Chem. Rev.* **1994**, *25*, 993–1019.

[49] N. H. Damrauer, G. Cerullo, A. Yeh, T. R. Boussie, C. V. Shank, J. K. McCusker, *Science* **1997**, *275*, 54–57.

[50] J. K. McCusker, *Science* **2019**, *363*, 484–488.

[51] P. Dierks, Y. Vukadinovic, M. Bauer, *Inorg. Chem. Front.* **2022**, *9*, 206–220.

[52] Z. E. Gagnon, C. Newkirk, S. Hicks, *J. Environ. Health* **2006**, *41*, 397–414.

[53] J. Corredor, M. J. Rivero, C. M. Rangel, F. Gloaguen, I. Ortiz, *J. Chem. Technol. Biot.* **2019**.

[54] K. S. Egorova, V. P. Ananikov, *Organometallics* **2017**, *36*, 4071–4090.

[55] D. W. Fink, W. E. Ohnesorge, *J. Am. Chem. Soc.* **1969**, *91*, 4995–4998.

[56] L. L. Jamula, A. M. Brown, D. Guo, J. K. McCusker, *Inorg. Chem* **2014**, *53*, 15–17.

[57] Y. Liu, T. Harlang, S. E. Canton, P. Chábera, K. Suárez-Alcántara, A. Fleckhaus, D. A. Vithanage, E. Göransson, A. Corani, R. Lomoth, V. Sundström, K. Wärnmark, *ChemComm.* **2013**, *49*, 6412–6414.

[58] C. Förster, K. Heinze, *Chem. Soc. Rev.* **2020**.

[59] O. S. Wenger, *Chem. Eur. J.* **2019**, *25*, 6043–6052.

[60] A. K. C. Mengel, C. Förster, A. Breivogel, K. Mack, J. R. Ochsmann, F. Laquai, V. Ksenofontov, K. Heinze, *Chem. Eur. J.* **2015**, *21*, 704–714.

[61] J. Moll, C. Wang, A. Päpcke, C. Förster, U. Resch-Genger, S. Lochbrunner, K. Heinze, *Chem. Eur. J.* **2020**, *26*, 6820–6832.

[62] C. Förster, M. Dorn, T. Reuter, S. Otto, G. Davarci, T. Reich, L. Carrella, E. Rentschler, K. Heinze, *Inorganics* **2018**, *6*, 86.

[63] M. Darari, A. Francés-Monerris, B. Marekha, A. Doudouh, E. Wenger, A. Monari, S. Haacke, P. C. Gros, *Molecules* **2020**, *25*.

[64] L. Liu, T. Duchanois, T. Etienne, A. Monari, M. Beley, X. Assfeld, S. Haacke, P. C. Gros, *PCCP* **2016**, *18*, 12550–12556.

[65] P. Zimmer, L. Burkhardt, A. Friedrich, J. Steube, A. Neuba, R. Schepper, P. Müller, U. Flörke, M. Huber, S. Lochbrunner, M. Bauer, *Inorg. Chem.* **2018**, *57*, 360–373.

[66] Y. Liu, P. Persson, V. Sundström, K. Wärnmark, *Acc. Chem. Res.* **2016**, *49*, 1477–1485.

[67] T. Duchanois, T. Etienne, C. Cebrián, L. Liu, A. Monari, M. Beley, X. Assfeld, S. Haacke, P. C. Gros, *Chem. Ber.* **2015**, *2015*, 2469–2477.

[68] T. C. B. Harlang, Y. Liu, O. Gordivska, L. A. Fredin, C. S. Ponseca, P. Huang, P. Chábera, K. S. Kjaer, H. Mateos, J. Uhlig, R. Lomoth, R. Wallenberg, S. Styring, P. Persson, V. Sundström, K. Wärnmark, *Nat. Chem.* **2015**, *7*, 883–889.

[69] L. A. Fredin, K. Wärnmark, V. Sundström, P. Persson, *ChemSusChem* **2016**, *9*, 667–675.

[70] I. M. Dixon, F. Alary, M. Boggio-Pasqua, J.-L. Heully, *Dalton Trans.* **2015**, *44*, 13498–13503.

[71] S. Mukherjee, D. E. Torres, E. Jakubikova, *Chemical Science* **2017**, *8*, 8115–8126.

[72] D. C. Ashley, S. Mukherjee, E. Jakubikova, *Dalton Trans.* **2019**, *48*, 374–378.

[73] I. M. Dixon, F. Alary, M. Boggio-Pasqua, J.-L. Heully, *Inorg. Chem* **2013**, *52*, 13369–13374.

[74] J. Steube, L. Burkhardt, A. Päpcke, J. Moll, P. Zimmer, R. Schoch, C. Wölper, K. Heinze, S. Lochbrunner, M. Bauer, *Chem. Eur. J.* **2019**, *25*, 11826–11830.

[75] Y. Liu, K. S. Kjaer, L. A. Fredin, P. Chábera, T. Harlang, S. E. Canton, S. Lidin, J. Zhang, R. Lomoth, K.-E. Bergquist, P. Persson, K. Wärnmark, V. Sundström, *Chem. Eur. J.* **2015**, *21*, 3628–3639.

[76] P. Chábera, Y. Liu, O. Prakash, E. Thyrhaug, A. E. Nahhas, A. Honarfar, S. Essén, L. A. Fredin, T. C. B. Harlang, K. S. Kjær, K. Handrup, F. Ericson, H. Tatsuno, K. Morgan, J. Schnadt, L. Häggström, T. Ericsson, A. Sobkowiak, S. Lidin, P. Huang, S. Styring, J. Uhlig, J. Bendix, R. Lomoth, V. Sundström, P. Persson, K. Wärnmark, *Nature* **2017**, *543*, 695–699.

[77] K. S. Kjær, N. Kaul, O. Prakash, P. Chábera, N. W. Rosemann, A. Honarfar, O. Gordivska, L. A. Fredin, K.-E. Bergquist, L. Häggström, T. Ericsson, L. Lindh, A. Yartsev, S. Styring, P. Huang, J. Uhlig, J. Bendix, D. Strand, V. Sundström, P. Persson, R. Lomoth, K. Wärnmark, *Science* **2019**, *363*, 249–253.

[78] N. Kaul, R. Lomoth, *J. Am. Chem. Soc.* **2021**.

[79] H. Drevs, *Z. Anorg. Allg. Chem.* **1979**, *19*, 31–32.

[80] H. Drevs, *Z. Anorg. Allg. Chem.* **1991**, *605*, 145–150.

[81] E. J. Nam, J. H. Kim, B.-O. Kim, S. M. Kim, N. G. Park, Y. S. Kim, Y. K. Kim, Y. Ha, *Bull. Chem. Soc. Jpn.* **2004**, *77*, 751–755.

[82] A. B. Tamayo, B. D. Alleyne, P. I. Djurovich, S. Lamansky, I. Tsyba, N. N. Ho, R. Bau, M. E. Thompson, *J. Am. Chem. Soc.* **2003**, *125*, 7377–7387.

[83] W. R. Browne, D. Hesek, J. F. Gallagher, C. M. O'Connor, J. S. Killeen, F. Aoki, H. Ishida, Y. Inoue, C. Villani, J. G. Vos, *Dalton Trans.* **2003**, 2597.

[84] K. Magra, E. Domenichini, A. Francés-Monerris, C. Cebrián, M. Beley, M. Darari, M. Pastore, A. Monari, X. Assfeld, S. Haacke, P. C. Gros, *Inorg. Chem.* **2019**, *58*, 5069–5081.

[85] S. Peruncheralathan, A. K. Yadav, H. Ila, H. Junjappa, *J. Org. Chem.* **2005**, *70*, 9644–9647.

[86] Q. Yang, Y. Wang, D. Lin, M. Zhang, *Tetrahedron Lett.* **2013**, *54*, 1994–1997.

[87] H.-J. Cristau, P. P. Cellier, J.-F. Spindler, M. Taillefer, *Chem. Eur. J.* **2004**, *10*, 5607–5622.

[88] H.-J. Cristau, P. P. Cellier, J.-F. Spindler, M. Taillefer, *Eur. J. Org. Chem.* **2004**, *2004*, 695–709.

[89] K. P. C. Vollhardt, N. E. Schore, H. Butenschön, B. Elvers, *Organische Chemie 4th ed.*, Wiley-VCH, Weinheim, **2005**.

[90] James W. Pavlik, Robert E. Connors, Douglas S. Burns, Edyth M. Kurzweil, J. W. Pavlik, R. E. Connors, D. S. Burns, E. M. Kurzweil, *J. Am. Chem. Soc.* **1993**, *115*, 7645–7652.

[91] G. Löbbert, *Ullmann's Encyclopedia of Industrial Chemistry* **2000**.

[92] I. Fabre, L. A. Perego, J. Bergès, I. Ciofini, L. Grimaud, M. Taillefer, *Eur. J. Org. Chem.* **2016**, *2016*, 5887–5896.

[93] F. Chevallier, Y. S. Halauko, C. Pecceu, I. F. Nassar, T. U. Dam, T. Roisnel, V. E. Matulis, O. A. Ivashkevich, F. Mongin, *OBC* **2011**, *9*, 4671–4684.

[94] A. Marxer, M. Siegrist, *Helv. Chim. Acta* **1974**, *57*, 1988–2000.

[95] T. Kauffmann, H. Lexy, *Angew. Chem.* **1978**, *90*, 804–805.

[96] S. D. Ittel, A. D. English, C. A. Tolman, J. P. Jesson, *Inorganica Chim. Acta* **1979**, *33*, 101–106.

[97] F. Cotton, R. L. Luck, K.-A. Son, *Inorganica Chim. Acta* **1991**, *179*, 11–15.

[98] X. Ren, B. D. Alleyne, P. I. Djurovich, C. Adachi, I. Tsyba, R. Bau, M. E. Thompson, *Inorg. Chem.* **2004**, *43*, 1697–1707.

[99] T. Hirschhausen, L. Fritsch, F. Lux, J. Steube, R. Schoch, A. Neuba, H. Egold, M. Bauer, *Inorganics* **2023**, *11*, 282.

[100] K. Teramoto, T. Kawasaki, T. Nishide, Y. Ikeda, *Acta Crystallogr.* **2015**, *71*, m8–9.

[101] S. Grimme, J. G. Brandenburg, C. Bannwarth, A. Hansen, *Chem. Phys.* **2015**, *143*, 054107.

[102] T.Hirschhausen, H. Egold, L. Fritsch, F. Lux, J. Steube, R. Schoch, M. Nowakowski, A. Velić, S. Demeshko, F. Meyer, and M. Bauer, *[Manuscript in preparation]* **2024**.

[103] Akira Naito, Tetsuo Asakura, Ichio Shimada, Kiyonori Takegoshi, Yasuhiko Yamamoto (Eds.), *Experimental Approaches of NMR Spectroscopy: Methodology and Application to Life Science and Materials Science 1st ed.*, Springer Singapore, Singapore, **2018**.

[104] I. Bertini, C. Luchinat, G. Parigi, E. Ravera, *NMR of Paramagnetic Molecules - Applications to Metallobiomolecules and Models 2nd ed.*, Vol. 2nd ed. of *Issn Ser*, Elsevier Science, Oxford, **2015**.

[105] A. J. Pell, G. Pintacuda, C. P. Grey, *Progress in nuclear magnetic resonance spectroscopy* **2019**, *111*, 1–271.

[106] P. B. Tsitovich, F. Gendron, A. Y. Nazarenko, B. N. Livesay, A. P. Lopez, M. P. Shores, J. Autschbach, J. R. Morrow, *Inorg. Chem.* **2018**, *57*, 8364–8374.

[107] E. Medina, C. Sandoval-Pauker, P. Salvador, B. Pinter, *Inorg. Chem* **2022**, *61*, 18923–18933.

[108] P. B. Tsitovich, J. M. Cox, J. B. Benedict, J. R. Morrow, *Inorg. Chem.* **2016**, *55*, 700–716.

[109] T. L. Davis, J. O. McLean, *Journal of the American Chemical Society* **1938**, *60*, 720–722.

[110] M. Lehr, T. Paschelke, E. Trumpf, A.-M. Vogt, C. Näther, F. D. Sönnichsen, A. J. McConnell, *Chem. Angew. Chem., Int. Ed.* **2020**, *59*, 19344–19351.

[111] F. H. Köhler, *eMagRes,* **2011**.

[112] A. J. McConnell, C. M. Aitchison, A. B. Grommet, J. R. Nitschke, *Journal of the American Chemical Society* **2017**, *139*, 6294–6297.

[113] H. Amouri, L. Mimassi, M. N. Rager, B. E. Mann, C. Guyard-Duhayon, L. Raehm, *Angewandte Chemie* **2005**, *117*, 4619–4622.

[114] I. Solomon, *Physical Review* **1955**, *99*, 559–565.

[115] W. Nam, *Acc. Chem. Res.* **2007**, *40*, 522–531.

[116] M. Newcomb, R. Zhang, R. E. P. Chandrasena, J. A. Halgrimson, J. H. Horner, T. M. Makris, S. G. Sligar, *Journal of the American Chemical Society* **2006**, *128*, 4580–4581.

[117] O. Prakash, P. Chábera, N. W. Rosemann, P. Huang, L. Häggström, T. Ericsson, D. Strand, P. Persson, J. Bendix, R. Lomoth, K. Wärnmark, *Chemistry (Weinheim an der Bergstrasse, Germany)* **2020**, *26*, 12728–12732.

[118] D. Nonaka, H. Wariishi, K. G. Welinder, H. Fujii, *Biochemistry* **2010**, *49*, 49–57.

[119] M. Swart, M. Costas **2015**, 409–434.

[120] P. Gütlich, *Zeitschrift fr anorganische und allgemeine Chemie* **2012**, *638*, 15–43.

[121] J. Steube, A. Kruse, O. S. Bokareva, T. Reuter, S. Demeshko, R. Schoch, M. A. Argüello Cordero, A. Krishna, S. Hohloch, F. Meyer, K. Heinze, O. Kühn, S. Lochbrunner, M. Bauer, *Nat. Chem.* **2023**, *15*, 468–474.

[122] B. P. Sullivan, D. J. Salmon, T. J. Meyer, J. Peedin, *Inorg. Chem* **1979**, *18*, 3369–3374.

[123] P. Chábera, L. Lindh, N. W. Rosemann, O. Prakash, J. Uhlig, A. Yartsev, K. Wärnmark, V. Sundström, P. Persson, *Coord. Chem. Rev.* **2021**, *426*, 213517.

[124] D. C. Ashley, E. Jakubikova, *Inorg. Chem* **2018**, *57*, 5585–5596.

[125] B. C. Paulus, S. L. Adelman, L. L. Jamula, J. K. McCusker, *Nature* **2020**, *582*, 214–218.

[126] V. Pace, P. Hoyos, L. Castoldi, P. Domínguez de María, A. R. Alcántara, *ChemSusChem* **2012**, *5*, 1369–1379.

[127] K. Eastham, P. A. Scattergood, D. Chu, R. Z. Boota, A. Soupart, F. Alary, I. M. Dixon, C. R. Rice, S. J. O. Hardman, P. I. P. Elliott, *Inorg. Chem* **2022**, *61*, 19907–19924.

[128] A. J. Atkins, M. Bauer, C. R. Jacob, *PCCP* **2013**, *15*, 8095–8105.

[129] L. Burkhardt, M. Holzwarth, B. Plietker, M. Bauer, *Inorg. Chem* **2017**, *56*, 13300–13310.

[130] A. J. Atkins, C. R. Jacob, M. Bauer, *Chem. Eur. J.* **2012**, *18*, 7021–7025.

[131] M. Bauer, *PCCP* **2014**, *16*, 13827–13837.

[132] P. Glatzel, U. Bergmann, *Coord. Chem. Rev.* **2005**, *249*, 65–95.

[133] U. Bergmann, P. Glatzel, *Photosynth. Res.* **2009**, *102*, 255–266.

[134] M. U. Delgado-Jaime, S. DeBeer, M. Bauer, *Chemistry* **2013**, *19*, 15888–15897.

[135] Y. A. Pankratova, Y. V. Nelyubina, V. V. Novikov, A. A. Pavlov, *Russ. J. Coord. Chem.* **2021**, *47*, 10–16.

[136] B. Weber, F. A. Walker, *Inorg. Chem.* **2007**, *46*, 6794–6803.

[137] S. Tretiakov, M. Lutz, C. J. Titus, F. de Groot, J. Nehrkorn, T. Lohmiller, K. Holldack, A. Schnegg, M. F. X. Tarrago, P. Zhang, S. Ye, D. Aleshin, A. Pavlov, V. Novikov, M.-E. Moret, *Inorg. Chem.* **2023**.

[138] T. Shibata, Y. Kanai, R. Nishimura, L. Xu, Y. Moritaka, A. Suzuki, S. Neya, M. Nakamura, Y. Yamamoto, *Inorganic chemistry* **2016**, *55*, 12128–12136.

[139] L. Banci, I. Bertini, C. Luchinat, R. Pierattelli, N. V. Shokhirev, F. A. Walker, *Journal of the American Chemical Society* **1998**, *120*, 8472–8479.

[140] E. N. Zapolotsky, S. P. Babailov, *J. Struct. Chem.* **2021**, *62*, 1740–1744.

[141] S. Mugiraneza, A. M. Hallas, *Commun. Phys.* **2022**, *5*.

[142] D. Y. Aleshin, R. Diego, L. A. Barrios, Y. V. Nelyubina, G. Aromí, V. V. Novikov, *Angew. Chem. Int. Ed. Engl.* **2022**, *61*, e202110310.

[143] R. Orbach, *Proc. R. Soc. Lond. A* **1961**, *264*, 458–484.

[144] S. G. McAdams, A.-M. Ariciu, A. K. Kostopoulos, J. P. Walsh, F. Tuna, *Coord. Chem. Rev.* **2017**, *346*, 216–239.

[145] D. L. Tierney, *J. Phys. Chem.* **2012**, *116*, 10959–10972.

[146] C. Rajnák, J. Titiš, R. Boča, *Magnetochemistry* **2021**, *7*, 76.

[147] Y. Vukadinovic, L. Burkhardt, A. Päpcke, A. Miletic, L. Fritsch, B. Altenburger, R. Schoch, A. Neuba, S. Lochbrunner, M. Bauer, *Inorganic chemistry* **2020**.

[148] W. L. F. Armarego, *Purification of laboratory chemicals eighth edition ed.*, Butterworth-Heinemann, Kidlington, Oxford, United Kingdom and Cambridge, MA, **2017**.

[149] G. R. Fulmer, A. J. M. Miller, N. H. Sherden, H. E. Gottlieb, A. Nudelman, B. M. Stoltz, J. E. Bercaw, K. I. Goldberg, *Organometallics* **2010**, *29*, 2176–2179.

[150] P. Y. Bruice, *Organische Chemie 5th ed.*, of *che - Chemie*, Pearson Studium, München and Boston and San Francisco and Harlow and Don Mills, Ontario and Sydney and Mexico City and Madrid and Amsterdam, **2007**.

[151] K. Cammann (Ed.), *Instrumentelle analytische Chemie: Verfahren, Anwendungen und Qualitätssicherung*, of *Spektrum Lehrbuch*, Spektrum Akademischer Verlag, Heidelberg, **2001**.

[152] C. Gauthier, V. A. Solé, R. Signorato, J. Goulon, E. Moguiline, *J. Synchrotron Rad.* **1999**, *6*, 164–166.

[153] H. H. Johann, *Z. Physik* **1931**, *69*, 185–206.

[154] F. Neese, *WIREs Comput. Mol. Sci.* **2012**, *2*, 73–78.

[155] V. N. Staroverov, G. E. Scuseria, J. Tao, J. P. Perdew, *Chem. Phys.* **2003**, *119*, 12129–12137.

[156] F. Weigend, R. Ahlrichs, *Physical chemistry chemical physics : PCCP* **2005**, *7*, 3297–3305.

[157] F. Neese, F. Wennmohs, A. Hansen, U. Becker, *Chem. Phys.* **2009**, *356*, 98–109.

[158] M. Cossi, N. Rega, G. Scalmani, V. Barone, *J. Comput. Chem.* **2003**, *24*, 669–681.

[159] F. Neese, *Inorganica Chim. Acta* **2002**, *337*, 181–192.

[160] M. U. Delgado-Jaime, S. DeBeer, *J. Comput. Chem.* **2012**, *33*, 2180–2185.

[161] G. Knizia, J. E. M. N. Klein, *Angew. Chem. Int. Ed. Engl.* **2015**, *54*, 5518–5522.

List of Figures

1.1 Observed global mean surface temperature change 4
1.2 Primary energy consumption for electricity generation by source 5
1.3 Hydrogen production pathways. 6
1.4 Schematic representation of photosynthesis. 9
1.5 Requirements for photocatalytic water splitting systems. 10
1.6 Semiconducting or molecular photoactive materials for water splitting . . . 11
1.7 Reaction pathways for the PS 12
1.8 Excited state landscape and simplified MO-scheme for $(Ru(bpy)_3)^{2+}$. . . . 13
1.9 Excited state landscape and simplified MO-scheme for $(Fe(bpy)_3)^{2+}$ 15
1.10 Complex with optimized octahedral structure. 16
1.11 Chemical structure of two NHC-based complexes and the position of their molecular orbitals. 17
1.12 Excited state landscape for iron(III)-complexes. 19
1.13 $Ru(bpy)_3^{2+}$ 20
1.14 Scheme for $M(ppz)_3$ with M = Fe, Co or Ir metal centres. 21

2.1 Proposed workflow of this thesis. 25

3.1 Reaction scheme of ligand syntheses. 28
3.2 Overview of the EDG/π-extension- ligand scope implemented in complex synthesis 29
3.3 Overview of the EWG ligand scope implemented in complex synthesis. . . 30
3.4 GC-MS overview of multi fluor-substituted phenylpyrazoles 31
3.5 Calculated pK_a Values. 33
3.6 Reaction scheme towards the activated ligand with grignard. 34
3.7 Reaction scheme of the complexation reaction, both pathways 34
3.8 Oxidation of the complex $\mathbf{Fe(ppz)_3}$ on silica 35
3.9 Complex overview for the unsubstituted standard complex and electron donating groups. 36
3.10 Complex overview for π-system extension. 37
3.11 Complex overview for EWG substitutions. 37
3.12 Mass spectrum for double substituted ligands. 38
3.13 Reduction/oxidation pathways 40

4.1 Microscopic view of crystals of $\mathbf{Fe^{III}(3Me\text{-}ppz)_3)}$ **and** $\mathbf{Fe^{III}(bppz)_3)}$. 43

4.2 single crystal structure of $Fe^{III}(ppz)_3$ and $Fe^{III}(bppz)_3$ 44
4.3 *mer*-$\mathbf{Fe^{III}(ppz)_3}$ and *fac*-$\mathbf{Fe^{III}(ppz)_3}$ 44
4.4 Single crystal structure of $\mathbf{Fe^{III}(3Me\text{-}ppz)_3}$ with the indicated planes for the ligand orientation. 46
4.5 PBEh-3c optimised lowest quartet state of *fac*-$\mathbf{Fe^{III}(ppz)_3}$. 47
4.6 Gibbs energy difference (δG) between the *fac*- and *mer*-isomers of optimised geometries 48
4.7 ^{1}H-NMR for all three oxidation states, exemplarily for $\mathbf{Fe^{III}(ppz)_3}$. 50
4.8 DFT calculations on the preferred species for all oxidation states. 51
4.9 DFT calculations on the preferred species for all oxidation states. 52
4.10 ^{1}H-NMR spectrum in THF-d_8 for $\mathbf{[Fe^{II}ppz_3]^+}$ time-dependent measurements under increased temperature. 52
4.11 ^{1}H-NMR spectra in THF-d_8 for $\mathbf{[Fe^{II}ppz_3]^+}$ time-dependent measurements under illumination. 53
4.12 Schematic representation of the complexes and their proton assignment . . 54
4.13 Through-space distance between proton and iron(III)-centre. 57
4.14 ^{13}C-NMR of the complex with the three oxidation numbers. 60
4.15 Spin density plot of the PBEh-3c optimized ***fac***-$\mathbf{Fe^{III}(ppz)_3}$ structure. . . 62
4.16 ^{57}Fe Mössbauer spectra. 63
4.17 Experimental X_HMMT vs. T values for iron(III) and iron(IV). 64
4.18 Cyclic voltammagram of all investigated complexes. 65
4.19 TPSSh/def2-TZVP calculated spatial distribution 68
4.20 TPSSh calculated spin up and spin down orbitals 69
4.21 Absorption spectra in BuCN for the investigated compounds. 70
4.22 TPSSh calculated vertical transitions; *fac*-optimised structure of $\mathbf{Fe^{III}(ppz)_3}$. 72
4.23 Change in the absorptive behaviour of $\mathbf{Fe^{III}(ppz)_3}$ 73
4.24 Experiments on complex stability for all functionalities ^{1}H-NMR. 74
4.25 Irradiation of $\mathbf{Fe^{III}(ppz)_3}$. 75
4.26 Irradiation of $\mathbf{Fe^{III}(ppz)_3}$ 76
4.27 Mass spectrum of $\mathbf{Fe^{III}(ppz)_3}$ after irradiation in MeCN 76
4.28 Degradation of $\mathbf{Fe^{III}(ppz)_3}$ under illumination 77
4.29 NMR-spectra after irradiation 78
4.30 Decomposition of $\mathbf{Fe^{III}(ppz)_3}$, with different wavelengths depended filters. 79
4.31 Experimental XANES an VtC 81
4.32 Comparison of experimental and calculated XANES. 82
4.33 Experimental CtC spectra 82
4.34 ^{1}H-NMR-resonance shift for $\mathbf{Fe^{III}(ppz)_3}$ from 253 to 333 K 85
4.35 Temperature dependent shift of $\mathbf{Fe^{III}(ppz)_3}$ against the chemical shift in ppm for the respective position 86
4.36 Plot of the temperature dependence, according to Curie´s law and the Boltzmann Distribution 87
4.37 Scheme of direct relaxation and the Orbach relaxation 89
4.38 Determination of the relaxation pathways, following the Orbach process for $\mathbf{Fe^{III}(ppz)_3}$ 90

4.39 Determination of the relaxation pathways, following the Orbach process for $\mathbf{Fe}^{IV}\mathbf{(ppz)}_3$ 91

5.1 Achieved Complexes within this work. 95
5.2 Possible new reaction pathways towards novel PS. 97

List of Tables

3.1 Overview of ligand scope, their respective abbreviations and their synthetic yield. . . . 32
3.2 Overview of ligand scope,their respective abbreviations and their synthetic yield. . . . 39
3.3 Reduction and oxiation of the complexes 41

4.1 Crystallographic data for the investigated iron(III)-complexes; averaged over all binding distances.[99] 45
4.2 Data for the PBEh-3c geometry optimised *fac*-complexes. . . . 47
4.3 Assigned chemical proton shifts of the iron complexes 55
4.4 ^{13}C-NMR data of ***mer*-[Fe^{II}(ppz)$_3$]Na**, **Fe^{III}(ppz)$_3$** and **[Fe^{IV}(ppz)$_3$]PF$_6$** 61
4.5 Electrochemical properties of the complexes, with 10^{-3} M in MeCN with 0.1 M [Bu$_4$N]PF$_6$ as electrolyte. . . . 66
4.6 Electronic properties of the reported complexes, in BuCN (10^{-5} M). . . . 71
4.7 Fit-parameters for Fe^{III}(ppz)$_3$ and Fe^{IV}(ppz)$_3$ for fig. 4.35 86
4.8 Determination of the total chemical shift. . . . 88

A1 List of Oral and Poster presentations 133
A2 List of Beamtimes 133
A3 List of Publications 134

A4 Analysis of the main acceptor and donor orbital contribution 135

Publications and Beamtimes

Table A1: List of Oral and Poster presentations

Conference	Contribution	Date
BYOP - Postersession 2023, Paderborn, Germany	Poster Presentation - Could tris-cyclometalated Iron(III) complexes with *N*-phenylpyrazoles act as photocatalysts?	24.10.2023
8th EuChemS Chemistry Congress, Lissabon, Portugal	Oral Presentation - The capability of iron(III) complexes for photocatalytic water splitting	28.08-01.09.2022
KCT - Koordinationschemikertagung, Freiburg, Germany	Poster Presentation - Increasing the pi-system of *N*-heterocyclic carbenes for photoactive iron complexes	29.02.2020-30.02.2020
BYOP - Postersession 2020, Paderborn, Germany	Poster Presentation - Increasing the pi-system of *N*-heterocyclic carbenes for photoactive iron complexes	26.02.2020

Table A2: List of Beamtimes

Institute	Beamline	Time Frame
DESY, Hamburg, Germany	P65	24.10.2023
DESY, Hamburg, Germany	P64	28.08-01.09.2022
ESRF, Grenoble, France	24	29.02.2020-30.02.2020
ESRF, Grenoble, France	16	29.02.2020-30.02.2020
Diamond, Oxfordshire, United Kingdom	B18	26.02.2020
Diamond, Oxfordshire, United Kingdom	B18	26.02.2020

Table A3: List of Publications

Number	Publication
1	Hirschhausen, T.; Fritsch, L.; Lux, F.; Steube, J.; Schoch, R.; Neuba, A.; Egold, H.; Bauer, M. *Iron(III)-Complexes with N-Phenylpyrazole-Based Ligands*, **Inorganics 2023**, 11 (7), 282. DOI: 10.3390/inorganics11070282.
2	Issue Cover Contribution to "Iron(III)-Complexes with *N*-Phenylpyrazole-Based Ligands" 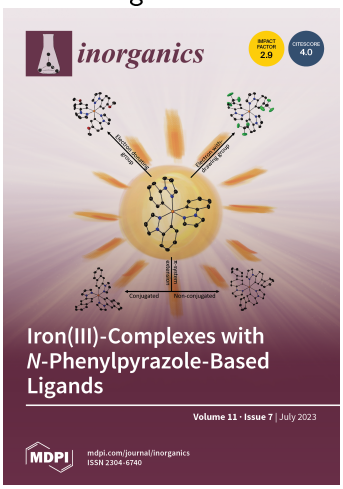
3	T.Hirschhausen, H. Egold, L. Fritsch, F. Lux, J. Steube, R. Schoch, M. Nowakowski, A. Velić, S. Demeshko, F. Meyer, and M. Bauer; +II, +III, +IV: Iron-phenylpyrazole in variable oxidation states - an NMR approach; **2024**, [*Manuscript in preparation*]

Appendix

DFT calculations

Table A4: Analysis of the main acceptor and donor orbital contribution to the TD-DFT calculated vertical transitions of *fac*-$Fe^{III}(ppz)_3$. The lettering of the transitions a-h refers to the assigned transitions. Additionally, the calculated wavelength λ and oscillator strength f is given for the selected transitions. Calculations performed by Msc. Lorena Fritsch.

Transition	Main Donor Orbital	Main Acceptor Orbital	Contribution to the transition
a λ = 451 nm f = 0.0022	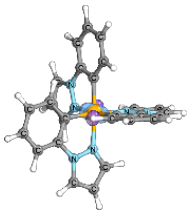 HOMO β	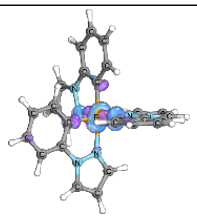 Lumo+8 β	13%
	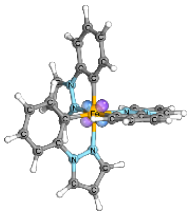 HOMO-1 β	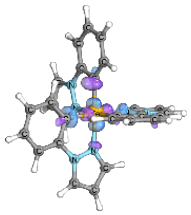 LUMO+7 β	11%
	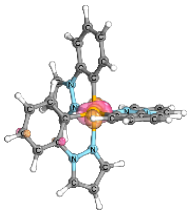 HOMO α	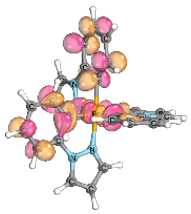 LUMO+5 β	10%
b λ = 449 nm f = 0.0022	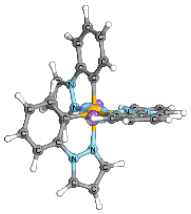 HOMO β β	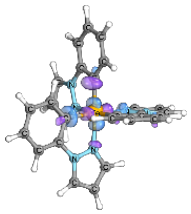 LUMO+7 β	13%

	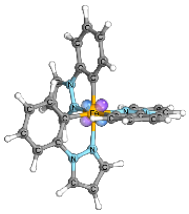 HOMO-1 β	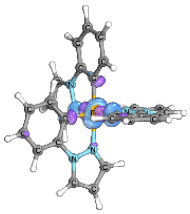 LUMO+8 β	11%
	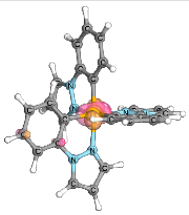 HOMO α	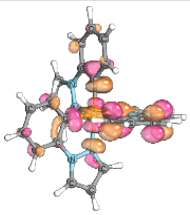 LUMO+3 β	10%
c λ = 400 nm f = 0.0085	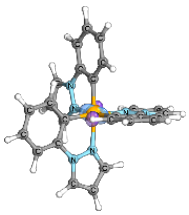 HOMO β	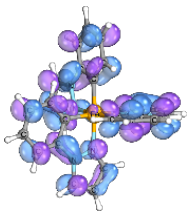 LUMO+1 β	84%
d λ = 388 nm f = 0.0128	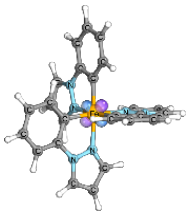 HOMO-1 β	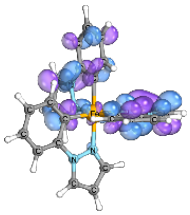 LUMO+3 β	30%
	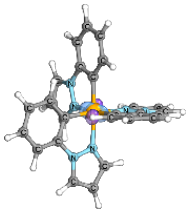 HOMO β	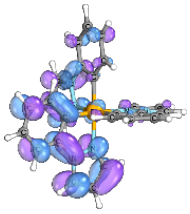 LUMO+2 β	30%
d´ λ = 389 nm f = 0.0108	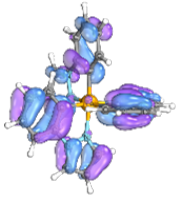 HOMO-2 β	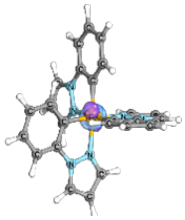 LUMO β	58%

e $\lambda = 351$ nm f = 0.0159	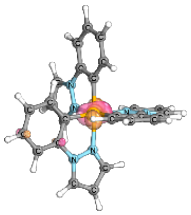 HOMO α	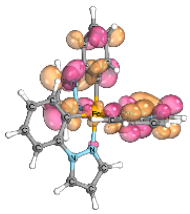 LUMO+3 α	15%
	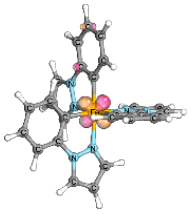 HOMO-1 α	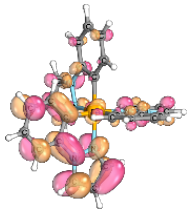 LUMO+1 α	12%
	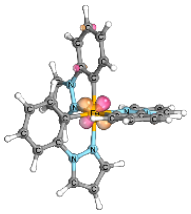 HOMO-1 α	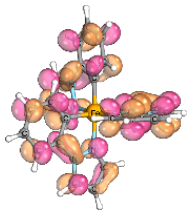 LUMO α	12%
f $\lambda = 346$ nm f = 0.0251	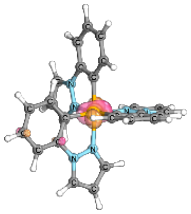 HOMO α	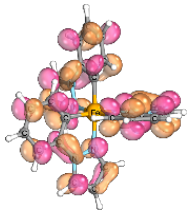 LUMO α	68%
g $\lambda = 281$ nm f = 0.0328	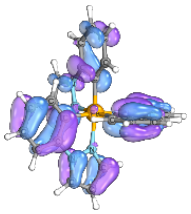 HOMO-2 β	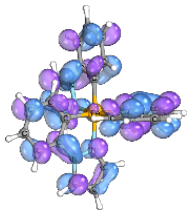 LUMO+1 β	26%
	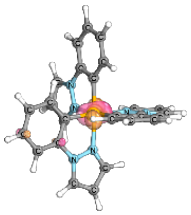 HOMO α	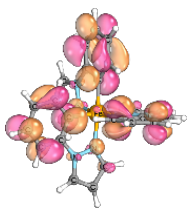 LUMO+5 α	16%

	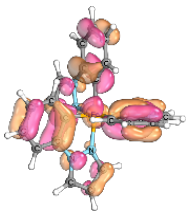 HOMO-2 α	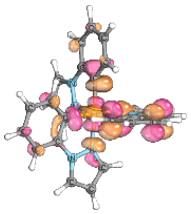 LUMO+3 α	7%
h $\lambda = 264$ nm f = 0.02085	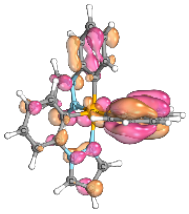 HOMO-4 α	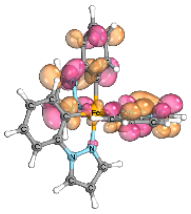 LUMO+2 α	10%
	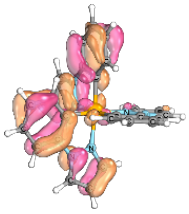 HOMO-3 α	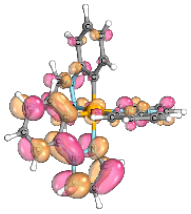 LUMO+1 α	9%
	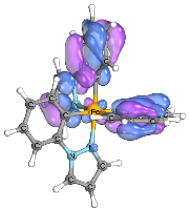 HOMO-4 β	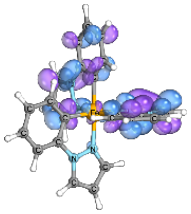 LUMO+3 β	7%
	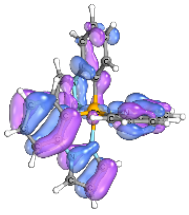 HOMO-3 β	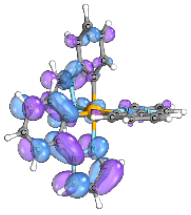 LUMO+2 β	7%
	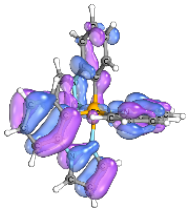 HOMO-5 β	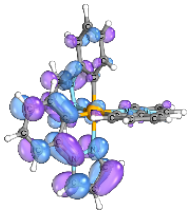 LUMO α	6%

Ligand Spectra

(MeOppz)

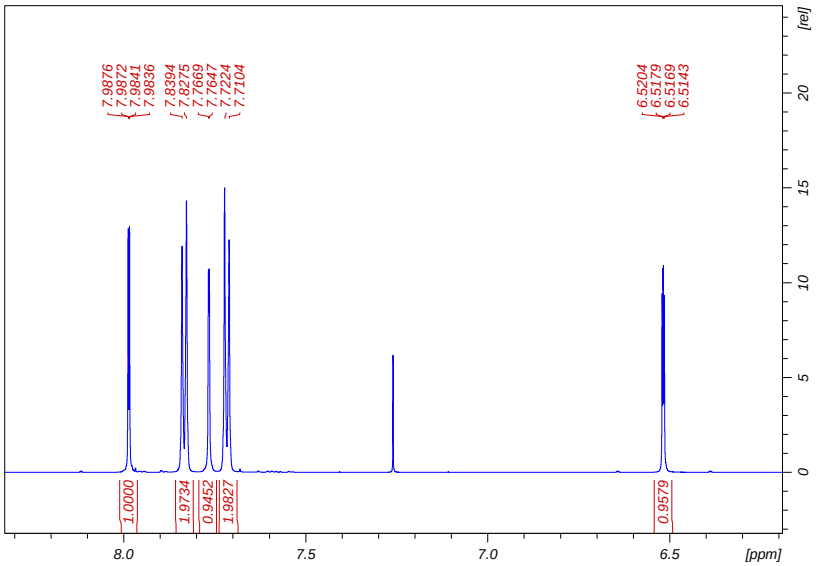

Figure A1: ^{1}H-NMR spectrum for ligand **(MeOppz)** in $CDCl_3$.

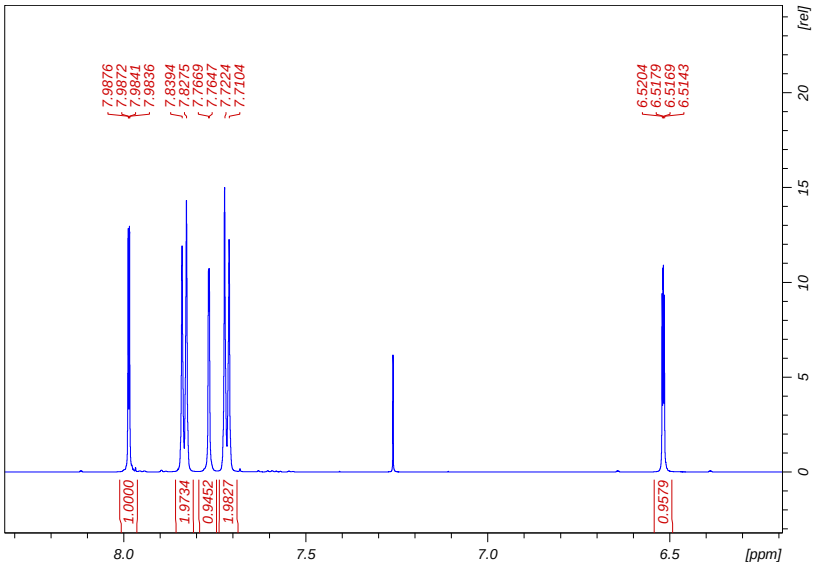

Figure A2: ^{13}C-NMR spectrum for ligand **(MeOppz)** in $CDCl_3$.

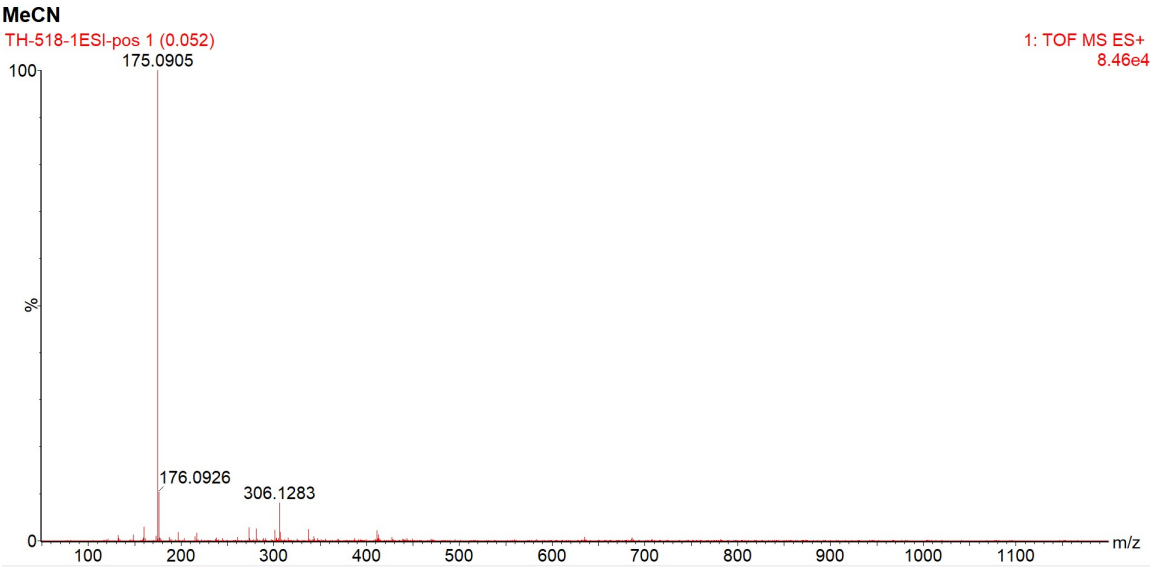

Figure A3: ESI-MS spectrum of ligand **(MeOppz)** in MeCN.

(p-CF_3ppz)

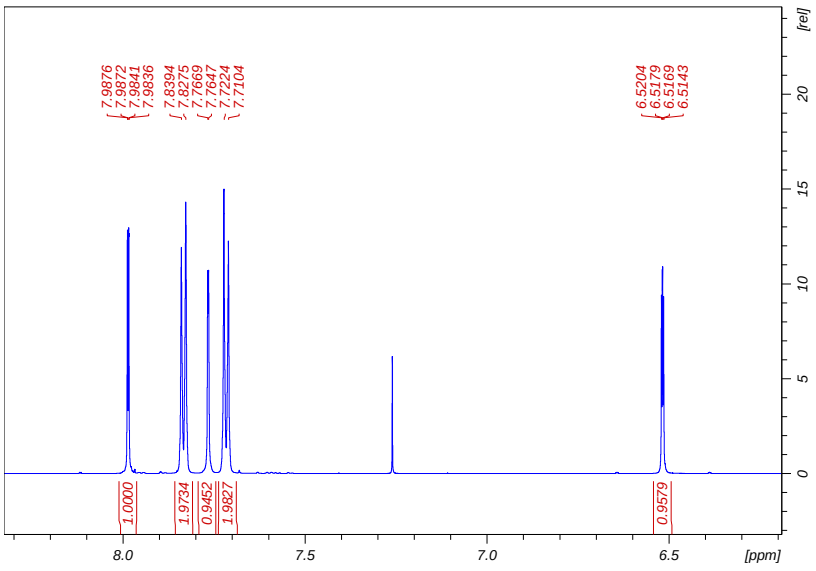

Figure A4: ^{1}H-NMR spectrum for ligand **(*p*-CF_3ppz)** in $CDCl_3$.

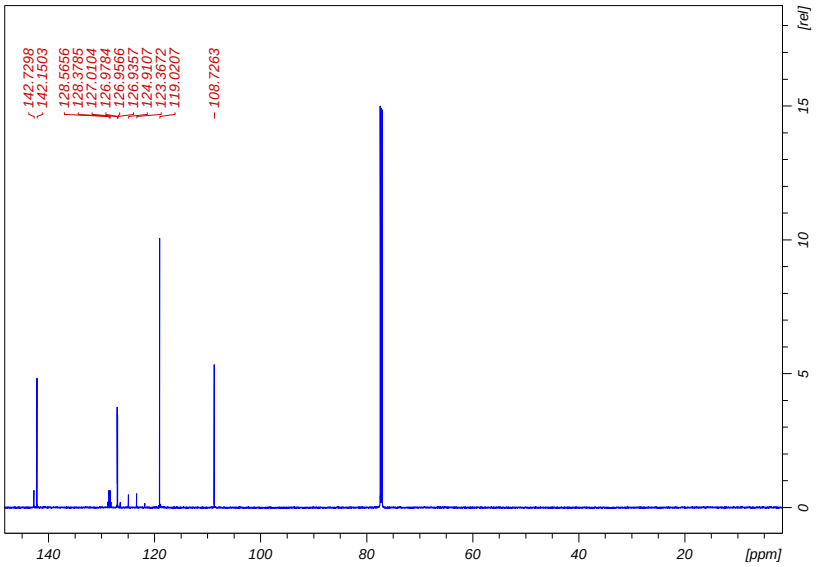

Figure A5: ^{13}C-NMR spectrum for ligand **(*p*-CF$_3$ppz)** in $CDCl_3$.

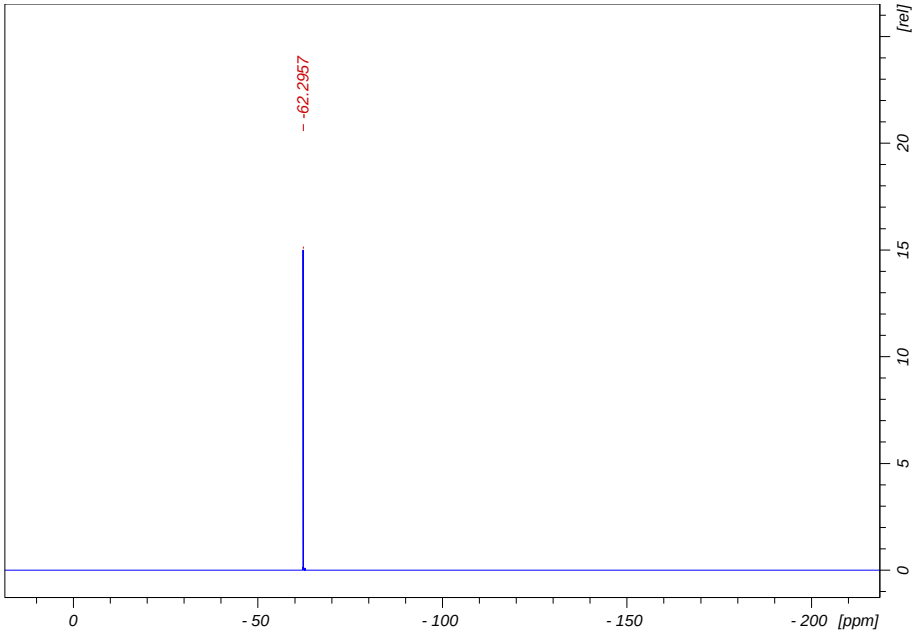

Figure A6: ^{19}F-NMR spectrum for ligand **(*p*-CF$_3$ppz)** in $CDCl_3$.

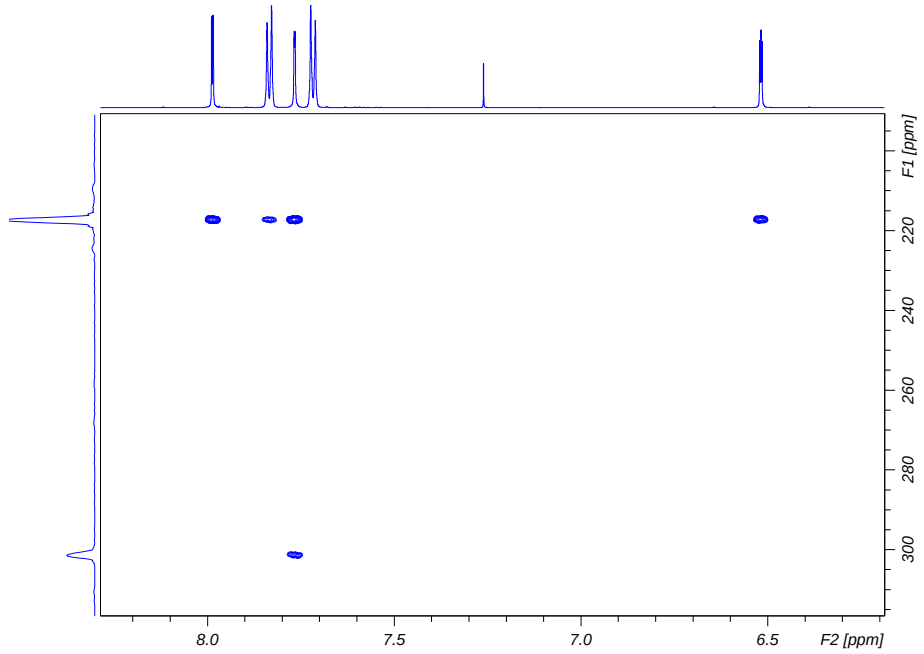

Figure A7: ^{15}N-HMBC-NMR spectrum for ligand **(*p*-CF$_3$ppz)** in $CDCl_3$.

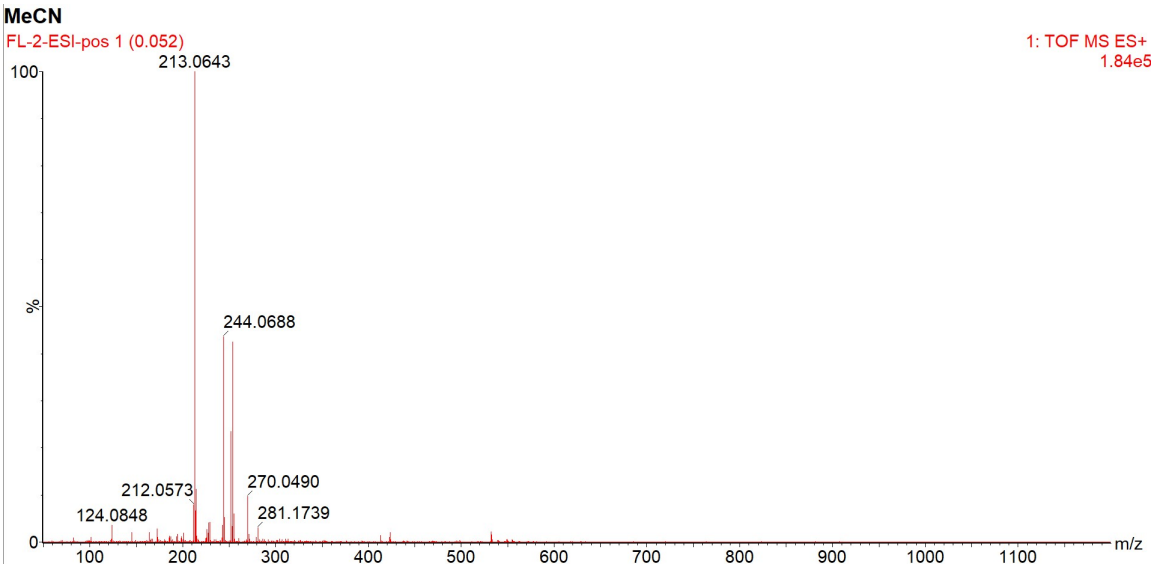

Figure A8: ESI-MS spectrum of ligand **(*p*-CF$_3$ppz)** in MeCN.

(p-CF_3ppz)

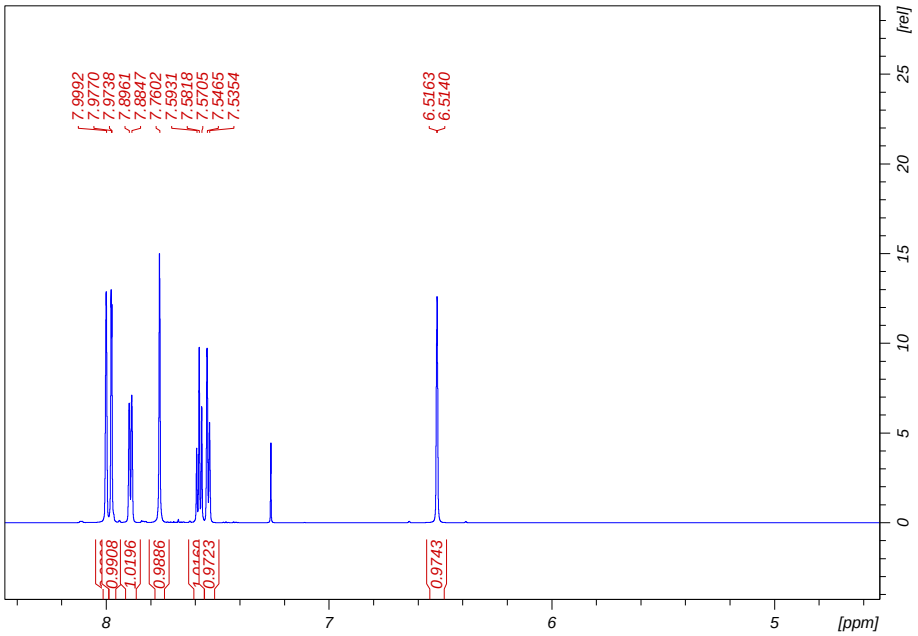

Figure A9: ^{1}H-NMR spectrum for ligand **(p-CF_3ppz)** in $CDCl_3$.

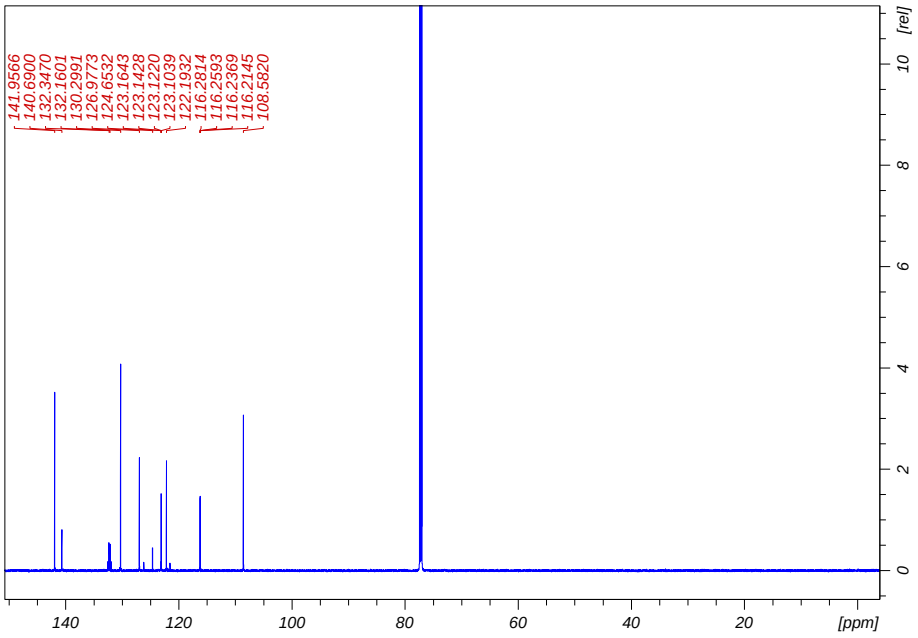

Figure A10: ^{13}C-NMR spectrum for ligand **(p-CF_3ppz)** in $CDCl_3$.

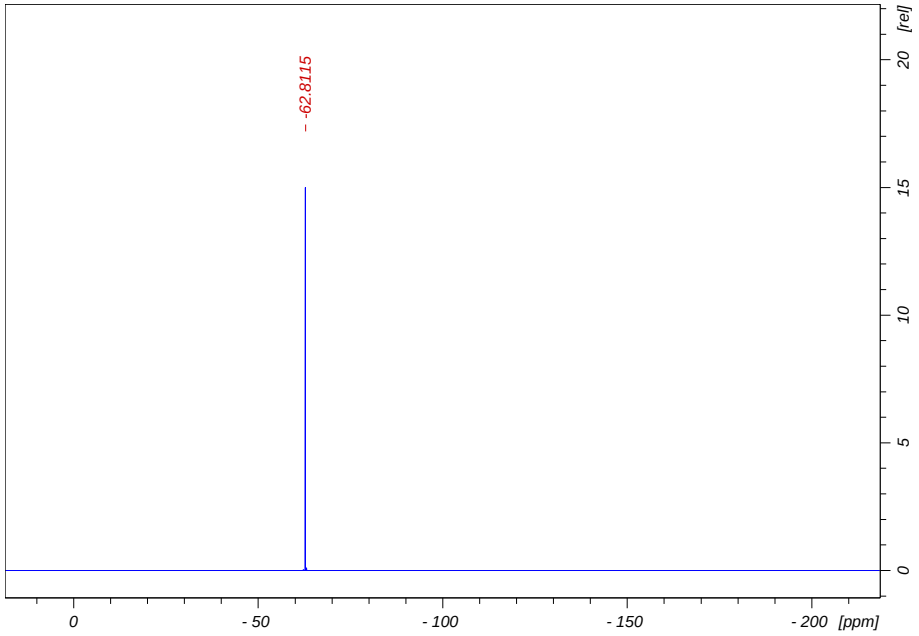

Figure A11: ^{19}F-NMR spectrum for ligand **(p-CF$_3$ppz)** in $CDCl_3$.

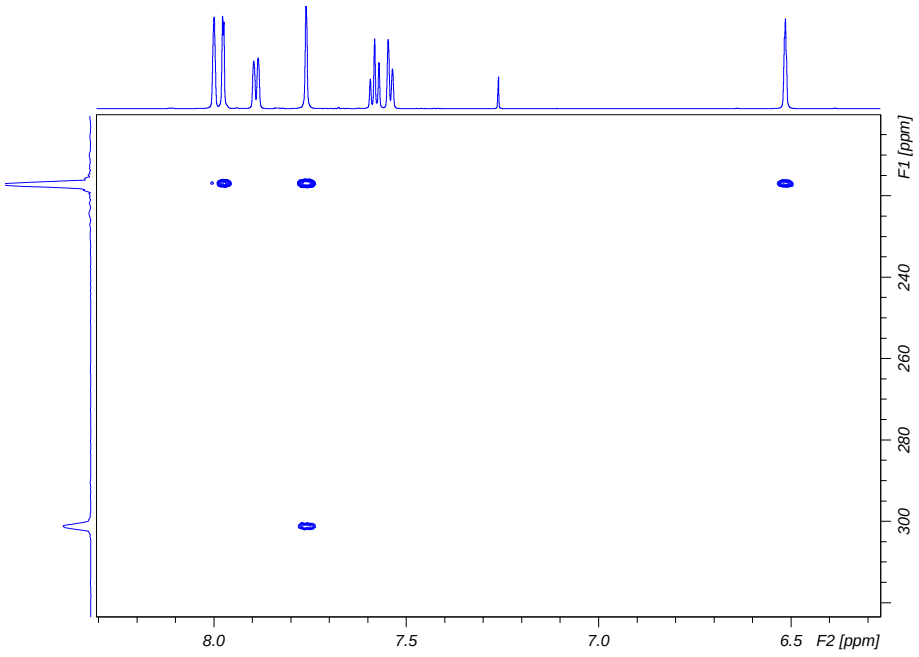

Figure A12: ^{15}N-HMBC-NMR spectrum for ligand **(p-CF$_3$ppz)** in $CDCl_3$.

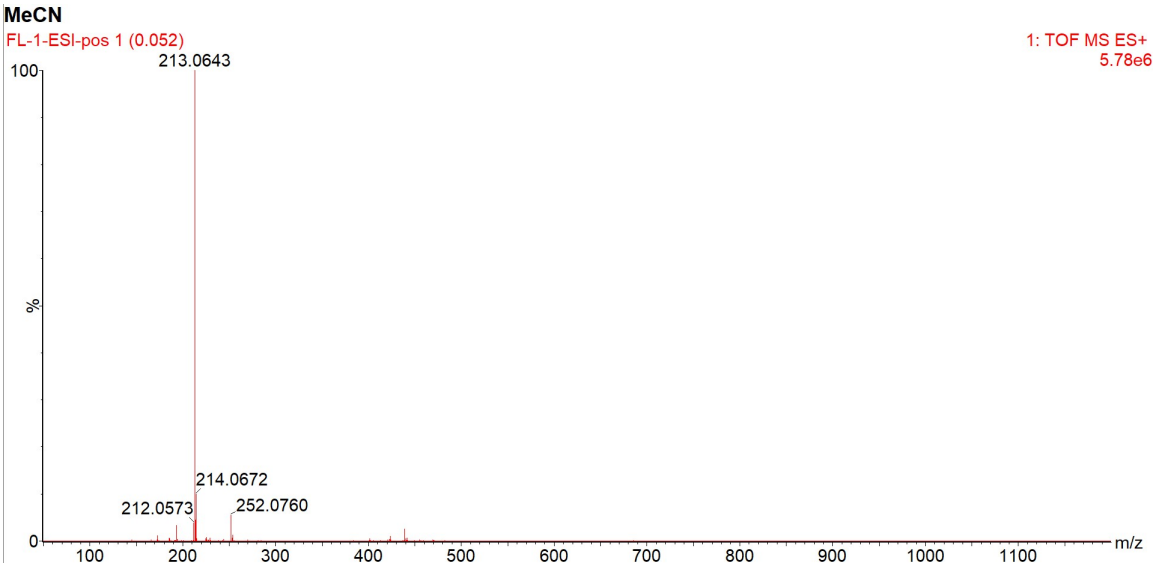

Figure A13: ESI-MS spectrum of complex **p-CF_3ppz** in MeCN.

(Fppz)

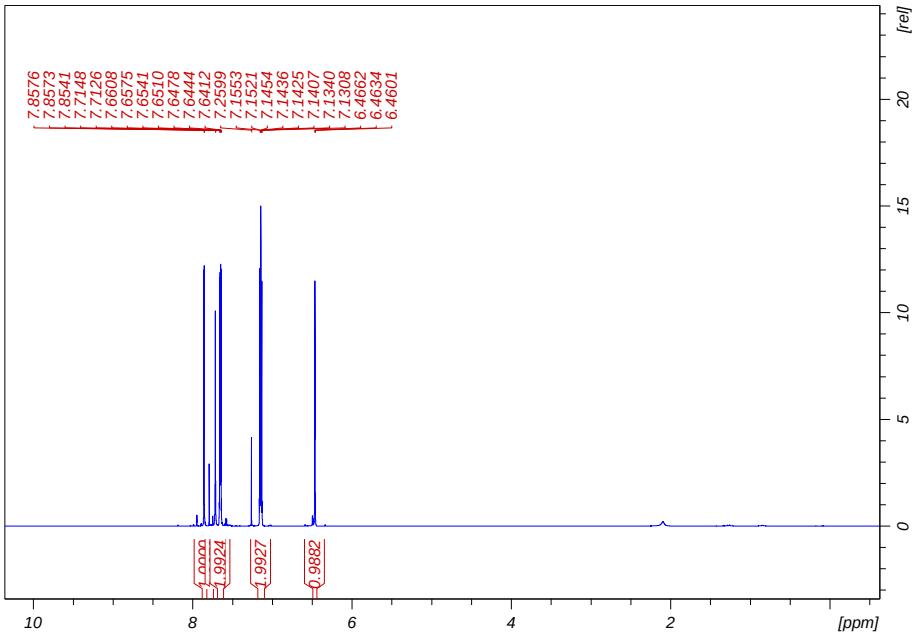

Figure A14: ^{1}H-NMR spectrum for ligand **(Fppz)** in $CDCl_3$.

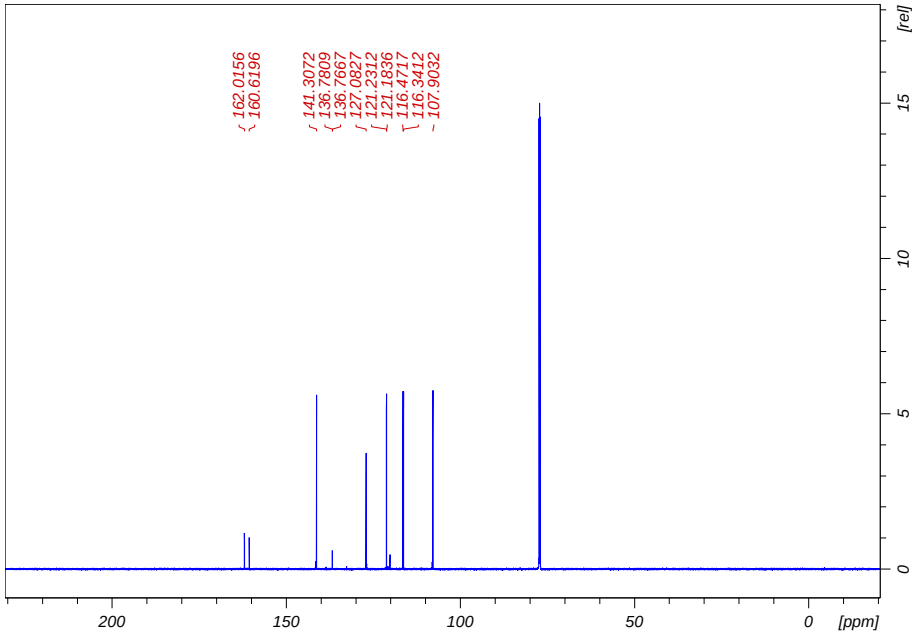

Figure A15: ^{13}C-NMR spectrum for ligand **(Fppz)** in $CDCl_3$.

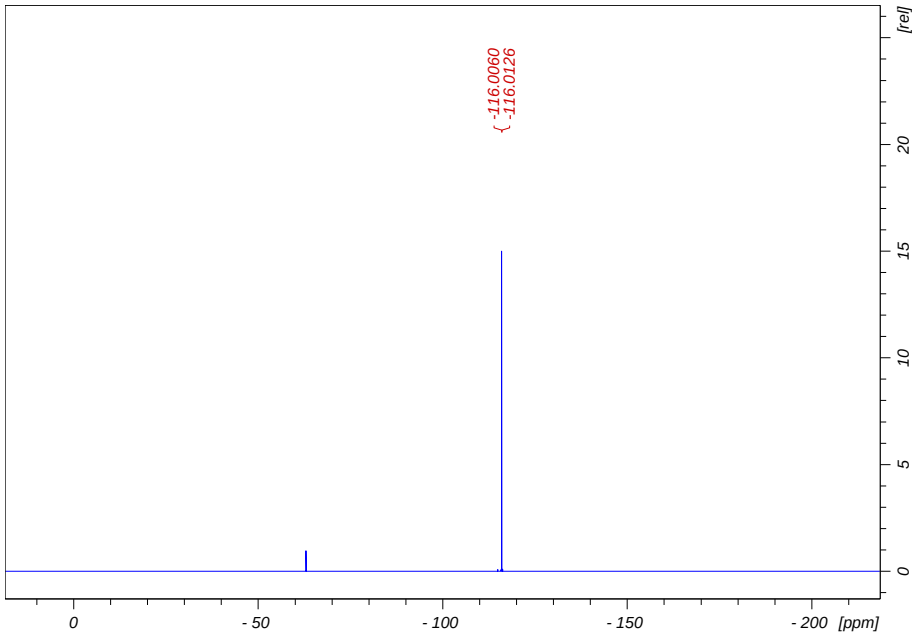

Figure A16: ^{19}F-NMR spectrum for ligand **(Fppz)** in $CDCl_3$.

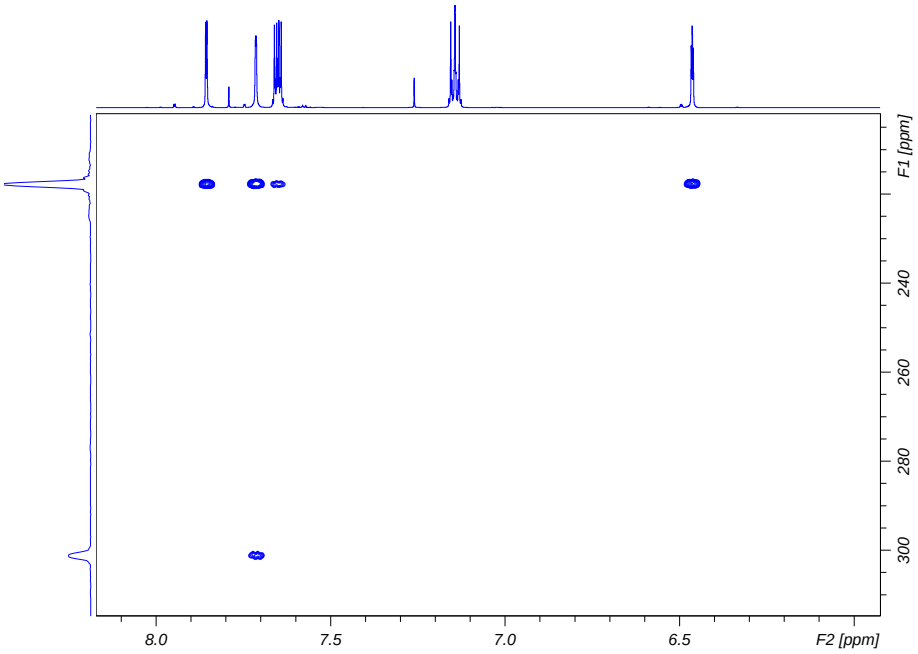

Figure A17: ^{15}N-HMBC-NMR spectrum for ligand **(Fppz)** in $CDCl_3$.

Figure A18: ESI-MS spectrum of complex **Fppz** in MeCN.

$(CF_3)_2$ppz

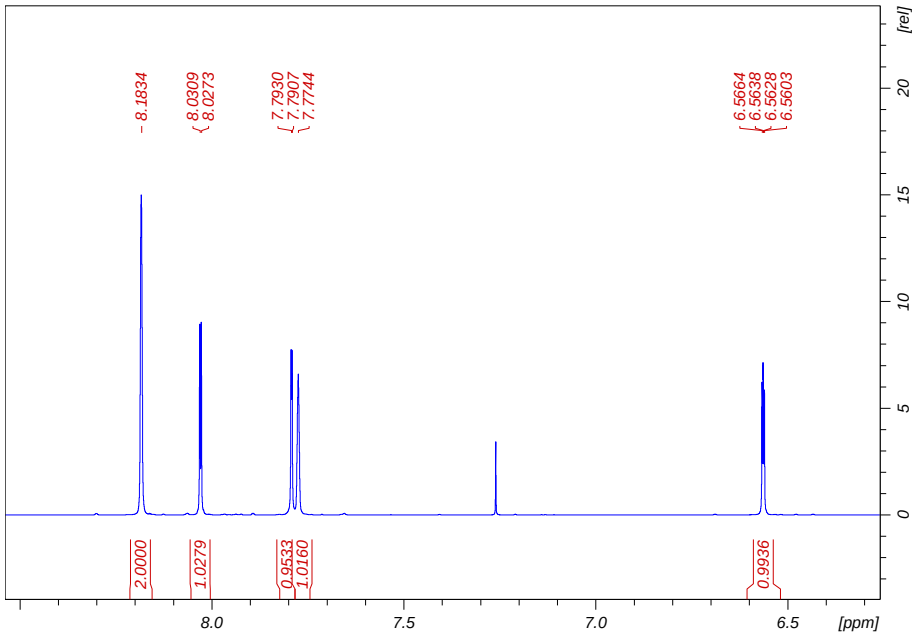

Figure A19: ^{1}H-NMR spectrum for ligand **$(CF_3)_2$ppz** in $CDCl_3$.

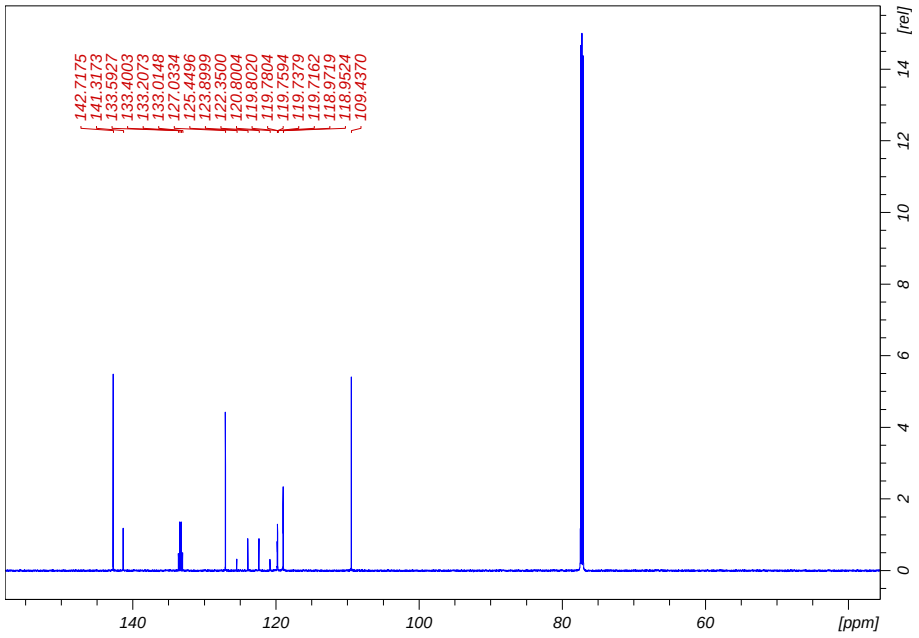

Figure A20: ^{13}C-NMR spectrum for ligand **$(CF_3)_2$ppz** in $CDCl_3$.

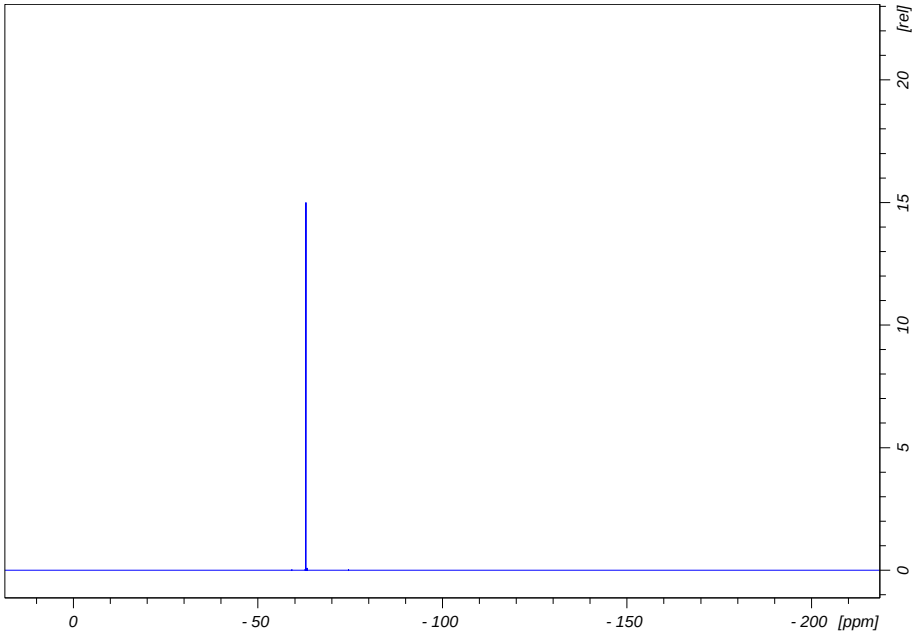

Figure A21: ^{19}F-NMR spectrum for ligand **(CF$_3$)$_2$ppz** in CDCl$_3$.

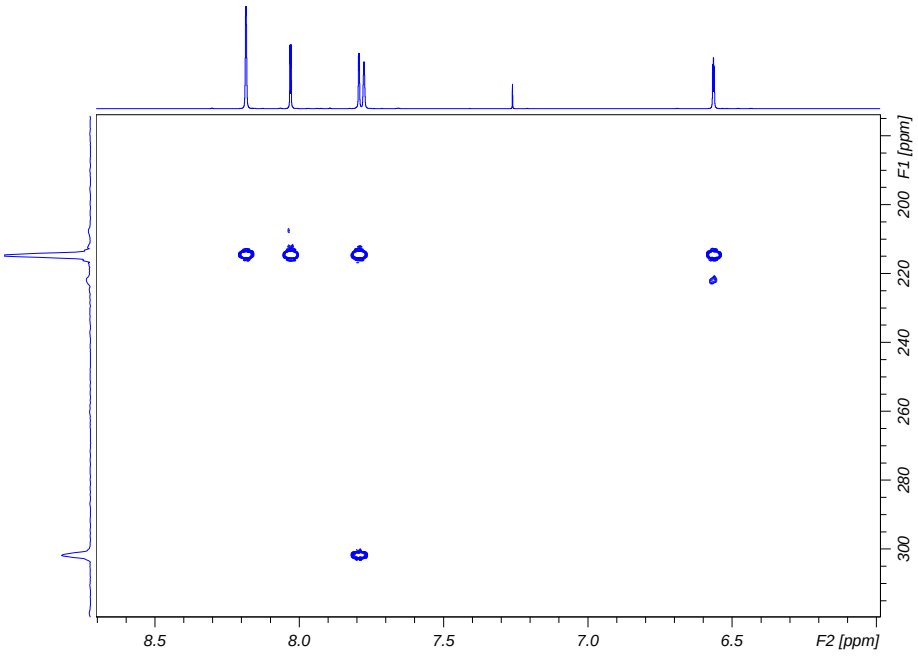

Figure A22: ^{15}N-HMBC-NMR spectrum for ligand **(CF$_3$)$_2$ppz** in CDCl$_3$.

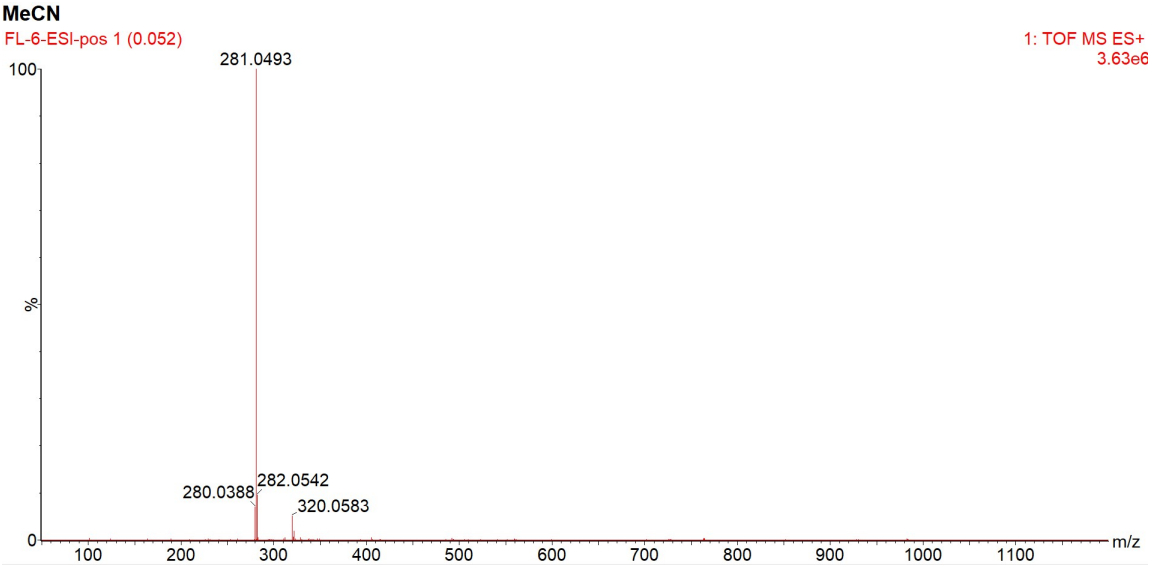

Figure A23: ESI-MS spectrum of complex **$(CF_3)_2$ppz** in MeCN.

bppz

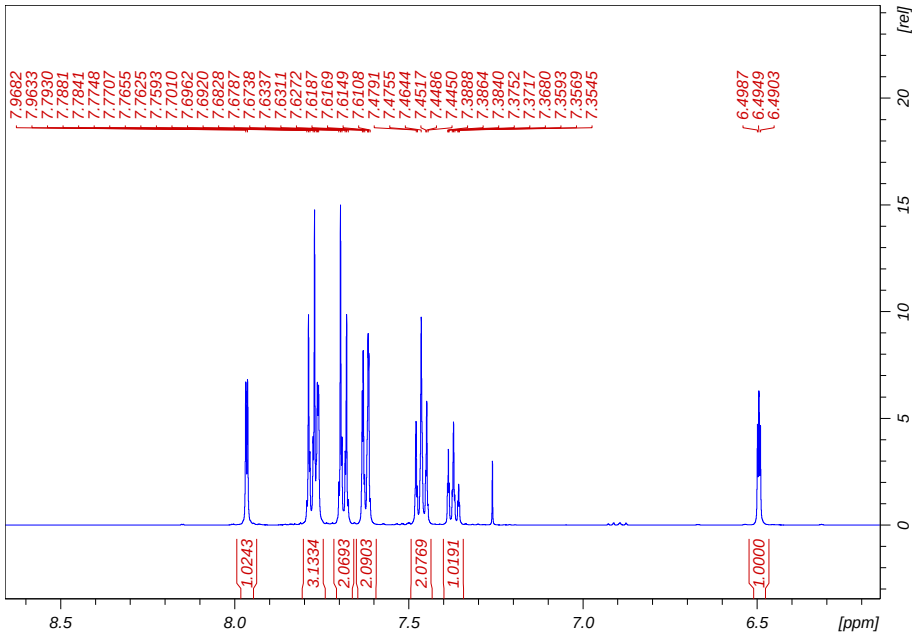

Figure A24: ^{1}H-NMR spectrum for ligand **bppz** in $CDCl_3$.

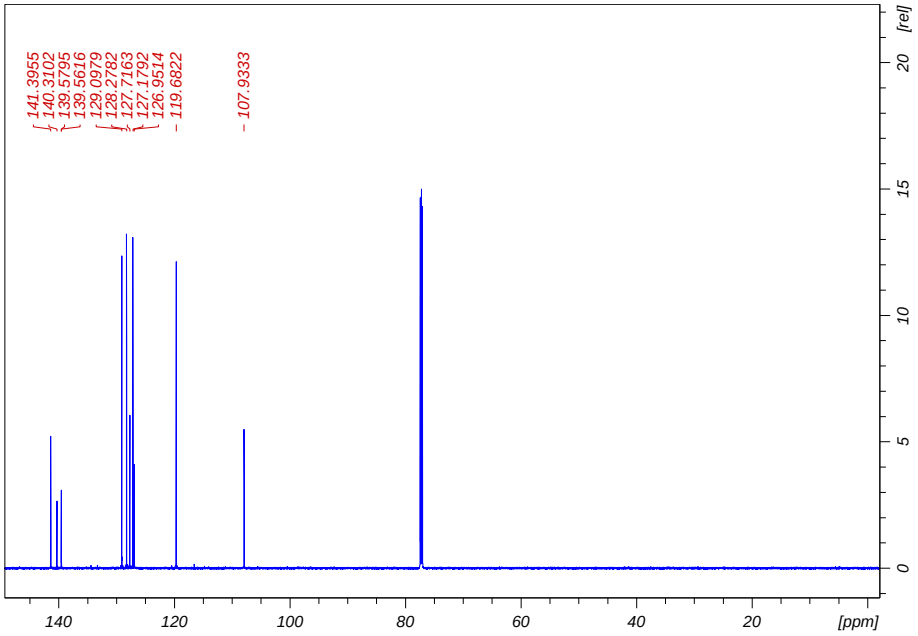

Figure A25: ^{13}H-NMR spectrum for ligand **bppz** in $CDCl_3$.

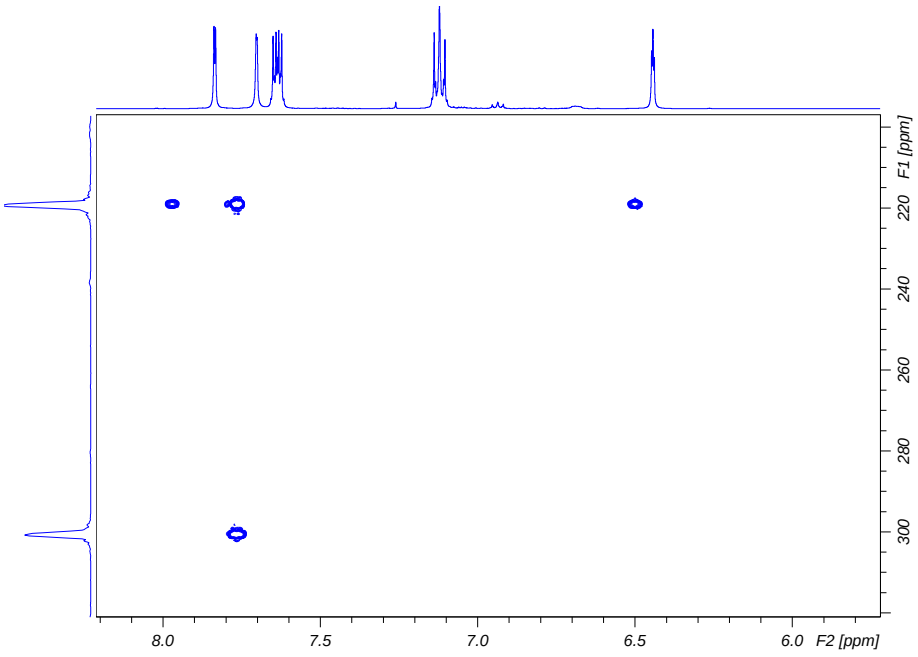

Figure A26: ^{15}N-HMBC-NMR spectrum for ligand **bppz** in $CDCl_3$.

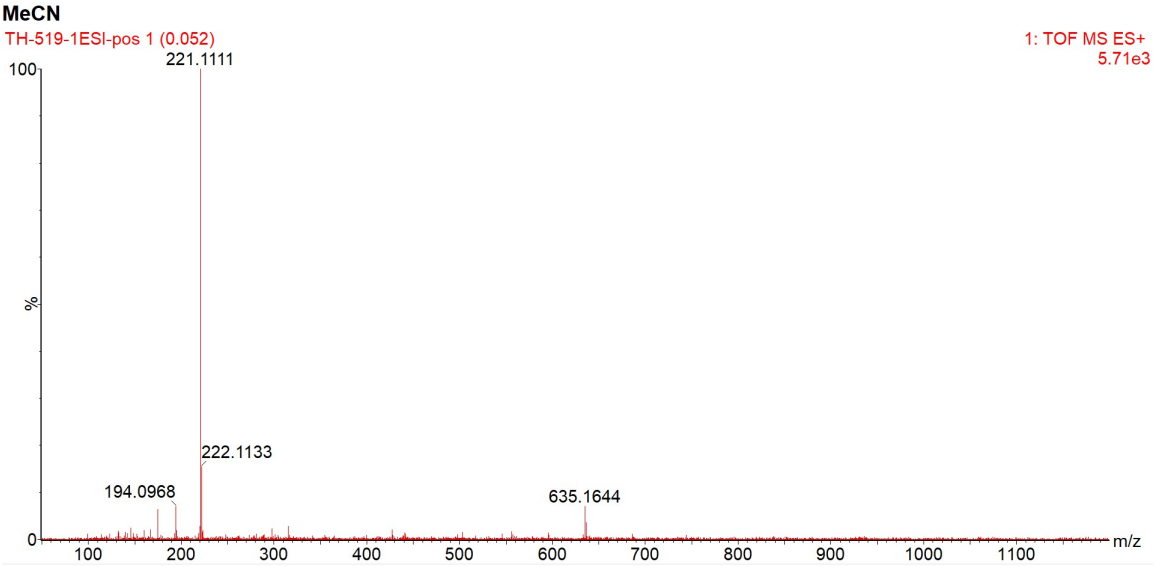

Figure A27: ESI-MS spectrum of ligand **bppz** in MeCN.

naphpz

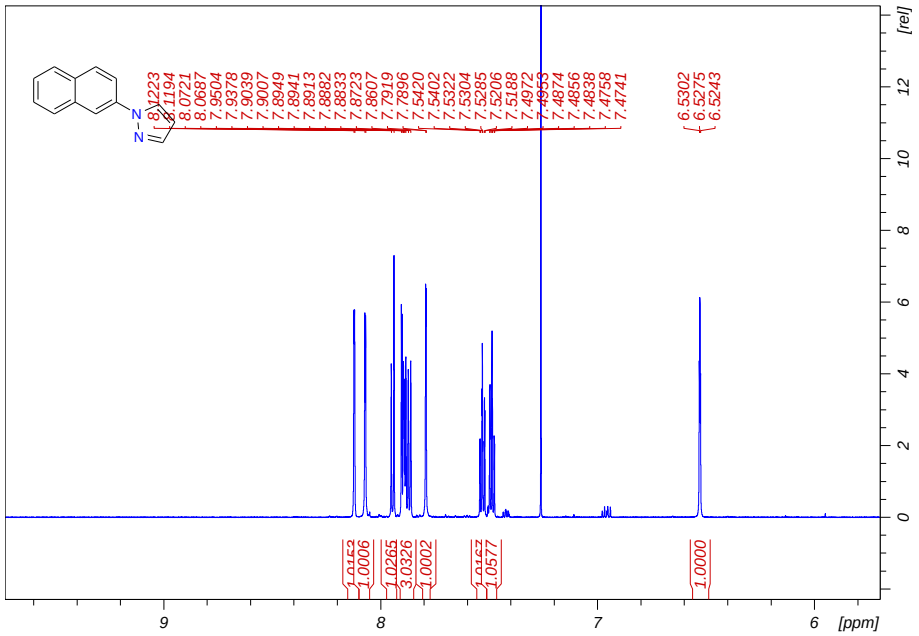

Figure A28: ^{1}H-NMR spectrum for ligand **naphpz** in $CDCl_3$.

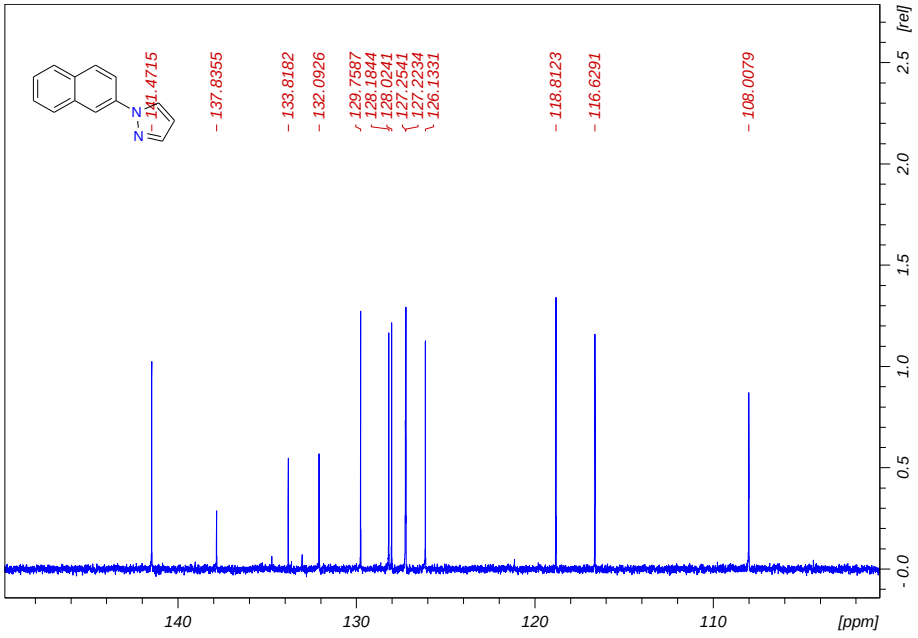

Figure A29: ^{13}H-NMR spectrum for ligand **naphpz** in $CDCl_3$.

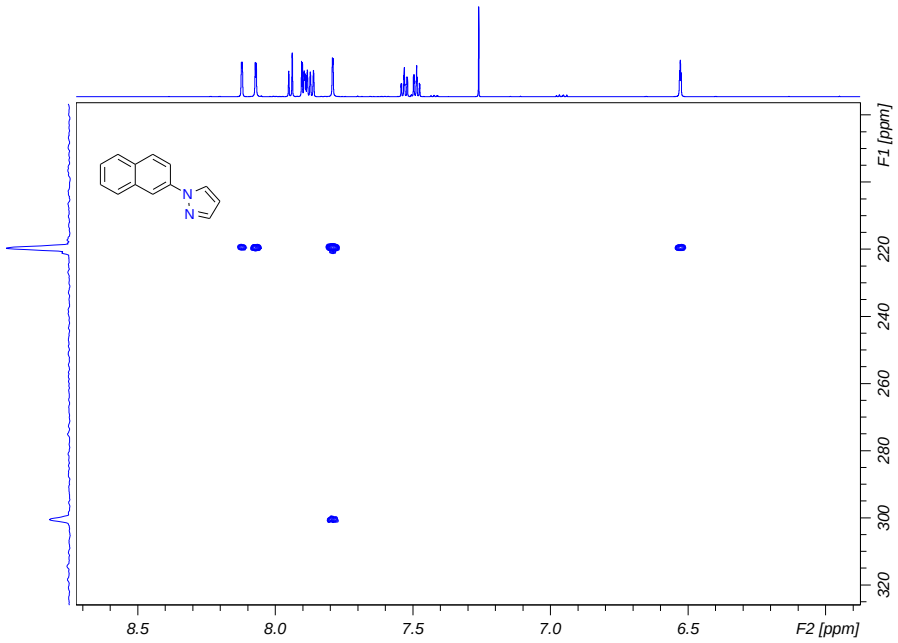

Figure A30: ^{15}N-HMBC-NMR spectrum for ligand **naphpz** in $CDCl_3$.

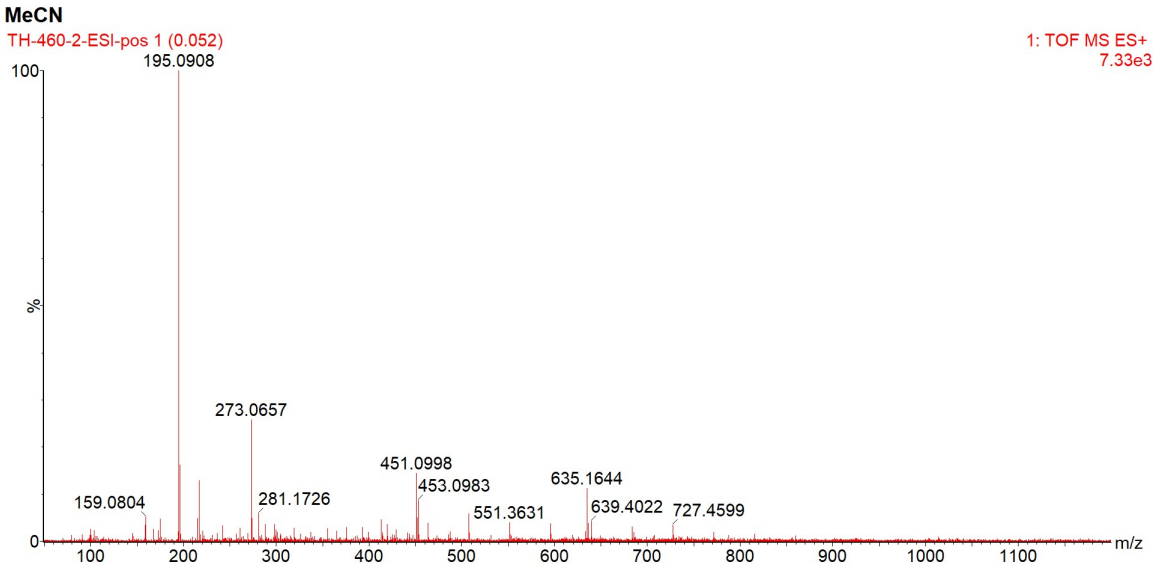

Figure A31: ESI-MS spectrum of ligand **naphpz** in MeCN.

Complex Spectra

Table A5: Crystal structure data and refinement for **Fe(ppz)$_3$**

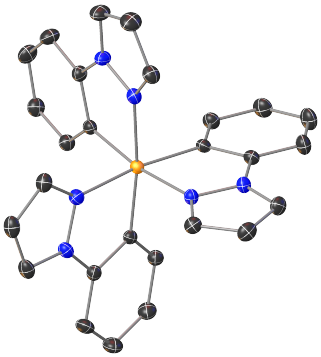

Identification code	TH-439-1 (TH_0188)
CCDC number	219100
Empirical formula	$C_{55}H_{44}Cl_2Fe_2N_{12}$
Moiety formula	$C_{27}H_{21}N_6Fe$
Formula weight	1055.62 Da
Color	brown
Shape	needle
Temperature	119(2) K
Wavelength	0.71073 Å
Crystal system	Orthorhombic
Space group	$P2_12_12_1$
Unit cell dimensions	a = 13.6656(7) Å α =90°
	b = 15.4759(8) Å β = 90°
	c = 22.6671(11) Å γ = 90°
Volume	4793.8(4) Å^3
Z	4
Density (calculated)	1.463 mg/m^3
Absorption coefficient	0.770 mm^{-1}
F(000)	2176
Crystal size	0.300 x 0.060 x 0.020 mm^3
Theta range for data collection	2.182 to 30.524°
Index ranges	-19≤h≤19, -22≤k≤22, -32≤l≤32
Reflections collected	144195
Independent reflections	14658 [R(int) = 0.0379]
Completeness to theta = 25.242°	99.8 %
Absorption correction	Semi-empirical from equivalents
Refinement method	Full-matrix least-squares on F^2
Data / restraints / parameters	14658 / 0 / 641
Goodness-of-fit on F2	1.075
Final R indices [I>2sigma(I)]	R1 = 0.0270, wR2 = 0.0694
R indices (all data)	R1 = 0.0321, wR2 = 0.0737
Largest diff. peak and hole	0.499 e/Å^{-3} (0.51 Å^{-3} from H223) and -0.367 e/Å^{-3} (0.52 Å^{-3} from Fe1)

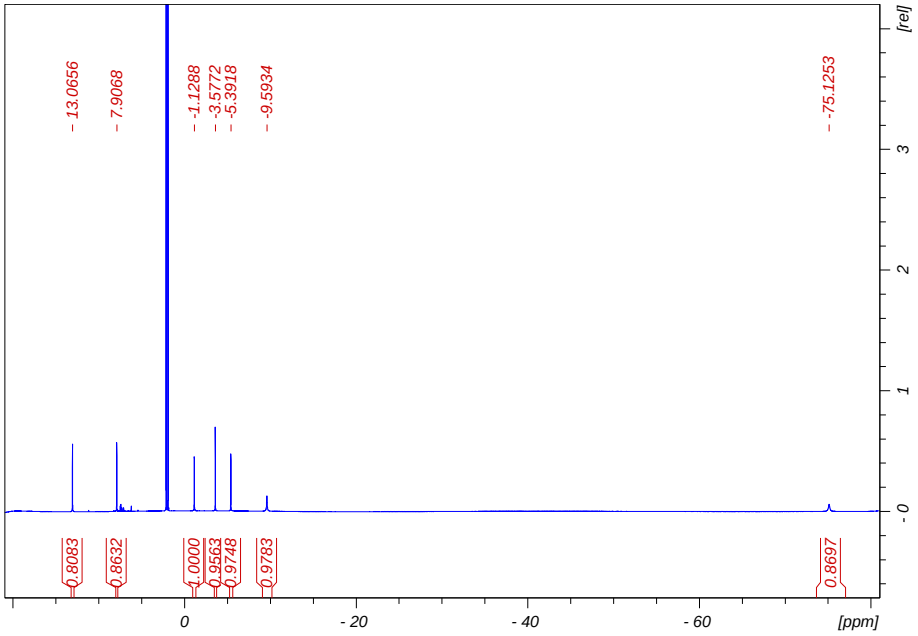

Figure A32: ^{1}H-NMR spectrum for complex $\mathbf{Fe^{III}(ppz)_3}$ in CD_3CN.

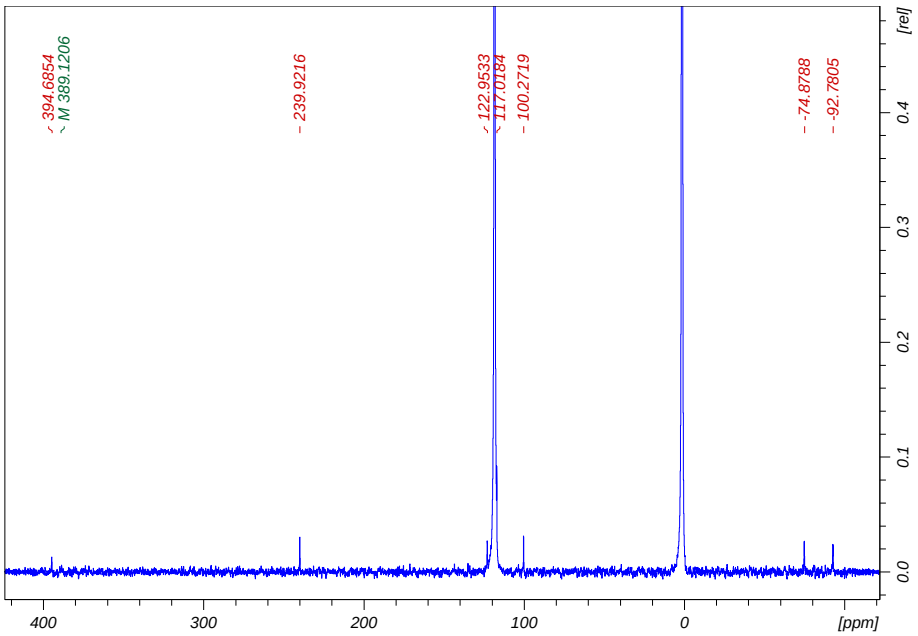

Figure A33: ^{13}C-NMR spectrum for complex $\mathbf{Fe^{III}(ppz)_3}$ in CD_3CN.

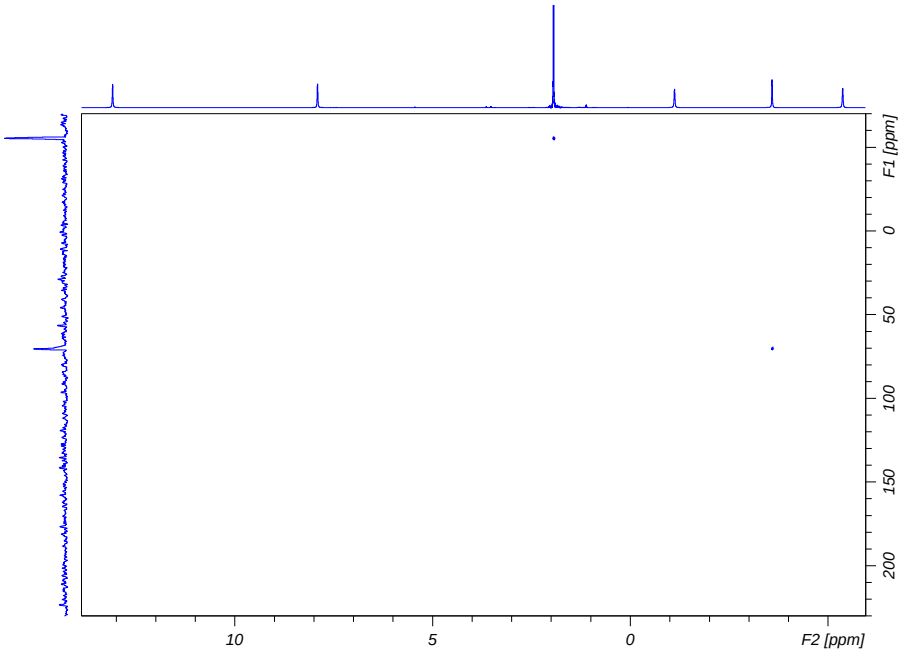

Figure A34: ^{15}N-HMBC-NMR spectrum for complex $\mathbf{Fe^{III}(ppz)_3}$ in CD_3CN.

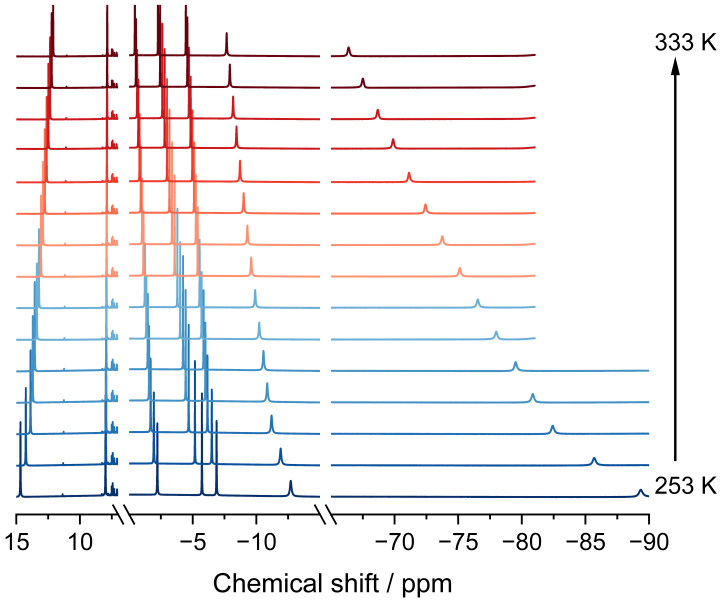

Figure A35: ^{1}H-NMR-spectra of complex $\mathbf{Fe^{III}(ppz)_3}$ from 243 to 333 K in CD_3CN.

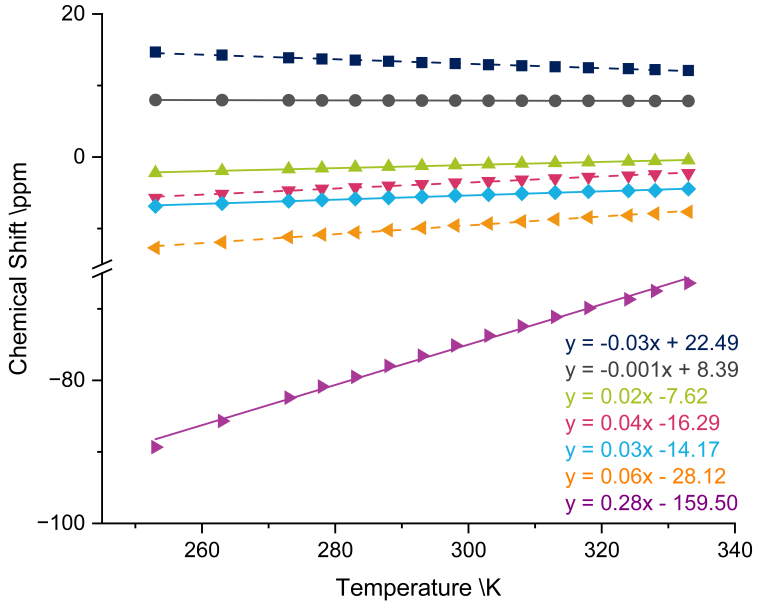

Figure A36: Curie-Plot of complex $\mathbf{Fe^{III}(ppz)_3}$ from 243 to 333 K in CD_3CN on the marked positions. Dashed line represents pyrazole-based protons, solid lines represent phenyl-based protons.

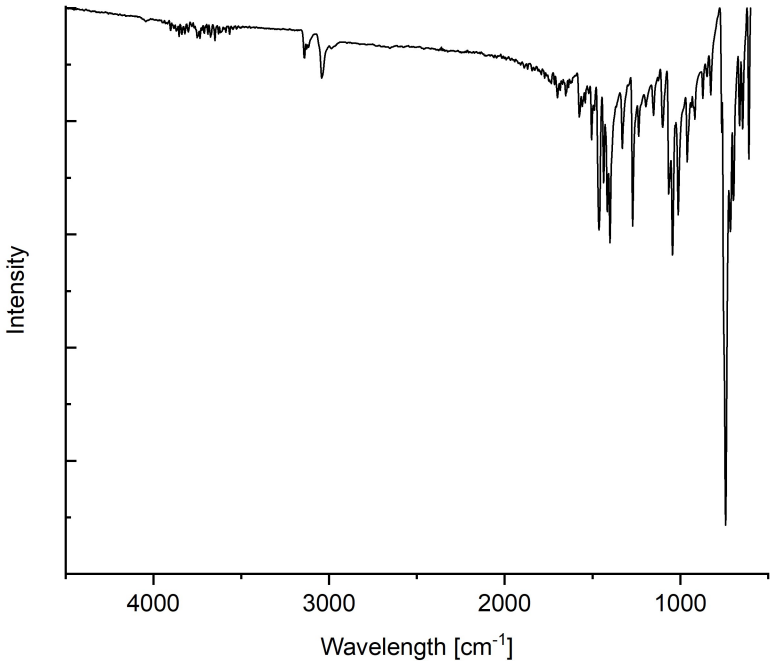

Figure A37: ATR-IR spectrum for complex $\mathbf{Fe^{III}(ppz)_3}$.

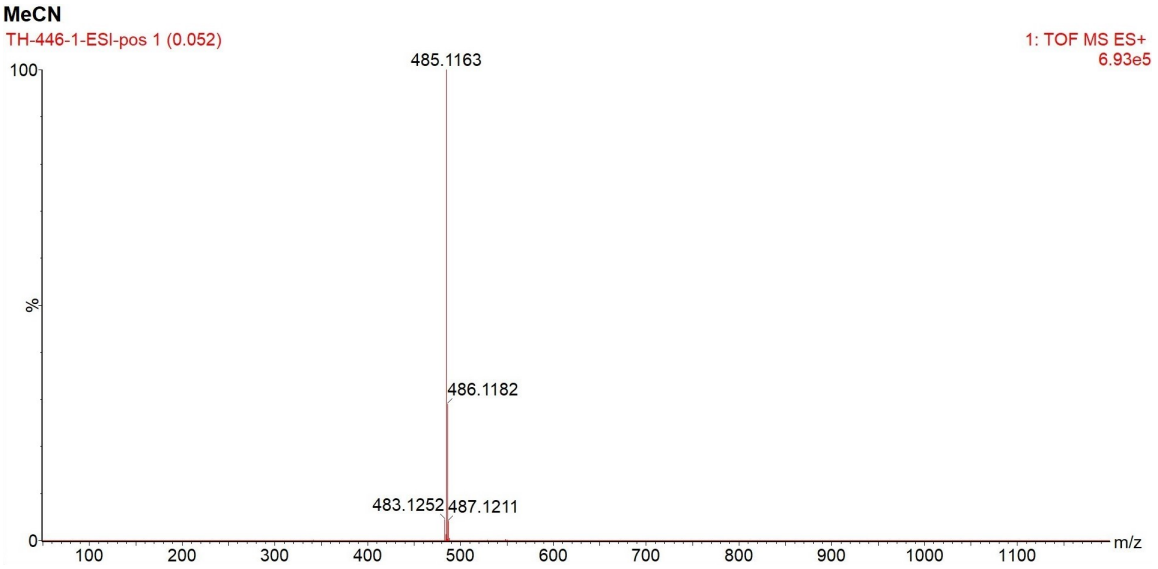

Figure A38: ESI-MS spectrum of complex $\mathbf{Fe^{III}(ppz)_3}$ in MeCN.

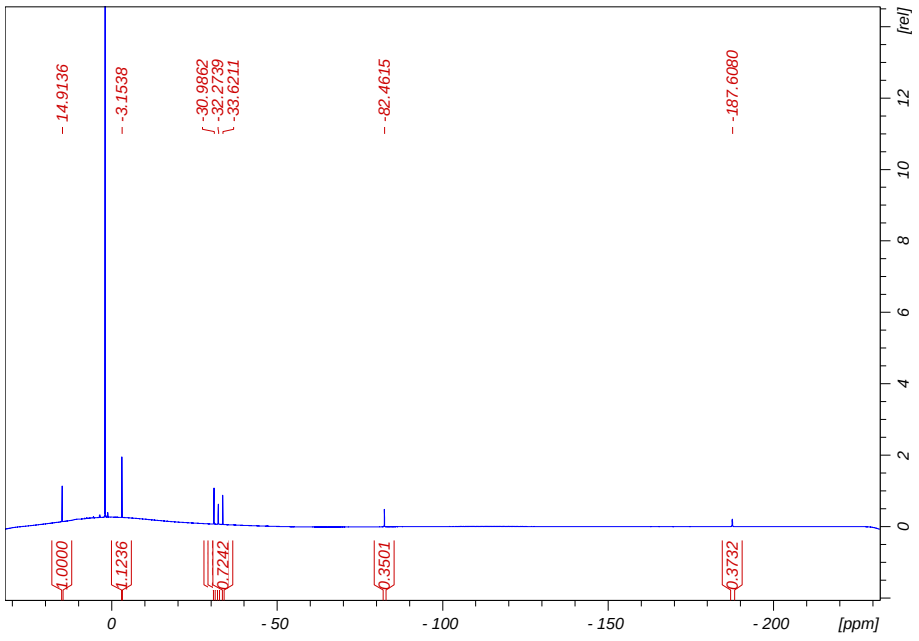

Figure A39: ^{1}H-NMR spectrum for complex $\mathbf{Fe^{IV}(ppz)_3}$.

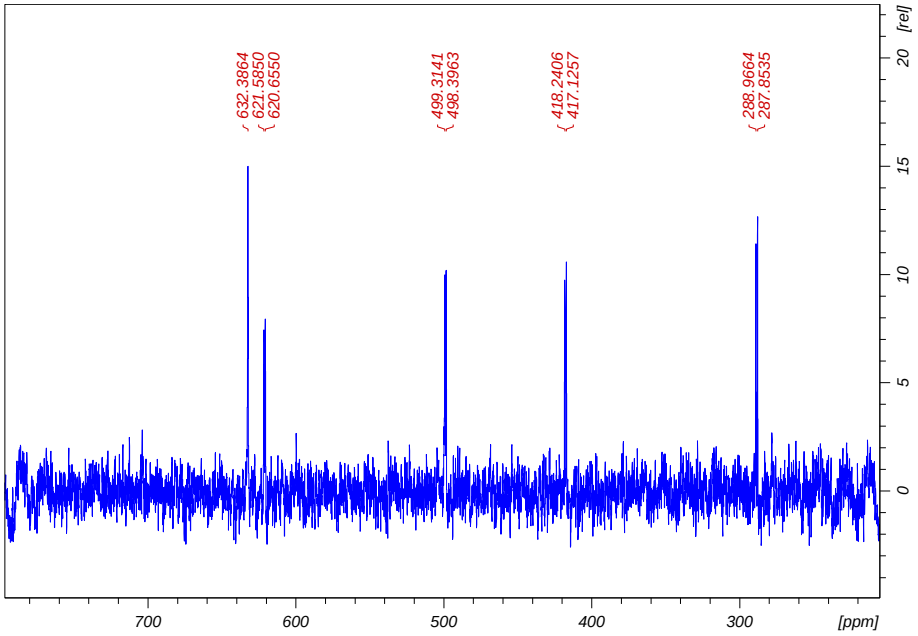

Figure A40: ^{13}C-NMR spectrum for complex $\mathbf{Fe^{IV}(ppz)_3}$-part 1.

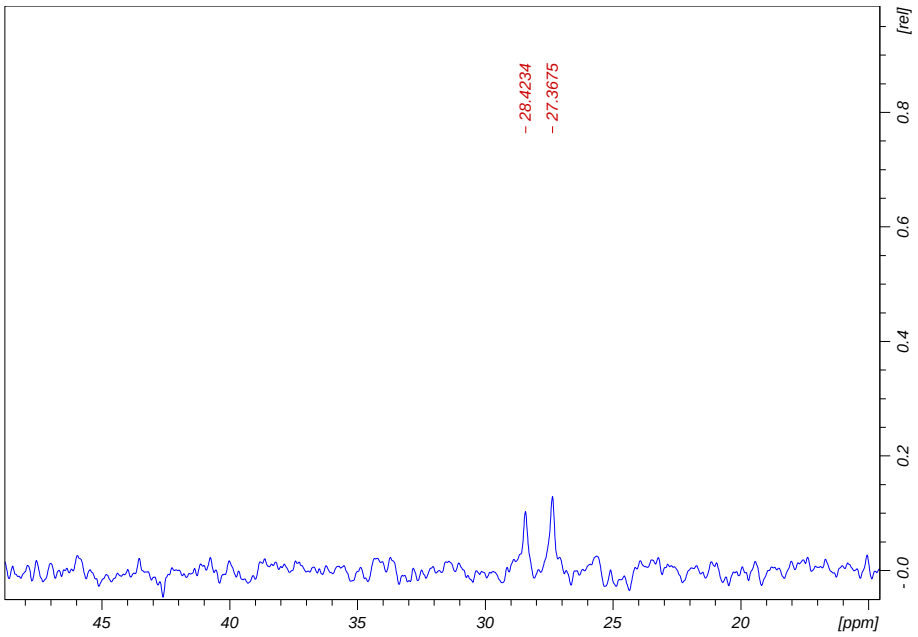

Figure A41: ^{13}C-NMR spectrum for complex $\mathbf{Fe^{IV}(ppz)_3}$-part 2.

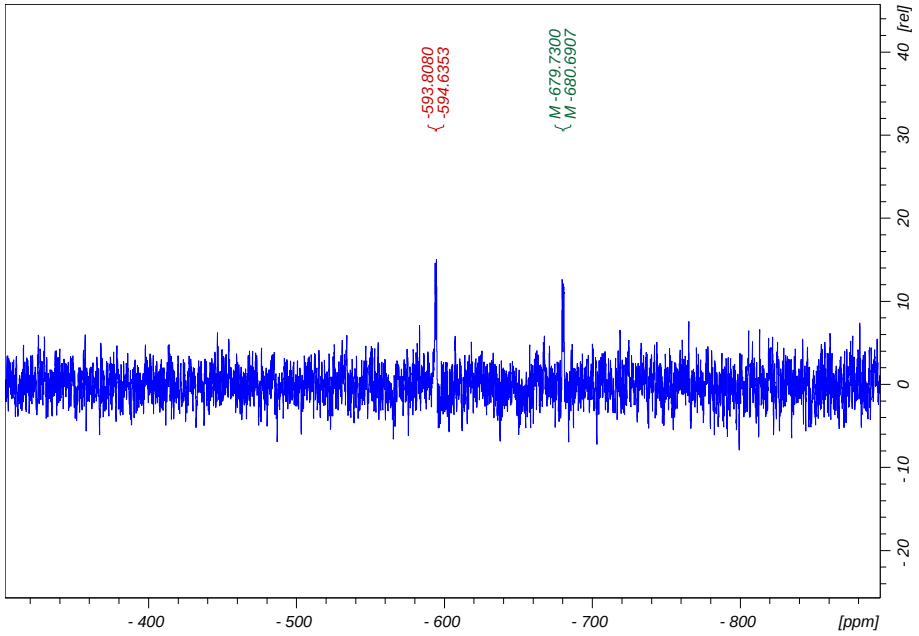

Figure A42: ^{13}C-NMR spectrum for complex $\mathbf{Fe^{IV}(ppz)_3}$-part 3.

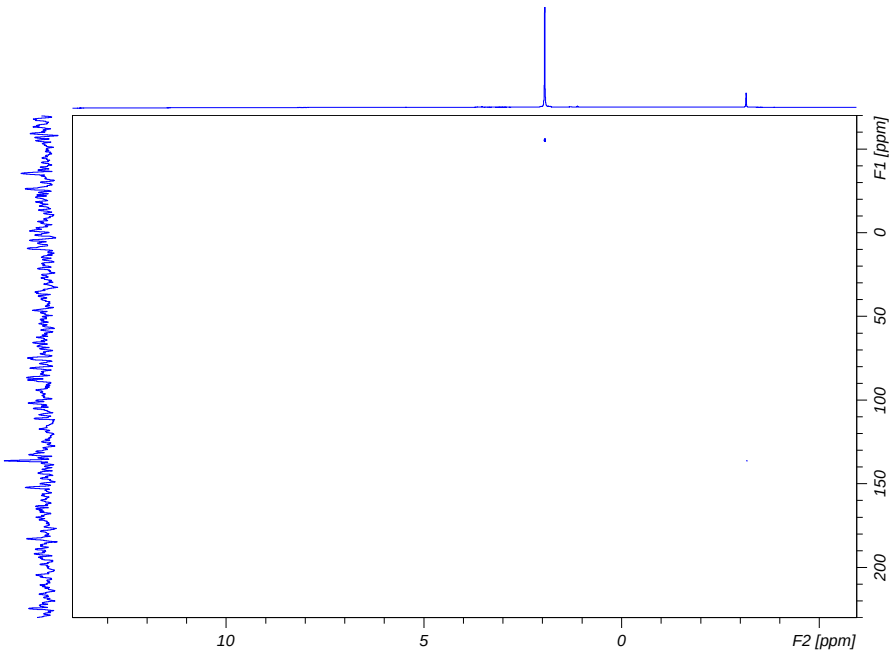

Figure A43: ^{15}N-HMBC-NMR spectrum for complex $\mathbf{Fe^{IV}(ppz)_3}$.

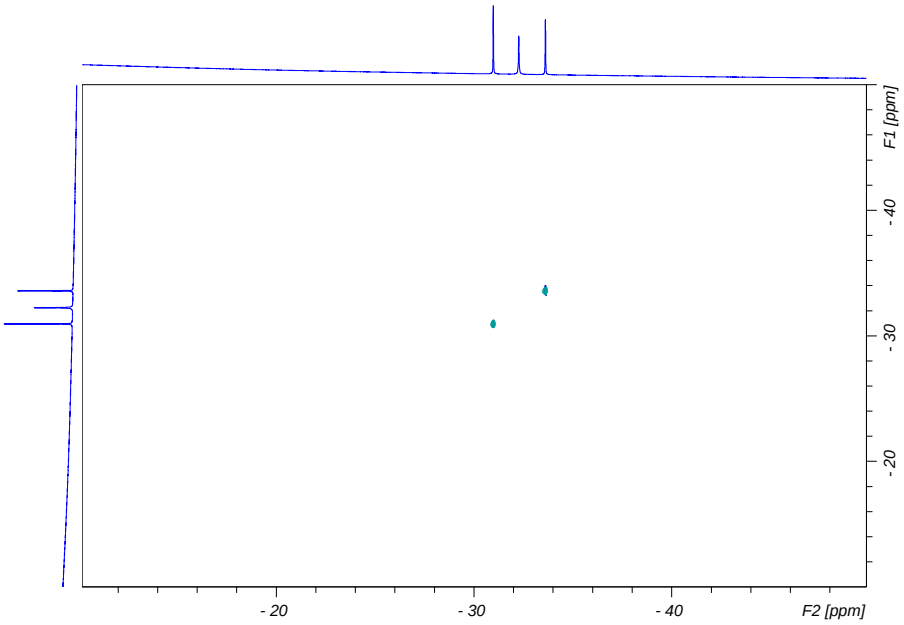

Figure A44: NOESY-NMR spectrum for complex $\mathbf{Fe^{IV}(ppz)_3}$.

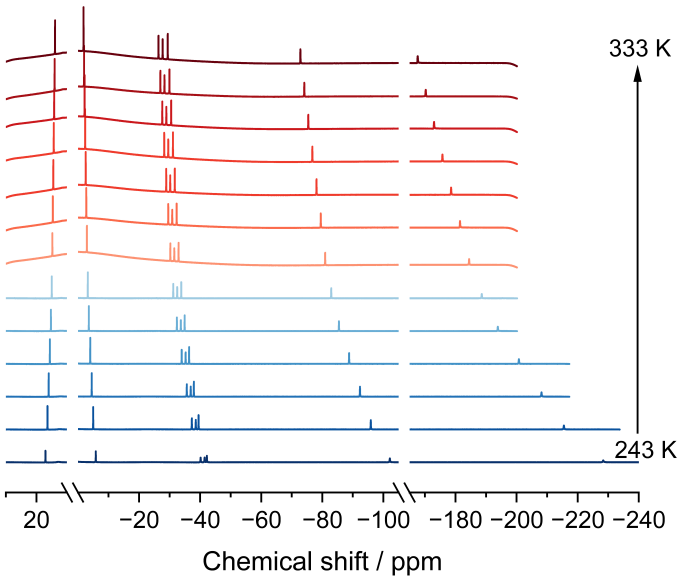

Figure A45: ^{1}H-NMR-spectra of complex $\mathbf{Fe^{IV}(ppz)_3}$ from 243 to 333 K.

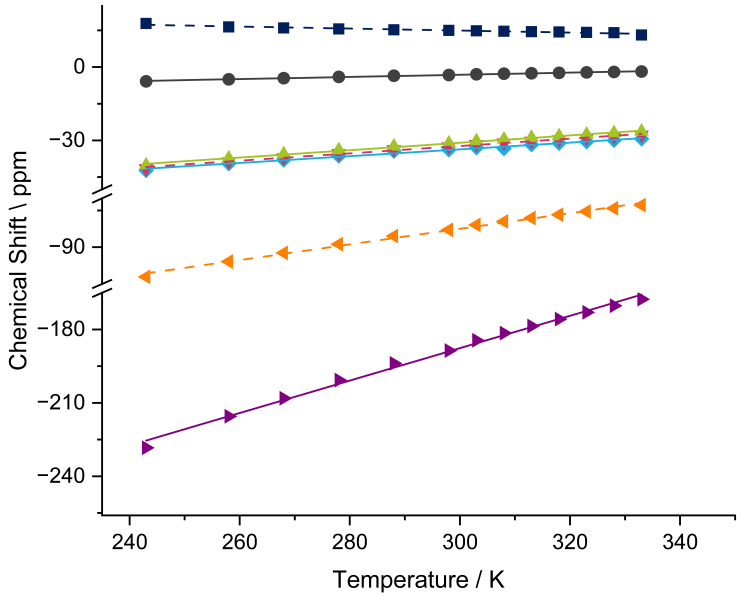

Figure A46: Curie-Plot of complex $\mathbf{Fe^{IV}(ppz)_3}$ from 243 to 333 K on the marked positions. Dashed line represents pyrazole-based protons, solid lines represent phenyl-based protons.

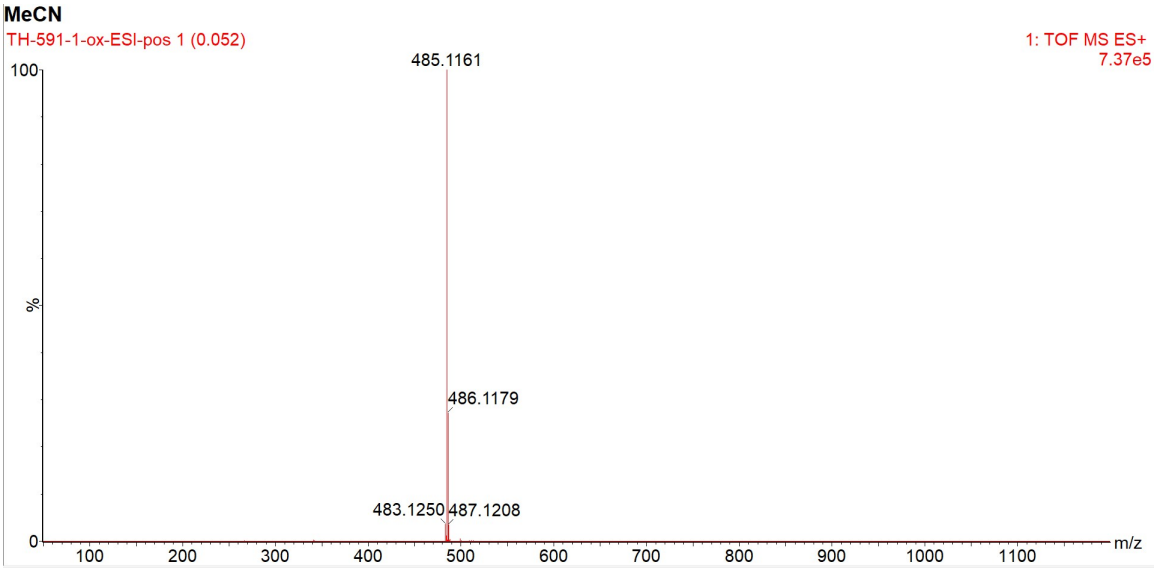

Figure A47: ESI-MS spectrum of complex $\mathbf{Fe^{IV}(ppz)_3}$ in MeCN.

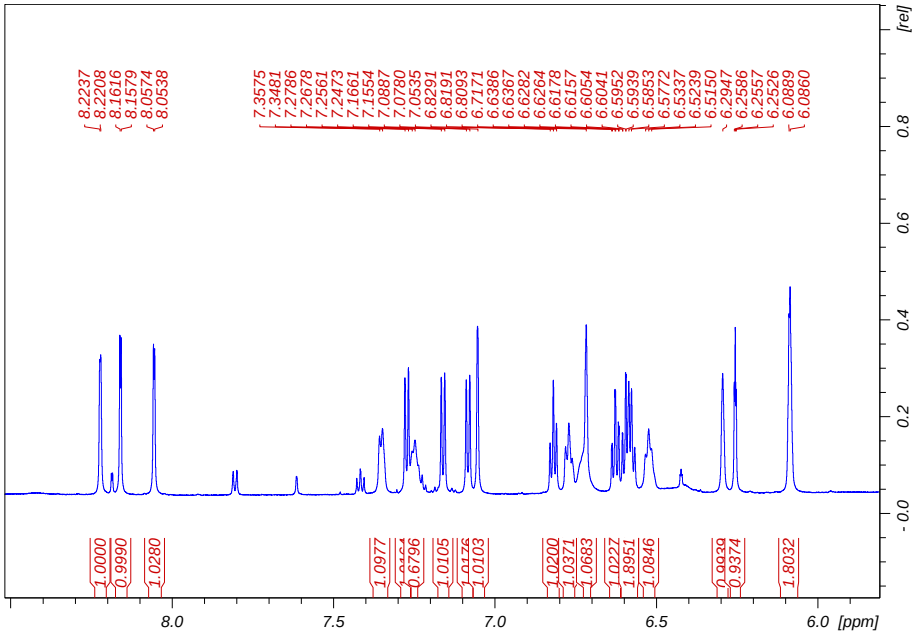

Figure A48: ^{1}H-NMR spectrum for complex $\mathbf{Fe^{II}(ppz)_3}$, integrated signals represent the *mer*-species of the complex.

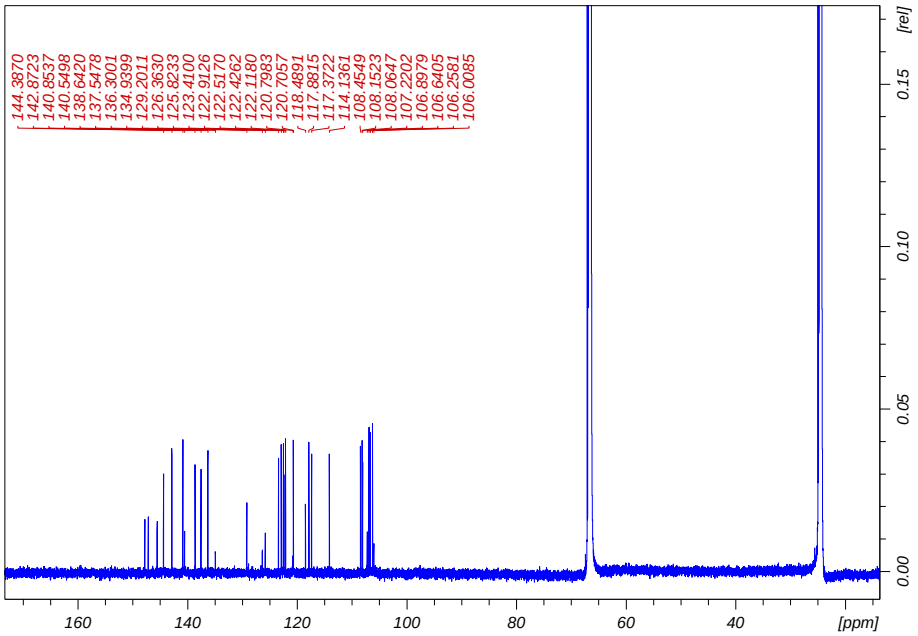

Figure A49: ^{13}H-NMR spectrum for complex $\mathbf{Fe^{II}(ppz)_3}$, integrated signals represent the *mer*-species of the complex.

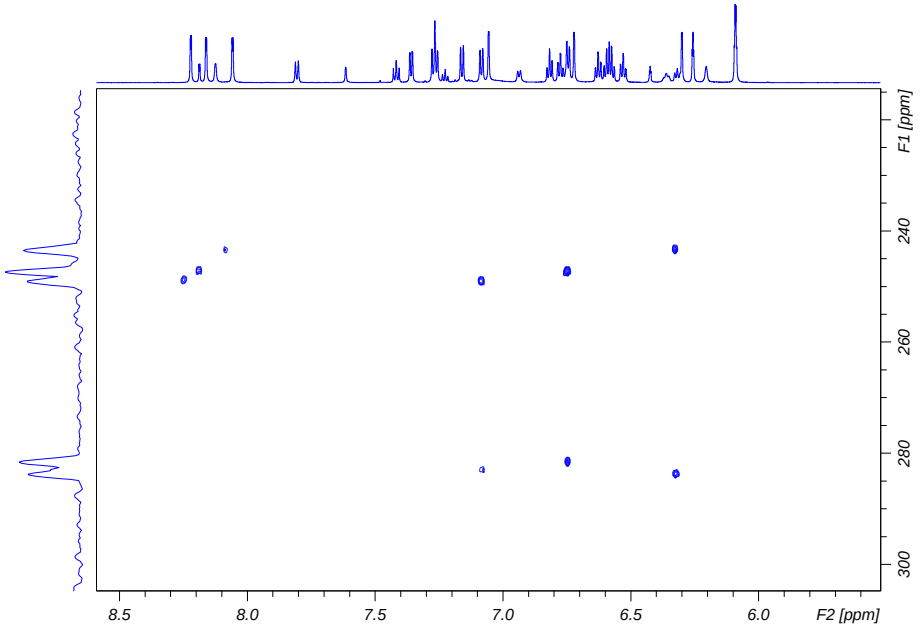

Figure A50: ^{15}N-HMBC-NMR spectrum for complex $\mathbf{Fe^{II}(ppz)_3}$.

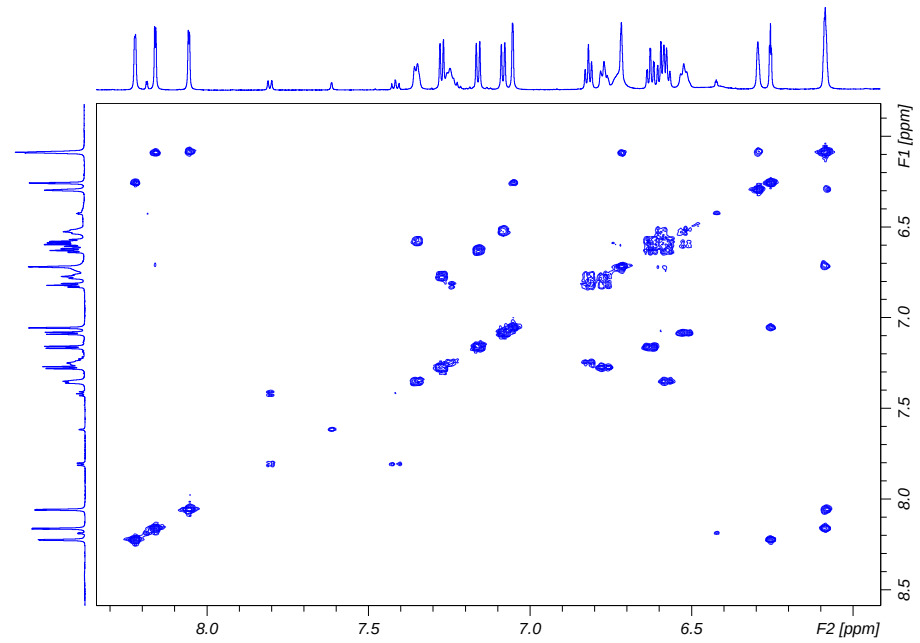

Figure A51: COSY-NMR spectrum for complex $\mathbf{Fe^{II}(ppz)_3}$.

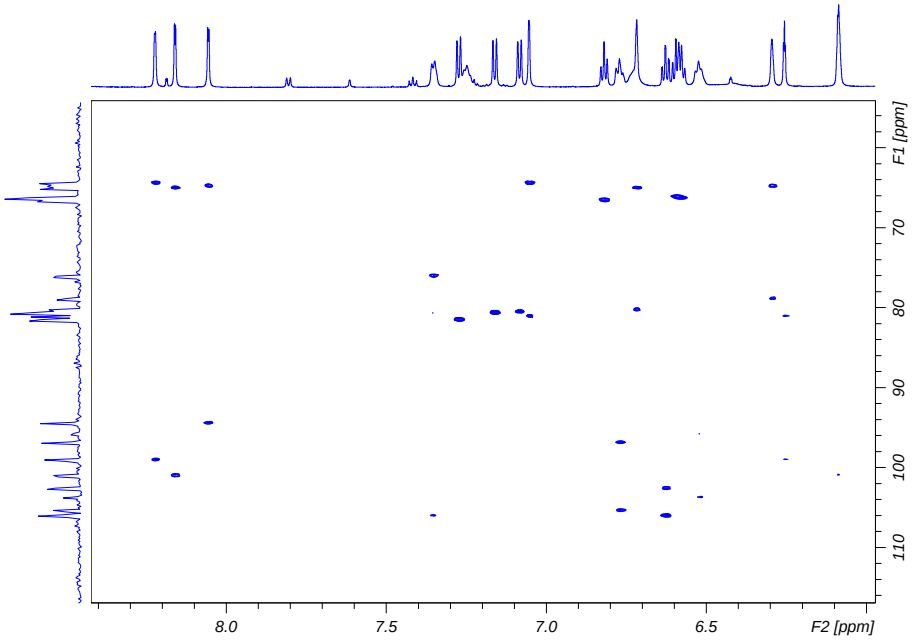

Figure A52: HMBC-NMR spectrum for complex $\mathbf{Fe^{II}(ppz)_3}$.

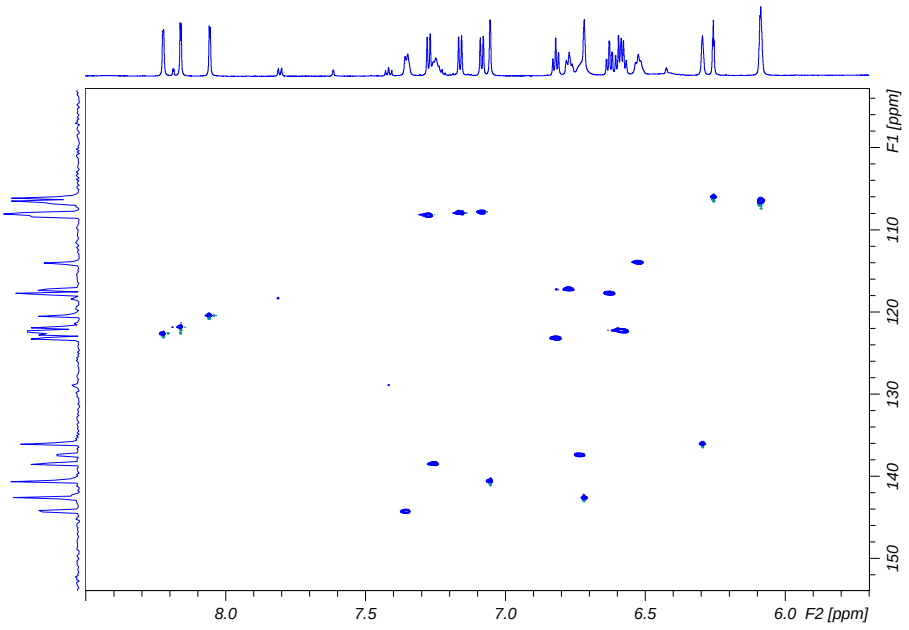

Figure A53: HSQC-NMR spectrum for complex $\mathbf{Fe^{II}(ppz)_3}$.

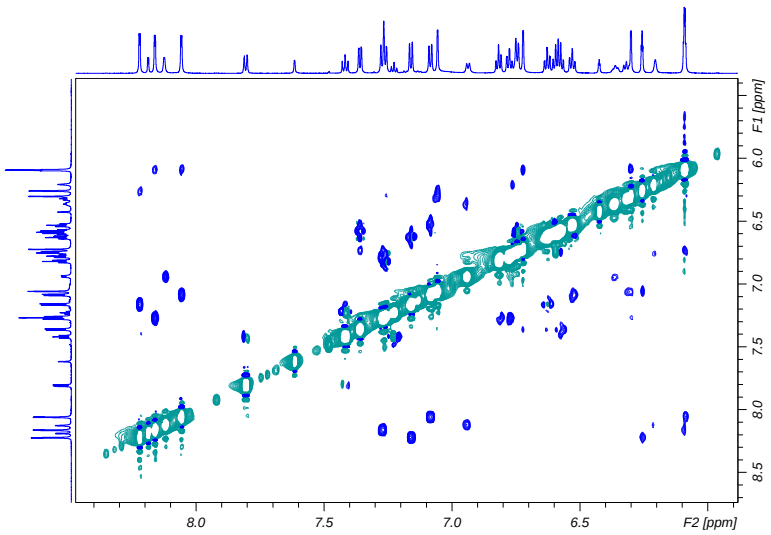

Figure A54: NOESY-NMR spectrum for complex $\mathbf{Fe^{II}(ppz)_3}$.

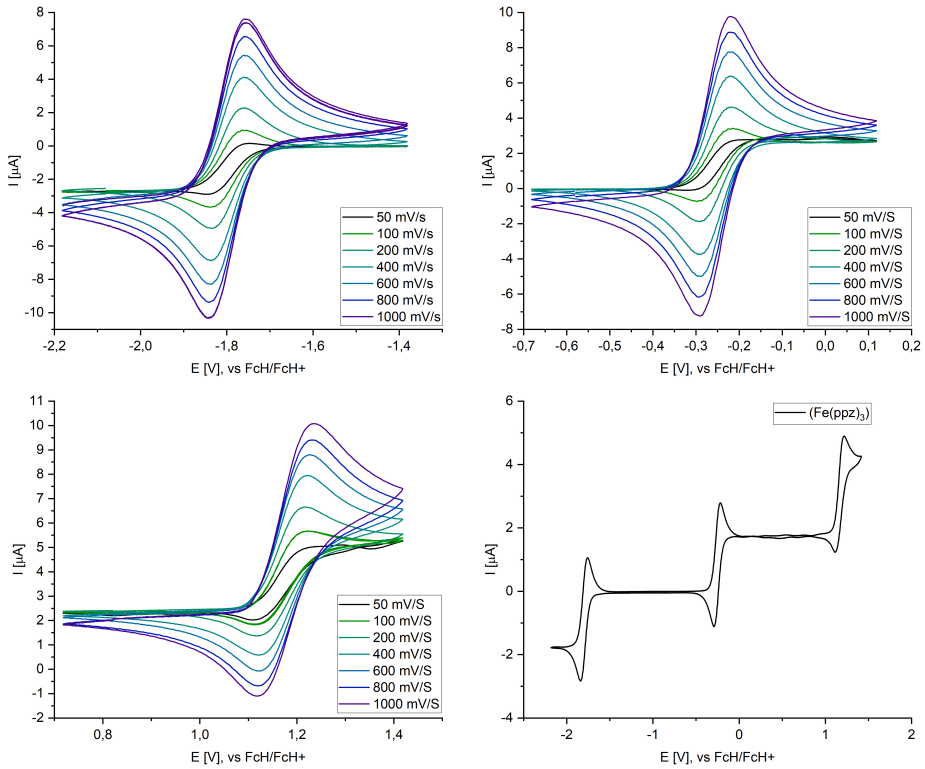

Figure A55: Overview of $\mathbf{Fe^{III}(ppz)_3}$ CV-data. Complete overview and the different redoxcouples at scanrates from 50 to 1000 mV/s.

Table A6: Cyclic Voltammetry data for **Fe(ppz)$_3$** at different scan rates at $E_{1/2}$= -1.80 V vs. Fc/Fc^+

Scanrate	[mV/s]	50	100	200	400	600	800	1000
E_{pc}	[V]	-1.835	-1.828	-1.833	-1.835	-1.835	-1.840	-1.838
E_{pa}	[V]	-1.762	-1.765	-1.759	-1.762	-1.760	-1.760	-1.762
$E_{1/2}$	[V]	-1.80	-1.80	-1.80	-1.80	-1.80	-1.80	-1.80
ΔE	[V]	0.073	0.063	0.074	0.073	0.076	0.081	0.076
I_{pc}	[µA]	-1.68	-2.73	-4.11	-5.76	-7.11	-8.17	-9.07
I_{pa}	[µA]	1.64	2.78	4.11	5.87	7.14	8,24	9.14
I_{pa}/I_{pc}		-0.98	-1.02	-1.00	-1.02	-1.00	-1.01	-1.01

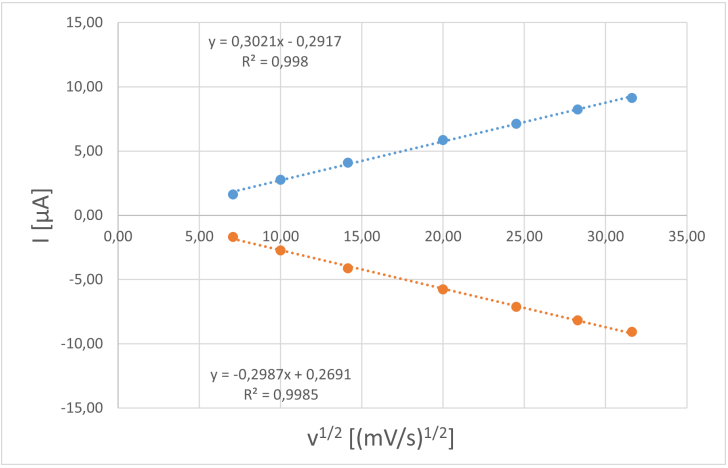

Figure A56: Plotted data of Randles-Sevcik-Equation at different scan rates for **Fe(ppz)$_3$** $E_{1/2}$= -1.80 V vs. Fc/Fc^+

Table A7: Cyclic Voltammetry data for $Fe(ppz)_3$ at different scan rates at $E_{1/2}$= -0.26 V vs. Fc/Fc^+

Scanrate	[mV/s]	50	100	200	400	600	800	1000
E_{pc}	[V]	-0.296	-0.286	-0.289	-0.289	-0.289	-0.294	-0.291
E_{pa}	[V]	-0.223	-0.225	-0.223	-0.223	-0.225	-0.223	-0.223
$E_{1/2}$	[V]	-0.26	-0.26	-0.26	-0.26	-0.26	-0.26	-0.26
ΔE	[V]	0.073	0.061	0.066	0.066	0.063	0.071	0.068
I_{pc}	[µA]	-1.88	-2.65	-3.80	-5.43	-6.88	-8.00	-9.00
I_{pa}	[µA]	1.55	2.41	3.80	5.53	6,69	7.79	8.72
I_{pc}/I_{pa}		-0.83	-0.91	-1.00	-1.02	-0.97	-0.97	-0.97

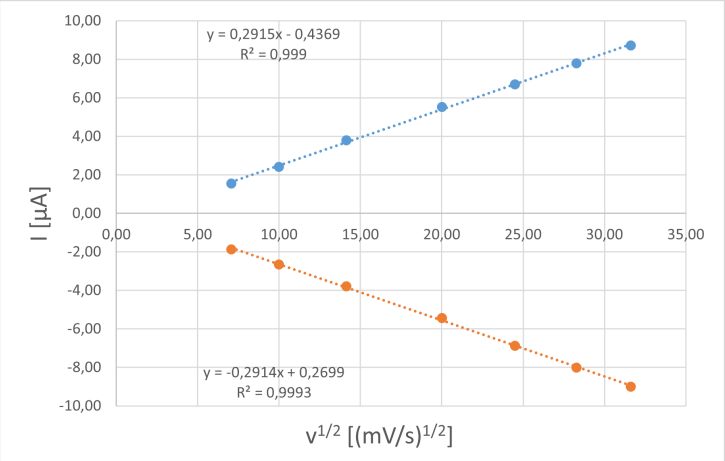

Figure A57: Plotted data of Randles-Sevcik-Equation at different scan rates for **$Fe(ppz)_3$** at $E_{1/2}$= -0.26 V vs. Fc/Fc^+

Table A8: Cyclic Voltammetry data for $Fe(ppz)_3$ at different scan rates at $E_{1/2}$= 1.17 V vs. Fc/Fc^+

Scanrate	[mV/s]	50	100	200	400	600	800	1000
E_{pc}	[V]	1.126	1.131	1.123	1.128	1.128	1.128	1.126
E_{pa}	[V]	1.211	1.209	1.209	1.216	1.216	1.221	1.226
$E_{1/2}$	[V]	1.17	1.17	1.17	1.17	1.17	1.17	1.18
ΔE	[V]	0.085	0.078	0.085	0.088	0.088	0.093	0.100
I_{pc}	[µA]	-1.70	-1.88	-2.77	-3.77	-4.57	-5.17	-5.73
I_{pa}	[µA]	1.35	2.02	2.92	3.97	4.64	5.12	5.52
I_{pc}/I_{pa}		-0.80	-1.08	-1.06	-1.05	-1.01	-0.99	-0.96

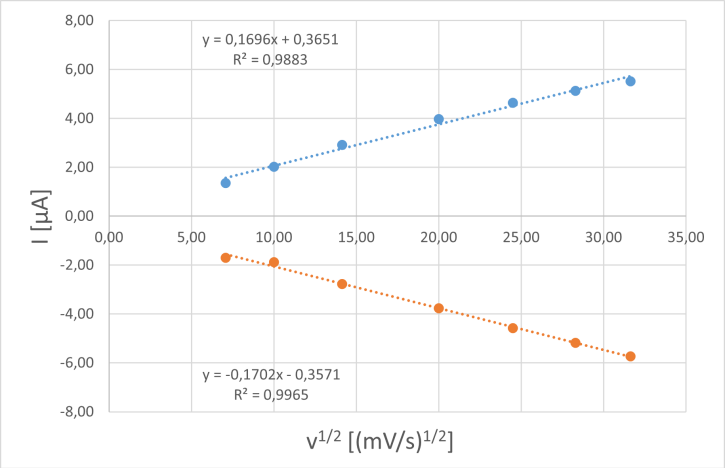

Figure A58: Plotted data of Randles-Sevcik-Equation at different scan rates for **$Fe(ppz)_3$** at $E_{1/2}$= 1.17 V vs. Fc/Fc^+

Table A9: Crystal structure data and refinement for **Fe(MeOppz)$_3$**

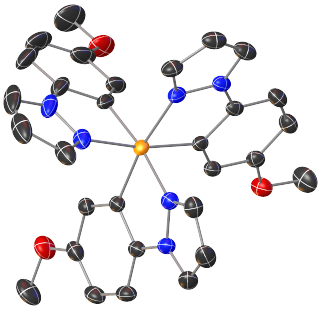

Identification code	TH-455-1 (TH_0231)
CCDC number	2191104
Empirical formula	$C_{30}H_{27}FeN_6O_3$
Moiety formula	$C_{30}H_{27}FeN_6O_3$
Formula weight	575.42 Da
Color	red
Shape	block
Temperature	120(2) K
Wavelength	0.71073 Å
Crystal system	Trigonal
Space group	R-3
Unit cell dimensions	a = 19.9138(11) Å α =90°
	b = 19.9138(11) Å β = 90°
	c = 48.704(4) Å γ = 120°
Volume	16727(2) Å^3
Z	24
Density (calculated)	1.371 mg/m^3
Absorption coefficient	0.584 mm^{-1}
F(000)	7176
Crystal size	0.18 x 0.18 x 0.10 mm^3
Theta range for data collection	2.400 to 32.048°
Index ranges	-29≤h≤29, -29≤k≤29, -72≤l≤72
Reflections collected	660843
Independent reflections	12775 [R(int) = 0.0674]
Completeness to theta = 25.242°	96.8 %
Absorption correction	Semi-empirical from equivalents
Refinement method	Full-matrix least-squares on F^2
Data / restraints / parameters	12775 / 0 / 505
Goodness-of-fit on F2	1.143
Final R indices [I>2sigma(I)]	R1 = 0.0350, wR2 = 0.0834
R indices (all data)	R1 = 0.0530, wR2 = 0.0997
Largest diff. peak and hole	0.701 e/Å^{-3} (0.2.28 Å^{-3} from H13D) and -0.556 e/Å^{-3} (0.64 Å^{-3} from Fe1)

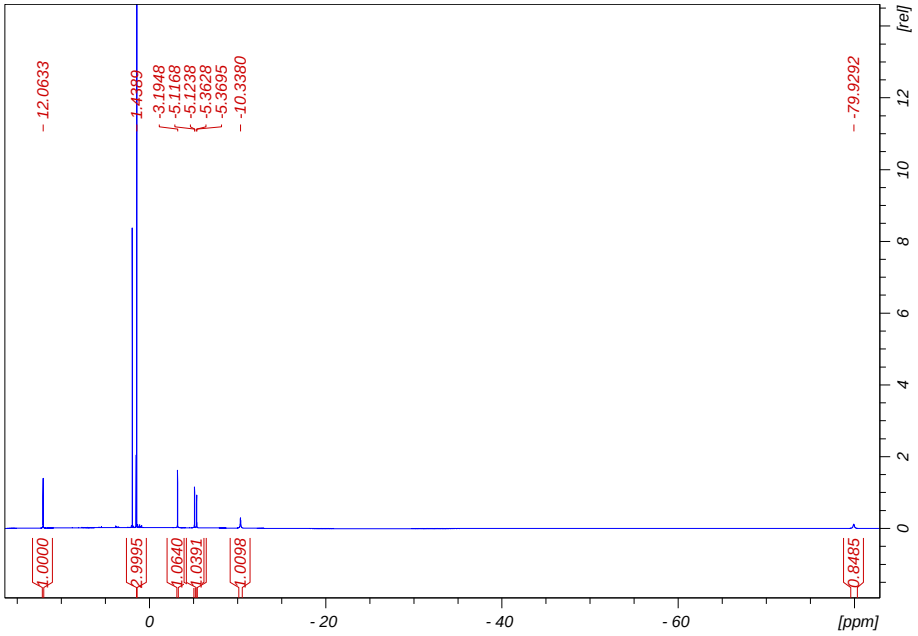

Figure A59: ^{1}H-NMR spectrum for complex **Fe(MeOppz)$_3$** in CD_3CN.

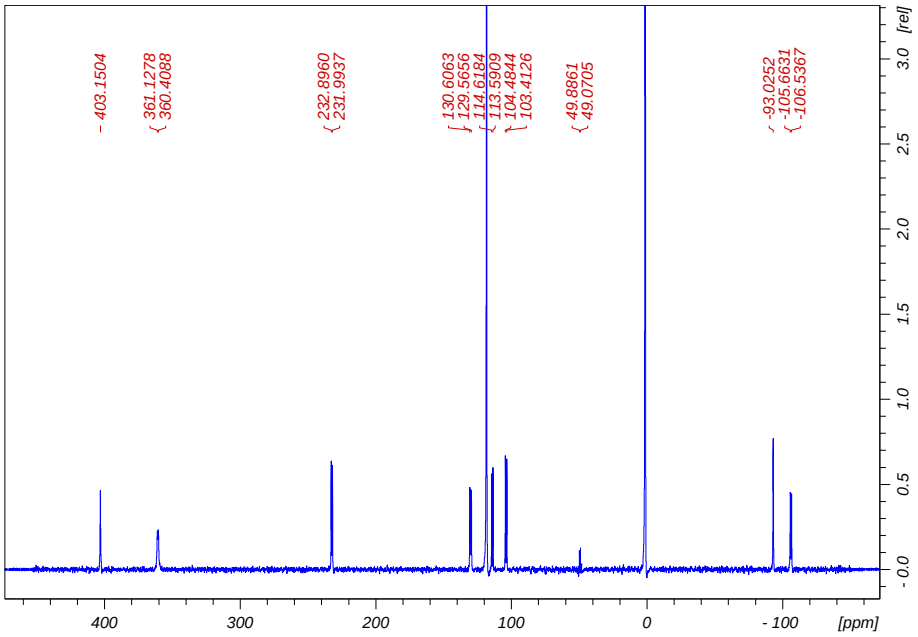

Figure A60: ^{13}C-NMR spectrum for complex **Fe(MeOppz)$_3$** in CD_3CN.

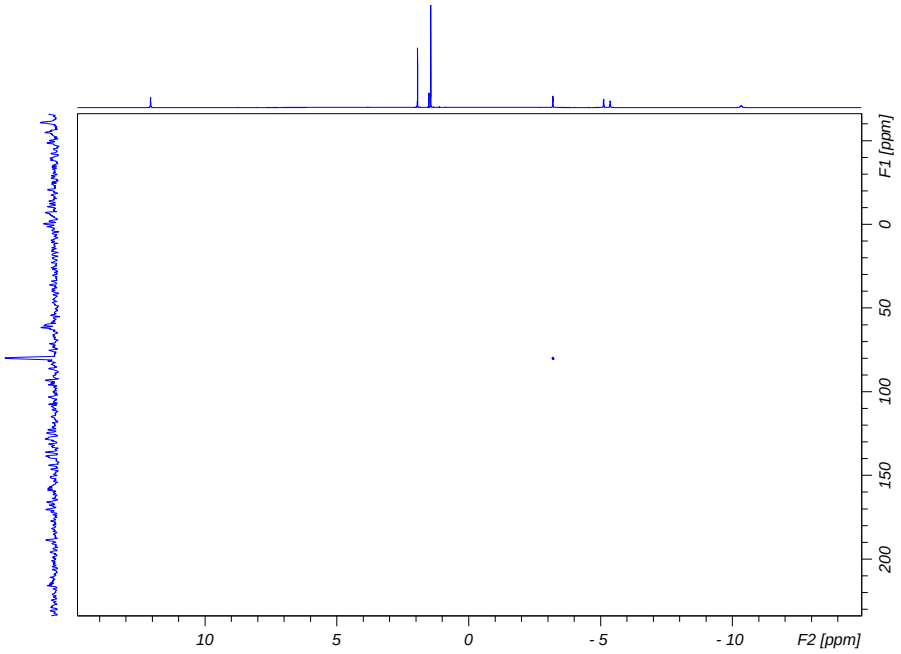

Figure A61: ^{15}N-HMBC-NMR spectrum for complex **Fe(MeOppz)$_3$** in CD_3CN.

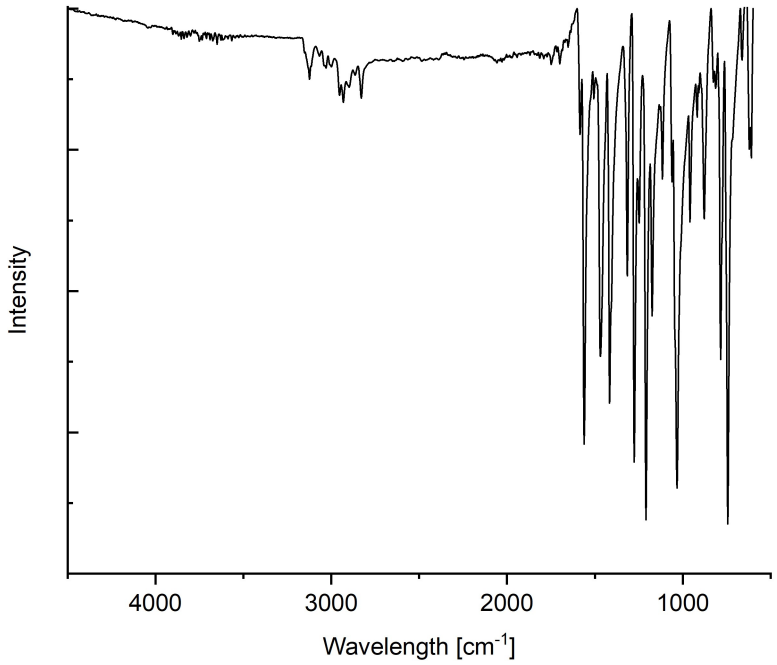

Figure A62: ATR-IR spectrum for complex **Fe(MeOppz)$_3$**

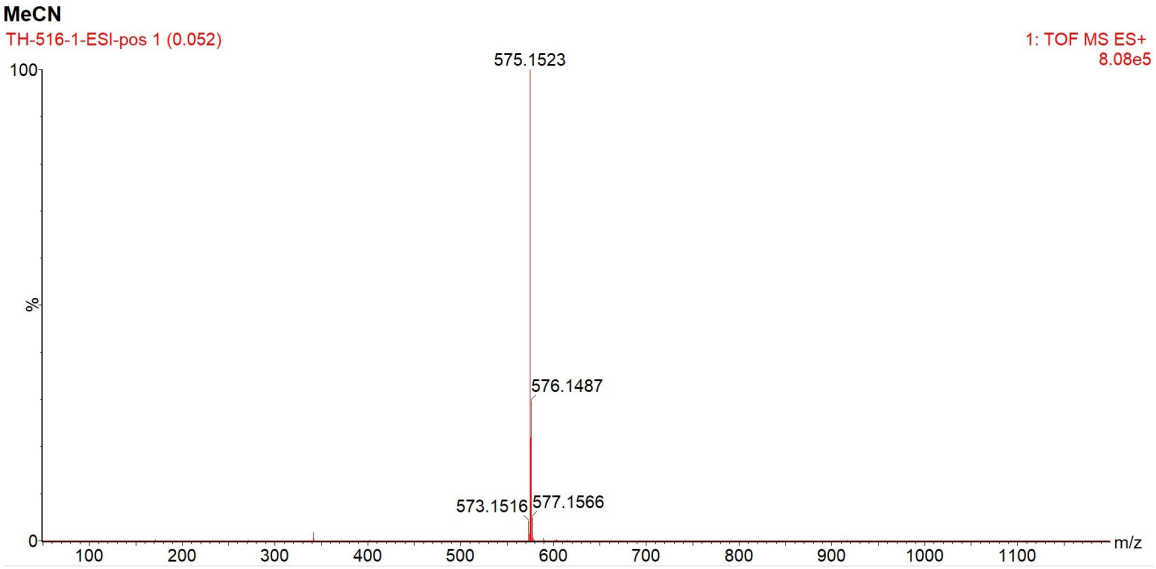

Figure A63: ESI-MS spectrum of complex **Fe(MeOppz)$_3$** in MeCN

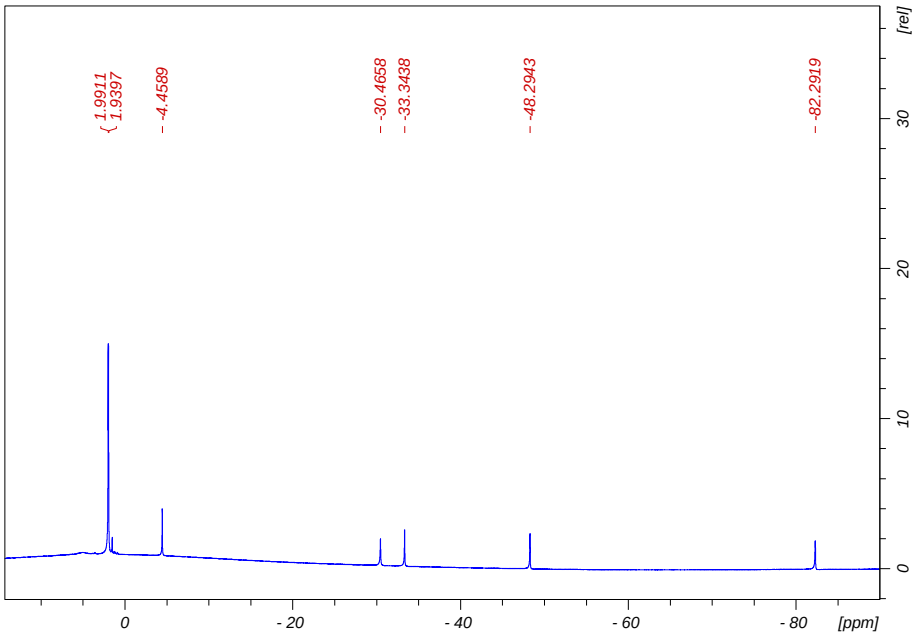

Figure A64: ^{1}H-NMR spectrum for complex **Fe^{IV}(MeOppz)$_3$** in CD_3CN, part 1.

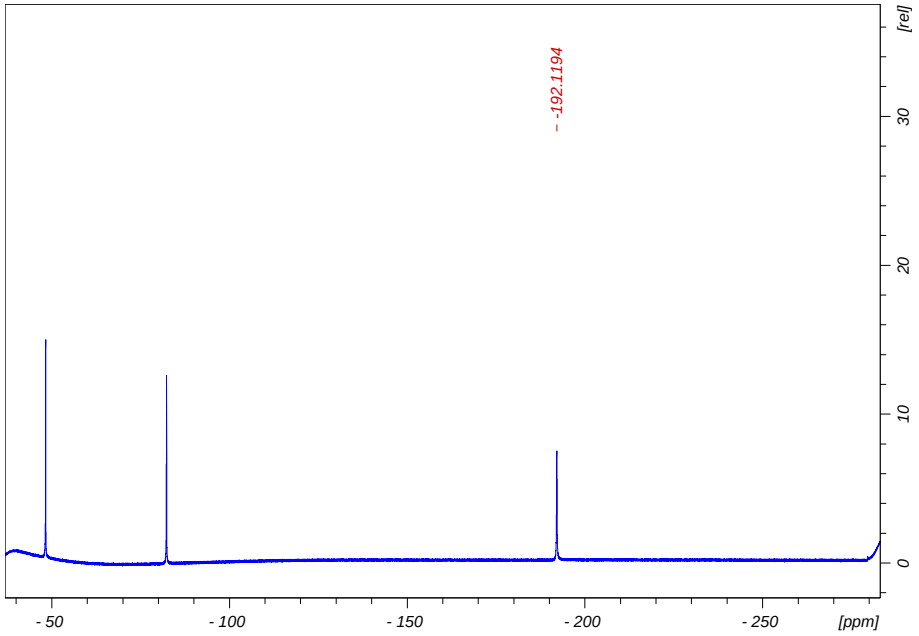

Figure A65: ^{1}H-NMR spectrum for complex $\mathbf{Fe^{IV}(MeOppz)_3}$ in CD_3CN, part 2.

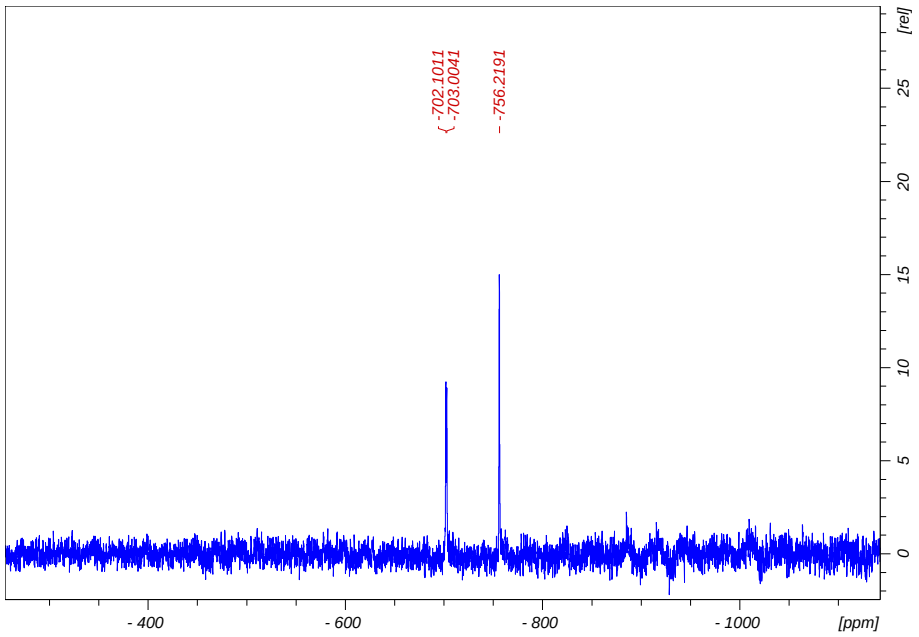

Figure A66: ^{13}C-NMR spectrum for complex $\mathbf{Fe^{IV}(MeOppz)_3}$ in CD_3CN, part 1.

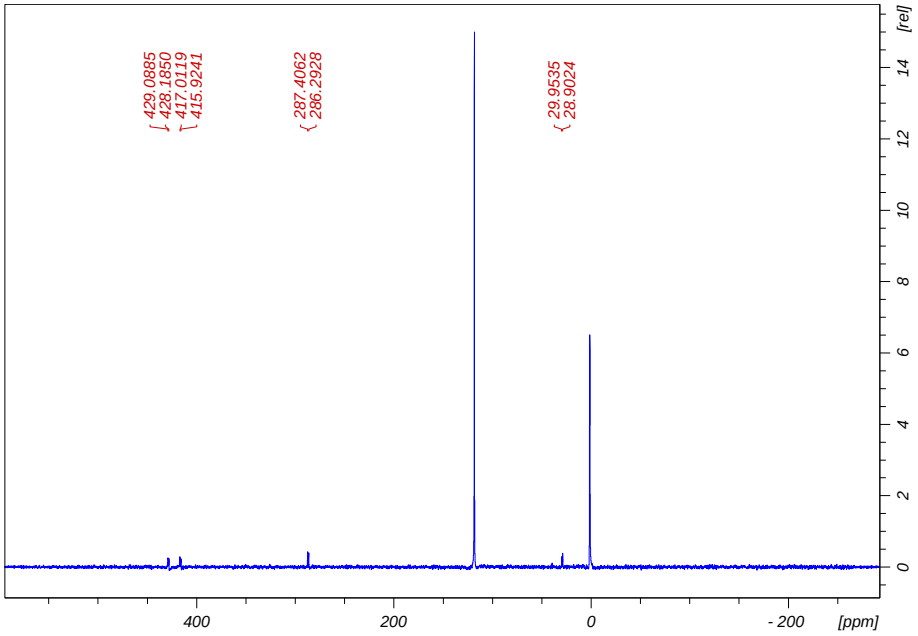

Figure A67: ^{13}C-NMR spectrum for complex $\mathbf{Fe^{IV}(MeOppz)_3}$ in CD_3CN, part 2.

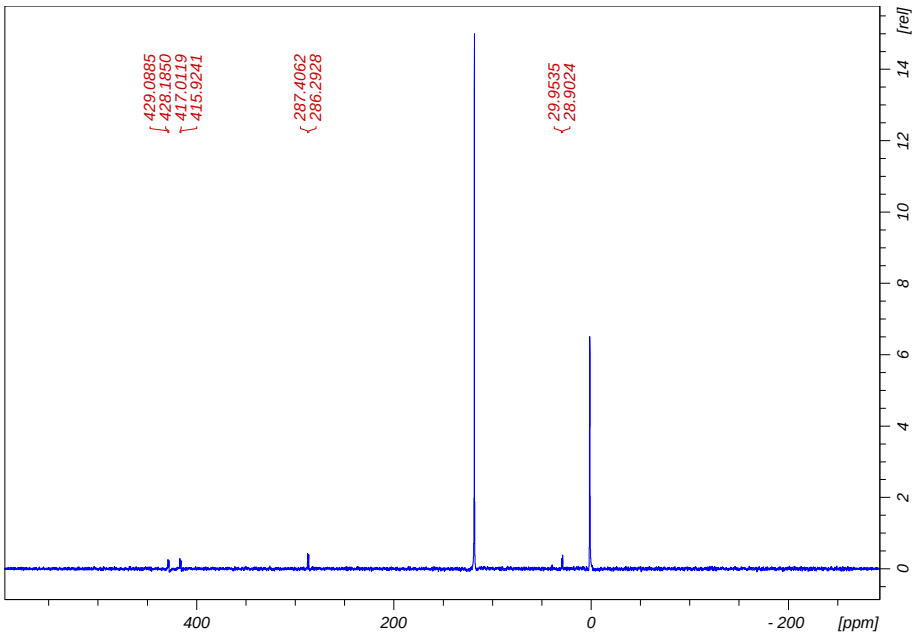

Figure A68: ^{13}C-NMR spectrum for complex $\mathbf{Fe^{IV}(MeOppz)_3}$ in CD_3CN, part 3.

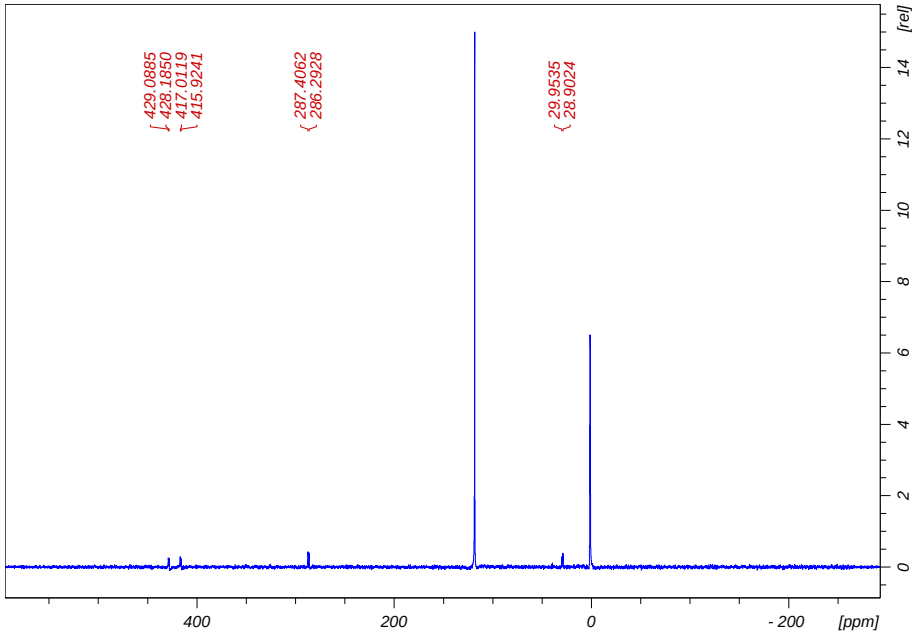

Figure A69: ^{13}C-NMR spectrum for complex $\mathbf{Fe^{IV}(MeOppz)_3}$ in CD_3CN, part 4.

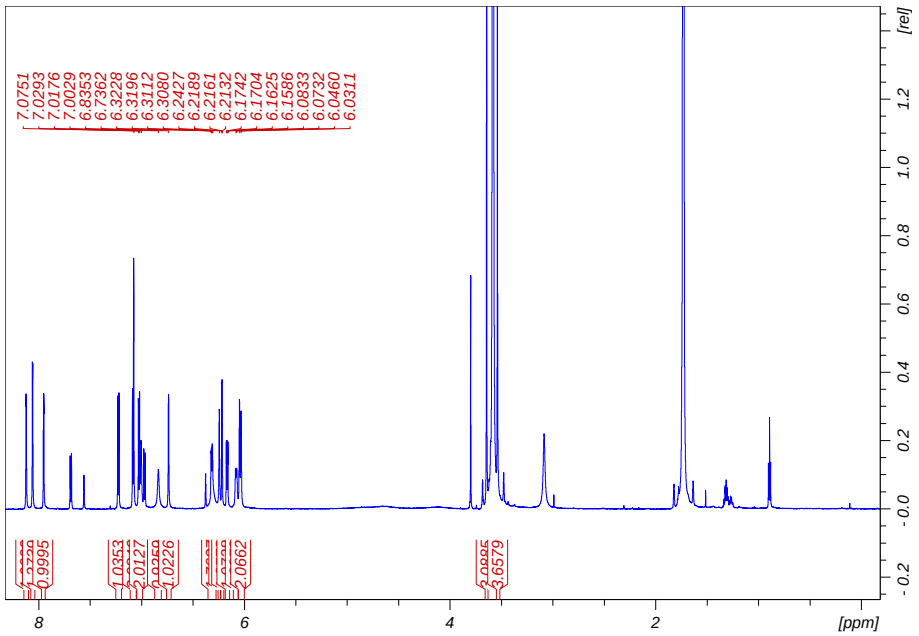

Figure A70: ^{1}H-NMR spectrum for complex ***mer*-$\mathbf{Fe^{II}(MeOppz)_3}$** in THF-$d_8$.

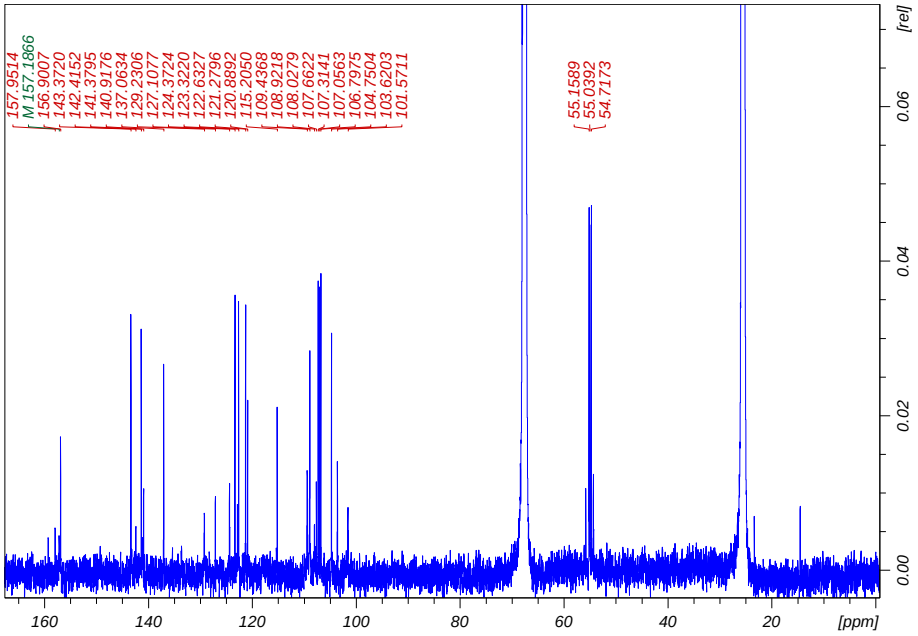

Figure A71: ^{13}C-NMR spectrum for complex ***mer*-Fe^{II}(MeOppz)$_3$** in THF-d$_8$.

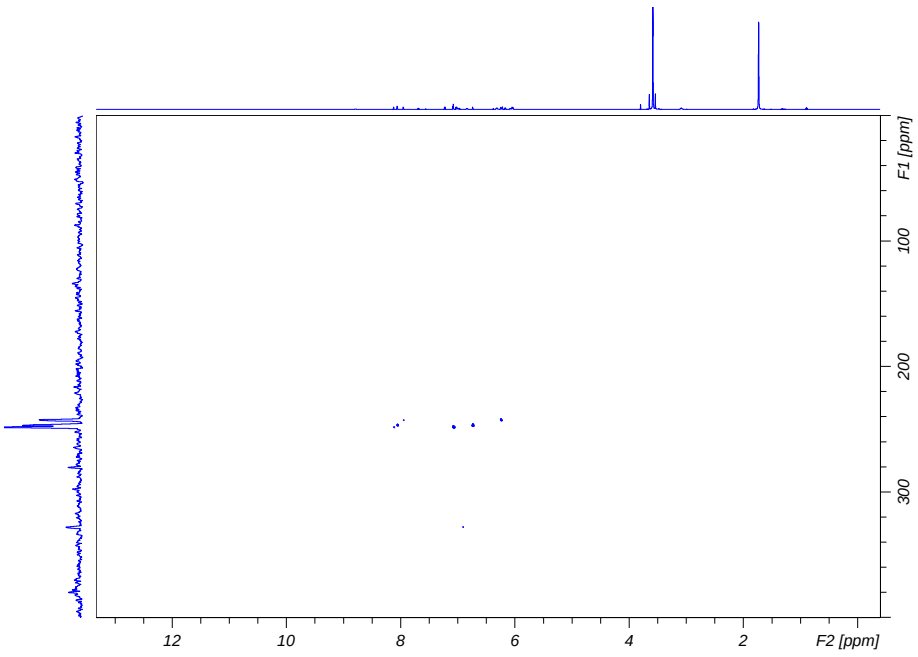

Figure A72: ^{15}N-HMBC-NMR spectrum for complex ***mer*-Fe^{II}(MeOppz)$_3$** in THF-d$_8$.

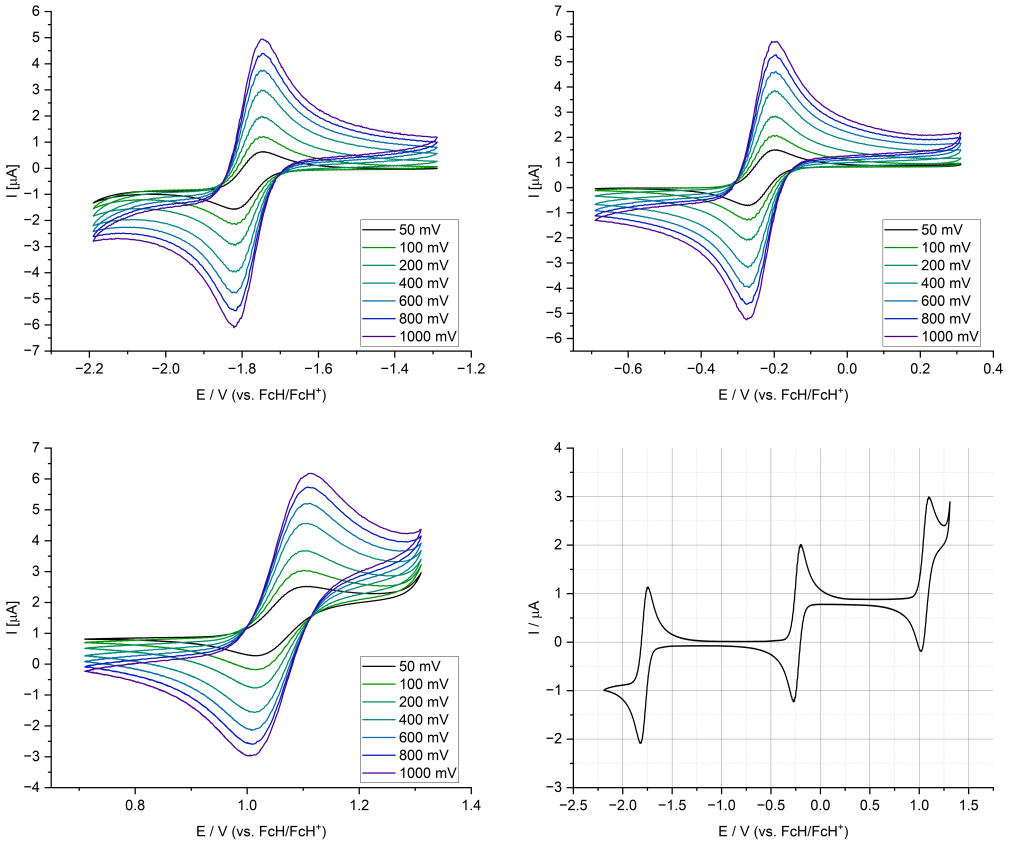

Figure A73: Overview of **Fe^{III}(MeOppz)$_3$** CV-data. Complete overview and the different redoxcouples at scan-rates from 50 to 1000 mV/s.

Table A10: Cyclic Voltammetry data for **Fe(MeOppz)$_3$** at different scan rates at $E_{1/2}$= -1.78 V vs. Fc/Fc^+

Scanrate	[mV/s]	50	100	200	400	600	800	1000
E_{pc}	[V]	-1.746	-1.753	-1.751	-1.748	-1.751	-1.748	-1.751
E_{pa}	[V]	-1.814	-1.812	-1.814	-1.812	-1.817	-1.814	-1.819
$E_{1/2}$	[V]	-1.78	-1.78	-1.78	-1.78	-1,78	-1.78	-1.78
ΔE	[V]	-0.068	-0.059	-0.063	-0.063	-0.066	-0.066	-0.068
I_{pc}	[µA]	-1.18	-1.61	-2.34	-3.35	-4.11	-4.71	-5.33
I_{pa}	[µA]	1.27	1.80	2.52	3.59	4,37	5.03	5.57
I_{pc}/I_{pa}		-1.08	-1.12	-1.08	-1,07	-1.06	-1.07	-1.04

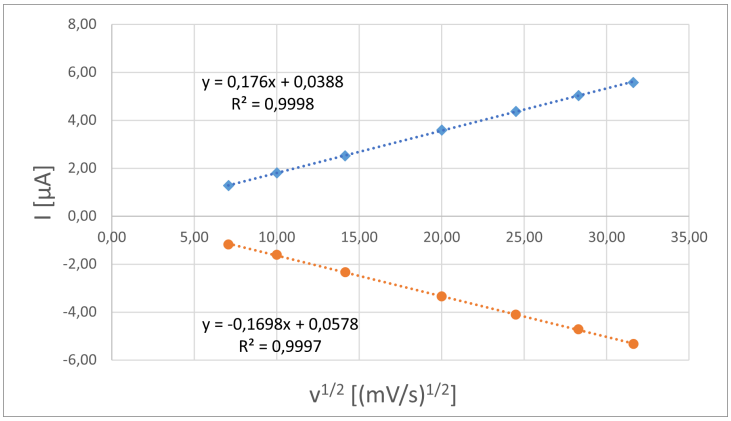

Figure A74: Plotted data of Randles-Sevcik-Equation at different scan rates for **Fe(MeOppz)$_3$** $E_{1/2}$= -1.78 V vs. Fc/Fc^+

Table A11: Cyclic Voltammetry data for **Fe(MeOppz)$_3$** at different scan rates at $E_{1/2}$= -0.23 V vs. Fc/Fc^+

Scanrate	[mV/s]	50	100	200	400	600	800	1000
E_{pc}	[V]	-0.268	-0.265	-0.265	-0.275	-0.268	-0.265	-0.265
E_{pa}	[V]	-0.207	-0.204	-0.197	-0.199	-0.197	-0.199	-0.207
$E_{1/2}$	[V]	-0.24	-0.23	-0.23	-0.24	-0.23	-0,23	-0.24
ΔE	[V]	0.061	0.061	0.068	0.076	0.071	0,066	0.059
I_{pc}	[µA]	-1.28	-1.72	-2.54	-3.62	-4.41	-5.05	-5.62
I_{pa}	[µA]	1.27	1.82	2.56	3.52	4,35	5.06	5.61
I_{pc}/I_{pa}		-0.99	-1.06	-1.01	-0.97	-0.99	-1.00	-1.00

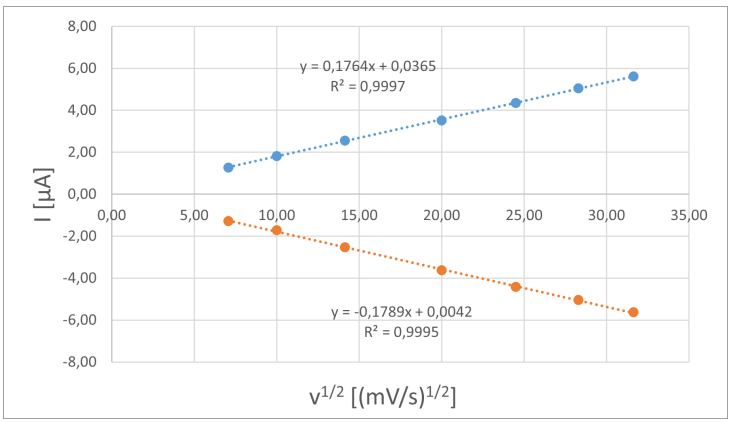

Figure A75: Plotted data of Randles-Sevcik-Equation at different scan rates for **Fe(MeOppz)$_3$** $E_{1/2}$= -0.23 V vs. Fc/Fc^+

Table A12: Cyclic Voltammetry data for **Fe(MeOppz)$_3$** at different scan rates at $E_{1/2}$= 1.06 V vs. Fc/Fc^+

Scanrate	[mV/s]	50	100	200	400	600	800	1000
E_{pc}	[V]	1.023	1.023	1.027	1.018	1.018	1.013	1.013
E_{pa}	[V]	1.091	1.088	1.096	1.093	1.103	1.103	1.106
$E_{1/2}$	[V]	1.06	1.06	1.06	1.06	1.06	1.06	1.06
ΔE	[V]	0.068	0.066	0.068	0.076	0.086	0.090	0.093
I_{pc}	[µA]	-1.29	-1.73	-2.10	-3.24	-3.84	-4.31	-4.72
I_{pa}	[µA]	0.94	1.38	1.90	2.71	3.27	3.67	4.05
I_{pc}/I_{pa}		-0.73	-0.80	-0.91	-0.84	-0.85	-0.85	-0.86

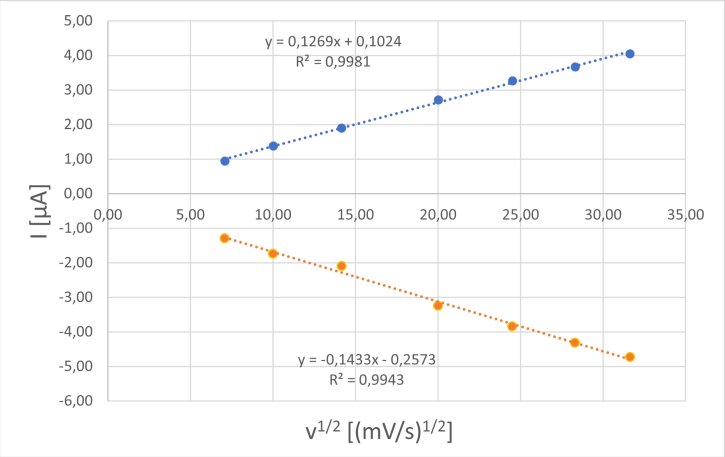

Figure A76: Plotted data of Randles-Sevcik-Equation at different scan rates for **Fe(MeOppz)$_3$** $E_{1/2}$= 1.06 V vs. Fc/Fc^+

Table A13: Crystal structure data and refinement for **Fe(3Me-ppz)$_3$**

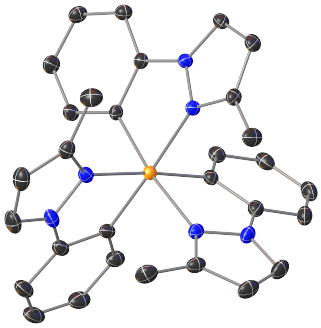

Identification code	mo_TanHir_0256_0ma_a
CCDC number	
Empirical formula	$C_{30}H_{27}FeN_6$
Moiety formula	
Formula weight	527.42 Da
Color	
Shape	
Temperature	120(2) K
Wavelength	0.71073 Å
Crystal system	Monoclinic
Space group	$P2_1/c$
Unit cell dimensions	a = 16.4050(14) Å α =90° b = 8.9136(8) Å β = 90.331(3)° c = 16.7064(14) Å γ = 90°
Volume	2442.9(4) Å^3
Z	4
Density (calculated)	1.343 mg/m^3
Absorption coefficient	0.650 mm^{-1}
F(000)	1100
Crystal size	0.200 x 0.100 x 0.040 mm^3
Theta range for data collection	2.743 to 32.039°
Index ranges	-24≤h≤24, -13≤k≤13, -24≤l≤24
Reflections collected	259512
Independent reflections	8504 [R(int) = 0.0686]
Completeness to theta = 25.242°	99.8 %
Absorption correction	Semi-empirical from equivalents
Refinement method	Full-matrix least-squares on F^2
Data / restraints / parameters	8504 / 0 / 337
Goodness-of-fit on F2	1.106
Final R indices [I>2sigma(I)]	R1 = 0.0359, wR2 = 0.0849
R indices (all data)	R1 = 0.0413, wR2 = 0.0880
Largest diff. peak and hole	

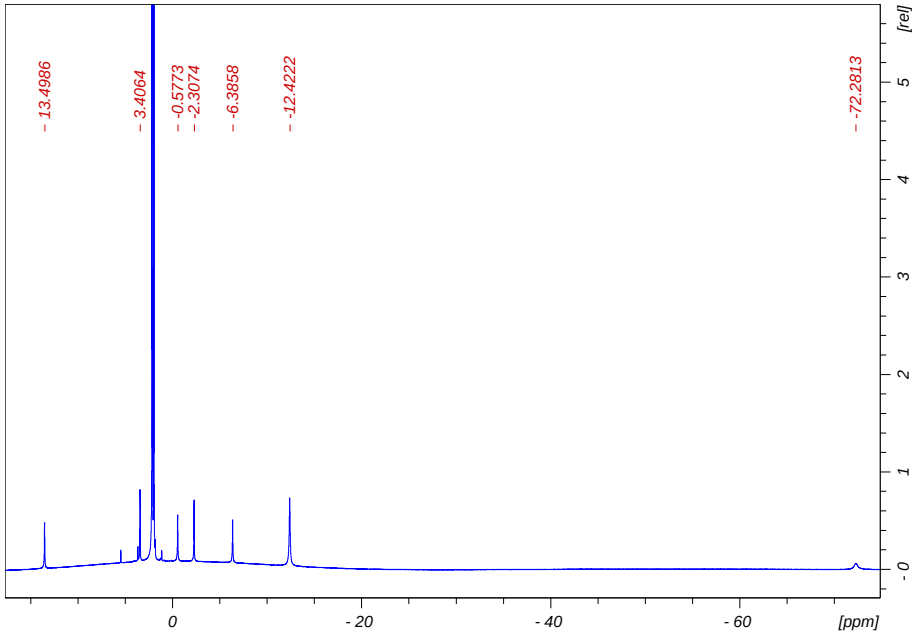

Figure A77: ^{1}H-NMR spectrum for complex $\mathbf{Fe^{III}(3Me\text{-}ppz)_3}$ in CD_3CN.

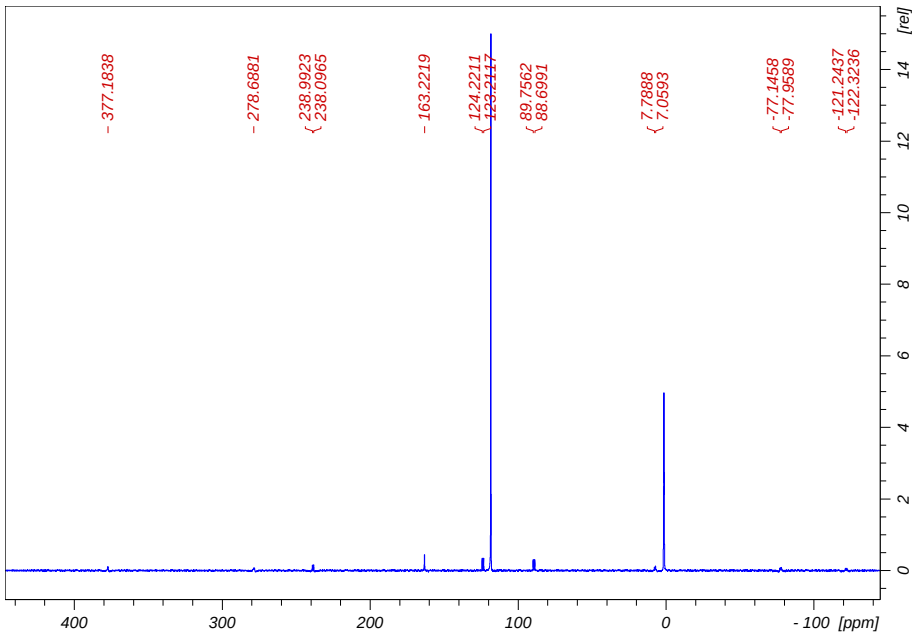

Figure A78: ^{13}C-NMR spectrum for complex $\mathbf{Fe^{III}(3Me\text{-}ppz)_3}$ in CD_3CN.

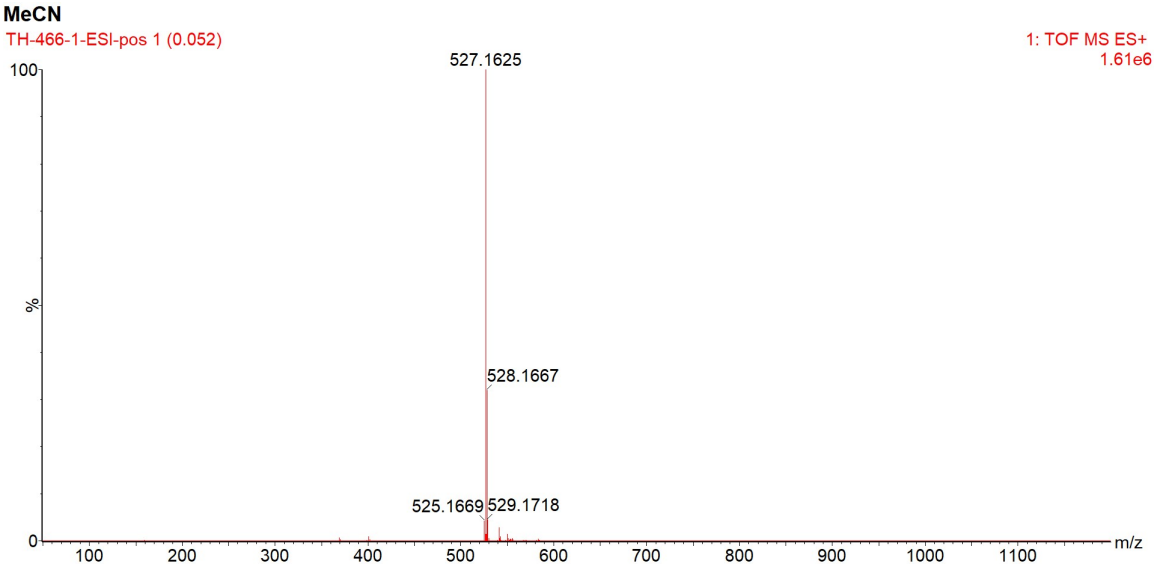

Figure A79: ESI-MS spectrum of complex **Fe(3Me-ppz)$_3$** in MeCN

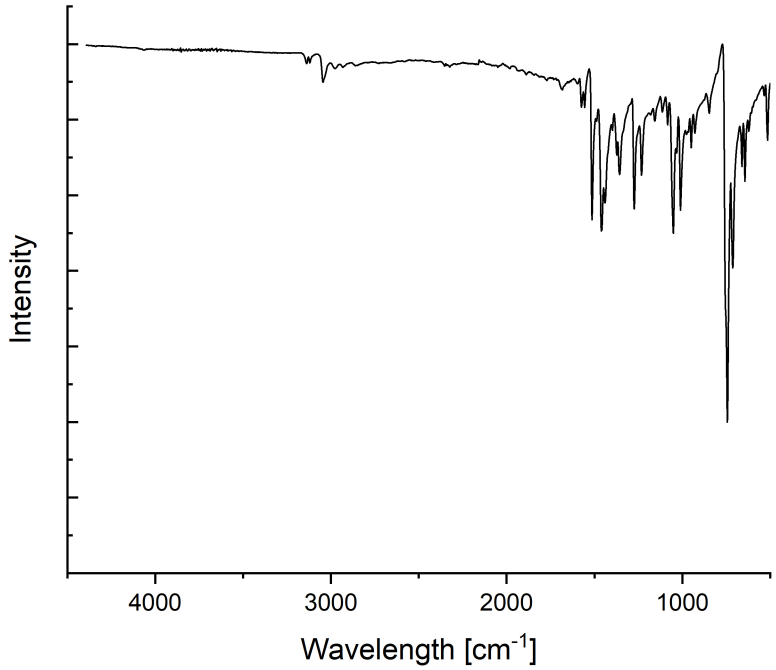

Figure A80: ATR-IR spectrum for complex **Fe^{III}(3Me-ppz)$_3$**.

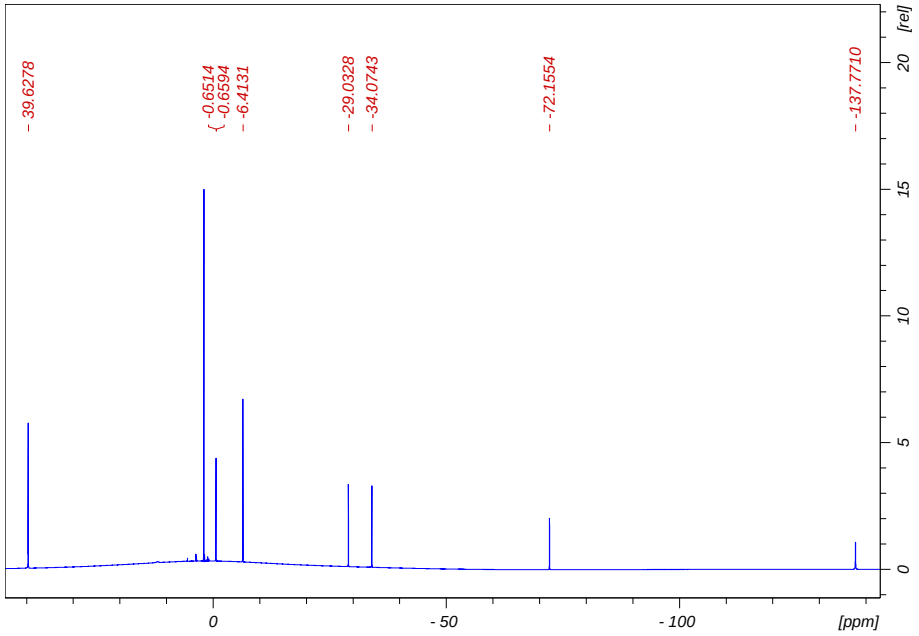

Figure A81: ^{1}H-NMR spectrum for complex $\mathbf{Fe^{IV}(3Me\text{-}ppz)_3}$ in CD_3CN.

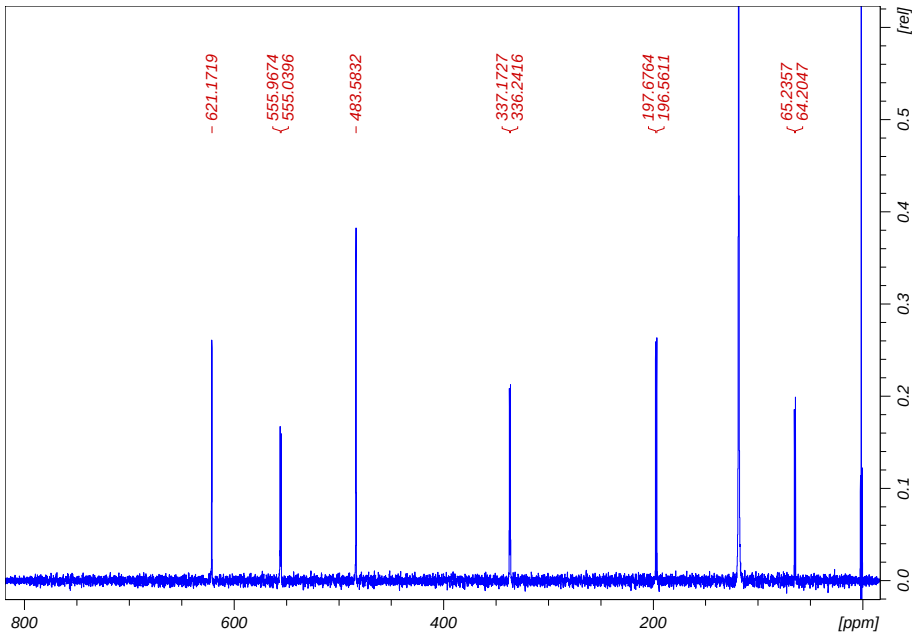

Figure A82: ^{13}C-NMR spectrum for complex $\mathbf{Fe^{IV}(3Me\text{-}ppz)_3}$ in CD_3CN, part 1.

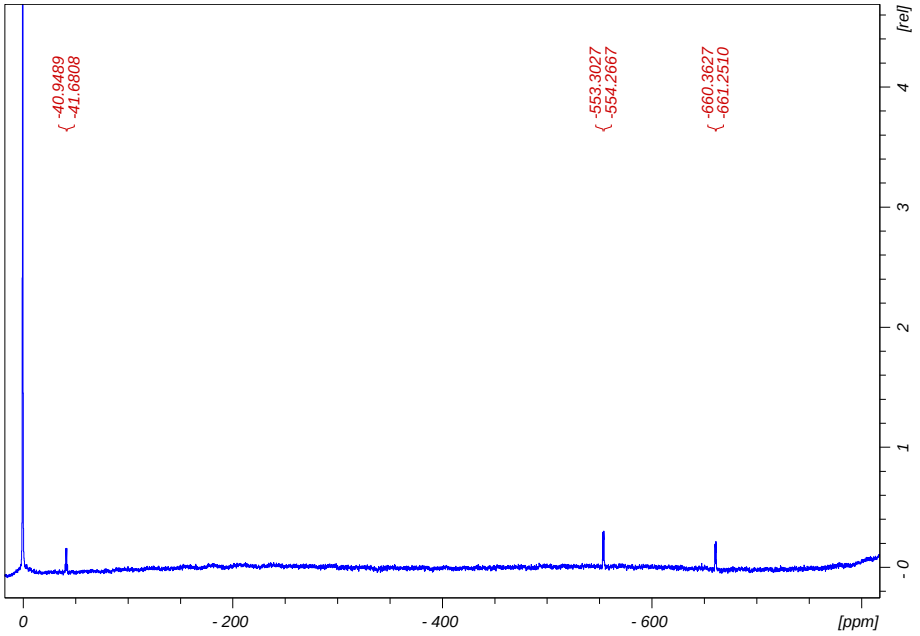

Figure A83: ^{13}C-NMR spectrum for complex **Fe^{IV}(3Me-ppz)$_3$** in CD_3CN, part 2.

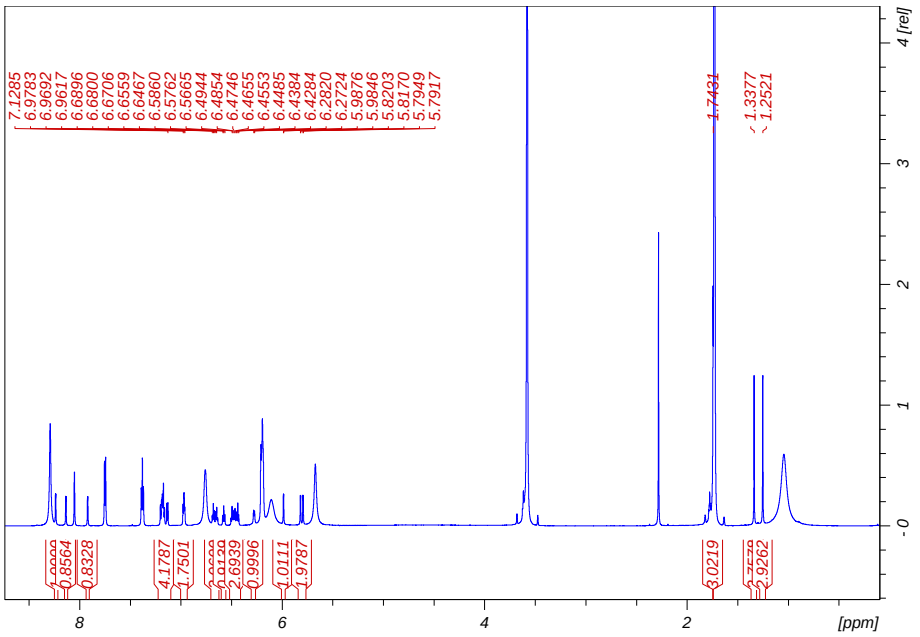

Figure A84: ^{1}H-NMR spectrum for complex **Fe^{II}(3Me-ppz)$_3$** in THF-d_8.

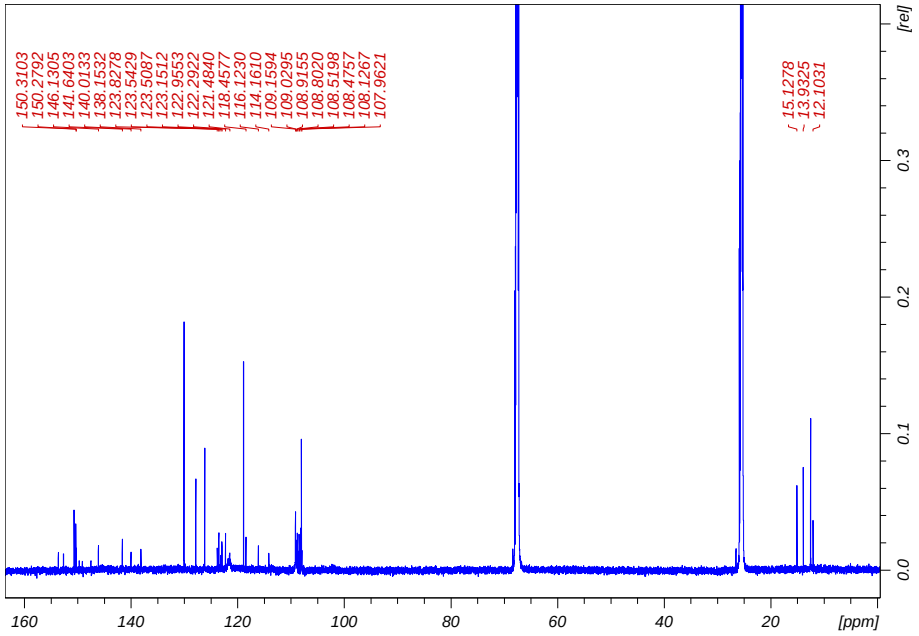

Figure A85: ^{13}C-NMR spectrum for complex **Fe^{II}(3Me-ppz)$_3$** in THF-d$_8$.

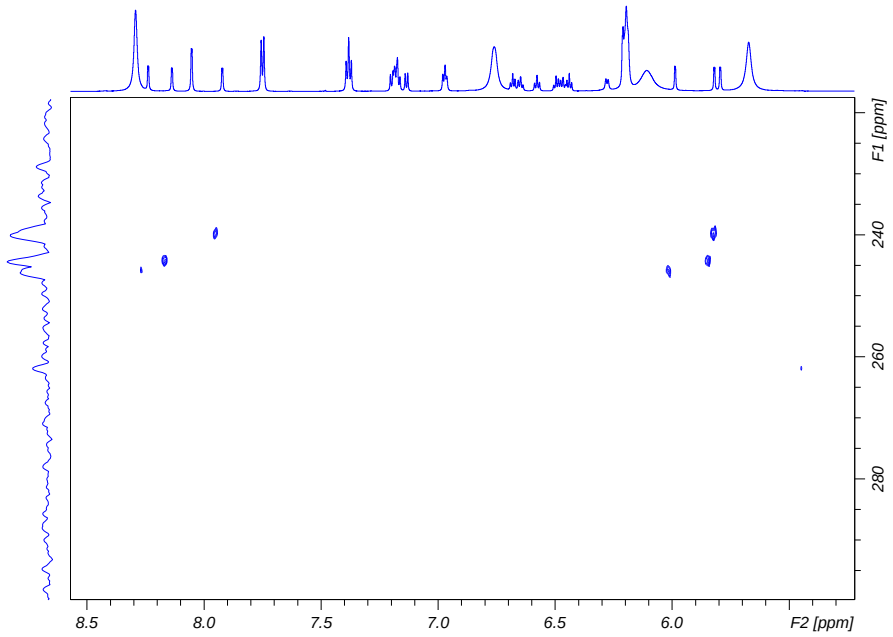

Figure A86: ^{15}N-HMBC-NMR spectrum for complex **Fe^{II}(3Me-ppz)$_3$** in THF-d$_8$.

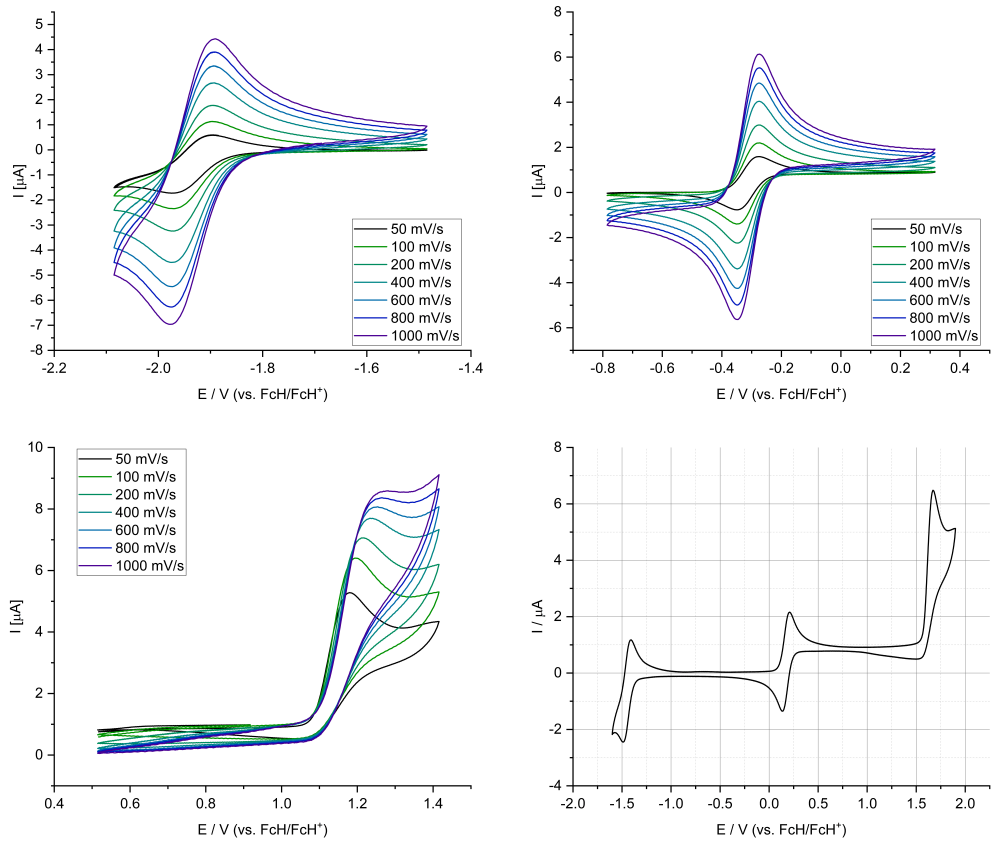

Figure A87: Overview of $\mathbf{Fe^{III}(3Me\text{-}ppz)_3}$ CV-data. Complete overview and the different redoxcouples at scan-rates from 50 to 1000 mV/s.

Table A14: Cyclic Voltammetry data for $\mathbf{Fe(3Me\text{-}ppz)_3}$ at different scan rates at $E_{1/2}$= -1.96 V vs. Fc/Fc^+

Scanrate	[mV/s]	50	100	200	400	600	800	1000
E_{pc}	[V]	-1.900	-1.902	-1.902	-1.897	-1.897	-1.900	-1.895
E_{pa}	[V]	-1.958	-1.963	-1.961	-1.963	-1.966	-1.966	-1.966
$E_{1/2}$	[V]	-1.93	-1.93	-1.93	-1.93	-1.93	-1.93	-1.93
ΔE	[V]	-0.059	-0.061	-0.059	-0.066	-0.068	-0.066	-0.071
I_{pc}	[µA]	-0.82	-1.28	-1.84	-2.62	-3.19	-3.66	-4.06
I_{pa}	[µA]	1.36	2.08	3.18	4.11	5.04	5.78	6.52
I_{pa}/I_{pc}		-1.65	-1.63	-1.73	-1.57	-1.58	-1.58	-1.61

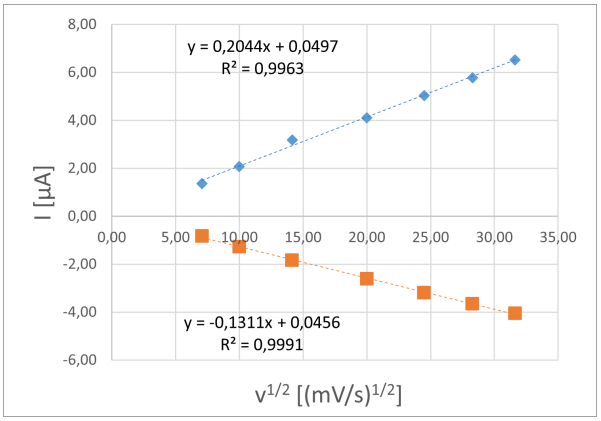

Figure A88: Plotted data of Randles-Sevcik-Equation at different scan rates for **Fe(3Me-ppz)$_3$** at $E_{1/2}$= -1.96 V vs. Fc/Fc^+

Table A15: Cyclic Voltammetry data for **Fe(3Me-ppz)$_3$** at different scan rates at $E_{1/2}$= -0.28 V vs. Fc/Fc^+

Scanrate	[mV/s]	50	100	200	400	600	800	1000
E_{pc}	[V]	-0.346	-0.344	-0.346	-0.348	-0.344	-0.346	-0.346
E_{pa}	[V]	-0.278	-0.275	-0.278	-0.275	-0.278	-0.278	-0.280
$E_{1/2}$	[V]	-0.31	-0.31	-0.31	-0.31	-0.31	-0.31	-0.31
ΔE	[V]	0.068	0.068	0.068	0.073	0.066	0,068	0.066
I_{pc}	[µA]	-1.35	-1.92	-2.71	-3.81	-4.66	-5.37	-6.01
I_{pa}	[µA]	1.37	1.95	2.80	3.88	4.76	5.51	6.14
I_{pa}/I_{pc}		-1.02	-1.01	-1.03	-1.02	-1.02	-1.02	-1.02

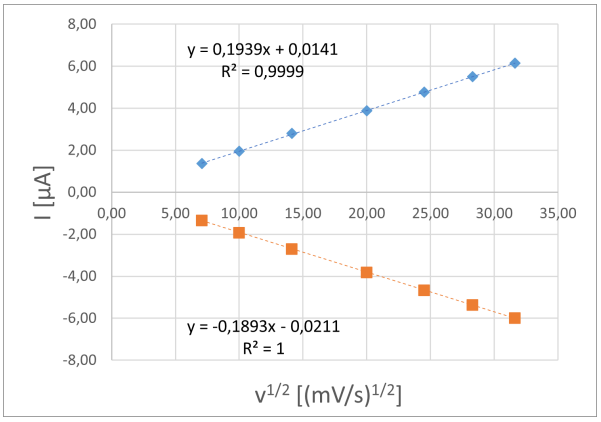

Figure A89: Plotted data of Randles-Sevcik-Equation at different scan rates for **Fe(3Me-ppz)$_3$** at $E_{1/2}$= -1.12 V vs. Fc/Fc^+

Table A16: Cyclic Voltammetry data for **Fe(3Me-ppz)$_3$** at different scan rates at $E_{1/2}$= 1.20 V vs. Fc/Fc^+

Scanrate	[mV/s]	50	100	200	400	600	800	1000
E_{pc}	[V]	1.081	1.098	1.105	1.115	1.115	1.115	1.118
E_{pa}	[V]	1.169	1.184	1.198	1.210	1.218	1.220	1.223
$E_{1/2}$	[V]	1.12	1.14	1.15	1.16	1.17	1.17	1.17
ΔE	[V]	0.088	0.085	0.093	0.095	0.103	0.105	0.105
I_{pc}	[µA]	-1.03	-1.07	-0.92	-0.84	-0.99	-1.29	-1.39
I_{pa}	[µA]	2.86	2.55	3.43	3.49	3.36	3.19	2.90
I_{pa}/I_{pc}		-2.79	-2.38	-3.74	-4.13	-3.40	-2.47	-2.09

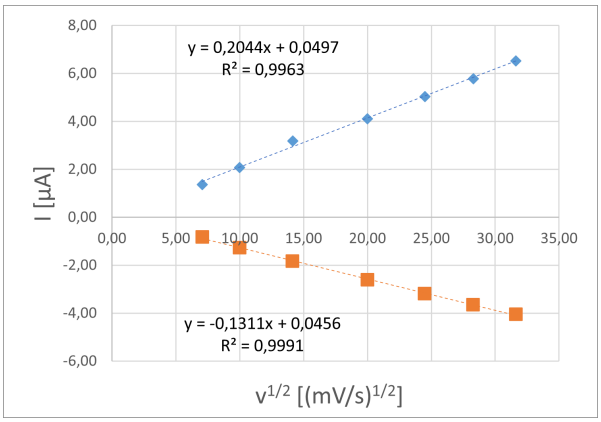

Figure A90: Plotted data of Randles-Sevcik-Equation at different scan rates for **Fe(3Me-ppz)$_3$** at $E_{1/2}$= 1.20 V vs. Fc/Fc^+

Table A17: Crystal structure data and refinement for **Fe(bppz)$_3$**

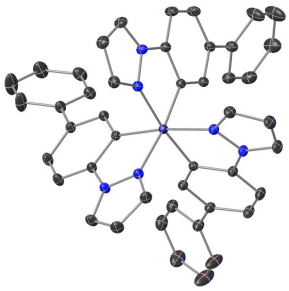

Identification code	TH-444-2 (TH_0193)
CCDC number	2191101
Empirical formula	$C_{46.20}H_{35.40}Cl_{2.40}FeN_6$
Moiety formula	$C_{45}H_{33}FeN_6$
Formula weight	815.53 Da
Color	red
Shape	prism
Temperature	120(2) K
Wavelength	0.71073 Å
Crystal system	Trigonal
Space group	R-3
Unit cell dimensions	a = 14.3819(5) Å α =90°
	b = 14.3819(5) Å β = 90°
	c = 32.0647(16) Å γ = 120°
Volume	5743.7(5) Å^3
Z	6
Density (calculated)	1.415 mg/m^3
Absorption coefficient	0.605 mm^{-1}
F(000)	2528
Crystal size	0.200 x 0.200 x 0.180 mm^3
Theta range for data collection	2.833 to 36.372°
Index ranges	-23≤h≤24, -24≤k≤23, -53≤l≤53
Reflections collected	198137
Independent reflections	6215 [R(int) = 0.0423]
Completeness to theta = 25.242°	99.7 %
Absorption correction	Semi-empirical from equivalents
Refinement method	Full-matrix least-squares on F^2
Data / restraints / parameters	6215 / 0 / 157
Goodness-of-fit on F2	1.046
Final R indices [I>2sigma(I)]	R1 = 0.0332, wR2 = 0.0909
R indices (all data)	R1 = 0.0368, wR2 = 0.0940
Largest diff. peak and hole	0.538 e/Å^{-3} (0.65 Å^{-3} from C4) and -0.355 e/Å^{-3} (0.53 Å^{-3} from Fe1)

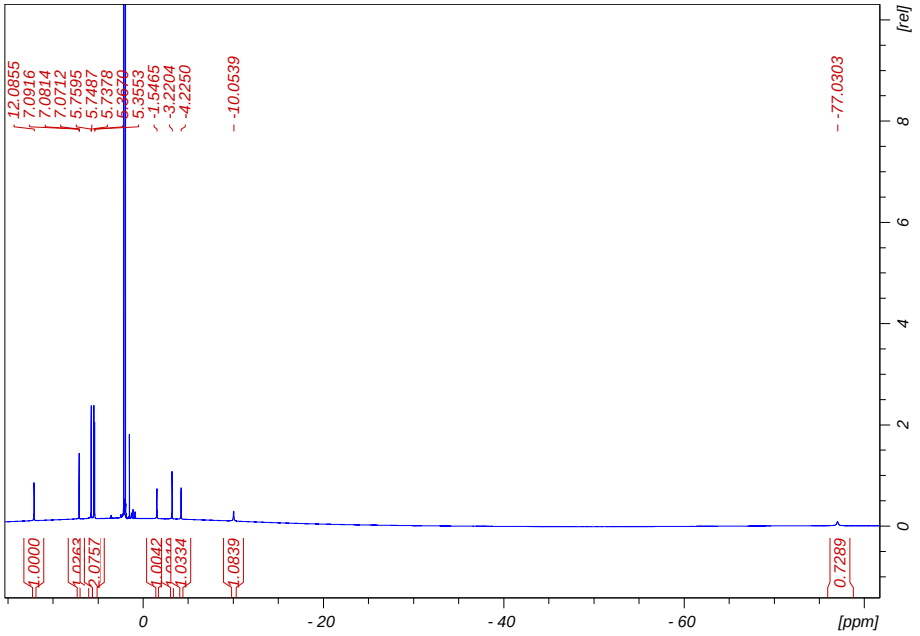

Figure A91: ^{1}H-NMR spectrum for complex $\mathbf{Fe^{III}(bppz)_3}$ in CD_3CN.

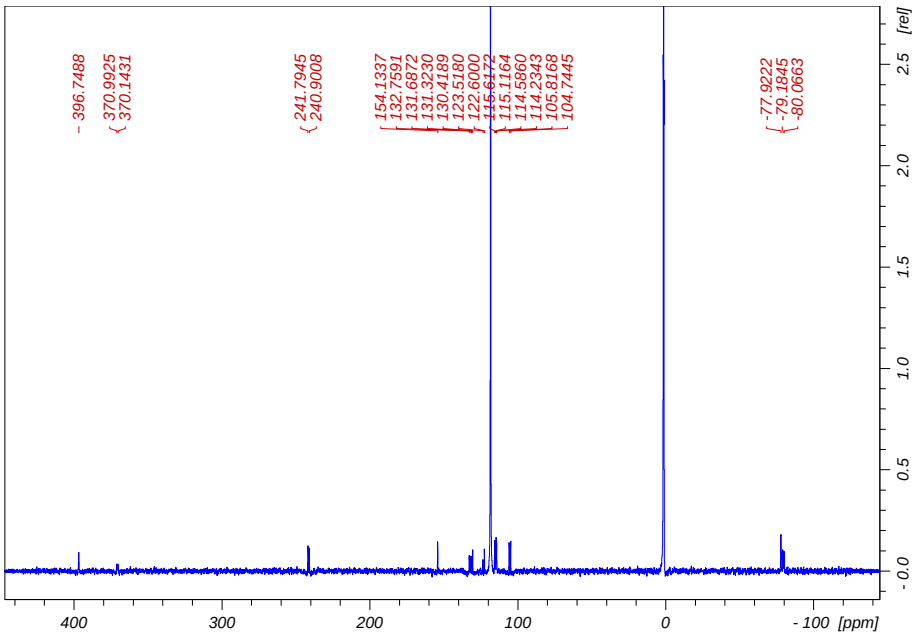

Figure A92: ^{13}C-NMR spectrum for complex $\mathbf{Fe^{III}(bppz)_3}$ in CD_3CN.

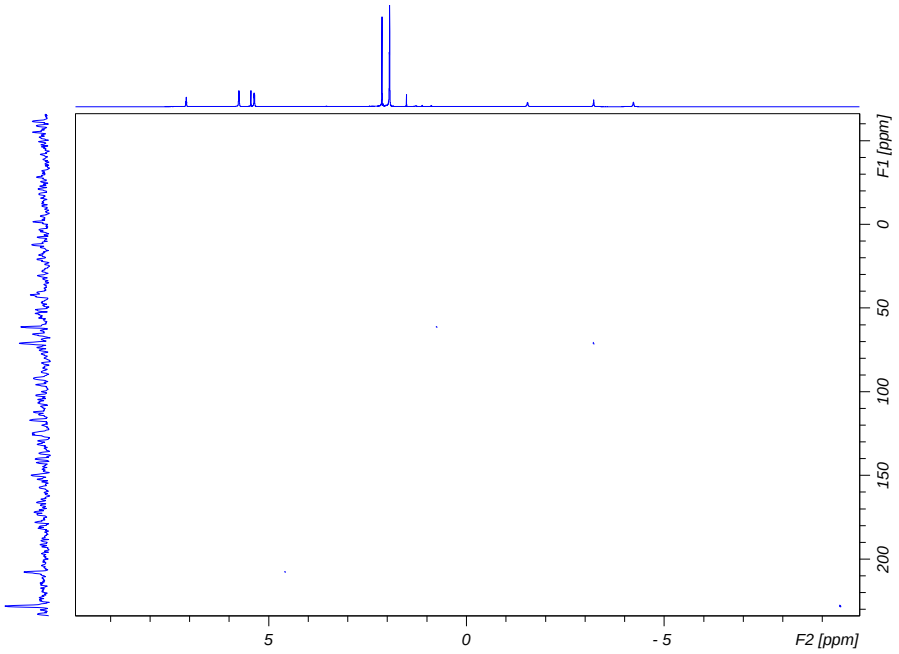

Figure A93: ^{15}N-HMBC-NMR spectrum for complex $\mathbf{Fe^{III}(bppz)_3}$ in CD_3CN.

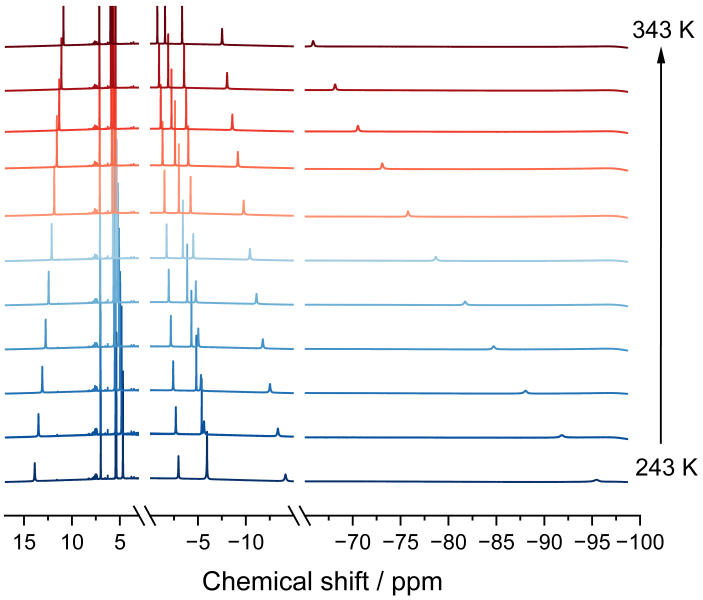

Figure A94: ^{1}H-NMR-spectra of complex $\mathbf{Fe^{III}(bppz)_3}$ from 243 to 333 K in CD_3CN.

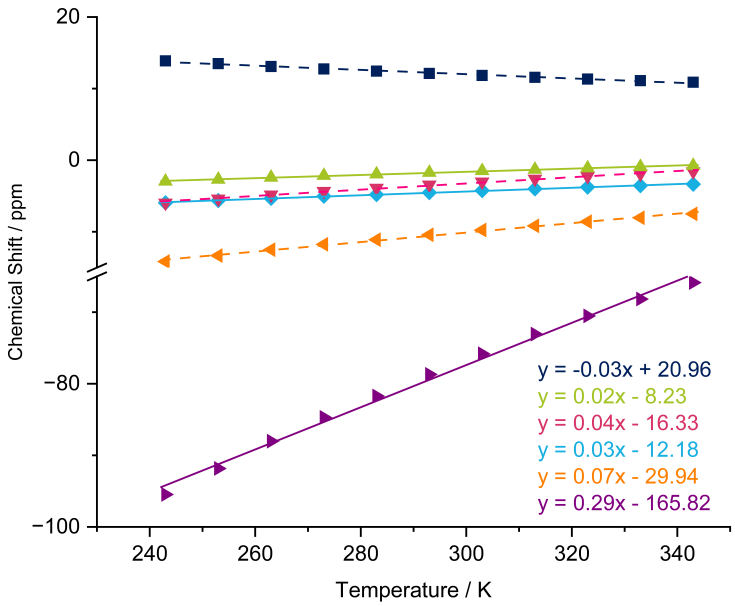

Figure A95: Curie-Plot of complex $\mathbf{Fe^{III}(bppz)_3}$ from 243 to 343 K in CD_3CN on the marked positions. Dashed line represents pyrazole-based protons, solid lines represent phenyl-based protons.

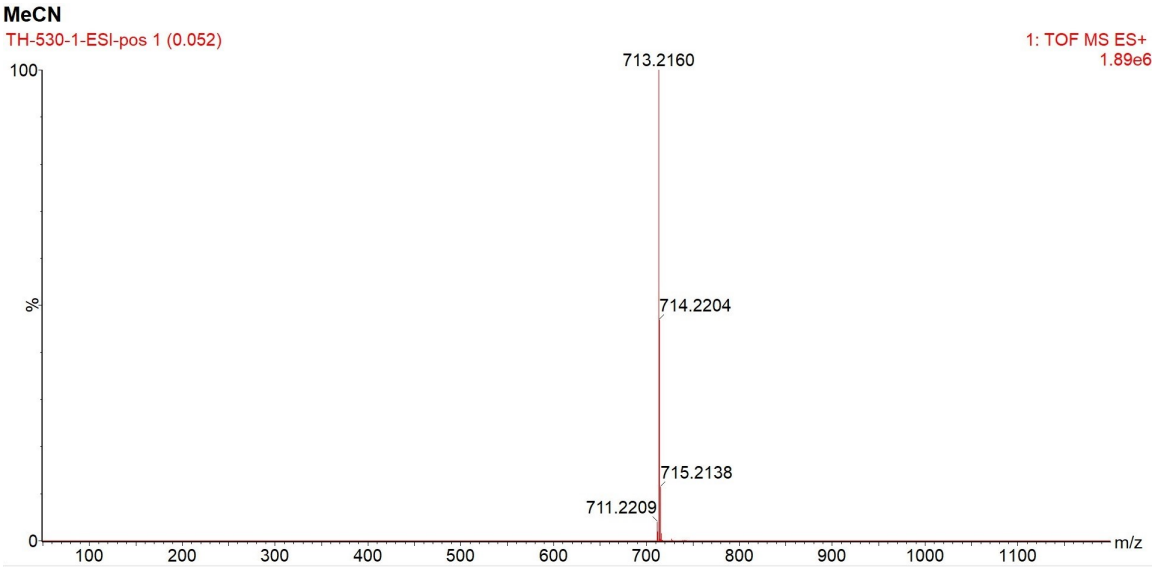

Figure A96: ESI-MS spectrum of complex $\mathbf{Fe(bppz)_3}$ in MeCN

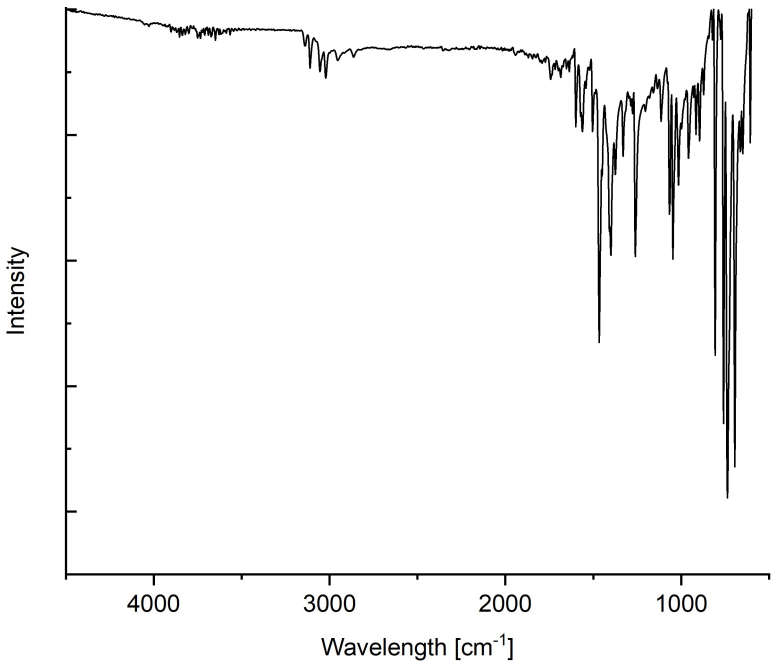

Figure A97: ATR-IR spectrum for complex **Fe(bppz)**$_3$

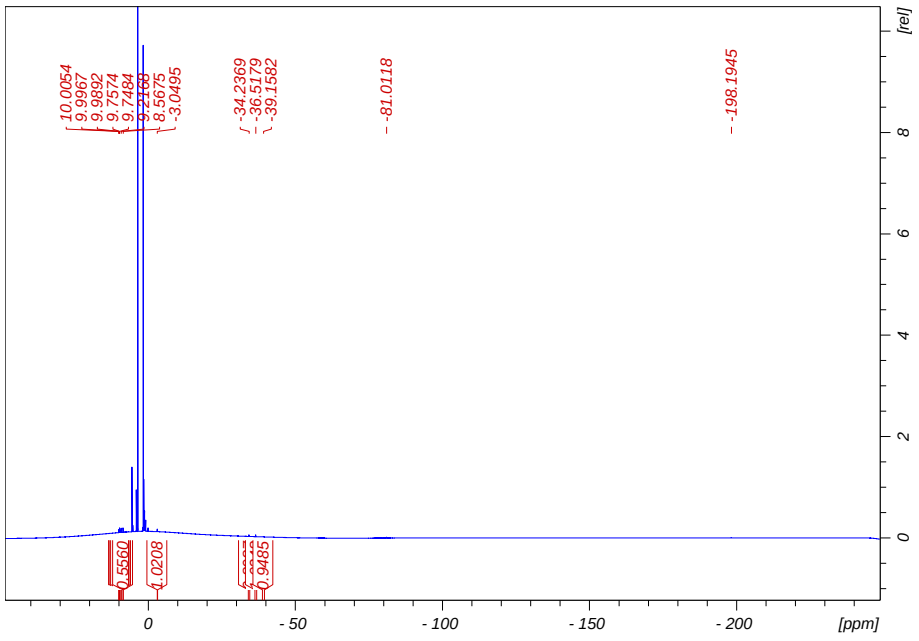

Figure A98: ^{1}H-NMR spectrum for complex **Fe^{IV}(bppz)**$_3$ in DMSO-d$_6$.

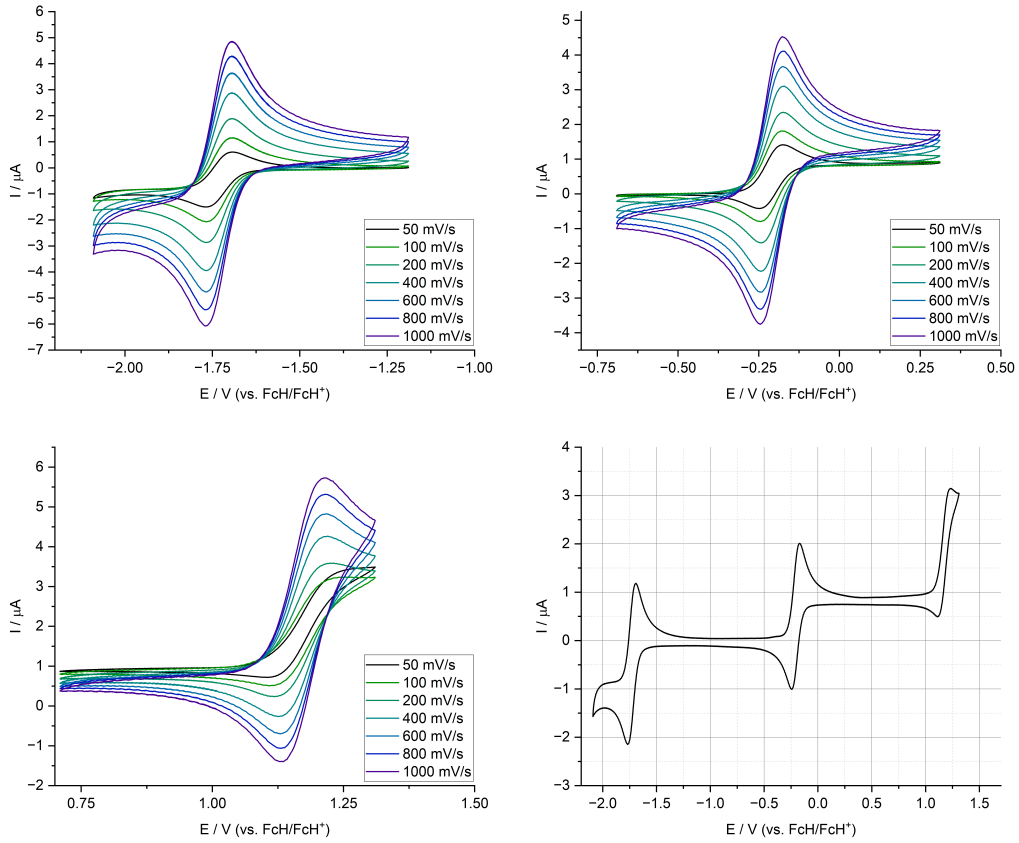

Figure A99: Overview of $\mathbf{Fe^{III}(bppz)_3}$ CV-data. Complete overview and the different redoxcouples at scanrates from 50 to 1000 mV/s.

Table A18: Cyclic Voltammetry data for $\mathbf{Fe(bppz)_3}$ at different scan rates at $E_{1/2}$= -1.69 V vs. Fc/Fc^+

Scanrate	[mV/s]	50	100	200	400	600	800	1000
E_{pc}	[V]	-1.774	-1.777	-1.772	-1.777	-1.777	-1.779	-1.777
E_{pa}	[V]	-1.699	-1.699	-1.696	-1.694	-1.699	-1.696	-1.696
$E_{1/2}$	[V]	-1.74	-1.74	-1.73	-1.74	-1.74	-1,.74	-1.74
ΔE	[V]	0.076	0.078	0.076	0.083	0.078	0.083	0.081
I_{pc}	[µA]	-1.12	-1.58	-2.24	-3.10	-3,.76	-4.27	-4.75
I_{pa}	[µA]	1.36	1.67	2.19	2.95	3.54	4.01	4.43
I_{pa}/I_{pc}		-1.21	-1.06	-0.98	-0.95	-0.94	-0.94	-0.93

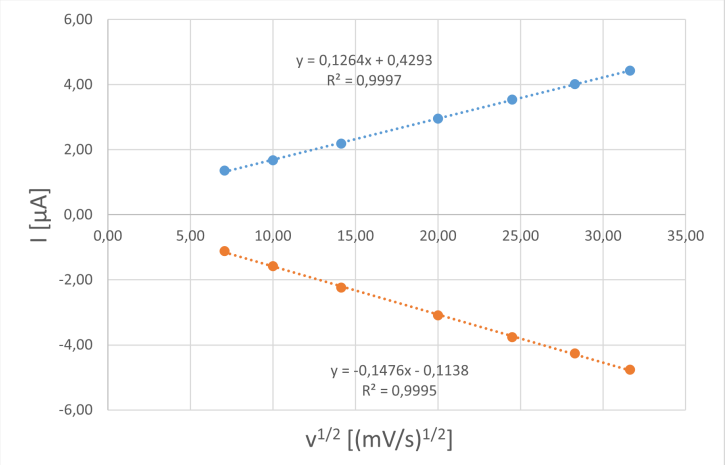

Figure A100: Plotted data of Randles-Sevcik-Equation at different scan rates for **Fe(bppz)**$_3$ $E_{1/2}$= -1.74 V vs. Fc/Fc^+

Table A19: Cyclic Voltammetry data for **Fe(bppz)**$_3$ at different scan rates at $E_{1/2}$= -0.21 V vs. Fc/Fc^+

Scanrate	[mV/s]	50	100	200	400	600	800	1000
E_{pc}	[V]	-0.241	-0.241	-0.246	-0.241	-0.241	-0.249	-0.244
E_{pa}	[V]	-0.175	-0.175	-0.180	-0.180	-0.175	-0.183	-0.173
$E_{1/2}$	[V]	-0.21	-0.21	-0.21	-0.21	-0.21	-0.22	-0.21
ΔE	[V]	0.066	0.066	0.066	0.061	0.066	0.066	0.071
I_{pc}	[µA]	-0.75	-1.09	-1.55	-2.18	-2.62	-3.04	-3.41
I_{pa}	[µA]	0.87	1.14	1.60	2.21	2.69	3.08	3.43
I_{pa}/I_{pc}		-1.17	-1.05	-1.04	-1.01	-1.03	-1.01	-1.01

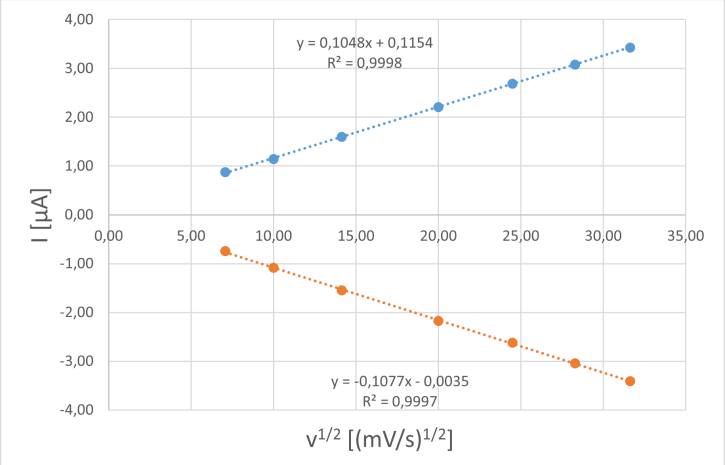

Figure A101: Plotted data of Randles-Sevcik-Equation at different scan rates for **Fe(bppz)**$_3$ at $E_{1/2}$= -0.21 V vs. Fc/Fc^+

Table A20: Cyclic Voltammetry data for **Fe(bppz)**$_3$ at different scan rates at $E_{1/2}$= 1.17 V vs. Fc/Fc^+

Scanrate	[mV/s]	50	100	200	400	600	800	1000
E_{pc}	[V]	1.129	1.127	1.134	1.132	1.124	1.122	1.110
E_{pa}	[V]	1.217	1.222	1.232	1.239	1.244	1.246	1.261
$E_{1/2}$	[V]	1.17	1.17	1.18	1.19	1.18	1.18	1.19
ΔE	[V]	0.088	0.095	0.098	0.107	0.120	0.125	0.151
I_{pc}	[µA]	-0.49	-0.58	-0.71	-0.95	-1.21	-1.33	-1.44
I_{pa}	[µA]	0.53	0.64	0.76	0.88	1.02	1.08	1.13
I_{pa}/I_{pc}		-1.08	-1.10	-1.07	-0.92	-0.84	-0.82	-0.78

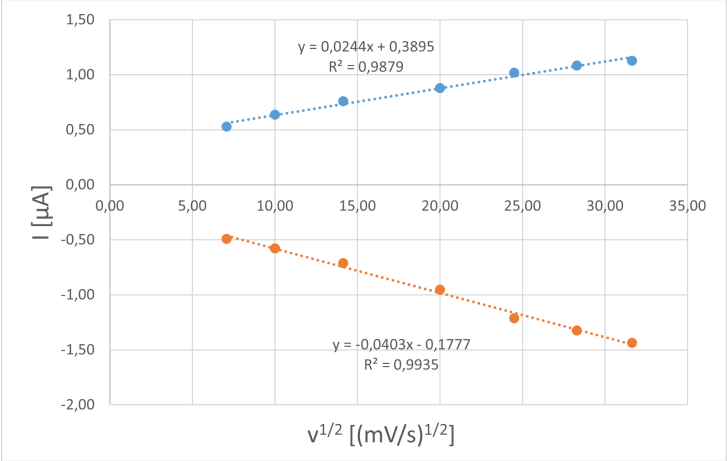

Figure A102: Plotted data of Randles-Sevcik-Equation at different scan rates for **Fe(bppz)**$_3$ at $E_{1/2}$= 1.17 V vs. Fc/Fc^+

Table A21: Crystal structure data and refinement for **Fe(naphpz)$_3$**

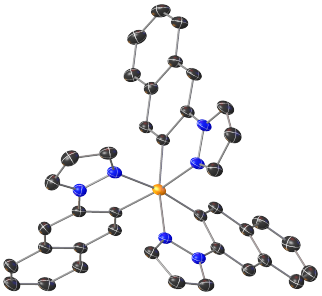

Identification code	TH-524-1 (TH_0228)
CCDC number	2191103
Empirical formula	$C_{52}H_{37}FeN_8$
Moiety formula	$C_{39}H_{27}FeN_6$
Formula weight	829.74 Da
Color	orange
Shape	plate
Temperature	120(2) K
Wavelength	0.71073 Å
Crystal system	Monoclinic
Space group	$P2_1/n$
Unit cell dimensions	a = 11.3521(10) Å α =90° b = 30.655(3) Å β = 110.723(2)° c = 12.3313(11) Å γ = 90°
Volume	4013.7(6) Å^3
Z	4
Density (calculated)	1.373 mg/m^3
Absorption coefficient	0.425 mm^{-1}
F(000)	1724
Crystal size	0.280 x 0.180 x 0.100 mm^3
Theta range for data collection	2.030 to 30.546°
Index ranges	-16≤h≤16, -43≤k≤43, -17≤l≤17
Reflections collected	190973
Independent reflections	12271 [R(int) = 0.0682]
Completeness to theta = 25.242°	99.9 %
Absorption correction	Semi-empirical from equivalents
Refinement method	Full-matrix least-squares on F^2
Data / restraints / parameters	12271 / 0 / 550
Goodness-of-fit on F2	1.131
Final R indices [I>2sigma(I)]	R1 = 0.0455, wR2 = 0.1075
R indices (all data)	R1 = 0.0734, wR2 = 0.1274
Largest diff. peak and hole	1.196 e/Å^{-3} (0.763 Å^{-3} from H405) and -0.689 e/Å^{-3} (0.69 Å^{-3} from Fe1)

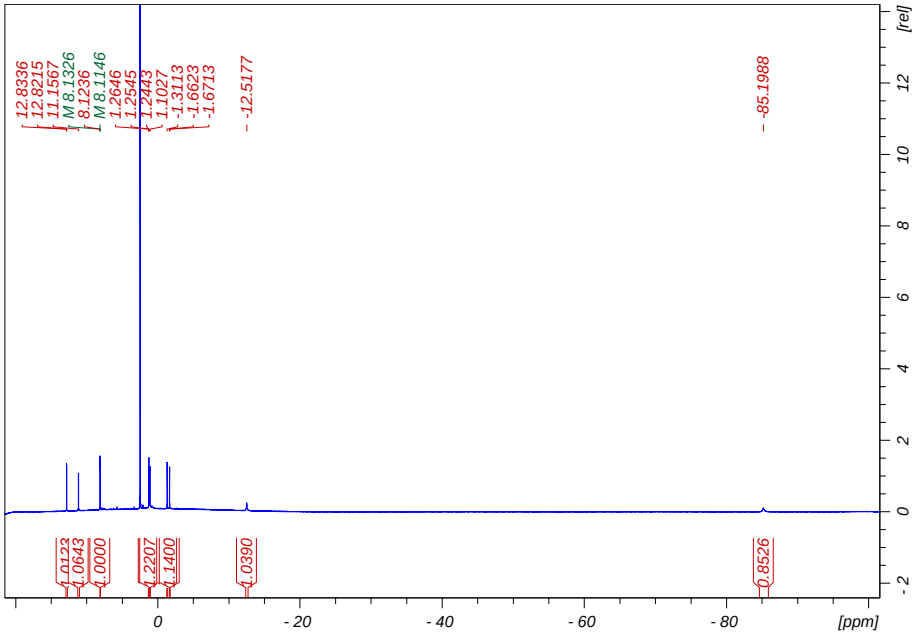

Figure A103: ^{1}H-NMR spectrum for complex **Fe^{III}(naphpz)$_3$** in DMSO-d$_6$.

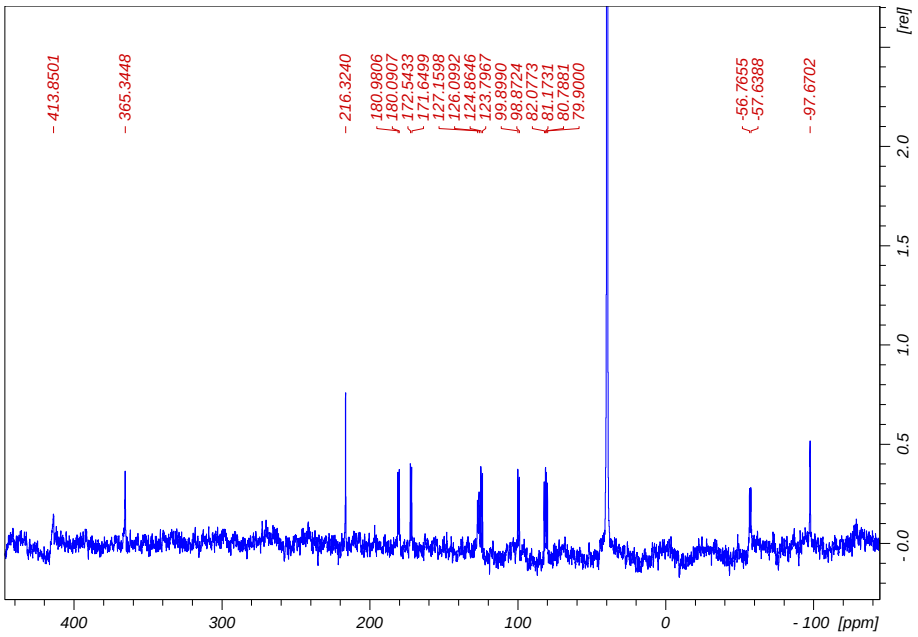

Figure A104: ^{13}C-NMR spectrum for complex **Fe^{III}(naphpz)$_3$** in DMSO-d$_6$.

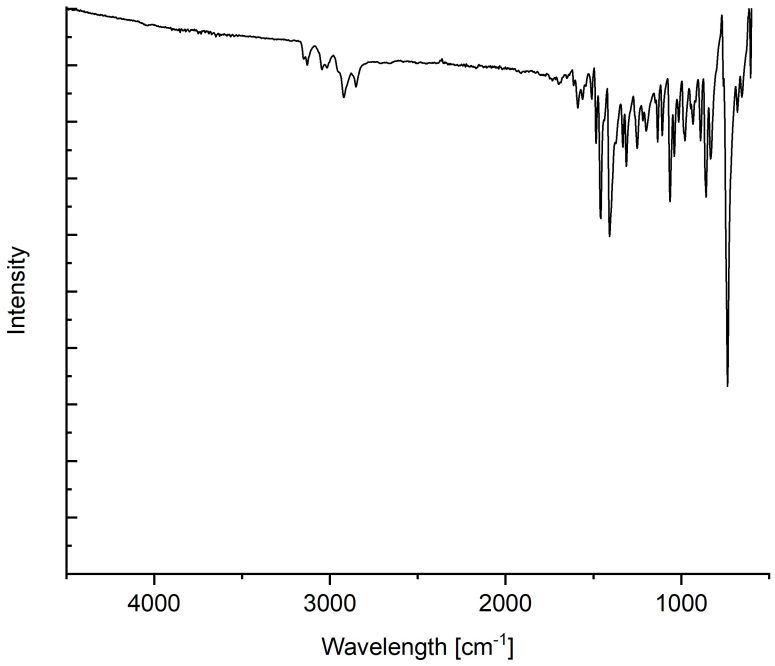

Figure A105: ATR-IR spectrum for complex **Fe(naphpz)$_3$**

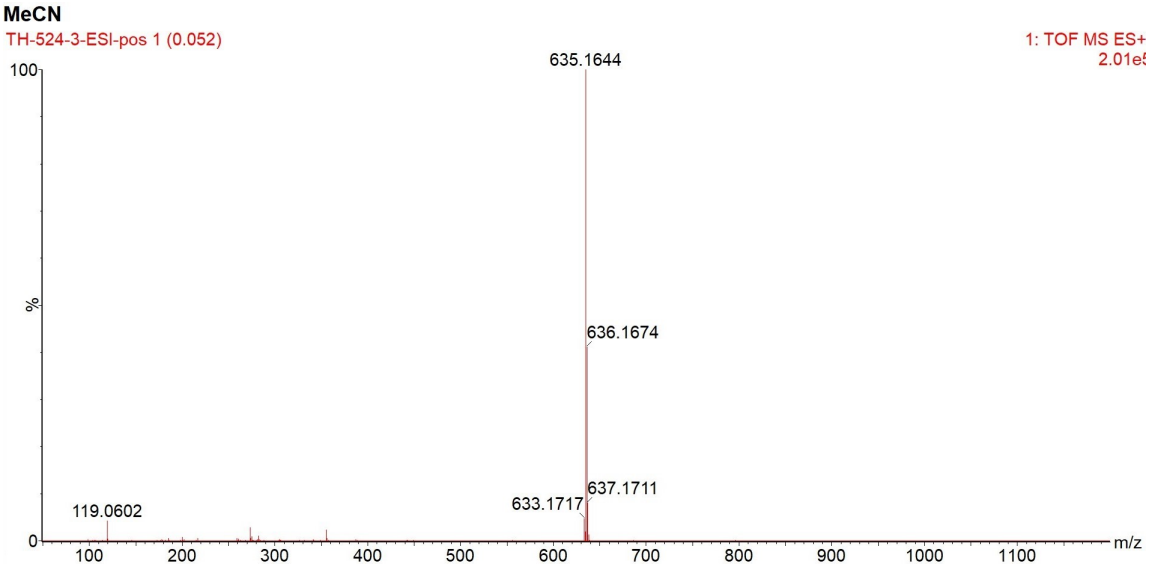

Figure A106: ESI-MS spectrum of complex **Fe(naphpz)$_3$** in MeCN

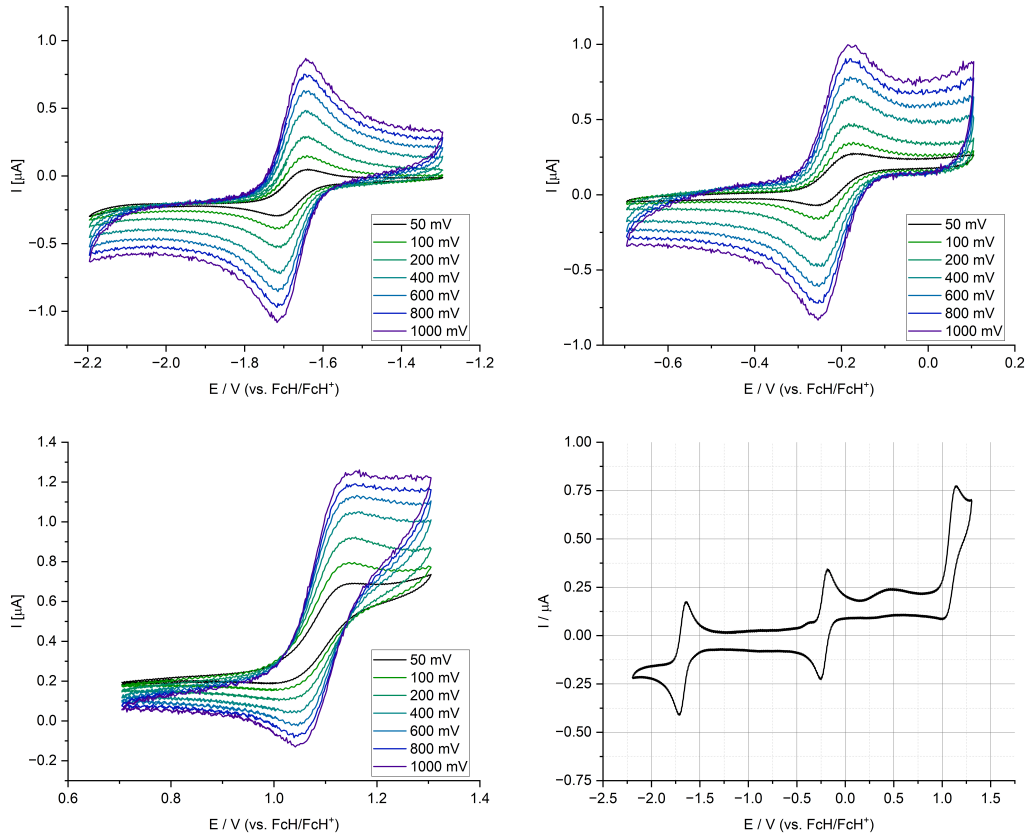

Figure A107: Overview of $\mathbf{Fe^{III}(naphpz)_3}$ CV-data. Complete overview and the different redoxcouples at scan-rates from 50 to 1000 mV/s.

Table A22: Cyclic Voltammetry data for **Fe(naphpz)$_3$** at different scan rates at $E_{1/2}$= -1.68 V vs. Fc/Fc^+

Scanrate	[mV/s]	50	100	200	400	600	800	1000
E_{pc}	[V]	-1.712	-1.712	-1.712	-1.717	-1.714	-1.709	-1.714
E_{pa}	[V]	-1.638	-1.641	-1.648	-1.643	-1.648	-1.648	-1.643
$E_{1/2}$	[V]	-1.68	-1.68	-1.68	-1.68	-1.68	-1.68	-1.68
ΔE	[V]	0.073	0.071	0.064	0.073	0.066	0.061	0.071
I_{pc}	[µA]	-0.18	-0.21	-0.39	-0.53	-0.59	-0.77	-0.81
I_{pa}	[µA]	0.18	0.25	0.37	0.56	0.62	0.75	0.88
I_{pc}/I_{pa}		-1.02	-1.18	-0.95	-1.05	-1.04	-0.98	-1.08

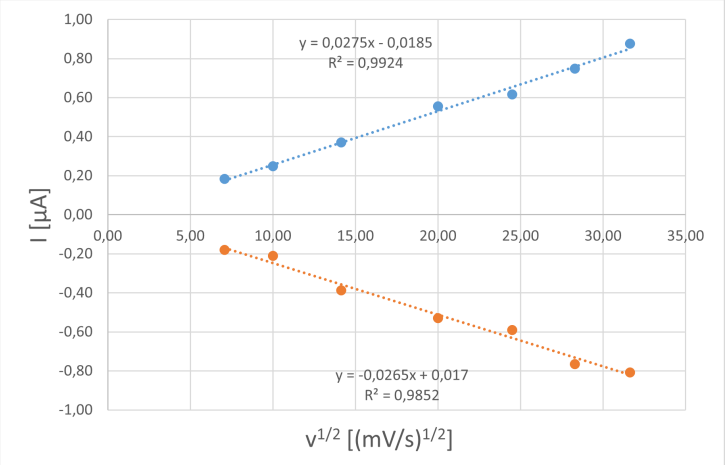

Figure A108: Plotted data of Randles-Sevcik-Equation at different scan rates for **Fe(naphpz)**$_3$ $E_{1/2}$= -1.68 V vs. Fc/Fc^+

Table A23: Cyclic Voltammetry data for **Fe(naphpz)**$_3$ at different scan rates at $E_{1/2}$= -0.22 V vs. Fc/Fc^+

Scanrate	[mV/s]	50	100	200	400	600	800	1000
E_{pc}	[V]	-0.248	-0.251	-0.246	-0.251	-0.257	-0.243	-0.253
E_{pa}	[V]	-0.177	-0.182	-0.182	-0.192	-0.191	-0.190	-0.185
$E_{1/2}$	[V]	-0.21	-0.22	-0.21	-0.22	-0.22	-0.22	-0.22
ΔE	[V]	0.071	0.068	0.063	0.059	0.066	0.054	0.068
I_{pc}	[µA]	-0.15	-0.22	-0.35	-0.65	-0.83	-0.71	-0.79
I_{pa}	[µA]	0.17	0.19	0.32	0.52	0.65	0.55	0.60
I_{pc}/I_{pa}		-1.10	-0.86	-0.91	-0.80	-0.79	-0.76	-0.76

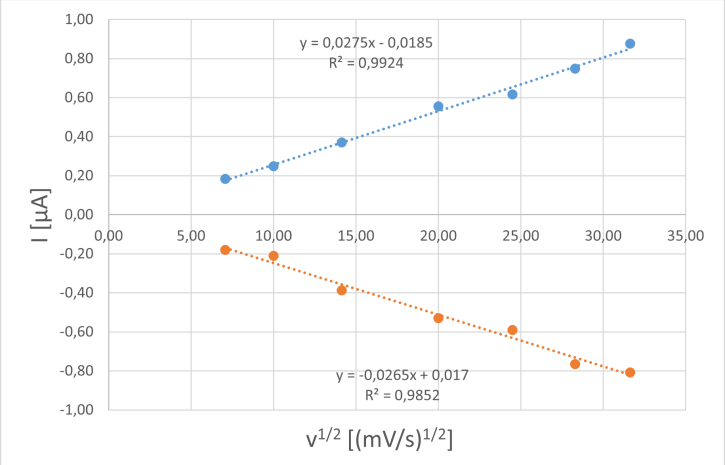

Figure A109: Plotted data of Randles-Sevcik-Equation at different scan rates for **Fe(naphpz)**$_3$ $E_{1/2}$= -0.22 V vs. Fc/Fc^+

Table A24: Cyclic Voltammetry data for **Fe(naphpz)**$_3$ at different scan rates at $E_{1/2}$= 1.08 V vs. Fc/Fc^+

Scanrate	[mV/s]	50	100	200	400	600	800	1000
E_{pc}	[V]	1.037	1.035	1.057	1.049	1.057	1.059	1.062
E_{pa}	[V]	1.125	1.130	1.127	1.140	1.130	1.127	1.125
$E_{1/2}$	[V]	1.08	1.08	1.09	1.09	1.09	1.09	1.09
ΔE	[V]	0.088	0.095	0.071	0.090	0.073	0.068	0.063
I_{pc}	[µA]	-0.18	-0.30	-0.37	-0.44	-0.51	-0.54	-0.61
I_{pa}	[µA]	0.20	0.25	0.35	0.43	0.46	0.50	0.52
I_{pc}/I_{pa}		-1.07	-0.84	-0.94	-0.98	-0.90	-0.92	-0.86

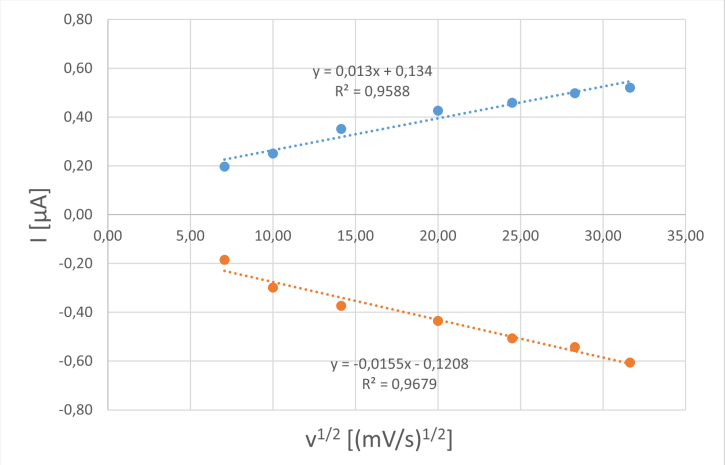

Figure A110: Plotted data of Randles-Sevcik-Equation at different scan rates for **Fe(naphpz)**$_3$ $E_{1/2}$= 1.08 V vs. Fc/Fc^+

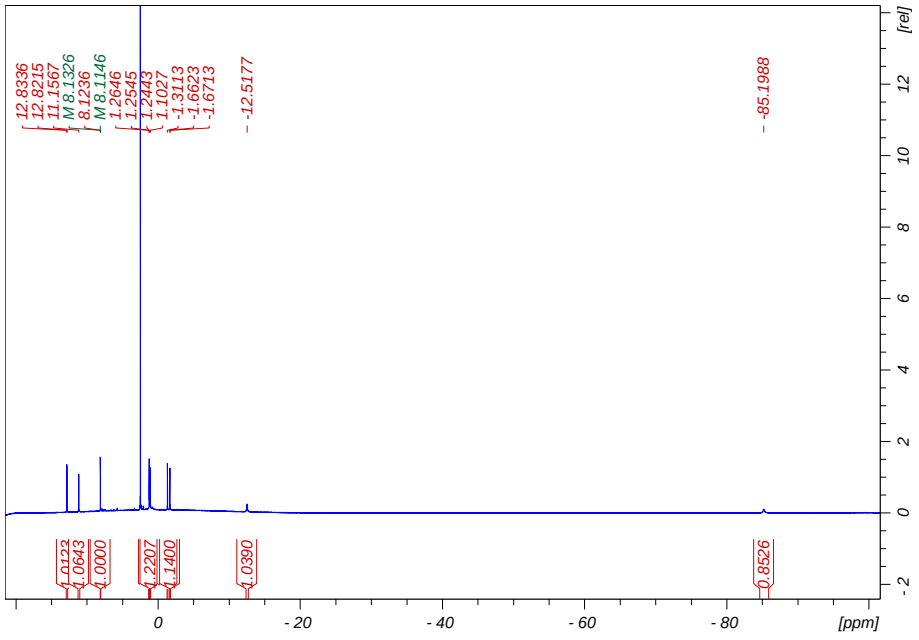

Figure A111: ^{1}H-NMR spectrum for complex **Fe^{IV}(naphpz)**$_3$ in DMSO-d_6.

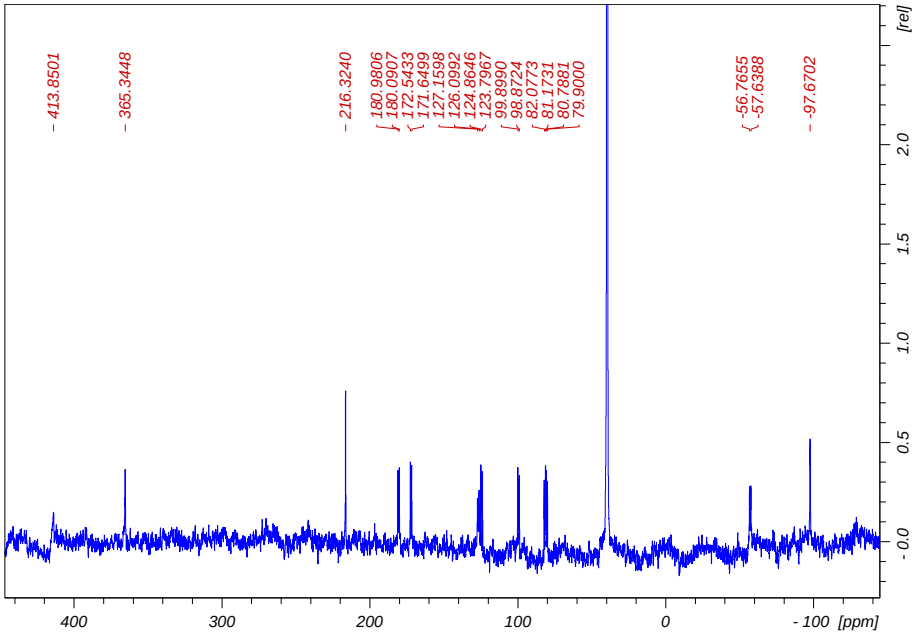

Figure A112: ^{13}C-NMR spectrum for complex $\mathbf{Fe^{IV}(naphpz)_3}$ in DMSO-d_6.

Table A25: Crystal structure data and refinement for **Fe(*m*-CF$_3$ppz)$_3$**

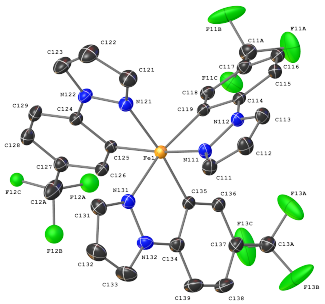

Identification code	TH-443-1 (TH_0198)
CCDC number	2191102
Empirical formula	$C_{67}H_{44}F_{18}Fe_2N_{12}$
Moiety formula	$C_{30}H_{18}F_9FeN_6$
Formula weight	1470.84 Da
Color	yellow
Shape	plate
Temperature	120(2) K
Wavelength	0.71073 Å
Crystal system	Triclinic
Space group	P-1
Unit cell dimensions	a = 13.5555(9) Å α =90° b = 16.6300(10) Å β = 108.952(2)° c = 16.8788(10) Å γ = 109.287(2)°
Volume	3111.8(3) Å^3
Z	2
Density (calculated)	1.570 mg/m^3
Absorption coefficient	0.575 mm^{-1}
F(000)	1488
Crystal size	0.100 x 0.100 x 0.020 mm^3
Theta range for data collection	2.339 to 32.121°
Index ranges	-20≤h≤20, -24≤k≤24, -25≤l≤25
Reflections collected	314702
Independent reflections	21751 [R(int) = 0.0566]
Completeness to theta = 25.242°	99.9 %
Absorption correction	Semi-empirical from equivalents
Refinement method	Full-matrix least-squares on F^2
Data / restraints / parameters	21751 / 163 / 987
Goodness-of-fit on F2	1.080
Final R indices [I>2sigma(I)]	R1 = 0.0447, wR2 = 0.1024
R indices (all data)	R1 = 0.0694, wR2 = 0.1226
Largest diff. peak and hole	1.147 e/Å^{-3} (0.77 Å^{-3} from F21D) and -0.789 e/Å^{-3} (0.49 Å^{-3} from Fe1)

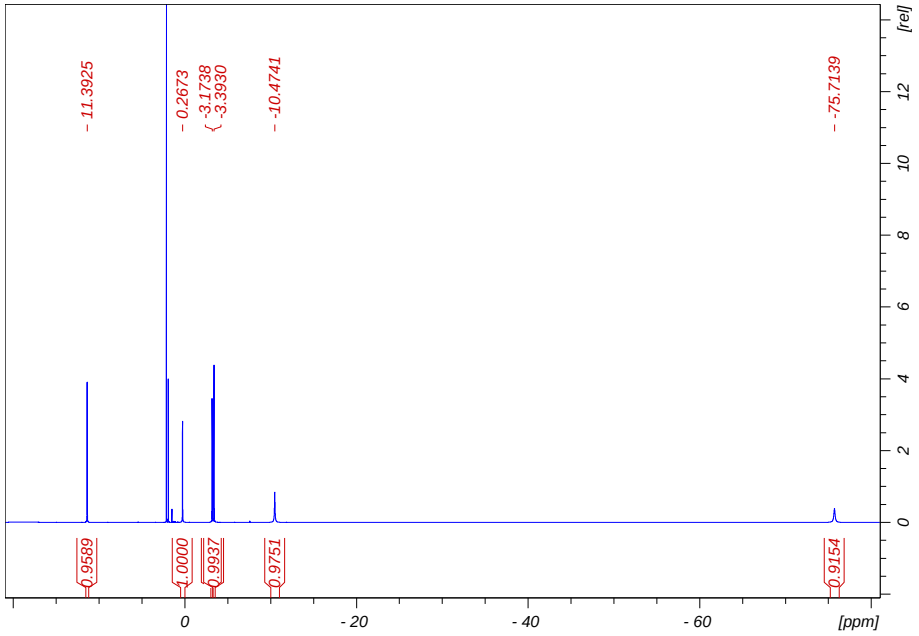

Figure A113: ^{1}H-NMR spectrum for complex $\mathbf{Fe^{III}(\mathit{m}\text{-}CF_3ppz)_3}$ in CD_3CN.

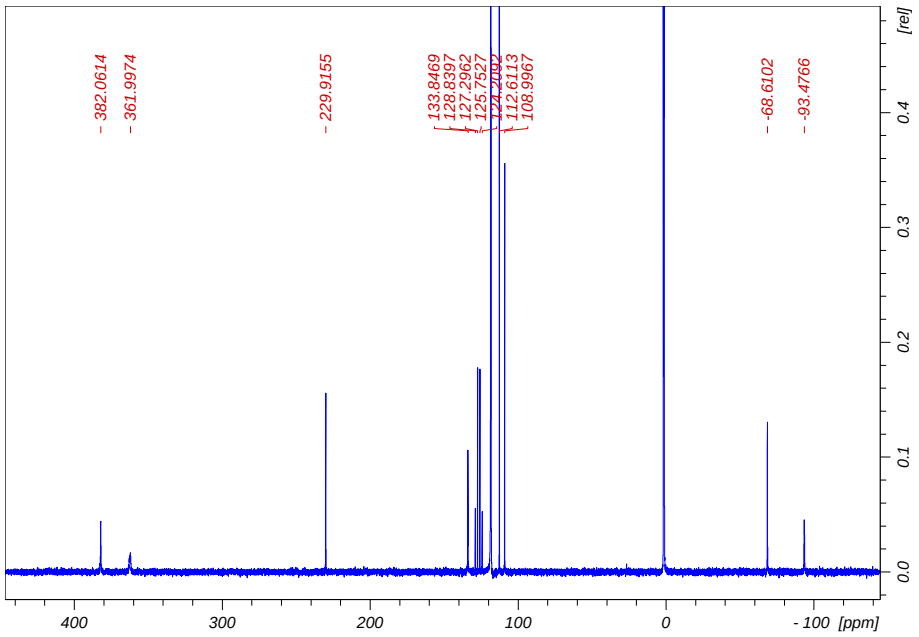

Figure A114: ^{13}C-NMR spectrum for complex $\mathbf{Fe^{III}(\mathit{m}\text{-}CF_3ppz)_3}$ in CD_3CN.

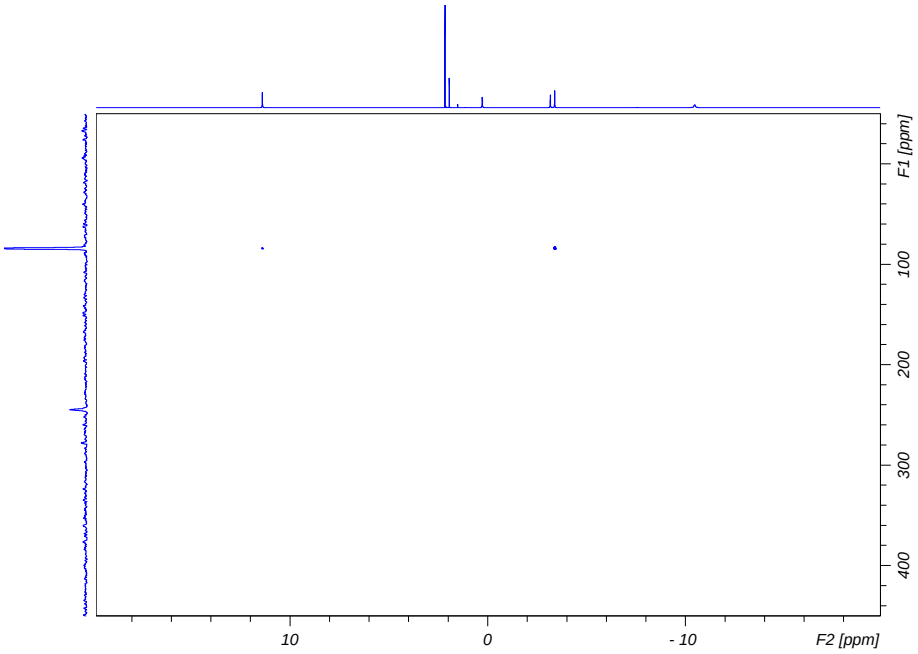

Figure A115: ^{15}N-HMBC-NMR spectrum for complex **Fe^{III}(*m*-CF$_3$ppz)$_3$** in CD_3CN.

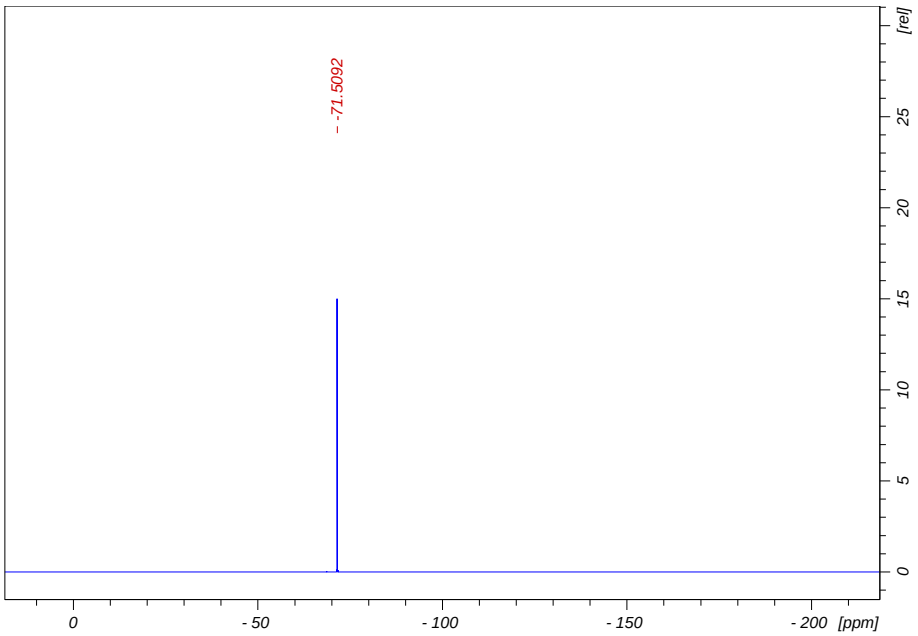

Figure A116: ^{19}F-NMR spectrum for complex **Fe^{III}(*m*-CF$_3$ppz)$_3$** in CD_3CN.

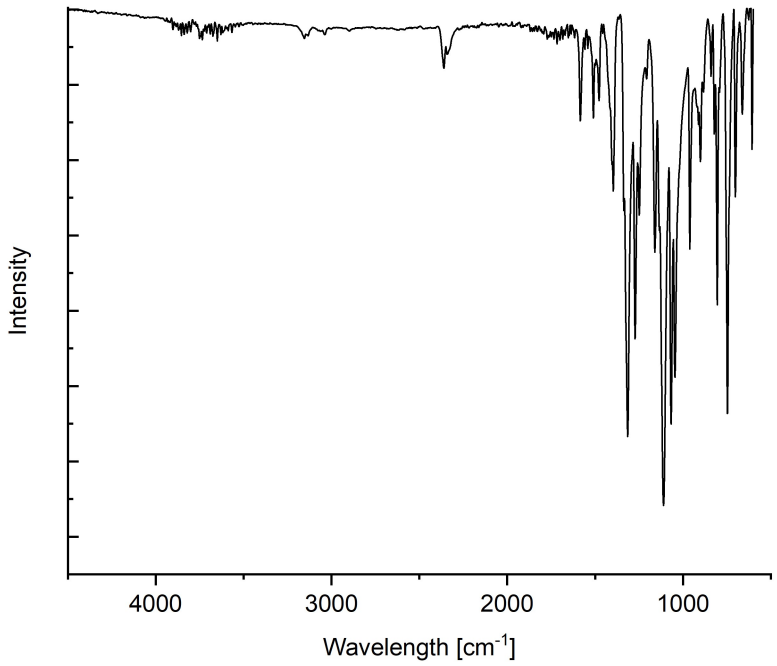

Figure A117: ATR-IR spectrum for complex $\mathbf{Fe^{III}(\textit{m}\text{-}CF_3ppz)_3}$.

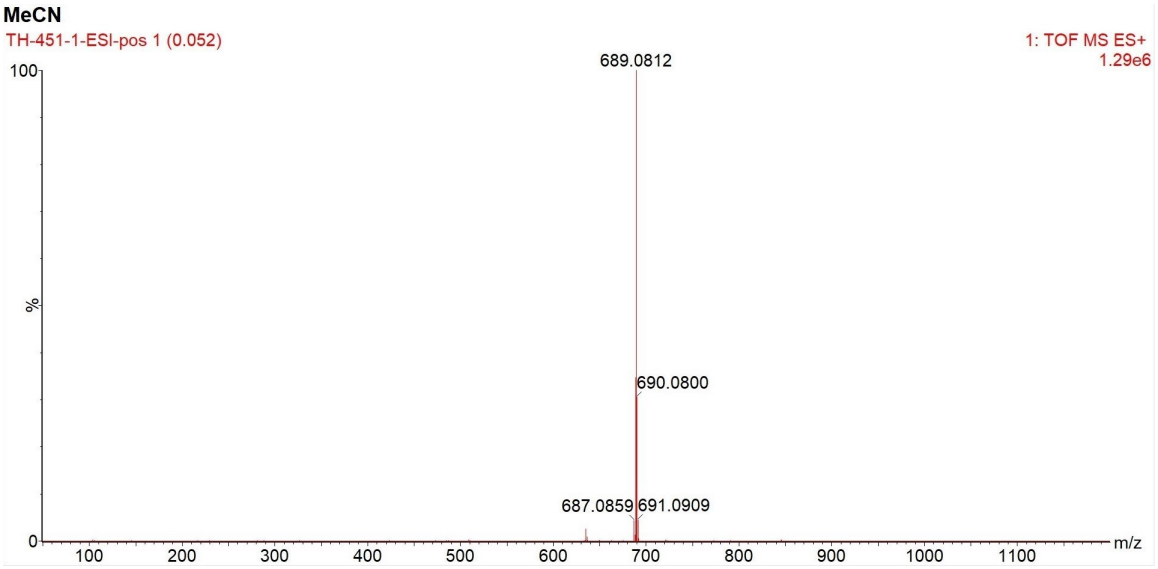

Figure A118: ESI-MS spectrum of complex $\mathbf{Fe^{III}(\textit{m}\text{-}CF_3ppz)_3}$ in MeCN.

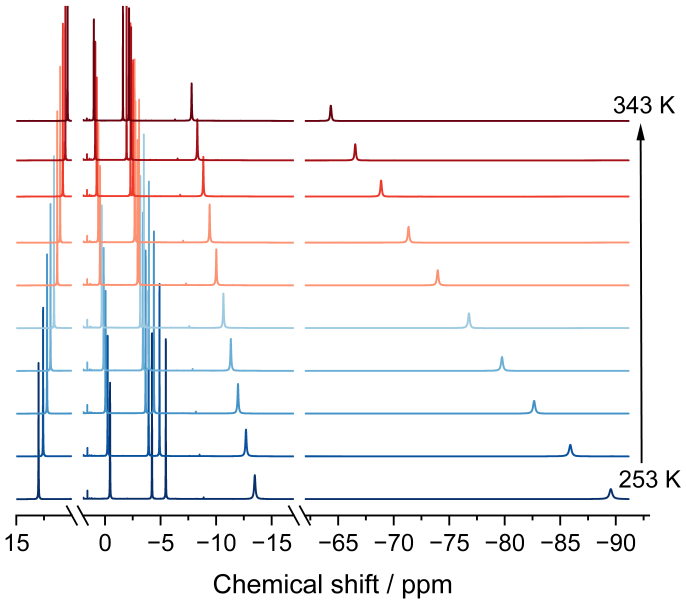

Figure A119: ^{1}H-NMR-spectra of complex $\mathbf{Fe^{III}(\textit{m}\text{-}CF_3ppz)_3}$ from 243 to 333 K.

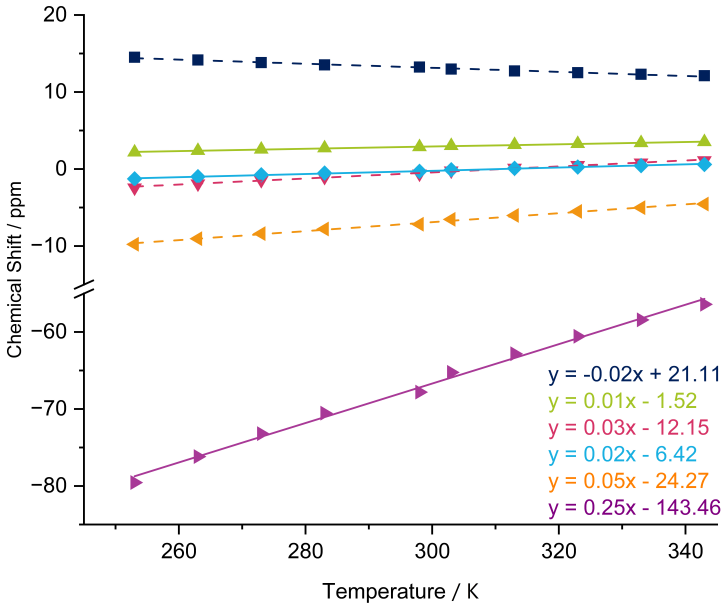

Figure A120: Curie-Plot of complex $\mathbf{Fe^{III}(\textit{m}\text{-}CF_3ppz)_3}$ from 253 to 343 K on the marked positions. Dashed line represents pyrazole-based protons, solid lines represent phenyl-based protons.

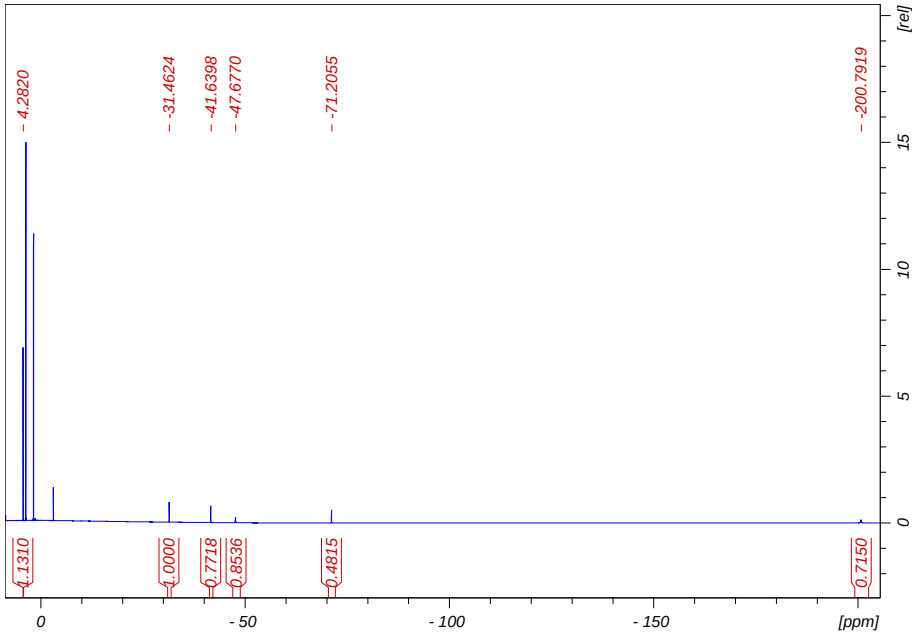

Figure A121: ^{1}H-NMR spectrum for complex $\mathbf{Fe^{IV}(\textit{m}\text{-}CF_3ppz)_3}$ in THF-d_8.

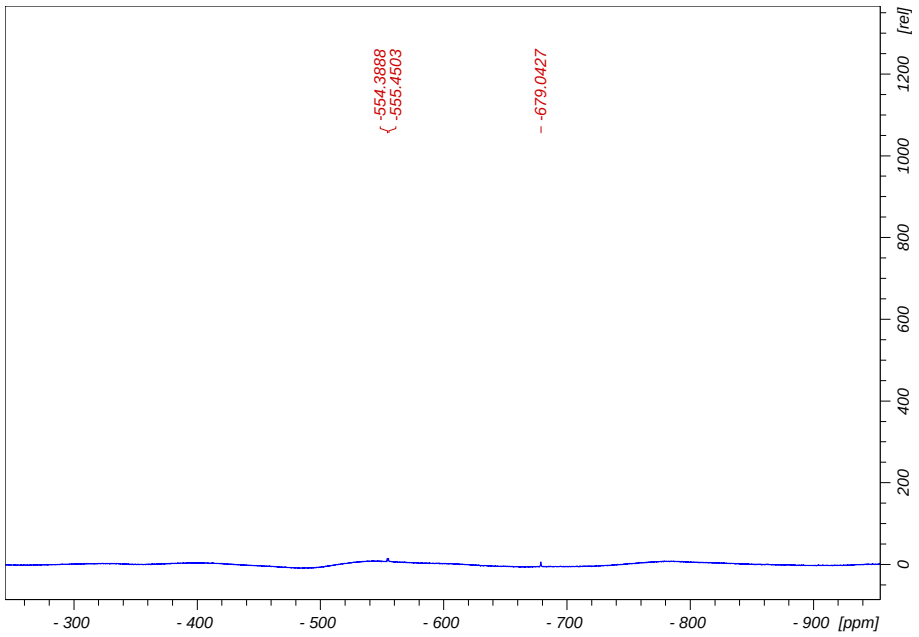

Figure A122: ^{13}C-NMR spectrum for complex $\mathbf{Fe^{IV}(\textit{m}\text{-}CF_3ppz)_3}$ in THF-d_8, part 1.

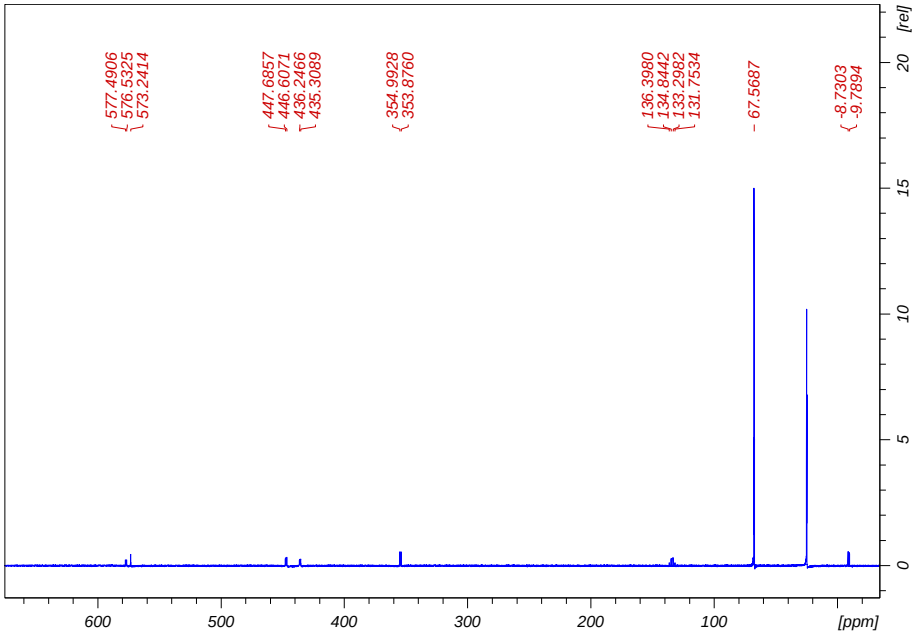

Figure A123: ^{13}C-NMR spectrum for complex $\mathbf{Fe^{IV}(\mathit{m}\text{-}CF_3ppz)_3}$ in THF-d_8, part 2.

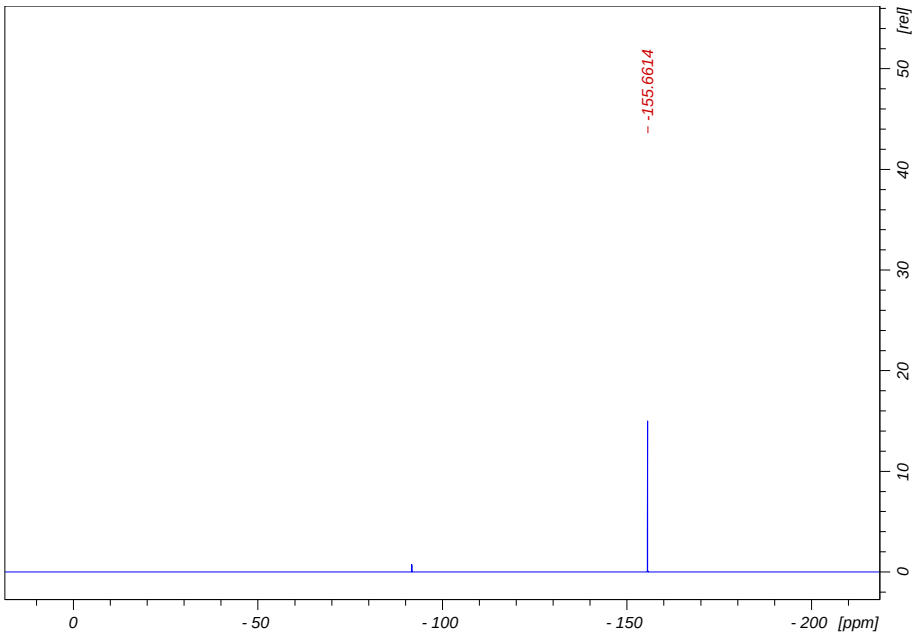

Figure A124: ^{19}F-NMR spectrum for complex $\mathbf{Fe^{IV}(\mathit{m}\text{-}CF_3ppz)_3}$ in THF-d_8.

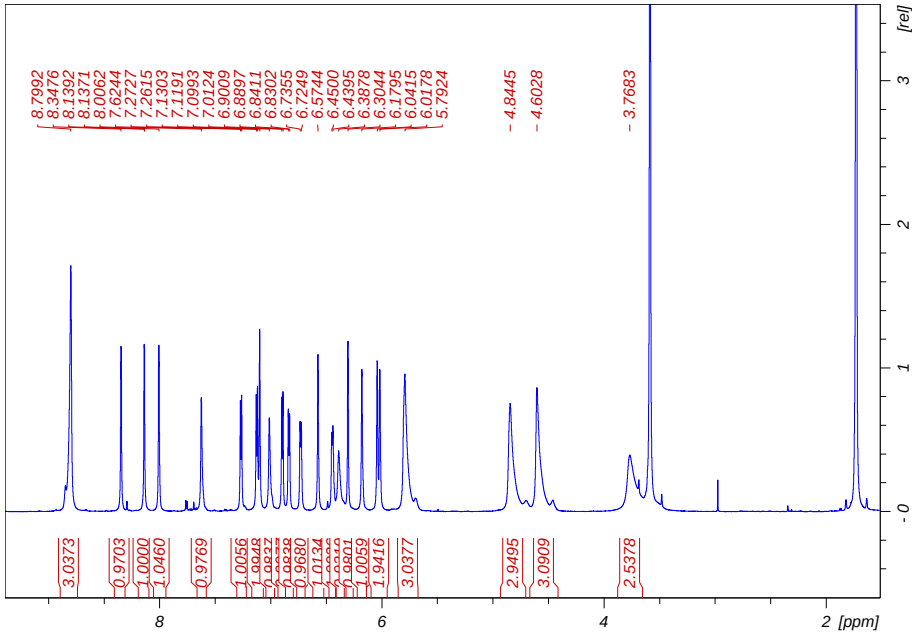

Figure A125: ^{1}H-NMR spectrum for complex $\mathbf{Fe^{II}(\textit{m}\text{-}CF_3ppz)_3}$ in THF-d_8.

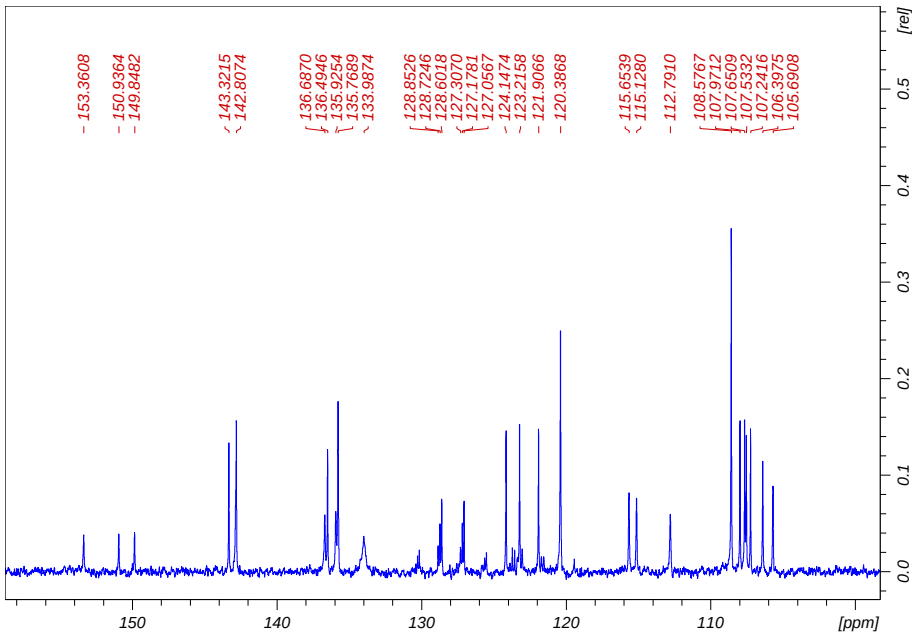

Figure A126: ^{13}C-NMR spectrum for complex $\mathbf{Fe^{II}(\textit{m}\text{-}CF_3ppz)_3}$ in THF-d_8.

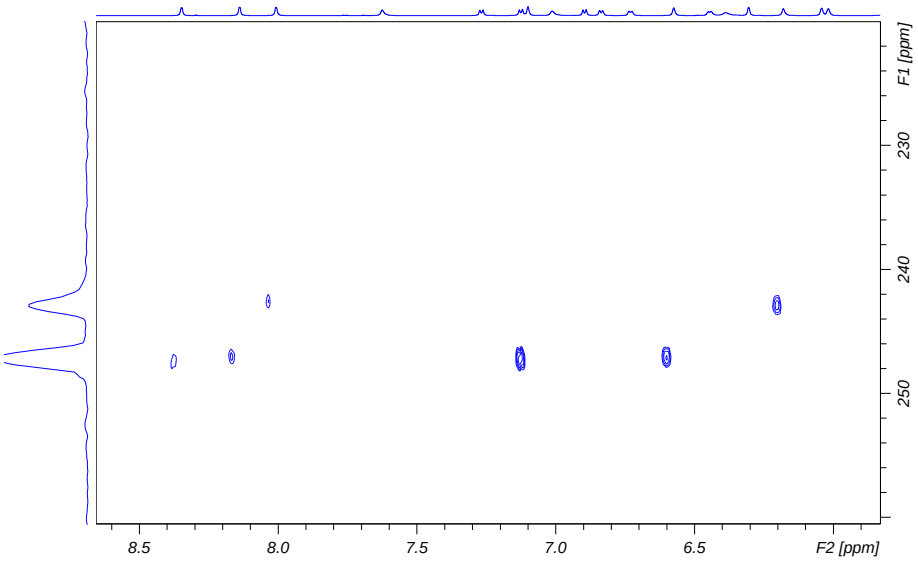

Figure A127: ^{15}N-HMBC-NMR spectrum for complex $\mathbf{Fe^{II}(\textit{m}\text{-}CF_3ppz)_3}$ in THF-d_8.

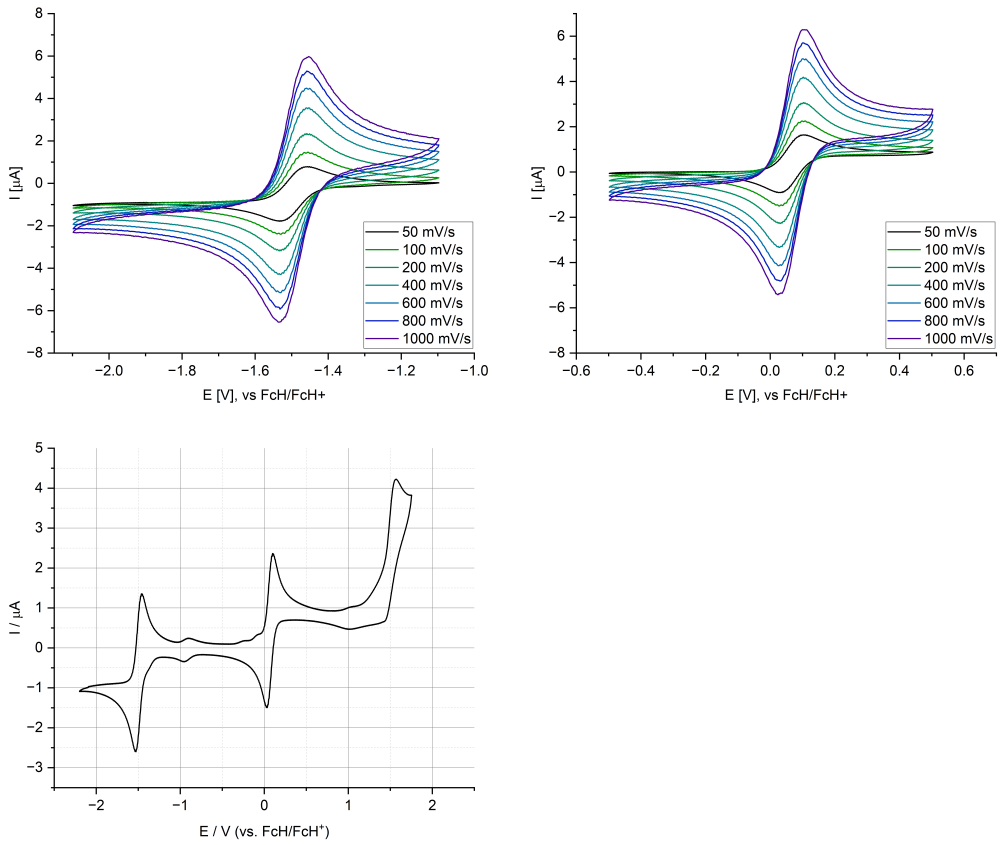

Figure A128: Overview of $\mathbf{Fe^{III}(\textit{m}\text{-}CF_3ppz)_3}$ CV-data. Complete overview and the different redoxcouples at scanrates from 50 to 1000 mV/s.

Table A26: Cyclic Voltammetry data for $\mathbf{Fe(\textit{m}\text{-}CF_3ppz)_3}$ at different scan rates at $E_{1/2}$= -1.48 V vs. Fc/Fc^+

Scanrate	[mV/s]	50	100	200	400	600	800	1000
E_{pc}	[V]	-1.522	-1.524	-1.531	-1.539	-1.541	-1.544	-1.541
E_{pa}	[V]	-1.448	-1.443	-1.441	-1.439	-1.436	-1.439	-1.434
$E_{1/2}$	[V]	-1.48	-1.48	-1.49	-1.49	-1.49	-1.49	-1.49
ΔE	[V]	0.073	0.081	0.090	0.100	0.105	0.105	0.107
I_{pc}	[µA]	-1.13	-1.59	-2.25	-2.99	-3.50	-3.95	-4.24
I_{pa}	[µA]	1.10	1.48	2.02	2.63	3.03	3.35	3.63
I_{pa}/I_{pc}		-0.97	-0.93	-0.90	-0.88	-0.86	-0.85	-0.86

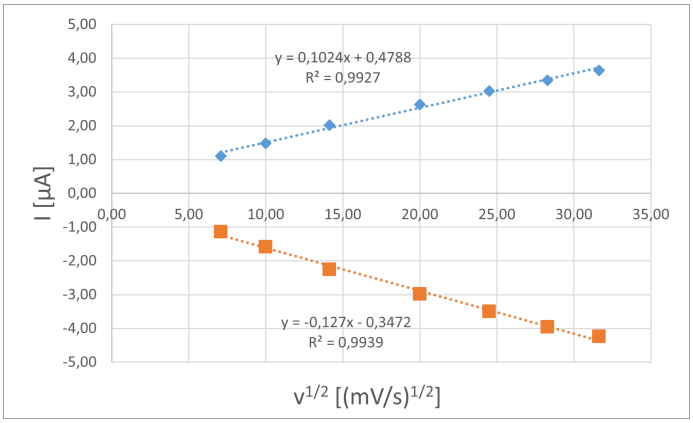

Figure A129: Plotted data of Randles-Sevcik-Equation at different scan rates for **Fe(*m*-CF$_3$ppz)$_3$** $E_{1/2}$= -1.48 V vs. Fc/Fc^+

Table A27: Cyclic Voltammetry data for **Fe(*m*-CF$_3$ppz)$_3$** at different scan rates at $E_{1/2}$= 0.08 V vs. Fc/Fc^+

Scanrate	[mV/s]	50	100	200	400	600	800	1000
E_{pc}	[V]	0.045	0.040	0.037	0.037	0.035	0.037	0.033
E_{pa}	[V]	0.113	0.113	0.118	0.120	0.123	0.118	0.118
$E_{1/2}$	[V]	0.08	0.08	0.08	0.08	0.08	0,08	0.08
ΔE	[V]	0.068	0.073	0.081	0.083	0.088	0.081	0.085
I_{pc}	[µA]	-1.11	-1.55	-2.22	-3.02	-3.63	-4.11	-4.54
I_{pa}	[µA]	1.03	1.47	2.04	2.79	3.33	3,77	4.13
I_{pa}/I_{pc}		-0.93	-0.95	-0.92	-0.92	-0,92	-0.92	-0.91

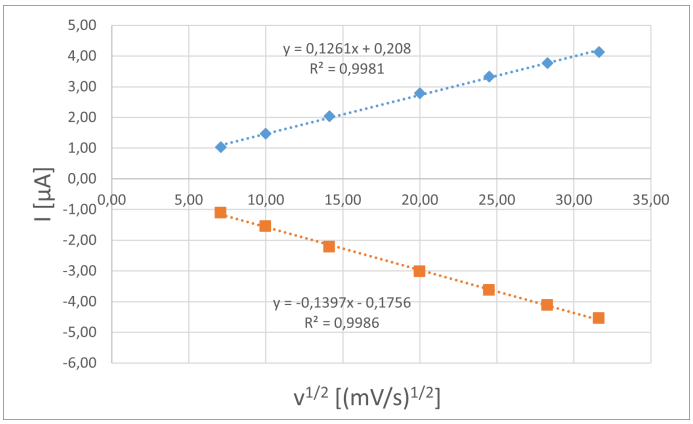

Figure A130: Plotted data of Randles-Sevcik-Equation at different scan rates for **Fe(*m*-CF$_3$ppz)$_3$** $E_{1/2}$= -0.23 V vs. Fc/Fc^+

For $\mathbf{Fe^{III}(\textit{p}\text{-}CF_3ppz)_3}$, no measurable single crystals were available.

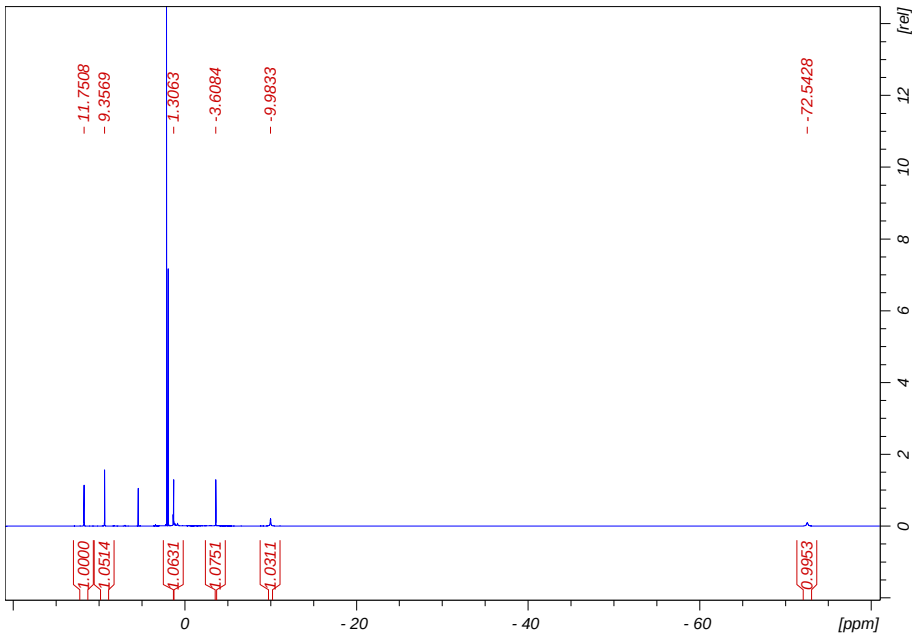

Figure A131: ^{1}H-NMR spectrum for complex $\mathbf{Fe^{III}(\textit{p}\text{-}CF_3ppz)_3}$ in CD_3CN.

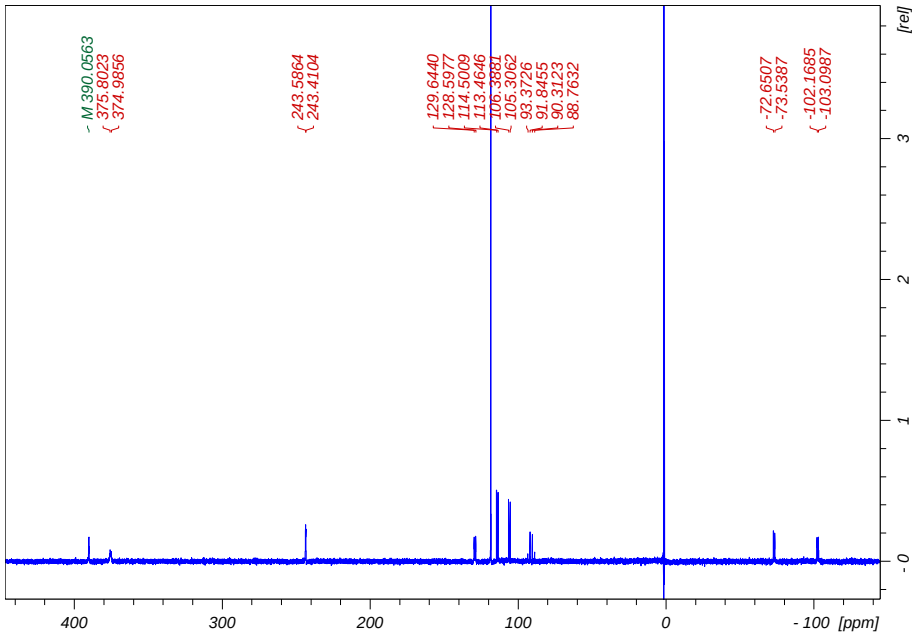

Figure A132: ^{13}C-NMR spectrum for complex $\mathbf{Fe^{III}(\textit{p}\text{-}CF_3ppz)_3}$ in CD_3CN.

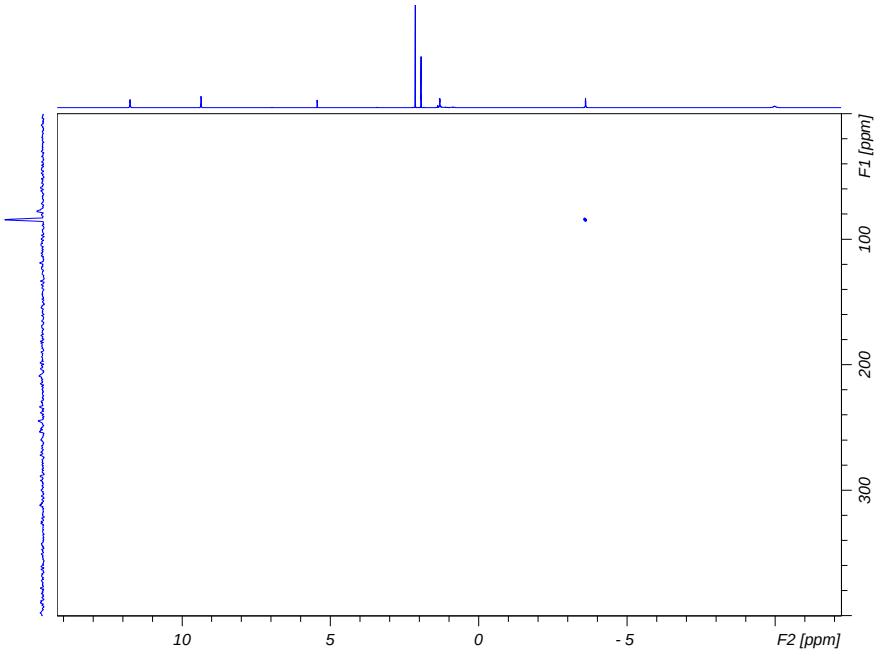

Figure A133: ^{15}N-HMBC-NMR spectrum for complex **Fe^{III}(*p*-CF$_3$ppz)$_3$** in CD_3CN.

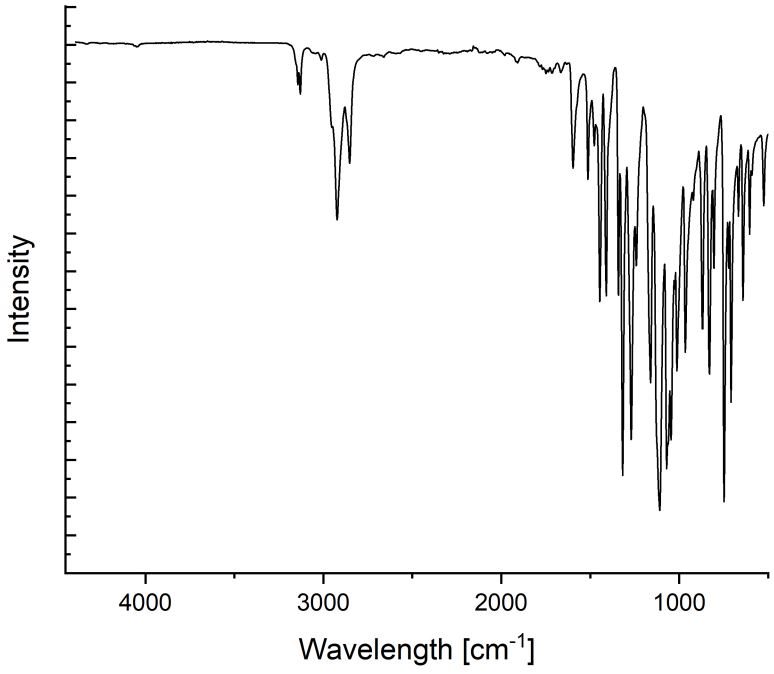

Figure A134: ATR-IR spectrum for complex **Fe^{III}(*p*-CF$_3$ppz)$_3$**.

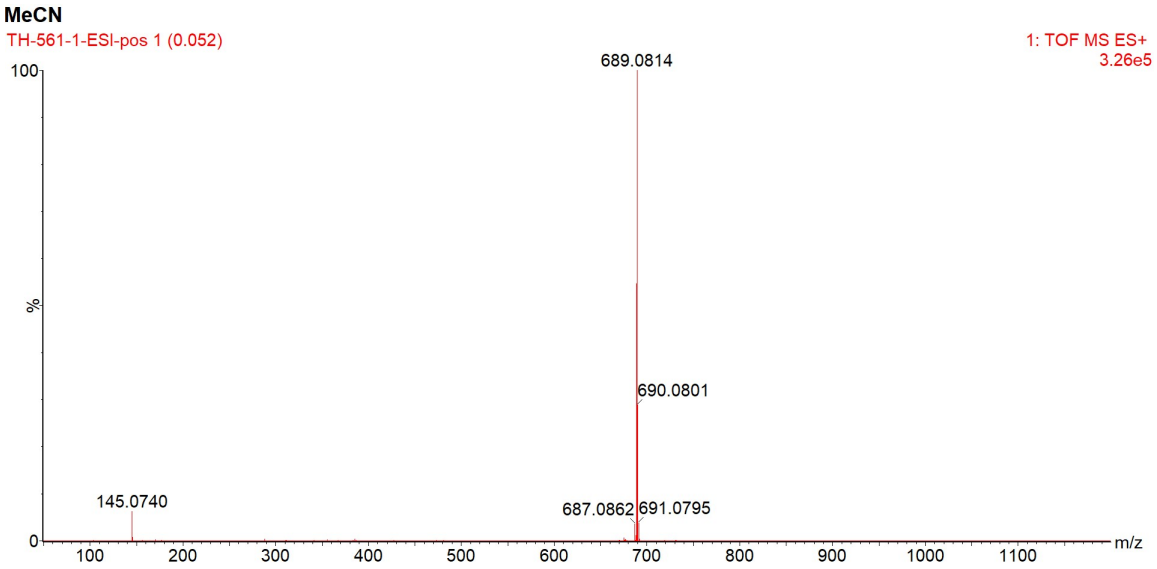

Figure A135: ESI-MS spectrum of complex $\mathbf{Fe^{III}(\textit{m}\text{-}CF_3ppz)_3}$ in MeCN.

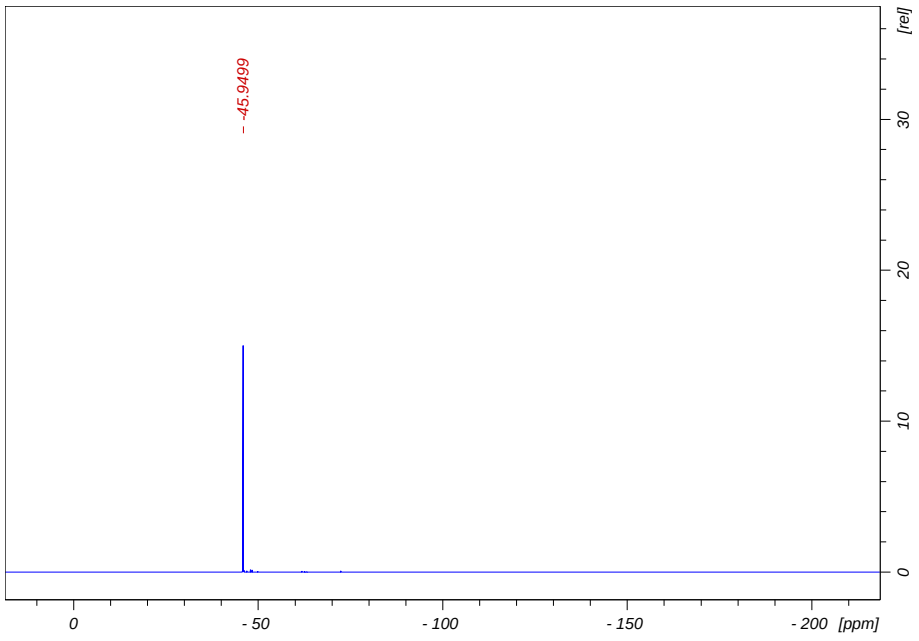

Figure A136: ^{19}F-NMR spectrum for complex $\mathbf{Fe^{III}(\textit{p}\text{-}CF_3ppz)_3}$ in CD_3CN.

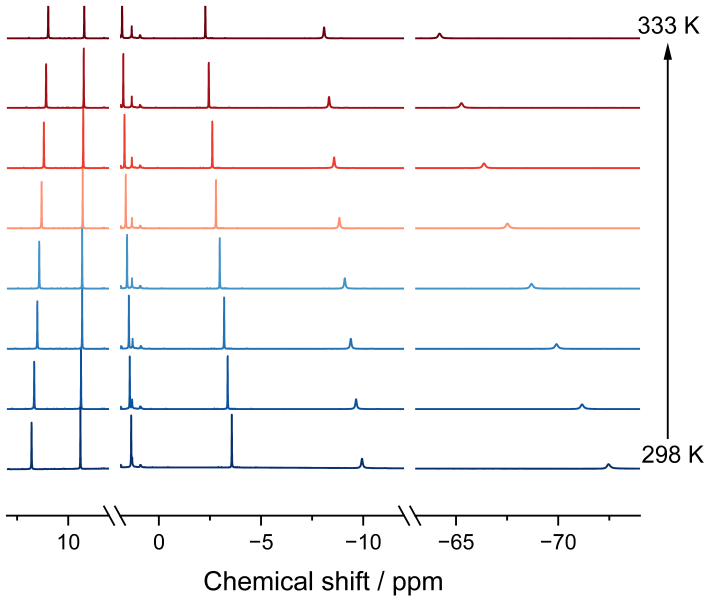

Figure A137: ^{1}H-NMR-spectra of complex $\mathbf{Fe^{III}(\textit{p}\text{-}CF_3ppz)_3}$ from 298 to 333 K.

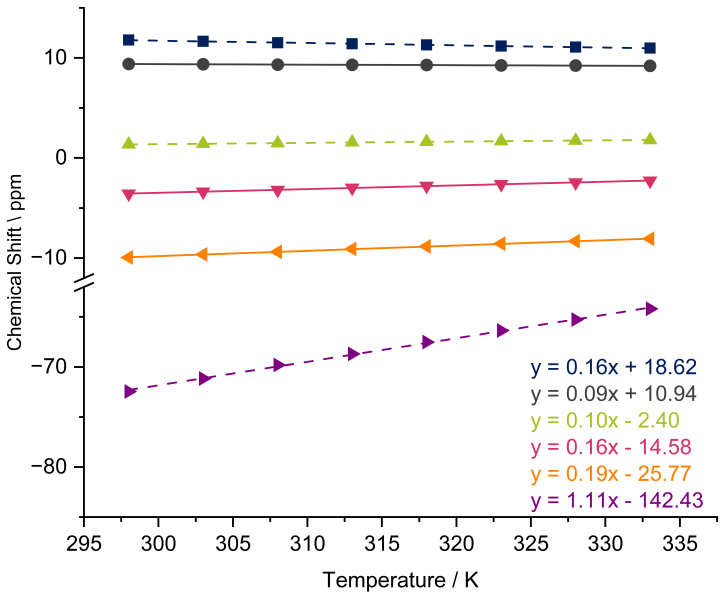

Figure A138: Curie-Plot of complex $\mathbf{Fe^{III}(\textit{p}\text{-}CF_3ppz)_3}$ from 298 to 333 K on the marked positions. Dashed line represents pyrazole-based protons, solid lines represent phenyl-based protons.

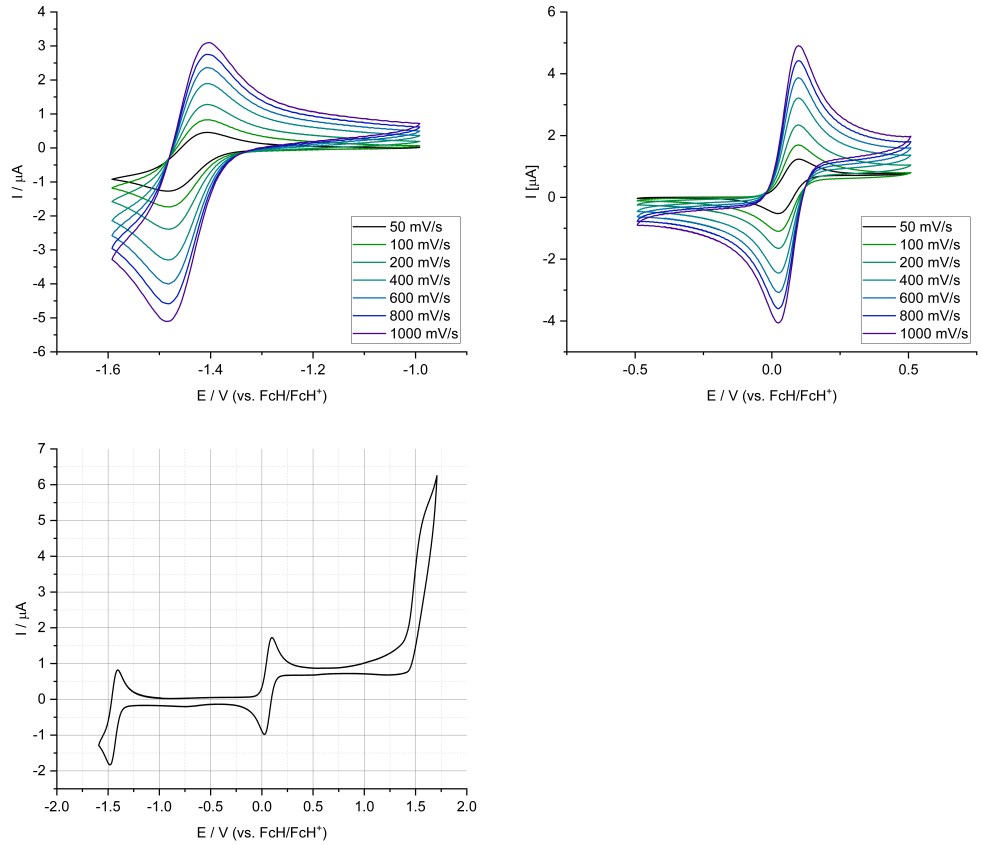

Figure A139: Overview of $\mathbf{Fe^{III}(\textit{p}\text{-}CF_3ppz)_3}$ CV-data. Complete overview and the different redoxcouples at scanrates from 50 to 1000 mV/s.

Table A28: Cyclic Voltammetry data for $\mathbf{Fe(\textit{p}\text{-}CF_3ppz)_3}$ at different scan rates at $E_{1/2}$= -1.53 V vs. Fc/Fc^+

Scanrate	[mV/s]	50	100	200	400	600	800	1000
E_{pc}	[V]	-1.475	-1.475	-1.473	-1.475	-1.473	-1.475	-1.475
E_{pa}	[V]	-1.412	-1.414	-1.409	-1.409	-1.409	-1.407	-1.409
$E_{1/2}$	[V]	-1.44	-1.44	-1.44	-1.44	-1.44	-1.44	-1.44
ΔE	[V]	0.063	0.061	0.063	0.066	0.063	0.068	0.066
I_{pc}	[µA]	-0.73	-1.04	-1.47	-2.07	-2.52	-2.90	-3.24
I_{pa}	[µA]	1.06	1.57	2.21	3.08	3.76	4.47	5.02
I_{pa}/I_{pc}		-1.45	-1.50	-1.51	-1.49	-1.49	-1.54	-1.55

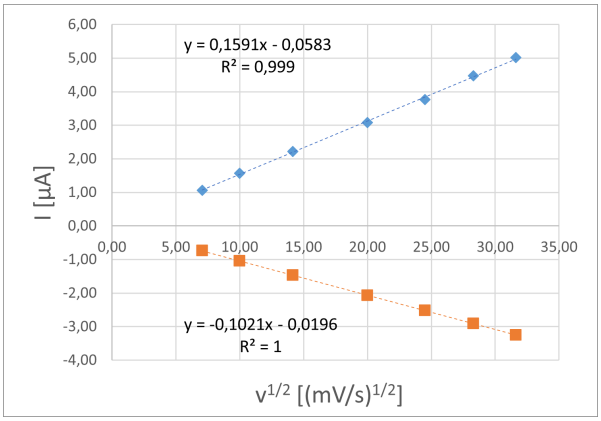

Figure A140: Plotted data of Randles-Sevcik-Equation at different scan rates for **Fe(*p*-CF$_3$ppz)$_3$** $E_{1/2}$= -1.41 V vs. Fc/Fc^+

Table A29: Cyclovoltammetry data for **Fe(*p*-CF$_3$ppz)$_3$** at different scan rates at $E_{1/2}$= -1.53 V vs. Fc/Fc^+

Scanrate	[mV/s]	50	100	200	400	600	800	1000
E_{pc}	[V]	0.028	0.028	0.028	0.025	0.025	0.028	0.028
E_{pa}	[V]	0.093	0.096	0,093	0.096	0.096	0.096	0.096
$E_{1/2}$	[V]	0.06	0.06	0.06	0.06	0.06	0.06	0.06
ΔE	[V]	0.066	0.068	0.066	0.071	0.071	0.068	0.068
I_{pc}	[µA]	-1.02	-1.51	-2.13	-2.98	-3.65	-4.19	-4.67
I_{pa}	[µA]	0.99	1.42	2.02	2.84	3.50	4.04	4.52
I_{pa}/I_{pc}		-0.97	-0.94	-0.95	-0.96	-0.96	-0.96	-0.97

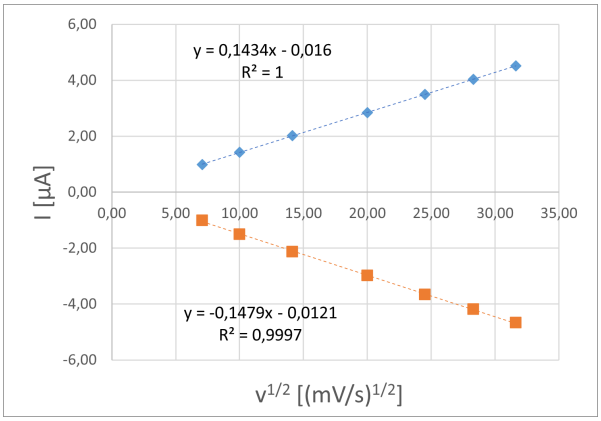

Figure A141: Plotted data of Randles-Sevcik-Equation at different scan rates for **Fe(*p*-CF$_3$ppz)$_3$** $E_{1/2}$= 0.096 V vs. Fc/Fc^+

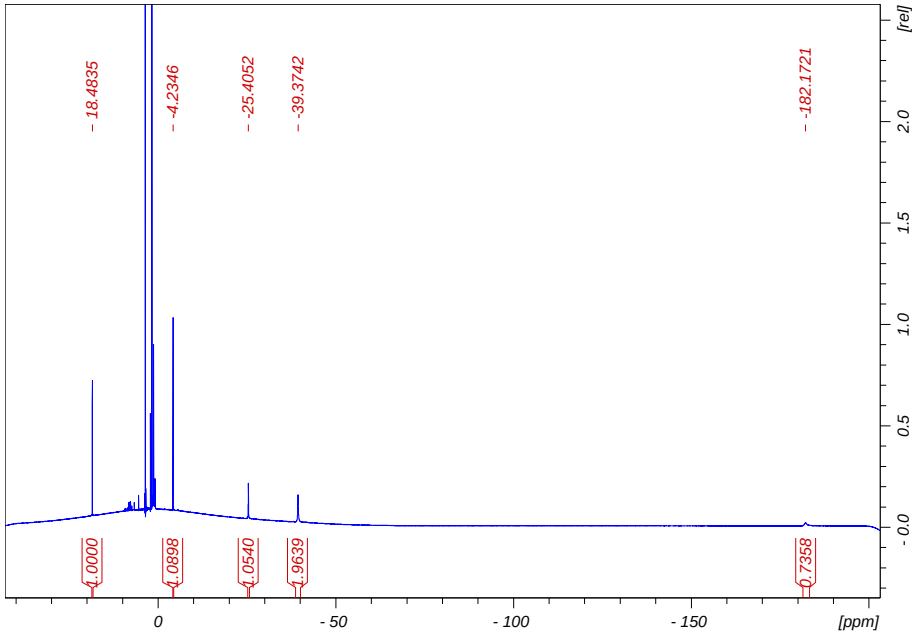

Figure A142: ^{1}H-NMR spectrum for complex $\mathbf{Fe^{IV}(\mathit{p}\text{-}CF_3ppz)_3}$ in THF-d_8.

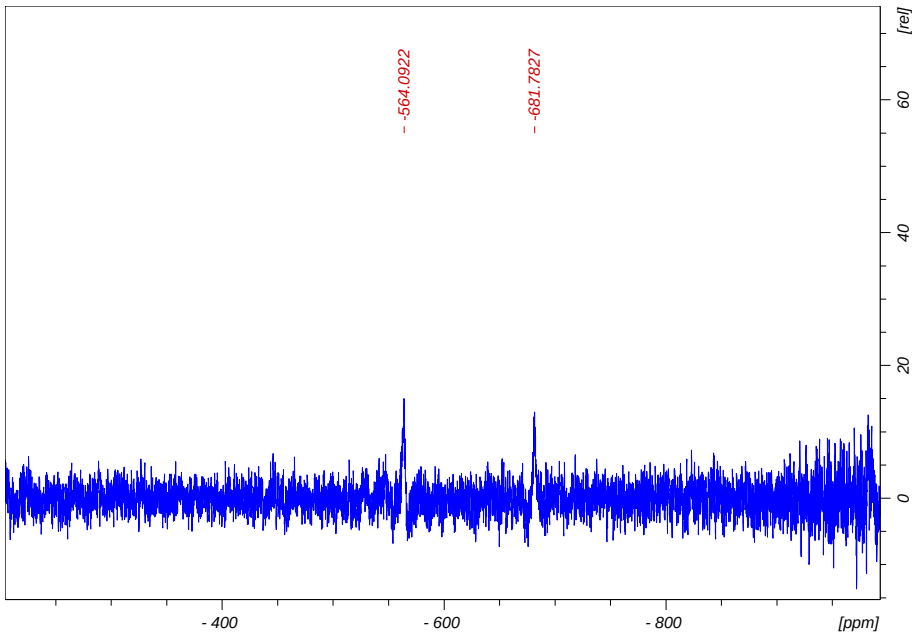

Figure A143: ^{13}C-NMR spectrum for complex $\mathbf{Fe^{IV}(\mathit{p}\text{-}CF_3ppz)_3}$ in THF-d_8, part 1.

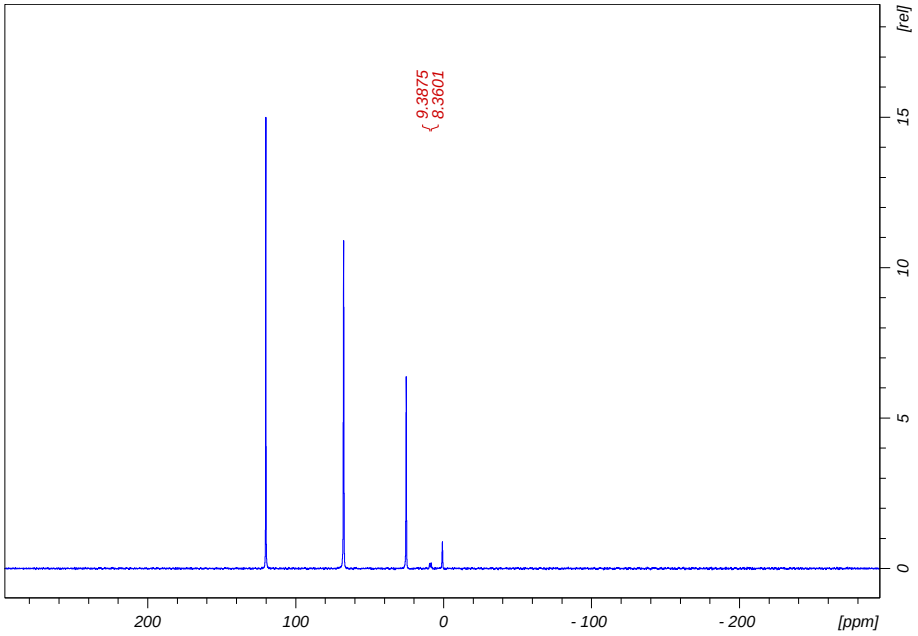

Figure A144: ^{13}C-NMR spectrum for complex $\mathbf{Fe^{IV}(\textit{p}\text{-}CF_3ppz)_3}$ in THF-d_8, part 2.

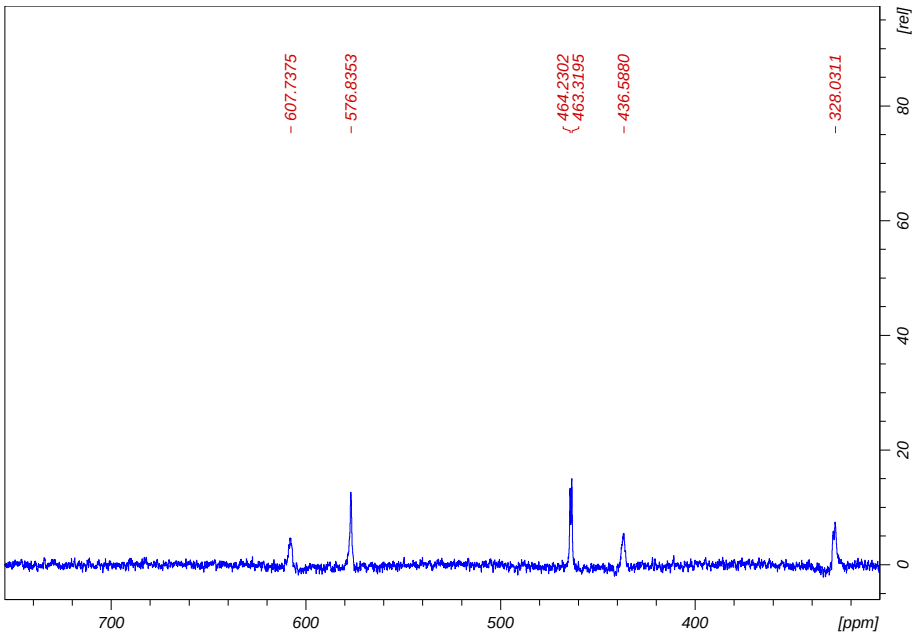

Figure A145: ^{13}C-NMR spectrum for complex $\mathbf{Fe^{IV}(\textit{p}\text{-}CF_3ppz)_3}$ in THF-d_8, part 3.

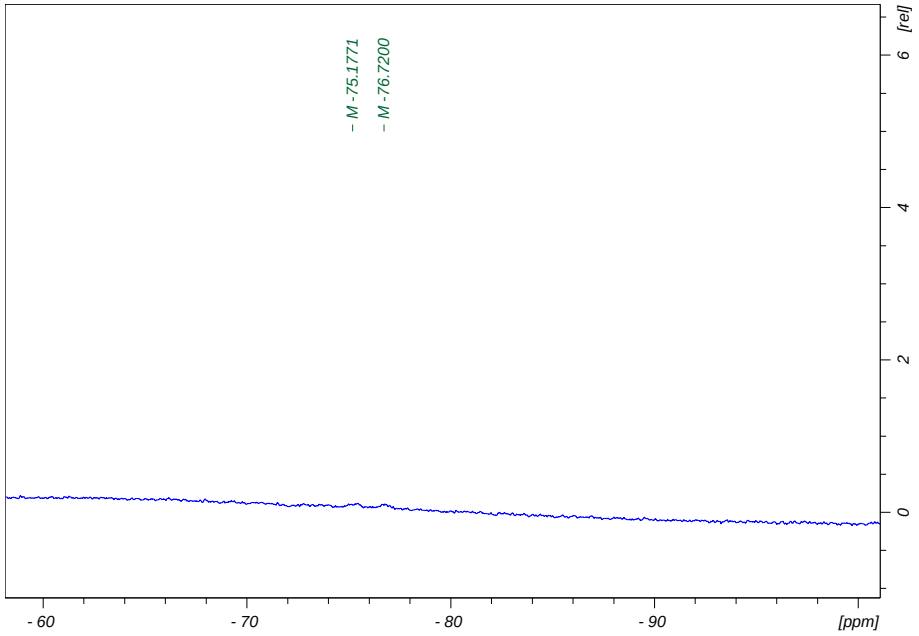

Figure A146: ^{13}C-NMR spectrum for complex $\mathbf{Fe^{IV}(\mathit{p}\text{-}CF_3ppz)_3}$ in THF-d_8, part 4.

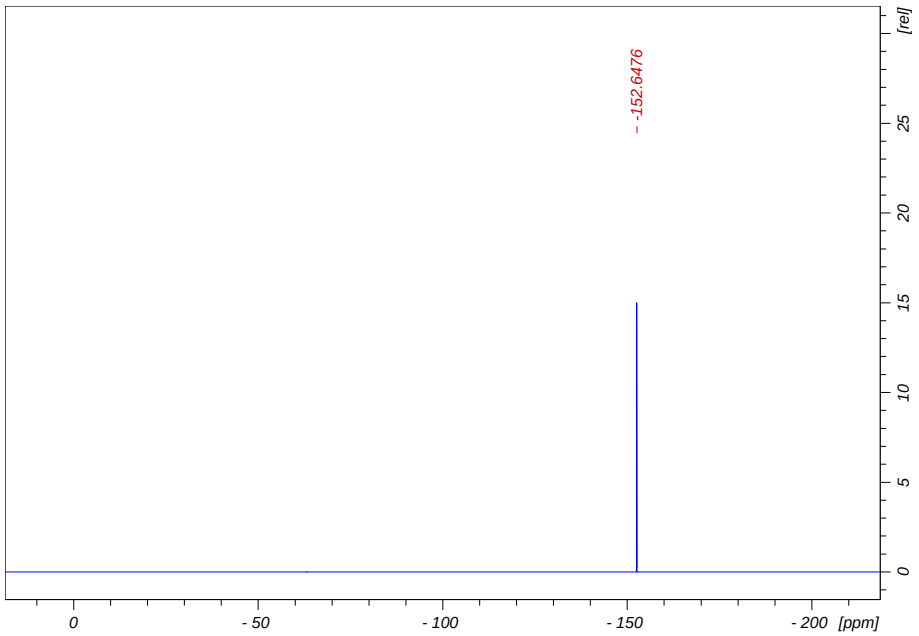

Figure A147: ^{19}F-NMR spectrum for complex $\mathbf{Fe^{IV}(\mathit{p}\text{-}CF_3ppz)_3}$ in THF-d_8.

$Fe^{III}(Fppz)_3$

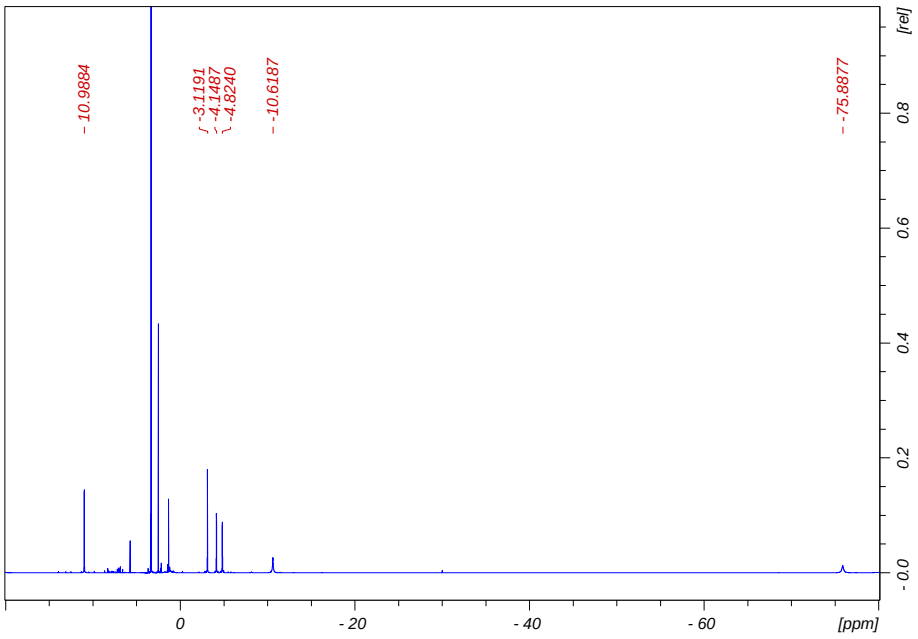

Figure A148: ^{1}H-NMR spectrum for complex $Fe^{III}(Fppz)_3$ in CD_3CN.

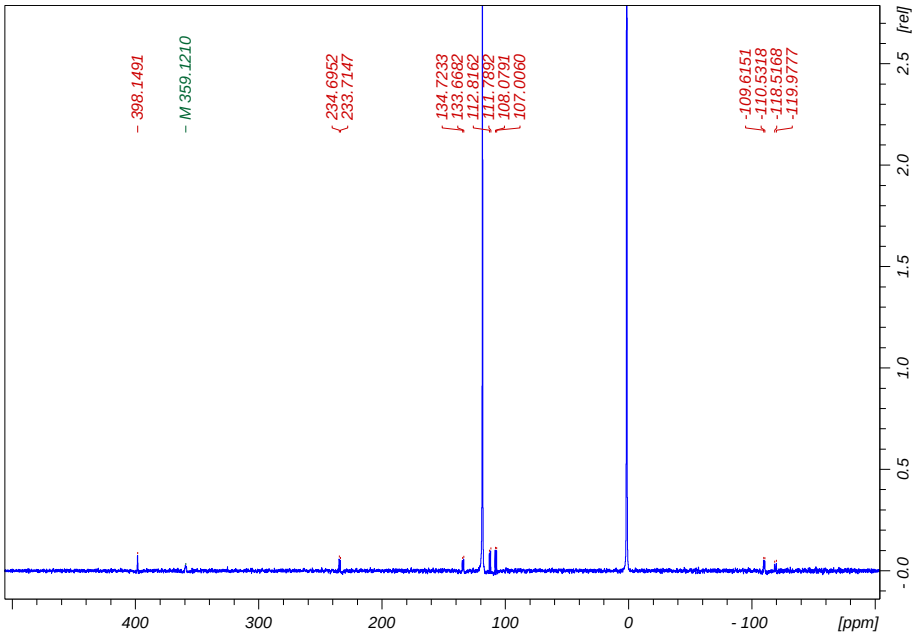

Figure A149: ^{13}C-NMR spectrum for complex $Fe^{III}(Fppz)_3$ in CD_3CN.

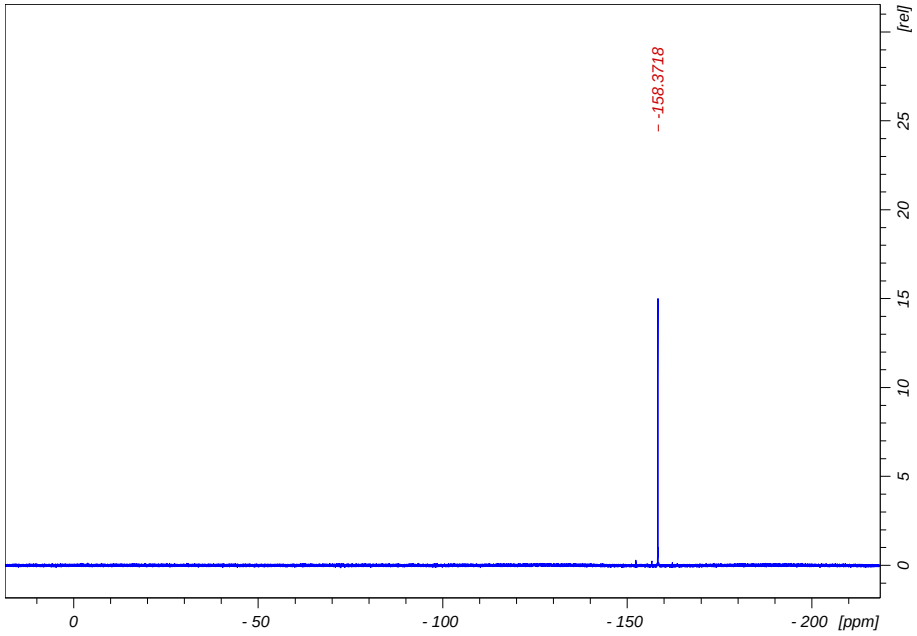

Figure A150: ^{19}F-NMR spectrum for complex $\mathbf{Fe^{III}(Fppz)_3}$ in CD_3CN.

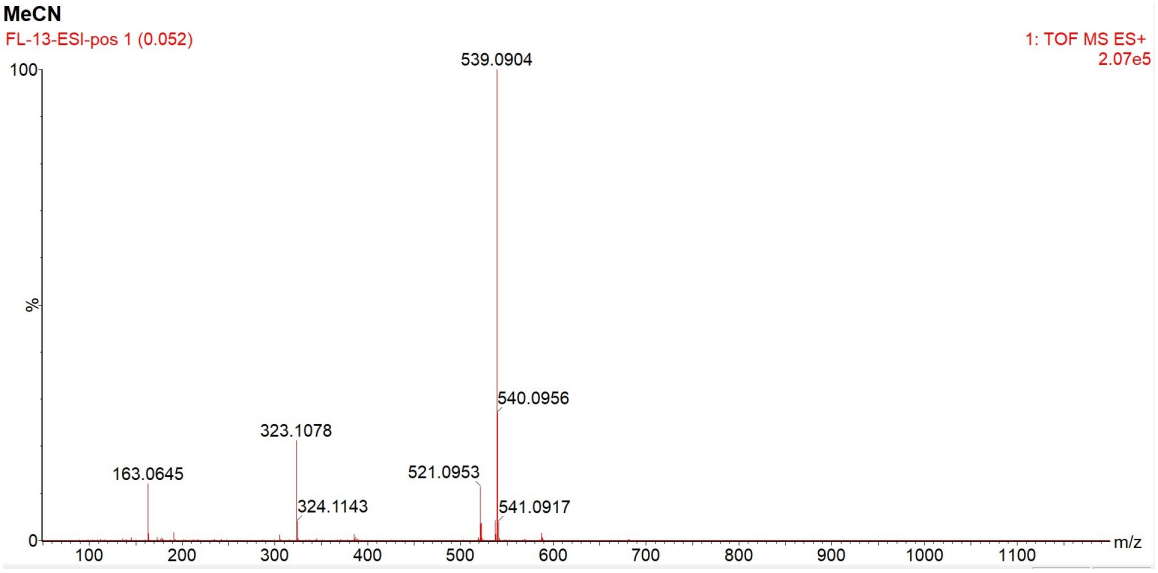

Figure A151: ESI-MS spectrum of complex $\mathbf{Fe(Fppz)_3}$ in MeCN

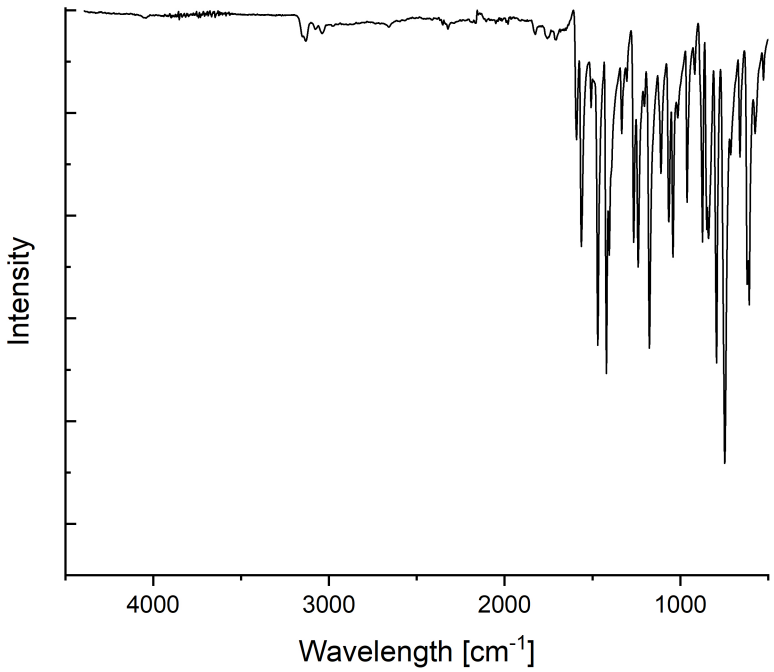

Figure A152: ATR-IR spectrum for complex $\mathbf{Fe^{III}(Fppz)_3}$.

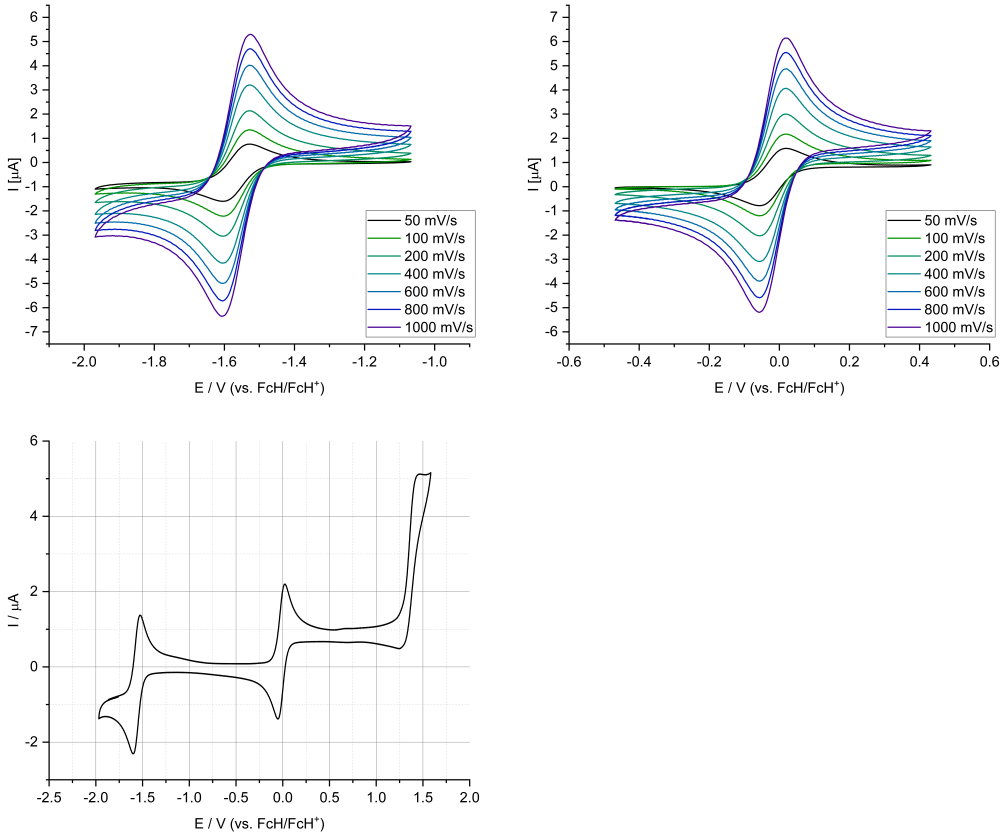

Figure A153: Overview of $\mathbf{Fe^{III}(Fppz)_3}$ CV-data. Complete overview and the different redoxcouples at scan-rates from 50 to 1000 mV/s.

Table A30: Cyclovoltammetry data for **Fe(Fppz)$_3$** at different scan rates at $E_{1/2}$= -1.53 V vs. Fc/Fc^+

Scanrate	[mV/s]	50	100	200	400	600	800	1000
E_{pc}	[V]	-1.598	-1.600	-1.602	-1.598	-1.598	-1.602	-1.602
E_{pa}	[V]	-1.534	-1.529	-1.529	-1.529	-1.529	-1.529	-1.574
$E_{1/2}$	[V]	-1.57	-1.56	-1.57	-1.56	-1.56	-1.57	-1.59
ΔE	[V]	0.063	0.071	0.073	0.068	0.068	0.073	0.028
I_{pc}	[µA]	-1.21	-1.74	-2.50	-3.53	-4.31	-4.93	-5.51
I_{pa}	[µA]	1.33	1.91	2.71	3.77	4.63	5.31	5.91
I_{pa}/I_{pc}		-1.09	-1.09	-1.08	-1.07	-1.07	-1.08	-1.07

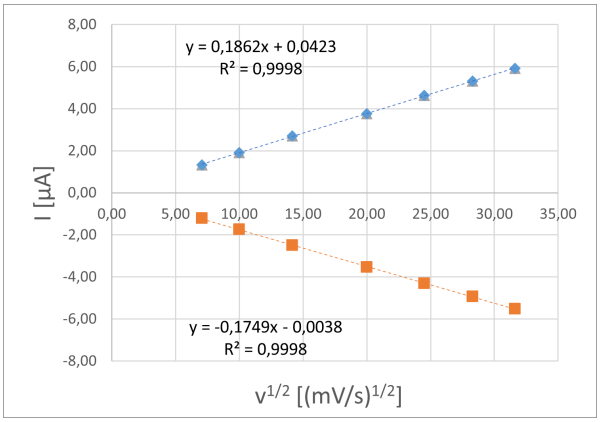

Figure A154: Plotted data of Randles-Sevcik-Equation at different scan rates for **Fe(Fppz)$_3$** $E_{1/2}$= -1.53 V vs. Fc/Fc^+

Table A31: Cyclovoltammetry data for **Fe(Fppz)$_3$** at different scan rates at $E_{1/2}$= -1.53 V vs. Fc/Fc^+

Scanrate	[mV/s]	50	100	200	400	600	800	1000
E_{pc}	[V]	-0.056	-0.053	-0.053	-0.056	-0.053	-0.053	-0.053
E_{pa}	[V]	0.017	0.016	0.015	0.017	0.015	0.015	0.015
$E_{1/2}$	[V]	-0.02	-0.02	-0.02	-0.02	-0.02	-0.02	-0.02
ΔE	[V]	0.073	0.069	0.068	0.073	0.068	0.068	0.068
I_{pc}	[µA]	-1.29	-1.82	-2.62	-3.68	-4.49	-5.18	-5.80
I_{pa}	[µA]	1.34	1.82	2.61	3.70	4.48	5.52	5.80
I_{pa}/I_{pc}		-1.04	-1.00	-1.00	-1.01	-1.00	-1.06	-1.00

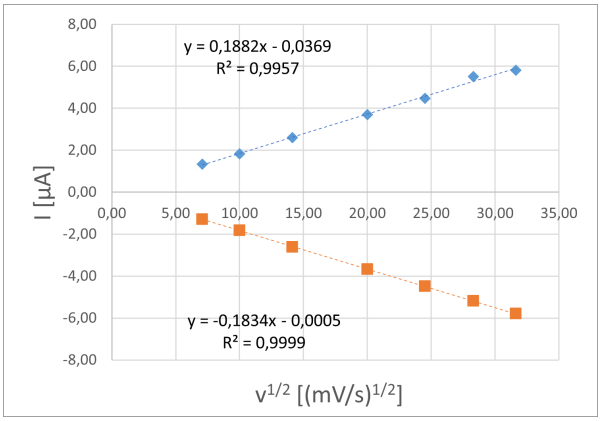

Figure A155: Plotted data of Randles-Sevcik-Equation at different scan rates for **Fe(Fppz)$_3$** $E_{1/2}$= 0.02 V vs. Fc/Fc^+

Imagination is more important than knowledge. For knowledge is limited, whereas imagination embraces the entire world, stimulation progress, giving birth to evolution.

Albert Einstein
1924